

Toward the Nonmetal-to-Metal Phase Transition of Helium

Kumulative Dissertation

zur Erlangung des akademischen Grades

doctor rerum naturalium (Dr. rer. nat.)

der Mathematisch-Naturwissenschaftlichen Fakultät

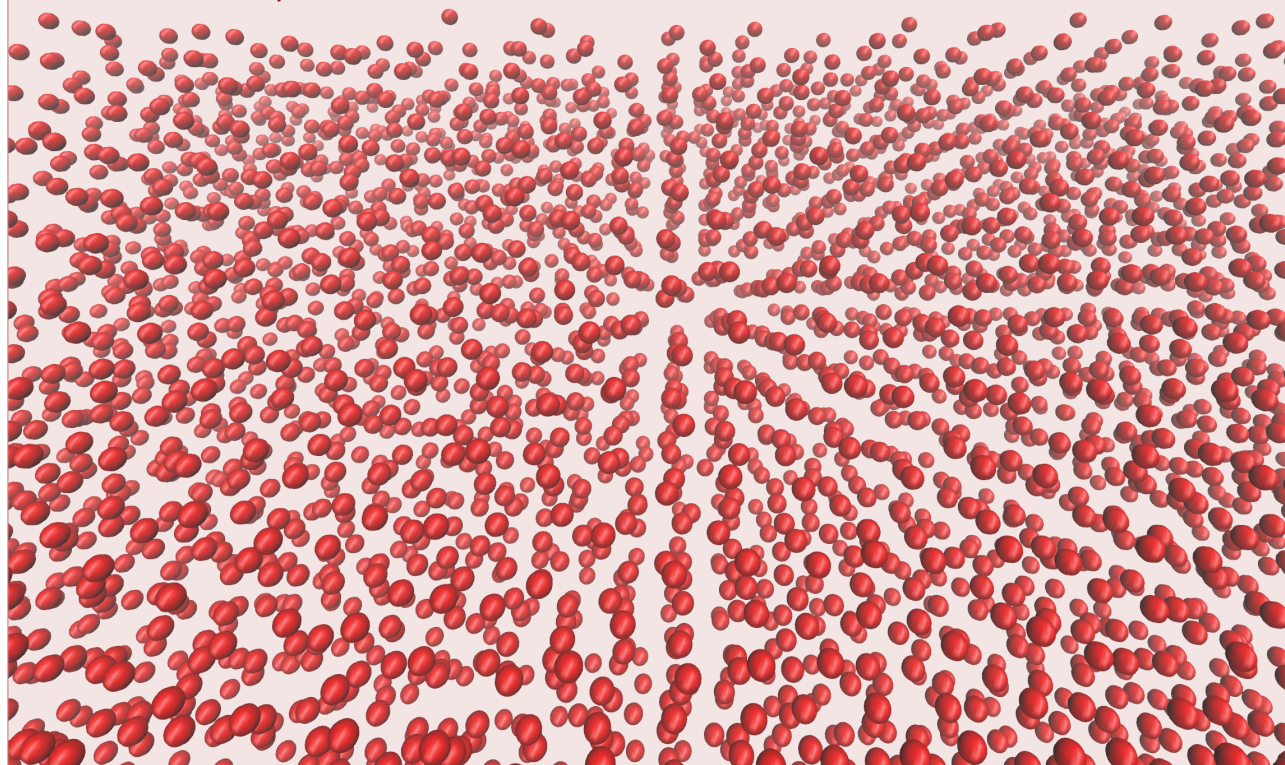
der Universität Rostock

vorgelegt von

Martin Preising, geb. am 12.08.1990 in Günzburg

Rostock, 17. Mai 2021

https://doi.org/10.18453/rosdok_id00003424



Gutachter:

Prof. Dr. Dr. h.c./RAS Ronald Redmer

Institut für Physik, Universität Rostock

Dr. Gerd Steinle-Neumann

Bayrisches Geoinstitut, Universität Bayreuth

Datum der Verteidigung:

Oktober 2021

Adresse:

Universität Rostock

Institut für Physik

18059 Rostock

<https://www.physik.uni-rostock.de>

Abstract

Due to its high abundance in the universe, the properties of helium under high pressure are of great importance for a variety of astrophysical objects. Despite its simple structure, experiments on high-pressure helium pose enormous difficulties. At the same time, the quantum nature of helium under extreme conditions is very challenging for theoretical models. This work presents the results of extensive *ab initio* calculations for high-pressure helium. A comparison of simulations and experiments ensured the viability of the theoretical results. Calculations at conditions beyond present experimental capabilities extended the knowledge of the melting line of helium into a regime that is relevant for the structure of old white dwarfs. Simulations at higher temperatures determined a higher-order phase transition from an insulating to a conducting phase which has been discussed for decades. Furthermore, they predicted physical properties like the equation of state, the reflectivity, and the ionization degree in this regime, providing a basis for future experiments. This work finally presents an update of the phase diagram of helium and discusses its implications on astrophysical objects like white and brown dwarfs, and giant planets like Jupiter and Saturn.

Zusammenfassung

Helium ist das zweithäufigste Element im Universum. Daher sind seine Eigenschaften unter hohem Druck wichtig für eine Vielzahl von astrophysikalischen Objekten. Trotz seiner recht einfachen Struktur sind Experimente an Helium unter extremen Bedingungen sehr aufwendig. Gleichzeitig ist die Abbildung von quantenmechanischen Effekten bei hohen Drücken für eine Vielzahl theoretischer Beschreibungen sehr herausfordernd. Diese Arbeit präsentiert die Ergebnisse umfangreicher *Ab-initio*-Berechnungen für Helium bei hohen Dichten. Der Vergleich von Simulationen mit Experimenten bezeugt die Qualität der theoretischen Methoden. Berechnungen bei Drücken, die in Experimenten an Helium noch nicht erreicht wurden, sagen die Schmelzdrucklinie bis zu Bedingungen voraus, die für alte Weiße Zwerge relevant sind. Simulationen bei höheren Temperaturen weisen einen kontinuierlichen Phasenübergang zwischen isolierendem und elektrisch leitfähigem Helium nach, der bereits seit Jahrzehnten diskutiert wurde. Die Ergebnisse von Berechnungen weiterer physikalischen Größen wie der Zustandsgleichung und der Reflektivität können zukünftig mit Experimenten überprüft werden. Schließlich zeigt diese Arbeit ein aktualisiertes Phasendiagramm von Helium und diskutiert die Konsequenzen für astrophysikalische Objekte wie Weiße und Braune Zwerge sowie die Riesenplaneten Jupiter und Saturn.

Contents

Abstract	III
1. Motivation	1
1.1. General properties of helium	2
1.2. Stars	4
1.3. Jupiter and Saturn	6
1.4. State-of-the-art experiments and theories	8
1.5. Outline of this thesis	10
2. Methods	11
2.1. Density functional theory molecular dynamics (DFT-MD)	11
2.1.1. Born-Oppenheimer approximation	11
2.1.2. Density functional theory (DFT)	12
2.1.3. Plane waves and pseudopotentials	15
2.1.4. Molecular dynamics (MD)	16
2.1.5. Implementation of DFT-MD in the VASP code	17
2.2. Calculation of thermophysical properties	19
2.2.1. Equation of state	19
2.2.2. Dynamic electrical conductivity	20
2.2.3. Direct current (DC) conductivity	20
2.2.4. Reflectivity	21
2.2.5. Ionization degree	23
2.3. Two-phase simulation method	26
2.4. Calculation of the band gap within DFT-MD	28
3. Results	33
3.1. Benchmark of the tools against a wide range of experiments	35
3.2. Calculation of the high-pressure melting line	39
3.3. Band gap closure at high pressures	42
3.4. Influence of different XC functionals on the location of the dissociation of hydrogen and deuterium	46
3.5. Conclusion	51
3.6. Outlook	54
4. Publications	55
4.1. Equation of state and optical properties of warm dense helium	55
4.2. The high-pressure melting line of helium	66

4.3. Metallization of Helium at High Densities from <i>ab initio</i> Simulations .	74
4.4. Evaluation of exchange-correlation functionals with multiple-shock conductivity measurements in hydrogen and deuterium at the molecular-to-atomic transition	83
A. Appendix	95
A.1. Convergence of the TPS method	95
A.2. Convergence of high-pressure properties around the band gap closure of helium	101
A.2.1. DC conductivity	102
A.2.2. Reflectivity	105
A.2.3. Ionization degree	108
B. Bibliography	112
C. Curriculum vitae	128

1. Motivation

Helium constitutes about 23% of the visible matter of the universe.¹ The vast majority of the remainder consists of hydrogen, while heavier elements like oxygen and carbon amount to only 2%. Most of the helium in the universe is a direct product of nucleosynthesis in the first few minutes after the big bang.^{2;3} To date, the alpha decay and the nuclear fusion of hydrogen in the interior of stars produce helium.⁴⁻⁶

Helium exists, for example, within the interior of stars like the Sun,⁷ giant gas planets like Jupiter⁸ and Saturn,⁹ and the atmospheres of giant ice planets like Uranus¹⁰ and Neptune.¹¹

Helium exhibits exceptional and unique low-temperature properties. It is predicted to remain liquid even at a temperature of absolute zero.¹² Therefore, liquid helium can cool other materials to very low temperatures at which they may become superconducting, depending on the material. From a physicist's point of view, the different properties of helium-4, a boson comprised of two protons and neutrons, and the isotope helium-3, a fermion with two protons and one neutron, are very intriguing. The unique properties of mixtures of helium-3 and helium-4 are utilized to cool down materials to temperatures of a few millikelvins^{13;14} in so-called dilution refrigerators. Such low temperatures are required, for example, in experiments on quantum information technology,¹⁵ in particle physics,¹⁶ and in superconductivity research.¹⁷

This chapter discusses the general chemical and physical properties of helium, its relevance for everyday life, as well as the relevance for astrophysical objects by the example of stars and the giant gas planets Jupiter and Saturn.

1.1. General properties of helium

Helium is the first and the lightest noble gas in the periodic system. Chemical compounds with helium only form under special conditions,¹⁸ such as high pressure^{19;20} and low temperatures.^{21–25} The reason is the very low electron affinity of 0.08 eV, as well as the first ionization energy of 24.59 eV,²⁶ which is the highest out of all elements. Helium is also the element with the smallest atomic radius, i.e., the smallest distance between the atomic nucleus and the surrounding two electrons.¹⁹ The very low reactivity qualifies the use as a protective gas in high-purity industrial processes,²⁷ while the high diffusivity due to the small atomic radius allows for detecting leaks in high-pressure and high-vacuum containers.²⁸ However, the high diffusivity has the disadvantage of making experiments on high-pressure helium more elaborate and expensive. Diamonds used to create high pressures become brittle and break due to the diffusion of helium into the diamond anvils. Gaseous helium is lighter than air. The resulting uplift is exploited by airships. Helium hardly interacts with light. Therefore, it has a refraction index very close to unity in the gas phase,²⁹ the liquid phase,³⁰ and the solid phase, to the point where it is difficult to distinguish the solid and the liquid phase in experiments.

Upon cooling, all elements except for helium enter the solid phase at standard atmospheric pressure. Helium, however, liquefies at temperatures T of about $T = 4$ K and remains liquid, even theoretically at absolute zero. This unusual behavior comes due to the weak attractive forces between the helium atoms, rendering helium a quantum fluid in this temperature regime. At such low temperatures, the effects of quantum mechanics play a major role by further lowering the attractive forces: Due to lower zero-point energy at greater interatomic distances, the ground state energy decreases correspondingly. At greater distances, however, the attractive forces decrease even further,³¹ which is why helium expands upon further cooling. Among all cryogenic fluids, helium has the lowest boiling point.¹² In combination with the very high heat conductivity, this is useful for cooling purposes: Most superconducting magnets employ liquid helium as a coolant, such as those used for magnetic resonance imaging and those employed in particle accelerators like the LHC at CERN and the XFEL. The physics Nobel Prize in 1913 was awarded for the first liquefaction of helium.³²

Below about 2 K, helium becomes superfluid, and its properties change dramatically. Its quantum nature manifests on a macroscopic scale, and it behaves like a mixture of a normal and a superfluid liquid. The latter has a viscosity of zero and therefore flows without friction, even through tubes that are only a few times larger than the helium atoms themselves.³³ The surface tension of superfluid helium leads to unusual strong creeping abilities called the film flow. An open container filled with a superfluid will empty itself by means of this 30 nm thick Rollin film³⁴ until hydrostatic equilibrium with the environment is achieved. Superfluid helium can also create fountains as a result of its macroscopic quantum properties: Forces usually act due to a gradient of potential energy. However, the potential energy in question is arbitrary. In superfluid helium, the gradient of the chemical potential

contributes significantly to the forces on the fluid. Therefore, under certain conditions, a resulting pressure can manifest as a fountain of superfluid helium. Certain types of extremely low-temperature refrigerators exploit this effect.^{13;14} Rotation also works differently in the superfluid state: Usually, a liquid adopts the rotation of the container. However, when superfluid helium is poured into a container that rotates slower than a critical velocity, the superfluid does not begin to rotate itself due to the non-existent internal friction within the liquid. At a higher angular velocity, the rotational energy leads to the formation of quantized vortices in so-called Abrikosov lattices,³⁵ where the number of vortices depends on the rotational speed of the container.³⁶ Superfluid helium has exceptional cooling abilities because it transports heat by convection instead of heat conduction, which is about a million times more efficient than that of non-superfluid helium and close to a hundred times better than that of copper.³⁷

Due to the low atomic weight and the relatively strong influence of quantum fluctuations, in order to transition to the solid phase, helium requires a pressure of 2.5 MPa (25 bar) at very low temperatures,³⁸ and about 11.7 GPa at room temperature.³⁹ As discussed earlier, helium is monoatomic, except for very special conditions. The solid forms the hexagonal close-packed (hcp) and the face-centered cubic structure,⁴⁰ depending on pressure and temperature. Calculations predict the body-centered cubic phase at extremely high pressures.⁴¹ Solid helium is about 100 times more compressible than water.²⁷ Over 60 years ago, a supersolid phase of helium was predicted,^{42;43} which combines the properties of a solid with superfluid properties: The superfluid atoms can flow between defects in the crystalline structure without resistance. Usually, the mobility of a fluid decreases at lower temperatures. In a supersolid, however, the flow results from quantum effects that grow more pronounced at lower temperatures. Experiments confirmed many of the predicted properties.⁴⁴⁻⁴⁶

Other than the previously discussed bosonic helium-4, consisting of two protons and neutrons, the other main isotope of helium is helium-3, consisting of two protons and one neutron. While helium-4 is a boson and therefore has a spin of zero, helium-3 is a fermion with a corresponding spin of 1/2. The quantum mechanical behavior of bosons strongly contrasts that of fermions. Due to the low atomic mass of the helium isotopes, the impact of the additional/missing mass of one neutron has a profound effect on the properties of the respective isotope. Helium-3 has a high absorption cross-section of neutrons and is therefore used in neutron detectors. The superfluidity of helium-4 is closely connected to its bosonic nature. Thus, the fermionic helium-3 can only enter the superfluid state upon forming pairs. While helium-4 becomes a superfluid at about 2 K, the temperature has to be below about 2.5 mK in the case of helium-3.⁴⁷⁻⁴⁹ The discovery of this phase transition led to a Nobel Prize in 1996 and another one in 2003.

1.2. Stars

The Sun generates energy from nuclear fusion and makes up over 99.8% of the total mass of our solar system. It is over 300 000 times more massive than our Earth.⁵⁰ The Earth, including its atmosphere, consists only of 260 parts per million (ppm) in the case of hydrogen, and only traces of helium can be found in the atmosphere (52 ppm) and the continental crust (0.008 ppm).²⁷ By contrast, over 73% of the Sun's mass is due to hydrogen, while helium makes up about 25%.⁵¹ The high density and temperature at the center of the Sun fuses hydrogen atoms to helium atoms via the so-called proton-proton chain.⁵² More massive stars can also convert hydrogen to helium with the CNO cycle.⁵³

In the past 4.6 billion years since its formation,^{54;55} the Sun converted roughly 100 times the mass of the Earth into energy. About 5.4 billion years in the future, the Sun will exhaust most of its hydrogen resources in the core, which will mark the end of the main-sequence stage in the life of the Sun.⁵⁶ In the further stages of the Sun's evolution, helium plays a major role in the so-called helium flash that will convert the majority of the helium within the Sun (about 40% of the Sun's mass) into carbon in a matter of minutes. This process will release the energy equivalent to roughly ten times the Earth's mass per second.⁵⁷ After that, the Sun will shrink from a size that could possibly encapsulate Earth's orbit⁵⁸ to about 10 times its current size and continue to burn helium. The fusion of the carbon core with the helium shell produces heavier elements like oxygen. Several more cycles of expansion and contraction will shed about half of the Sun's mass. Finally, the center of our solar system will become a white dwarf (WD), in which the Sun will have the size of the Earth but about 200 000 times Earth's mass.⁵⁸ As WDs do not undergo nuclear fusion, this stellar remnant remains stable and cools down over time. Models suggest that our galaxy contains about ten billion WDs to date,⁵⁹ and 97% of all the stars in our galaxy will eventually end up as WDs.⁶⁰

Stars with a mass below half of the Sun's mass will not ignite helium fusion but instead burn most of their hydrogen. In the end, they will contain mostly helium.⁶¹ Those helium WDs⁶² can exhibit such low temperatures of a few thousand Kelvin at very high densities that a large portion of the star's shell could exist as a solid, while the core remains a degenerate plasma. The rate of energy transport, and therefore the cooling rate of the helium WD,⁶³ strongly depends on the phase of the respective material: a metallic layer, either solid or fluid, conducts heat via electron transport, while the transport mechanism in solid insulators acts via phonons, and via convection in fluid insulators. Models predict metallic solid helium in the outer layers of WDs.^{64;65} Higher metallization pressures directly result in slower heat transfer, which in turn increases the time required for a WD to cool down and decreases its luminosity.

A common way to determine the age of a cosmic region is to count the number of WDs with certain luminosities: a high number of cold/dim WDs indicates a great age, a high number of hot/bright WDs implies a young region.^{60;66} The inference from the luminosity to the age of a given WD requires knowledge of the

cooling behavior, which in turn demands accurate measurements or models of the composition of the WDs. However, interior models rely on information about the behavior of matter under extreme conditions, such as the melting line and the location where metallization in dense helium occurs, as discussed above. Another important implication of the metallization is the magnetic field: While one can encounter the strongest magnetic fields of a few Teslas in everyday life in the form of Magnetic Resonance Imaging, WDs can have magnetic fields with a strength of up to 100 000 T.⁶⁷ However, only electrically conducting matter can contribute to the generation of magnetic fields. Therefore, accurate models of magnetic WDs require an accurate description of their components, such as their equation of state, electrical conductivity, and ionization degree.

1.3. Jupiter and Saturn

The first space probe to explore Jupiter was Pioneer 10, passing the giant planet at the end of 1973.⁶⁸ Among others, it encountered intense particle radiation and a magnetic field which is about ten times more intense than the Earth's and carries about 250 000 times the total energy.⁶⁹ The follow-up missions, Pioneer 11 in 1974,⁷⁰ Voyager 1⁷¹ and Voyager 2⁷² in 1979, and Ulysses in 1992,⁷³ recorded further information on the magnetosphere, the Jovian moons, its radiation belt, atmospheric properties, as well as thousands of images. At the end of 1995, the Galileo space probe arrived at Jupiter.⁷⁴ It carried an entry probe that entered the Jovian atmosphere. The recorded helium abundance of $23.8\pm 0.5\%$ ^{8;75} is significantly lower than the $27.5\pm 0.5\%$ of the Sun,^{76;77} which has a profound impact on the interior structure of Jupiter; see the discussion below. After two more fly-bys in the course of the Cassini-Huygens mission in 2000⁷⁸ and the New Horizons mission in 2006 and 2007,⁷⁹ the Juno spacecraft reached Jupiter in 2016.⁸⁰ It still orbits the giant planet and continues to measure, among others, atmospheric processes, its composition, and the Jovian magnetosphere.

Until today, four space probes visited Saturn: Pioneer 11 in 1979,⁸¹ Voyager 1 in 1980,⁸² Voyager 2 in 1981,⁸³ and the Cassini orbiter from 2004 to 2017.⁸⁴ Measurements of the Cassini spacecraft determined a helium mass fraction of 7.5 to 13%.⁸⁵ The reason for this very low helium abundance compared to the protosolar value of $27.5\pm 0.5\%$ and the Jovian value of $23.8\pm 0.5\%$ is under vivid discussion in the scientific community. In the future, the Hera entry probe mission,⁸⁶ scheduled to launch in 2027, will provide *in situ* measurements of Saturn's atmosphere.

The reason for the helium depletion in the gas giant planets compared to the protosolar helium fraction is probably the so-called helium rain: Hydrogen becomes metallic in the planetary interior due to pressure and temperature ionization.^{87;88} The metallization of hydrogen then causes the hydrogen-helium mixture in the atmosphere to separate into a helium-rich and a helium-depleted phase, a phenomenon called demixing.⁸⁹ Experimental measurements of demixing are very elaborate, even for mixtures of heavier elements. Due to the high diffusivity, among others, the measurement of any properties of hydrogen-helium mixtures poses a genuine challenge for experiments. Theoretical descriptions, although computationally demanding, provided an accurate prediction of the demixing diagram of hydrogen and helium,^{89;90} which can now serve as an input for planetary modeling. The demixing diagram predicts the helium melting line fundamentally different from usual first-principal calculations of the melting line, which can act as a consistency check within the theoretical framework.

The helium-rich droplets that form due to demixing are heavier than the helium-depleted ones and therefore sink toward the core.⁹¹ There, the helium might diffuse into the solid rock, effectively diluting it. Moreover, the helium rain might bind neon and therefore also account for the depletion of neon in the upper atmosphere of Jupiter and Saturn.⁹² Helium rain creates friction and releases gravitational energy, adding energy that slows the cooling of the gas giants and contributes to the heat

that Jupiter and Saturn radiate into space.⁹³ Both gas planets emit more heat than they receive from the Sun, 1.7 times more for of Jupiter and 2.5 times more for Saturn.^{94–97}

The helium rain could form a very helium-rich layer around the planetary core of the gas giants, where the extreme pressures might lead to the metallization and crystallization of helium. Solid layers within the planets would not convect and therefore inhibit convective heat transport, as well as the formation of a planetary dynamo. On the other hand, should the metallization of helium occur in the liquid, the conductive fluid helium would contribute to the magnetic field. Simulations of the magnetic field of Jupiter with an accurate prediction of the metallization behavior of hydrogen could reproduce the observational data with staggering accuracy.⁹⁸

To date, the most recent experiments on the metallization of helium extend to pressures of about 140 GPa and temperatures of close to 60 000 K.⁹⁹ Experiments on the melting line of helium demonstrated pressures of 80 GPa and temperatures of about 1 000 K.¹⁰⁰ However, models of the interiors of Jupiter¹⁰¹ and Saturn⁹⁷ predict pressures of up to 18 TPa and 50 000 K, i.e., pressures that are 100 times greater than those of the latest experiments. While accurate interior and evolution models of giant gas planets require the knowledge of the behavior of helium under those extreme conditions, they are probably out of experimental reach for decades to come, as high pressures at low temperatures are very challenging experimentally. However, the calculations in the course of this work provide the required data.

Of course, helium and its properties are not only crucial for Jupiter^{102–104} and Saturn^{97;105} but also for Uranus^{106–109} and Neptune,^{106;108;109} as well as for brown dwarfs^{110;111} and the planetary class of inflated hot Jupiters.¹¹²

1.4. State-of-the-art experiments and theories

The diffusivity and creeping abilities of helium make it notoriously difficult to perform high-pressure measurements at all. Then, as most diagnostic tools rely on optical measurements, the refractive index that is very close to unity further complicates precise experiments.

A few methods have been developed to compress matter to high pressures.¹¹³ One approach is using multiple-stage gas guns,¹¹⁴ which accelerate a flyer plate that subsequently hits a target and creates extreme conditions upon impact. Another dynamic approach uses explosives to compress a sample.⁶⁴ The irradiation with particle beams¹¹⁵ or strong laser pulses, be it direct¹¹⁶ or indirect,¹¹⁷ also induces high densities. Strong magnetic fields can either directly compress a plasma with a Z-pinch¹¹⁸ or alternatively accelerate a flyer plate towards a sample.⁸⁸ These dynamic compression experiments require precise diagnostics due to the short-lived nature of the experimental conditions of interest. Usually, dynamic shock wave experiments probe conditions on the Hugoniot curve, which describes all the thermodynamic states that start from a given density and temperature. Calculations of Hugoniot states from a given equation of state are straightforward. However, this type of experiment is limited to the conditions on the Hugoniot curve, and off-Hugoniot states, which are interesting for astrophysical and planetary modeling, cannot be accessed.

Static approaches employ diamond anvil cells, where anvils made of small diamonds compress even smaller samples in between them.^{39;119} Due to the static nature of the experiments, the measurements can be taken over a greater amount of time, thereby potentially reducing uncertainties. As of now, this approach is limited to low temperatures and to significantly lower densities than the dynamic experiments.¹⁰⁰ The heating of a sample after an initial static compression can provide temperatures of a few thousand kelvins. A particular problem with helium is the high diffusivity, which quickly destroys the diamond anvils under these conditions.

While high temperatures¹¹⁸ and highest pressures¹²⁰ can be achieved with dynamic shock wave experiments, only static experiments can access the low-temperature regime. However, the combination of high densities and comparably low-temperature states of a few thousand kelvins is very hard to accomplish. Starting from a precompressed sample¹²¹ and/or the use of experimental configuration with more than one shock,^{88;122} the compression path essentially consists of a combination of Hugoniot curves, where each Hugoniot starts from the endpoint of the last shock. When done correctly, this ramp compression path closely follows the isentrope of the system, rendering this type of experiment quasi-isentropic.¹²³ Most recent experiments in the regime that is relevant for this thesis employ quasi-isentropic compression techniques.

In dynamic experiments, velocity interferometer systems for any reflector (VISAR)¹²⁴ measure the velocities of the impactors as well as the shock wave profiles. The recorded fringe patterns contain information on the reflectivity and the velocity of the shock front.¹²⁵ Other quantities of interest, like the sample pressures,

result from postprocessing via the equation of state of other materials used in the experiments, usually lithium fluoride. Pyrometers can measure the temperature directly via the emitted black-body radiation.¹²⁶ Aside from a direct measurement of the electrical conductivity,^{127;128} models for the dynamic electrical conductivity provide conductivity data from optical reflectivities.¹²⁹ All optical properties of a system depend strongly on its ionization degree, which therefore often serves as an input parameter for experiments,¹³⁰ and many codes have been developed that predict the ionization degree.^{131–133}

The description of this warm dense matter regime poses a challenge for classical molecular dynamics and chemical models due to their inability to describe the strong quantum correlations under those conditions. While chemical models predicted two first-order phase transitions between the neutral and the conducting phase of helium,^{134–136} the most recent *ab initio* simulations^{137–139} discovered a continuous transformation to the metallic state. The main principle of *ab initio* simulations is to use only physical constants as input for the calculations and, ideally, not to rely on approximations. Among the variety of *ab initio* approaches, the Quantum Monte Carlo (QMC)^{140;141} method has extremely high accuracy at the expense of increased computational demand. QMC calculations therefore only allow the treatment of a few tens of particles. Another *ab initio* method is the combination of finite-temperature density functional theory (DFT) to describe the electronic system and classical molecular dynamics (MD)¹⁴² to treat the ionic part. Here, all the unknown components of quantum mechanical interaction are represented by the exchange-correlation (XC) functional. While no analytical expression of the exact XC is possible, many approximations give an accurate description of quantum systems. Due to the high efficiency and the accurate results in the warm dense matter regime, we employ DFT-MD methods in this thesis.

1.5. Outline of this thesis

The overall aim of this work is to predict the high-pressure phase diagram of helium, particularly the melting line and the phase transition from an insulating to a conducting (metallic) state beyond present experimental accessibility. Chapter 1 provides a brief overview of the general properties of helium, the significance of dense helium for our understanding of stars and giant gas planets, and a motivation for this work.

Chapter 2 presents the theoretical framework and the computational methods of this thesis. Sec. 2.1 discusses the DFT-MD method that couples a fully quantum mechanical description of the electronic system within the DFT framework (Sec. 2.1.2) with a classical description of the atomic nuclei (Sec. 2.1.4). DFT-MD allows for effective treatment of many-particle systems in the warm dense matter regime. The chapter then discusses the implementation of the DFT-MD framework within the plane-wave code VASP (Sec. 2.1.5), as well as technical details of the code (Sec. 2.1.3). The next section, Sec. 2.2, then outlines the calculation of thermophysical properties, including the equation of state (Sec. 2.2.1), DC conductivity (Sec. 2.2.3), optical reflectivity (Sec. 2.2.4), and the ionization degree (Sec. 2.2.5). After that, Sec. 2.3 explains the two-phase simulation (TPS) approach for the calculation of points on the melting line. TPSs employ calculations that simultaneously contain a solid and a fluid part within the simulation cell. Finally, this chapter illustrates approaches to calculate the band gap (Sec. 2.4) from DFT-MD simulations at finite temperatures by evaluating the statistics of the electronic bands.

Chapter 3 introduces the main results of three peer-reviewed and published first-author articles. Reliable predictions demand validation of the underlying theory. Therefore, the first publication, discussed in Sec. 3.1, validates and benchmarks the DFT-MD method with available experimental data for helium in the warm dense matter regime. The second publication documents the calculation of the high-pressure melting line, as explained in Sec. 3.2. The knowledge of the melting line then allows for the consistent calculation of the metallization in dense fluid helium, as discussed in Sec. 3.3. The chapter also contains a co-authored publication (Sec. 3.4) which discusses the efficacy of different exchange-correlation functionals to describe experimental conditions around the plasma phase transition of hydrogen and deuterium. The end of the chapter comprises the conclusion (Sec. 3.5) and the outlook (Sec. 3.6) of this thesis.

The corresponding publications make up chapter 4, followed by Appendix A which provides details regarding the convergence of the DFT-MD calculations.

2. Methods

2.1. Density functional theory molecular dynamics (DFT-MD)

The time-dependent Schrödinger equation,¹⁴³

$$i\hbar \frac{\partial}{\partial t} \psi(\{\mathbf{r}_i, \mathbf{R}_j\}; t) = \hat{H} \psi(\{\mathbf{r}_i, \mathbf{R}_j\}; t), \quad (2.1)$$

describes every aspect of a quantum mechanical system. The Hamilton operator \hat{H} specifies the evolution of the wave function ψ with time t . The spatial coordinates \mathbf{r}_i and \mathbf{R}_j specify the locations of the i electrons and j ions of the system, respectively. \hbar is the reduced Planck constant. Eq. 2.1 and all the following equations neglect the spin as this work focuses on spin-degenerate states. The Hamiltonian contains the operators for the kinetic energy of the electrons \hat{T}_e and the ions \hat{T}_i , the interaction of electrons with each other \hat{V}_{ee} and with the ions \hat{V}_{ei} , and the interaction between the ions \hat{V}_{ii} :

$$\hat{H} = \hat{T}_e + \hat{T}_i + \hat{V}_{ee} + \hat{V}_{ei} + \hat{V}_{ii}. \quad (2.2)$$

A solution of the Schrödinger equation is only possible for small systems. A system of n interacting particles with p parameters on which the Schrödinger equation depends results in p^{3n} variables that have to be saved. If every single one of the $N \approx 10^{80}$ atoms in the universe could store one variable, the universe could record the state of a Schrödinger equation of $n \approx \frac{1}{3} \log(N - p) \approx \frac{80}{3} \log 10 \approx 27$ interacting particles.¹⁴⁴ Each helium atom consists of a nucleus and two electrons. All the atoms in the universe could therefore store the states of a total of nine helium atoms. This rough calculation illustrates that the Schrödinger equation cannot be stored, processed, or solved for large systems. Therefore, the computation of quantum-mechanical many-body systems requires alternative approaches and approximations, of which the Born-Oppenheimer approximation¹⁴⁵ is often the initial step.

2.1.1. Born-Oppenheimer approximation

The mass ratio of electrons m_e and ions m_i is $m_e/m_i \approx 0.05\%$ for hydrogen and even smaller for more massive elements. This mass ratio allows a computational simplification, a decoupling of the electronic and ionic systems called the Born-Oppenheimer approximation.¹⁴⁵ At any given time, the electrons react almost instantaneously to the movements of the ions. Therefore, the wave function $\psi_e(\{\mathbf{r}_i, \mathbf{R}_j\})$ of the electrons

approximately does not depend on the time t . The total wave function $\psi(\{\mathbf{r}_i, \mathbf{R}_j\}; t)$ of an adiabatic system then reads as

$$\psi(\{\mathbf{r}_i, \mathbf{R}_j\}; t) = \psi_e(\{\mathbf{r}_i, \mathbf{R}_j\})\psi_i(\{\mathbf{R}_j\}; t), \quad (2.3)$$

with the ionic wave function $\psi_i(\{\mathbf{R}_j\}; t)$. Hence, the Hamiltonian (Eq.2.2) is splitted into an electronic and an ionic part,

$$[\hat{T}_e + \hat{V}_{ee} + \hat{V}_{ei}]\psi_e(\{\mathbf{r}_i, \mathbf{R}_j\}) = E_e(\{\mathbf{R}_j\})\psi_e(\{\mathbf{r}_i, \mathbf{R}_j\}), \quad (2.4)$$

$$[\hat{T}_i + \hat{V}_{ii} + E_e(\{\mathbf{R}_j\})]\psi_i(\{\mathbf{R}_j\}; t) = i\hbar \frac{\partial}{\partial t} \psi_i(\{\mathbf{R}_j\}; t), \quad (2.5)$$

with the Born-Oppenheimer energy surface $E_e(\{\mathbf{R}_j\})$ that couples the ionic and the electronic parts. A separate treatment of the ionic and electronic contributions in the system accelerates the computation of a given system drastically.

2.1.2. Density functional theory (DFT)

DFT does not employ the wave function as the central quantity of interest but instead focuses on the electron density $\rho(\mathbf{r})$,

$$\rho(\mathbf{r}) = N_e \int d\mathbf{r}_1 \cdots \int d\mathbf{r}_{N_e-1} |\psi_e(\mathbf{r}_1 \dots \mathbf{r}_{N_e-1})|^2. \quad (2.6)$$

Thus, the integral of $\rho(\mathbf{r})$ over all spatial dimensions has to give the number of electrons N_e ,

$$N_e = \int d\mathbf{r} \rho(\mathbf{r}). \quad (2.7)$$

The use of the three-dimensional electron density in preference to the very complex wave function greatly reduces the computational demand. Hohenberg and Kohn¹⁴⁶ demonstrated that the groundstate electron density $\rho(\mathbf{r})$ determines the external potential \hat{V}_{ei} except for an additive constant. \hat{V}_{ei} then determines the Hamiltonian (Eq. 2.2), and therefore all properties of the system. The second theorem of Hohenberg and Kohn states that only the groundstate electron density $\rho(\mathbf{r})$ reproduces the groundstate energy. This theorems, in principle, allow for the calculation of quantities based on the electron density. However, the Hohenberg-Kohn theorems do not demonstrate a way of doing this.

Kohn and Sham¹⁴⁷ developed a scheme to apply the Hohenberg-Kohn theorems and to actually calculate observables. The main idea is to map the interacting many-particle system with the groundstate electron density $\rho(\mathbf{r})$ on a non-interacting system with the groundstate density $\rho_{KS}(\mathbf{r})$ with a modified external potential, such that $\rho_{KS}(\mathbf{r}) = \rho(\mathbf{r})$.

The first step is to decompose the electron-electron interaction \hat{V}_{ee} and the kinetic energy of the electrons \hat{T}_e into the ideal Hartree interaction \hat{V}_H , the unknown

nonideal interaction \hat{V}_{xc} , the ideal kinetic energy \hat{T}_{id} , and the unknown nonideal kinetic energy \hat{T}_{xc} ,

$$\hat{V}_{\text{ee}} = \hat{V}_{\text{H}} + \hat{V}_{\text{xc}}, \quad (2.8)$$

$$\hat{T}_{\text{e}} = \hat{T}_{\text{id}} + \hat{T}_{\text{xc}}. \quad (2.9)$$

With the decompositions of Eqs. 2.8 and 2.9, the eigenvalue E_{e} of the electronic Hamiltonian reads as

$$\begin{aligned} E_{\text{e}} &= V_{\text{ee}} + V_{\text{ei}} + T_{\text{e}} \\ &= V_{\text{H}} + V_{\text{xc}} + V_{\text{ei}} + T_{\text{id}} + T_{\text{xc}}. \end{aligned} \quad (2.10)$$

Here,

$$\hat{V}_{\text{H}} = \frac{1}{2} \frac{e^2}{4\pi\epsilon_0} \int \int d\mathbf{r}_1 d\mathbf{r}_2 \frac{\rho(\mathbf{r}_1)\rho(\mathbf{r}_2)}{|\hat{\mathbf{r}}_1 - \hat{\mathbf{r}}_2|}, \quad (2.11)$$

$$\hat{V}_{\text{ei}} = - \sum_{j=1}^N \frac{Z_j e^2}{4\pi\epsilon_0} \int d\mathbf{r} \frac{\rho(\mathbf{r})}{|\hat{\mathbf{r}}_i - \hat{\mathbf{R}}_j|}, \quad (2.12)$$

$$\hat{T}_{\text{id}} = - \frac{\hbar^2}{2m_{\text{e}}} \sum_{n=1}^{\infty} f_n \Delta_n. \quad (2.13)$$

e is the elementary charge, ϵ_0 is the dielectric constant, $\hat{\mathbf{r}} = \mathbf{r}$, $\hat{\mathbf{R}} = \mathbf{R}$, N is the number of atoms in the system, Z_j is the charge of the j th atom. Moreover, f_n is the Fermi-Dirac distribution,¹⁴⁸

$$f_n = \frac{1}{e^{(\epsilon_n - \mu)/k_{\text{B}}T} + 1}, \quad (2.14)$$

with the self-energy ϵ_n of the n th state, the chemical potential μ , and the Boltzmann constant k_{B} .

Mermin¹⁴² introduced the Fermi-Dirac distribution into the Kohn-Sham formalism and therefore enhanced DFT, so far only applicable at $T = 0$ K, to a finite-temperature method. The extension to finite temperatures requires the minimization of the free energy F_{e} instead of the energy E_{e} from Eq. 2.10,

$$F_{\text{e}} = E_{\text{e}} - TS, \quad (2.15)$$

with the electronic and ionic temperature T and the entropy S . The ideal term for the entropy reads as

$$S_{\text{id}} = -k_{\text{B}} \sum_{n=1}^{\infty} (f_n \ln f_n + (1 - f_n) \ln(1 - f_n)). \quad (2.16)$$

The decomposition of the entropy S is analogous to Eqs. 2.8 and 2.9,

$$S = S_{\text{id}} + S_{\text{xc}}, \quad (2.17)$$

with the nonideal entropy S_{xc} . Inserting Eqs. 2.10 and 2.17 into Eq. 2.15 gives

$$\begin{aligned} F_e &= E_e - TS \\ &= V_{\text{H}} + V_{\text{xc}} + V_{\text{ei}} + T_{\text{id}} + T_{\text{xc}} - T(S_{\text{id}} + S_{\text{xc}}). \end{aligned} \quad (2.18)$$

The exchange-correlation (XC) term

$$F_{\text{xc}} = V_{\text{xc}} + T_{\text{xc}} - TS_{\text{xc}} \quad (2.19)$$

modifies Eq. 2.18 to

$$F_e = V_{\text{H}} + V_{\text{ei}} + T_{\text{id}} - TS_{\text{id}} + F_{\text{xc}} \quad (2.20)$$

and includes the nonideal contributions V_{xc} , T_{xc} , and S_{xc} .

Aside from F_{xc} , all the other parts of Eq. 2.20 have analytical expressions. The term V_{ei} is system-dependent. Variation of the free energy F_e with respect to the electron density $n(\mathbf{r})$ gives the effective potential V_{eff} in which the electrons exist

$$V_{\text{eff}} = V_{\text{H}} + V_{\text{ei}} + \frac{\delta F_{\text{xc}}}{\delta n(\mathbf{r})}. \quad (2.21)$$

Eq. 2.21 contains all the interactions of the system: the interaction due to non-ideal contributions in the XC functional F_{xc} and the interactions due to the Hartree potential V_{H} and the system-dependent external potential of the ions V_{ei} . The combination of Eq. 2.21 and Eq. 2.20 becomes

$$F_e = T_{\text{id}} - TS_{\text{id}} + V_{\text{eff}}, \quad (2.22)$$

describing a non-interacting system of particles, the so-called reference system, with the kinetic energy T_{id} , the temperature T , and the entropy S_{id} in an effective potential V_{eff} . The n th state of the reference system has the self-energy ε_n that corresponds to the n th one-particle Kohn-Sham orbital $\Psi_n(\mathbf{r})$. The connection between the electron density $\rho(\mathbf{r})$ and the Kohn-Sham orbitals reads

$$\rho(\mathbf{r}) = \sum_{n=1}^{\infty} f_n |\Psi_n(\mathbf{r})|^2, \quad (2.23)$$

while the effective Schrödinger equation of the n th Kohn-Sham orbital follows

$$\left[-\frac{\hbar^2}{2m_e} \Delta + V_{\text{eff}} \right] \Psi_n(\mathbf{r}) = \varepsilon_n \Psi_n(\mathbf{r}). \quad (2.24)$$

Eqs. 2.21, 2.23, and 2.24 constitute the Kohn-Sham equations and describe the reference system in a self-consistent way. Iteratively solving the Kohn-Sham equations gives the electron density of the electronic groundstate, facilitating the calculation of all quantities of the system.

	Heaven of chemical accuracy	
+ explicit dependence on unoccupied orbitals	rung 5	fully nonlocal
+ explicit dependence on occupied orbitals	rung 4	hybrid functionals
+ explicit dependence on kinetic energy density	rung 3	meta-GGAs
+ explicit dependence on gradients of the density	rung 2	GGAs
local density only	rung 1	LDA
	Hartree world	

Table 2.1.: A categorization of exchange-correlation approaches, adapted from Lorenzen.¹⁵⁰ Computational demand and potential accuracy increase with each rung.

There are many approximations for the exchange-correlation functional with vastly different approaches and computational demands. Tab. 2.1 shows an overview of the different classes of exchange-correlation functionals after Perdew *et al.*¹⁴⁹ Higher rungs provide greater predictive power at increased computational costs due to a more elaborate description of the electronic system. The Local Density Approximation (LDA)^{147;151;152} only considers a homogenous electron gas, while Generalized Gradient Approximations (GGAs) include gradients of the electron density. Meta-GGAs^{153;154} take the second derivative of the density or the kinetic energy density into account, while hybrid functionals^{155;156} employ a mixture of the Hartree-Fock exchange and DFT on the GGA level. The first publication employs a variety of exchange-correlation functionals from the LDA to the hybrid functional of Heyd, Scuseria, and Ernzerhof (HSE).¹⁵⁶ The first two publications also use GGAs that describe the van der Waals (vdW)-interactions between the nuclei via a nonlocal correlation term. While the first publication benchmarks a number of different implementation of vdW functionals, the second exclusively employs the vdW-DF1 functional of Dion *et al.*¹⁵⁷ However, all publications of this work utilize the GGA of Perdew, Burke, and Ernzerhof (PBE).¹⁵⁸

This chapter does not derive DFT and instead provides a brief overview of the main concepts. A plethora of books^{159–164} and articles^{144;165} contain further insight into this topic.

2.1.3. Plane waves and pseudopotentials

The use of specific sampling points of the Brillouin zone, the so-called \mathbf{k} points, ensure simple symmetry exploitation. Periodic boundary conditions¹⁶⁶ avoid surface effects and lower the number of particles that are required for convergence. Due to this translational symmetry, the Kohn-Sham wave functions $\Psi_n(\mathbf{r})$ obey the Bloch theorem. The symmetry also allows for the expansion of the wave functions into

plane waves,

$$\Psi_n(\mathbf{r}) = \frac{1}{\sqrt{V}} u_{\mathbf{k},\alpha}(\mathbf{r}) e^{i\mathbf{k}\cdot\mathbf{r}} = \frac{1}{\sqrt{V}} \sum_{\mathbf{G}} C_{\mathbf{k},\alpha}(\mathbf{G}) e^{i(\mathbf{k}+\mathbf{G})\cdot\mathbf{r}}, \quad (2.25)$$

with the box volume V , the Bloch factor $u_{\mathbf{k},\alpha}$ for a given \mathbf{k} point and band index α , and the wave number \mathbf{G} . Computational constraints restrict the sum over \mathbf{G} to values below the plane wave energy E_{cut} that results from

$$E_{\text{cut}} > \frac{\hbar^2}{2m_e} |\mathbf{k} + \mathbf{G}|^2. \quad (2.26)$$

Regions around the nuclei require a large number of plane waves in order to reproduce the strongly oscillating wave functions near the nuclei. Pseudopotentials envelop the strong oscillations and effectively include all but the valence electrons into the core potential, creating a smooth pseudo wave function within the radius r_{PP} of the pseudopotential while reproducing the real wave function outside r_{PP} . However, upon increasing densities and/or high kinetic energy induced by high temperatures, the distance between two nuclei can approach $2r_{\text{PP}}$, creating unphysical behavior. Higher densities hence require “harder“ pseudopotentials with smaller r_{PP} or even the use of the computationally expensive full Coulomb potential, depending on the density-temperature conditions.

2.1.4. Molecular dynamics (MD)

Chapter 2.1.2 describes the self-consistent treatment of the static quantum-mechanical electronic system within the DFT framework. The positions of the nuclei enter the Kohn-Sham equations implicitly as part of the effective potential V_{eff} . Classical molecular dynamics propagates the nuclei and therefore governs the temporal evolution of the system, employing Newton’s equations of motion,

$$\mathbf{F}_{\text{tot}} = \mathbf{F}_{\text{ii}} + \mathbf{F}_{\text{ei}} + \mathbf{F}_{\text{bath}}, \quad (2.27)$$

with the total force \mathbf{F}_{tot} on the nuclei, the Coulomb interaction \mathbf{F}_{ii} between the ions, the force on the nuclei due to the Hellman-Feynman forces of the electrons $\mathbf{F}_{\text{ei}} = -\nabla E_e$, derived from the Born-Oppenheimer energy surface E_e of Eqs. 2.4 and 2.5, and the force \mathbf{F}_{bath} due to the heat bath. Nosé¹⁶⁷ and Hoover¹⁶⁸ introduced a coupling of the system with a heat bath. This approach renders the system a canonical ensemble and introduces the temperature as an independent quantity. The bath adds/subtracts energy to/from the system periodically. This way, the mean kinetic energy $\langle T_i \rangle$ of the N_i nuclei follows

$$\langle T_i \rangle = \frac{3}{2} (N_i - 1) k_B T. \quad (2.28)$$

Classical MD can simulate over 10^{12} particles,¹⁶⁹ while the high computational demand limits DFT-MD to a maximum of a few thousand particles.

2.1.5. Implementation of DFT-MD in the VASP code

This work employs the Vienna Ab-Initio Simulation Package (VASP).^{170–174} Fig. 2.1.5 displays a brief outline of the underlying workflow.

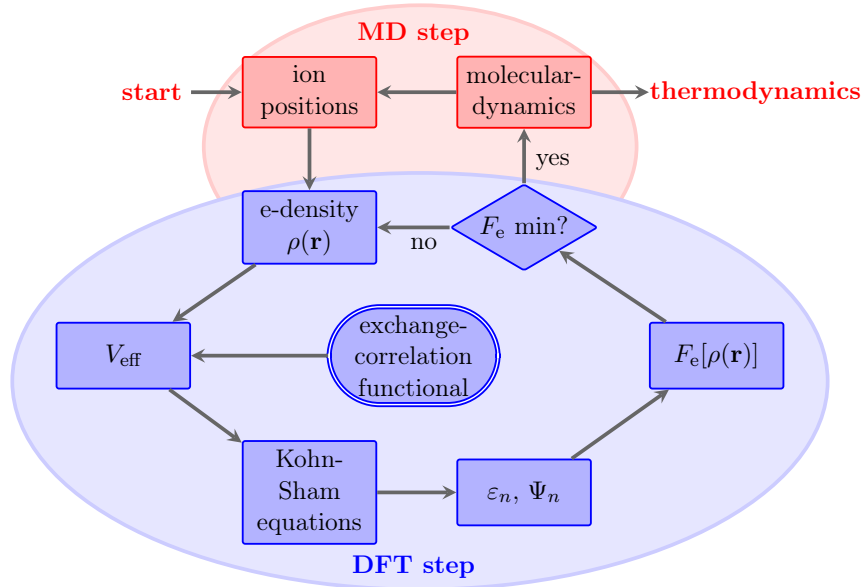


Figure 2.1.: The DFT-MD scheme of VASP, adapted from W. Lorenzen.¹⁵⁰

VASP implements a separate treatment of nuclei and electrons according to the Born-Oppenheimer approximation (Sec. 2.1.1). The initial position of the nuclei results in an initial guess of the electron density $\rho(\mathbf{r})$ within DFT (Sec. 2.1.2). The electron density, the exchange-correlation functional, and the projector-augmented wave (PAW) pseudopotentials¹⁷⁵ (Sec. 2.1.3) define the effective potential V_{eff} . The solution of the Kohn-Sham equations (Eqs. 2.21, 2.23, and 2.24) results in the eigen energies ε_n and the Kohn-Sham orbitals Ψ_n , with an expansion of the Bloch factor into plane waves according to Sec. 2.1.3. The \mathbf{k} -point sampling of the Kohn-Sham orbitals is a convergence parameter. Usually, the Baldereschi Mean Value Point (BMVP)¹⁷⁶ ensures converged results compared to more demanding grids from the Monkhorst and Pack scheme¹⁷⁷. Calculations in certain solid phases can employ special \mathbf{k} -points¹⁷⁸ for higher efficiency due to the high crystal symmetry. The self-consistent DFT cycle then minimizes the resulting free energy F_e . The final F_e determines the Hellman-Feynman forces that act on the nuclei and move the nuclei accordingly within classical MD (Sec. 2.1.4). The updated positions of the nuclei then result in an updated electron density, and the intertwined computation cycle of DFT and MD repeats for the specified number of MD steps. This thesis employs the VASP code in order to be consistent with earlier work, especially to studies of W. Lorenzen^{87;89;179;180}, A. Becker,¹¹⁰ and M. Schöttler.⁹⁰ However, there is a great and increasing number of *ab initio* codes, including, but not limited

to, ABINIT,^{181–183} CASTEP,¹⁸⁴ FHI-aims,^{185–187} Gaussian,¹⁸⁸ SIESTA,¹⁸⁹ TURBO-
MOLE,¹⁹⁰ Quantum ESPRESSO,¹⁹¹ and WIEN2k.¹⁹²

2.2. Calculation of thermophysical properties

The following sections provide a brief overview of the calculation of thermophysical properties such as the pressure p , the internal energy U , the dynamic electrical conductivity $\sigma(\omega)$ that depends on the frequency ω , the static electrical conductivity σ_{DC} , the optical reflectivity R , and the ionization degree α . Appendix A contains a display and discussion of the convergence of said quantities regarding the number of atoms, the cutoff energy E_{cut} , the \mathbf{k} -point set, the number of bands per atom, and the size of the time step in the MD.

2.2.1. Equation of state

The calculation of the pressure p and the internal energy U requires DFT-MD calculations. Fig. 2.2 shows the typical behavior of the pressure and the internal energy during a DFT-MD simulation.

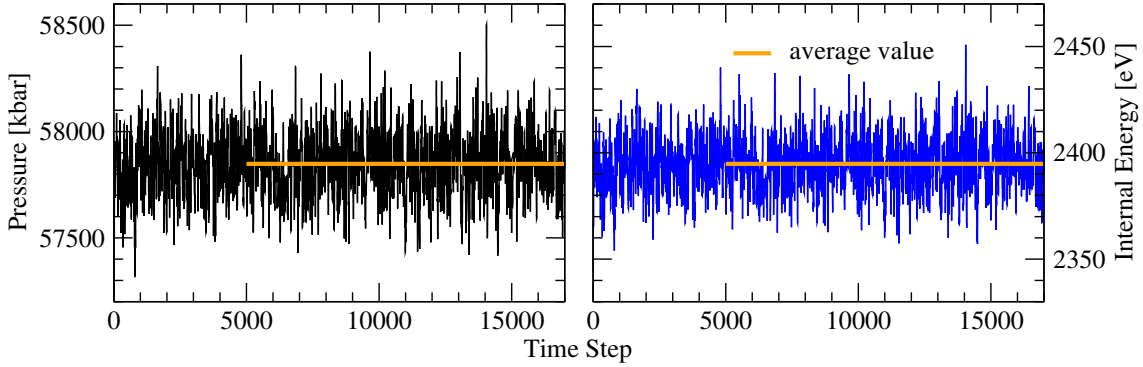


Figure 2.2.: The pressure (left panel, black) and the internal energy (right panel, blue) over the number of time steps for a typical DFT-MD simulation at 10 g/cm^3 and $10\,000 \text{ K}$ with the average value in thermodynamic equilibrium in orange.

After the simulations have reached the thermodynamic equilibrium for a given density $\varrho = \frac{m}{V}$ and temperature T , the total pressure p reads as:

$$p = p_{\text{id}} + \langle p_{\text{ii}} \rangle + \langle p_{\text{e}} \rangle. \quad (2.29)$$

It consists of the ideal pressure $p_{\text{id}} = \frac{N_i k_{\text{B}} T}{V}$ of the N_i nuclei, the additional pressure due to the interaction of the ions p_{ii} , and the pressure due to the Hellman-Feynman forces of the electronic system p_{e} . Similarly, the internal energy U of a system of N_i atoms is the sum of the ideal contribution $U_{\text{id}} = \frac{3}{2} N_i k_{\text{B}} T$, the energy due to the interaction of the ions U_{ii} , and the energy due to the electronic system U_{e} ,

$$U = U_{\text{id}} + \langle U_{\text{ii}} \rangle + \langle U_{\text{e}} \rangle. \quad (2.30)$$

Here, U_{e} depends on the free energy of the electrons F_{e} (Eq. 2.22), the entropy S_{e} (Eq. 2.16), and the temperature T ,

$$\langle U_{\text{e}} \rangle = \langle F_{\text{e}} + T S_{\text{e}} \rangle. \quad (2.31)$$

2.2.2. Dynamic electrical conductivity

This section gives an overview of the calculation of the dynamic electrical conductivity and quantities deduced from it, i.e., the direct current (DC) conductivity, the optical reflectivity, and the ionization degree. The real part of the complex dynamic electrical conductivity follows the Kubo-Greenwood formula,^{166;193–196}

$$\begin{aligned} \sigma(\omega) = & \frac{2\pi e^2}{3\omega V} \sum_{ij} [f(\varepsilon_{i,\mathbf{k}}) - f(\varepsilon_{j,\mathbf{k}})] \\ & \times |\langle \Psi_{j,\mathbf{k}} | \hat{\mathbf{v}} | \Psi_{i,\mathbf{k}} \rangle|^2 \delta(\varepsilon_{j,\mathbf{k}} - \varepsilon_{i,\mathbf{k}} - \hbar\omega). \end{aligned} \quad (2.32)$$

Here, the Fermi-Dirac occupation $f(\varepsilon_{i,\mathbf{k}})$ of the i th band that corresponds to the energy $\varepsilon_{i,\mathbf{k}}$ and the wavefunction $\Psi_{i,\mathbf{k}}$ at \mathbf{k} -point \mathbf{k} is summed up over the bands i and j . Due to the delta function, the Kubo-Greenwood formula only gives non-zero results at frequencies ω that correspond to the energy difference $\hbar\omega$ between two bands. A possible correction of this unphysical behavior is the multiplication with a Gaussian function where the width of the Gaussian is a convergence parameter that has to be checked carefully for every density, temperature, and particle number.

It is not feasible to calculate $\sigma(\omega)$ at every time step of a DFT-MD simulation in thermodynamic equilibrium. Instead, up to 50 snapshots usually suffice to converge the quantity of interest within 10%, depending on the exact conditions and the desired quantity.

2.2.3. Direct current (DC) conductivity

The DC conductivity is the low-frequency limit of the dynamic electrical conductivity,

$$\sigma_{\text{DC}} = \lim_{\omega \rightarrow 0} \sigma(\omega). \quad (2.33)$$

Due to the dependence on the mean band distance when calculated with the Kubo-Greenwood formula, $\sigma(\omega)$ exhibits a drop at frequencies whose corresponding energies are smaller than the mean band distance. Therefore, a decrease in the mean band distance, i.e., a greater number of atoms, allows for a physically meaningful calculation of $\sigma(\omega)$ to lower frequencies. A linear regression over a small energy range above the mean band distance then gives an extrapolation of $\sigma(\omega)$ to low frequencies and therefore σ_{DC} . Fig. 2.3 exemplifies the calculation of the DC conductivity.

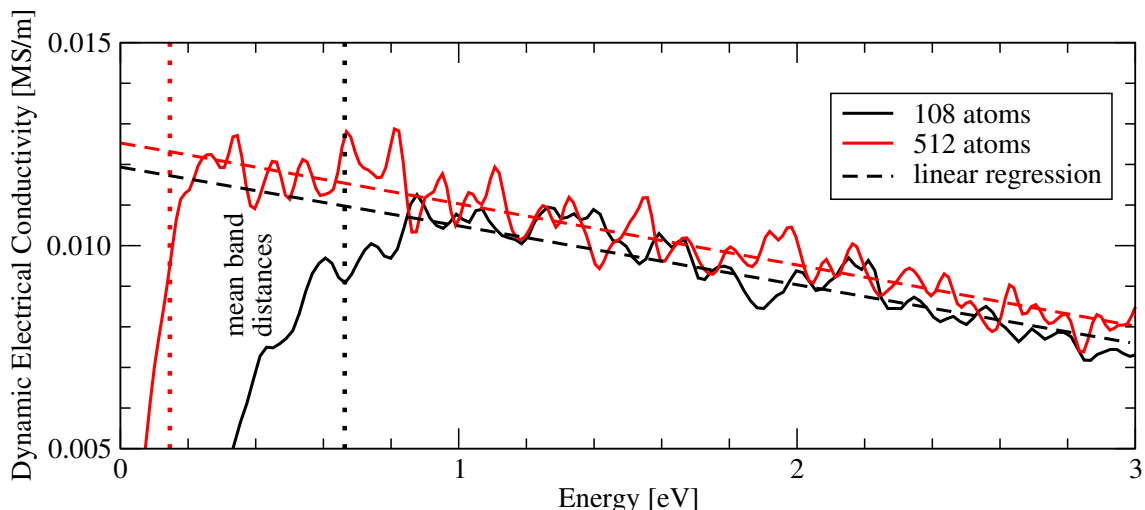


Figure 2.3.: The dynamic electrical conductivity over the energy with 108 atoms (solid black line) and 512 atoms (solid red line) at 10 g/cm^3 and $10\,000 \text{ K}$. Corresponding mean band distances and linear regressions are shown as dotted and dashed lines, respectively.

2.2.4. Reflectivity

The Fresnel formula¹⁹⁷

$$R(\omega) = \frac{[n_0(\omega) - n(\omega)]^2 + [k_0(\omega) - k(\omega)]^2}{[n_0(\omega) + n(\omega)]^2 + [k_0(\omega) + k(\omega)]^2} \quad (2.34)$$

states a connection between the frequency-dependent reflectivity $R(\omega)$ and the complex index of refraction, $n + ik$. Quantities with the subscript 0 refer to the material at the reflecting boundary, which results in $n_0 = 1$ and $k_0 = 0$ since the optical properties of uncompressed helium are approximately equal to that of a vacuum, see Sec. 1.1. The relations between $n + ik$ and the complex dielectric function $\varepsilon(\omega) = \varepsilon_1(\omega) + i\varepsilon_2(\omega)$ read^{198;199}

$$n(\omega) + ik(\omega) = \sqrt{\varepsilon(\omega)}, \quad (2.35)$$

$$\varepsilon_1(\omega) = \frac{\sigma_2(\omega)}{\epsilon_0\omega}, \quad (2.36)$$

$$\varepsilon_2(\omega) = 1 - \frac{\sigma_1(\omega)}{\epsilon_0\omega}. \quad (2.37)$$

While the real part of the dynamic electrical conductivity, $\sigma_1(\omega) = \sigma(\omega)$, results from the Kubo-Greenwood formula (Eq. 2.32), the following Kramers-Kronig relation gives the imaginary part $\sigma_2(\omega)$:^{195;196;200–202}

$$\sigma_2(\omega) = -\frac{2}{\pi} \mathcal{P} \int \frac{\sigma_1(\nu)\omega}{\nu^2 - \omega^2} d\nu, \quad (2.38)$$

with the frequency ν and where \mathcal{P} indicates a principal value integral. The components of the dielectric function, $\varepsilon_1(\omega)$ and $\varepsilon_2(\omega)$, are inversely proportional to the

frequency ω . Therefore, compared to the DC conductivity, a converged dielectric function requires a greater energy range of electronic transitions between the bands, which directly translates into a greater number of bands per atom at the same density and temperature conditions. Fig. 2.4 gives an example of the quantities discussed here at a density of 15 g/cm³ and a temperature of 16 000 K to energies

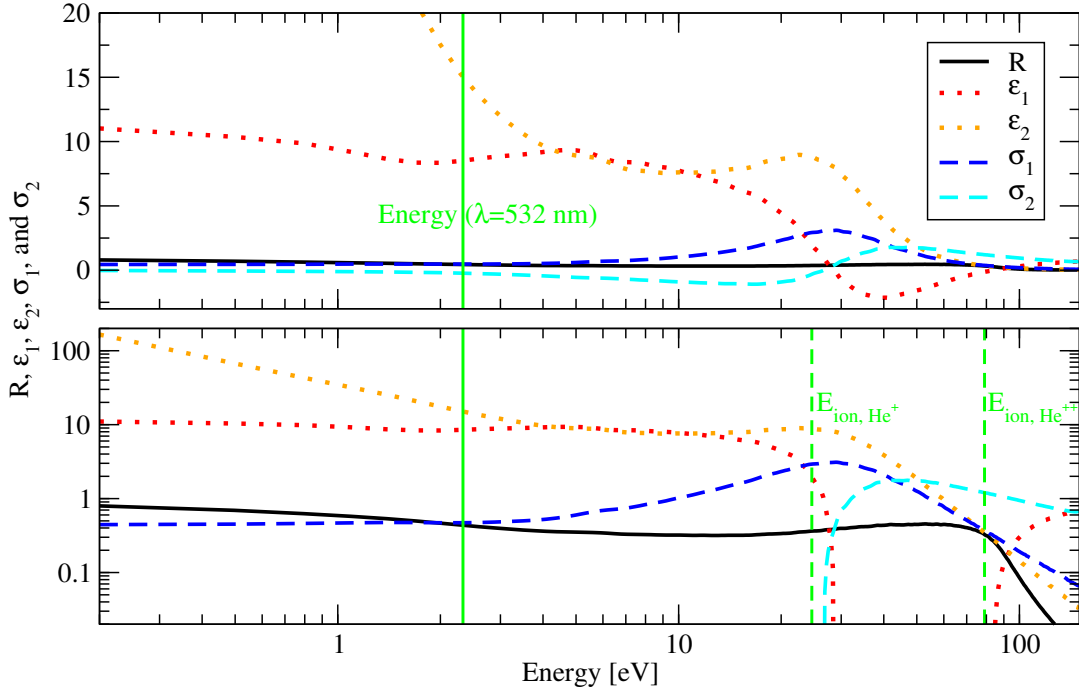


Figure 2.4.: Several frequency-dependent quantities over the energy spectrum in linear (upper panel) and logarithmic representation (lower panel): the reflectivity R (solid black line), the real and imaginary part of the dielectric function, $\varepsilon_1(\omega)$ (red dotted line) and $\varepsilon_2(\omega)$ (orange dotted line), and the real and imaginary part of the dynamic electrical conductivity, $\sigma_1(\omega)$ (dashed blue line) and $\sigma_2(\omega)$ (dashed cyan line). The vertical solid green lines indicate the energy of light with a wavelength of 532 nm. The vertical dashed green line depicts the energy E_{ion} required to ionize a helium atom once (He^+) and twice (He^{++}).

Most experiments use Nd:YAG lasers with an initial wavelength of 1064 nm and 532 nm via frequency-doubling. Therefore, in order to directly compare to experiments, the wavelength of interest is usually 532 nm with a corresponding energy of about 2.33 eV. The energy required to ionize helium to the first ionization state is $E_{\text{ion, He}^+} = 24.58739 \pm 0.00003$ eV.²⁶ The full ionization requires $E_{\text{ion, He}^{++}} = 79.00514 \pm 0.00003$ eV.²⁶ Accordingly, the electron-depleted bands at energies above $E_{\text{ion, He}^+}$ and $E_{\text{ion, He}^{++}}$ greatly affect R , ε_2 , σ_1 , ε_1 , and σ_2 .

2.2.5. Ionization degree

The ionization degree α is the ratio of free electrons N_e^{free} and the total number of electrons N_e^{tot} ,^{203;204}

$$\alpha = \frac{N_e^{\text{free}}}{N_e^{\text{tot}}}. \quad (2.39)$$

Until recently, the only method to obtain α from *ab initio* simulations was to calculate the density of states (DOS), multiply it with the Fermi function, integrate over it and normalize the result with respect to the total number of electrons N_e^{tot} . Within this DOS integration method,²⁰⁵⁻²⁰⁷ the value of the integral to the right of the chemical potential is identified with the number of free electrons N_e^{free} .

An alternative approach from Bethkenhagen *et al.*²⁰⁸ employs dynamic electrical conductivity $\sigma(\omega) = \sigma^{\text{tot}}(\omega)$ instead. Thomas, Reiche, and Kuhn (TRK) proposed that $\sigma(\omega)$ has to satisfy the following sum rule:²⁰⁹⁻²¹²

$$Z^{\text{tot}} = \frac{N_e^{\text{tot}}}{N_i} = \frac{2m_e V}{\pi e^2 N_i} \int_0^\infty d\omega \sigma^{\text{tot}}(\omega). \quad (2.40)$$

The total electronic Z^{tot} charge per atom is equal to the number of electrons per atom, i.e., $Z^{\text{tot}} = 2$ in the case of helium. Regarding the total system, Z^{tot} depends on the total number of electrons N_e^{tot} and the number of ions N_i in the system. $\sigma^{\text{tot}}(\omega)$ consists of transitions within the conduction bands (c-c), the valence bands (v-v), and interband transitions (v-c):

$$\sigma^{\text{tot}}(\omega) = \sigma^{\text{v-v}}(\omega) + \sigma^{\text{v-c}}(\omega) + \sigma^{\text{c-c}}(\omega), \quad (2.41)$$

which have to fulfill the partial TRK sum rule,

$$Z^{\text{x}} = \frac{2m_e V}{\pi e^2 N_i} \int_0^\infty d\omega \sigma^{\text{x}}(\omega), \quad (2.42)$$

with the individual contributions $\text{x}=\{\text{v-v}, \text{v-c}, \text{c-c}\}$. Here, different energy ranges select different x : Transitions within the valence bands have energies below the chemical potential, higher energies contribute to the conduction bands. Defining the electrons within the conduction bands as *free electrons* allows calculating the ionization state Z^{free} according to Eq. (2.42),

$$Z^{\text{free}} = \frac{N_e^{\text{free}}}{N_i} \equiv Z^{\text{c-c}}. \quad (2.43)$$

Therefore, the ionization α degree reads

$$\alpha = \frac{Z^{\text{free}}}{Z^{\text{tot}}} = \frac{N_e^{\text{free}}}{N_e^{\text{tot}}}. \quad (2.44)$$

Fig. 2.5 visualizes the DOS integration method as well as the TRK sum rule method at a sample condition of 21.6 g/cm³ and 10 000 K. The DOS integration

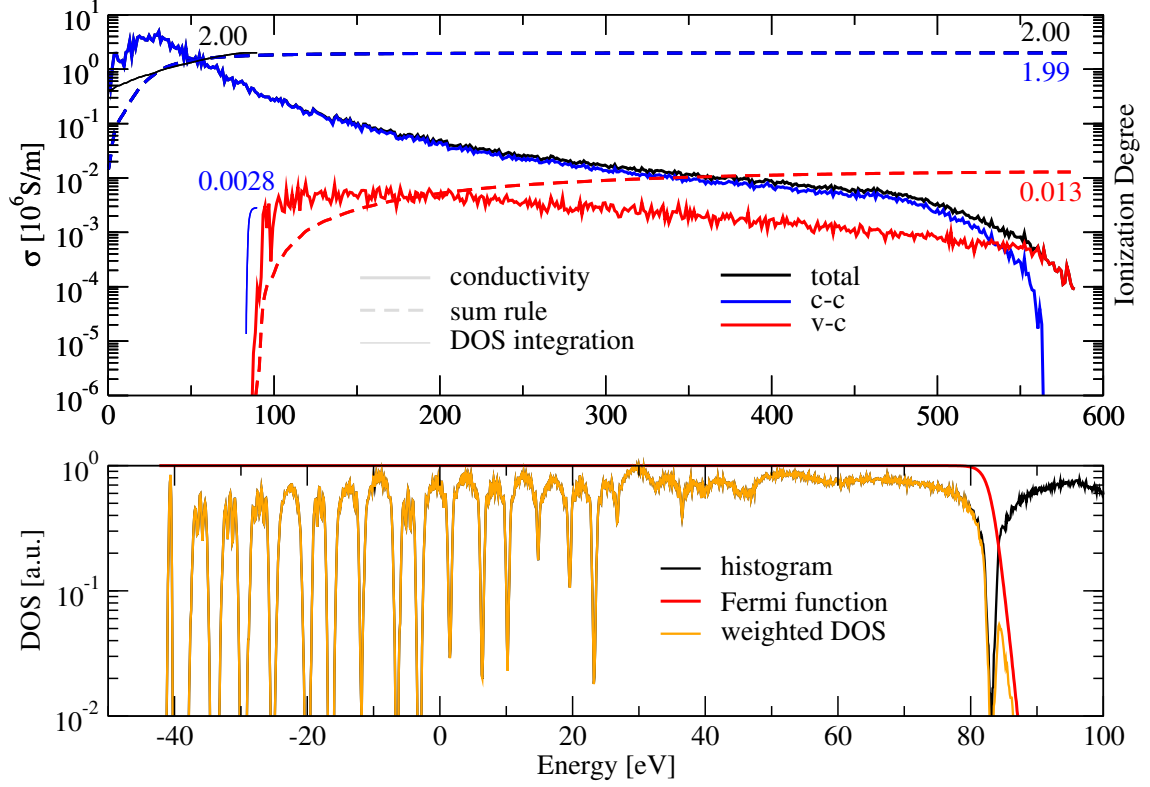


Figure 2.5.: Upper panel: the dynamic electrical conductivity σ (left y-axis) and the effective number of electrons Z for different electronic contributions (right y-axis) over the energy. The total, the c-c, and the v-c contributions are black, blue, and red, respectively. The panel compares the behavior of the sum rule (dashed lines) of the contributions of the conductivities (solid lines) with the results of the DOS integration method (bold lines). The numbers indicate the effective Z . Lower panel: The DOS over the energy. The raw and normalized DOS is black, the corresponding Fermi function is red, and the product of both are orange.

approach does not account for v-v contributions. At the sample conditions, the v-v contributions calculated with the sum rule are zero and therefore not displayed in Fig. 2.5.

The band gap of the DOS in Fig. 2.5 is almost closed. Due to the comparatively low temperature, the Fermi function displays a strong decrease around the chemical potential of about 83 eV. Hence, a multiplication of the DOS with the Fermi function results in small contributions of the DOS at energies above the chemical potential. The DOS integration method identifies the value of the integrated DOS over the total energy range with the total number of electrons. Accordingly, the number of free electrons is the corresponding fraction of the total integral at energies above the chemical potential. At the conditions of Fig. 2.5, this results in an effective number of 0.0028 free electrons. In contrast, the TRK sum rule method as an integral over σ_{c-c} results in 1.99 free electrons, i.e., almost complete ionization.

The exact energy that separates the conduction and valence bands can be chosen arbitrarily. The choice of said energy does not affect the general applicability of the TRK sum rule. The chemical picture treats bound and free states inherently. However, the usual approximations of the chemical picture, like the hard-sphere approximation, are not valid in the warm dense matter regime due to the strong correlations and high densities. The overall influence of quantum effects have to be taken into account. The chemical picture approximates the correlation terms of each species under consideration. In contrast, the TRK approach only uses a single parameter, which is the energy that separates the conduction and the valence bands. The description within DFT accounts for all the quantum effects. The drastical decrease in parameters makes the TRK sum rule approach superior to a treatment within the chemical picture, at least in a regime of strong correlations.

2.3. Two-phase simulation method

At the beginning of two-phase simulations (TPS), one half of the simulation cell contains a solid structure, while a liquid atomic configuration occupies the other half. Within the course of the calculation, either the liquid solidifies or the solid melts, whichever is more favorable energetically. Other approaches to TPS employ simulation where the liquid and the solid coexist throughout the TPS. Figure 2.6 displays a typical TPS cell, in this case with 2048 atoms in total, the maximum number of atoms considered in the respective study.²¹³

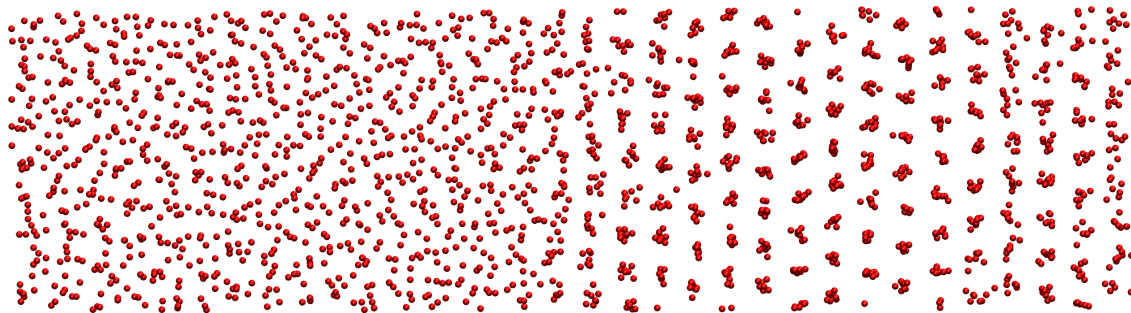


Figure 2.6.: A TPS cell with 2048 atoms after around 5000 time steps at $\rho = 1.6 \text{ g/cm}^3$ and $T = 850 \text{ K}$.

A recent study on the metallization of helium in the solid²¹⁴ demonstrated that at $T = 0 \text{ K}$, the most stable crystal structure is hexagonal close-packed (hcp) throughout the pressure range of interest for the TPS calculations of this work. Therefore, all the TPS cells of this study consist of an hcp crystal and a liquid configuration, which are stacked in the z-direction.

To date, the literature is not conclusive with respect to the setup of the liquid and the solid parts of a TPS box.^{215–222} Extensive tests (see Sec. A.1) demonstrated that a TPS box consisting of a perfect hcp crystal and a liquid distribution gives converged results compared to more demanding setup procedures. A slight compression of the solid part introduces a spacing between the liquid and solid constituents. It additionally equalizes the pressure mismatch between the liquid and the solid. The initial assignment of random velocity vectors to the atoms does not seem to play an important role in the result of the TPS due to the extensive number of time steps and atoms in the TPS.

An accurate description of the melting processes requires an accurate computation of the forces between the atoms. Lorenzen¹⁵⁰ demonstrated that converged pressures require converged forces between the atoms. The very wide pressure and density range of the second publication (Sec. 4.2) demanded the use of special \mathbf{k} -points, but ultimately, all calculations required only one \mathbf{k} -point for a convergence of the pressure to 0.05% with respect to reference calculations with 120 \mathbf{k} -points. Fig. 2.7 illustrates the change of pressure within a TPS simulation at 1.6 g/cm^3 for a liquid and a solid result and demonstrates the differences in the resulting pair distribution functions.

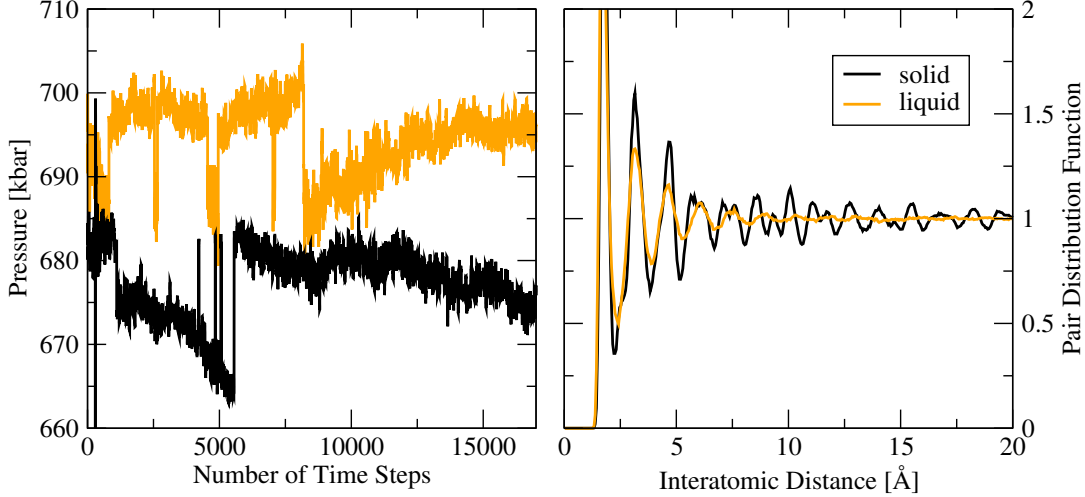


Figure 2.7.: Left panel: The pressure over the number of time steps. Right panel: The pair distribution function at the end of the respective TPS at $\rho = 1.6 \text{ g/cm}^3$ and $T = 850 \text{ K}$. The black (orange) graphs illustrate a TPS with a solid (liquid) result.

In the course of a TPS simulation, a change in pressure and radial distribution function reflects the process of melting/solidification. A solid result will exhibit lower pressures than a liquid result and will have the radial distribution function of a thermally excited solid. As Fig. 2.7 demonstrates, the pressures initially fluctuate until they steadily increase/decrease, and the TPS cell finally contains a liquid/solid configuration. The pair distribution function of said configuration is that of a liquid/a thermally excited hcp crystal.

The change of pressure, the final radial distribution function, and the direct visual representation of the TPS cell during the DFT-MD simulation with the Visual Molecular Dynamics (VMD) tool²²³ provide sufficient information to determine whether a given TPS resulted in a liquid or a solid simulation cell.

A melting line requires multiple melting points. They can result from two equivalent approaches: Calculations on isotherms/isochores iteratively find the densities/temperatures of the melting points that correspond to the respective temperatures/densities. The liquid-solid phase transition is of first order, which introduces a metastable region where the TPSs randomly result in either a liquid or a solid state. Careful sampling of the metastable region as displayed in Fig. A.4 in the appendix indicates that the metastable region in high-density helium has a width of about 3.5% in density at a fixed temperature.

Converged TPS calculations are computationally very demanding due to the high number of atoms in the simulation box. However, as soon as the TPS result in a liquid/solid cell, the calculation of the converged pressure of the corresponding point in the temperature-density plane requires only about 100 atoms. Therefore, after obtaining the density and temperature of a given melting point, DFT-MD simulations with only about 100 atoms provide the corresponding pressures with high accuracy and a more favorable computational demand.

2.4. Calculation of the band gap within DFT-MD

The literature is not conclusive on how to calculate the band gap within DFT.²²⁴⁻²²⁶

At $T = 0$ K, the band gap is the energy difference between the highest occupied molecular orbital, *HOMO*, and the lowest unoccupied molecular orbital, *LUMO*, with the chemical potential between the *HOMO* and the *LUMO*. Higher temperatures lead to a smearing of the Fermi edge and the previously strict definitions of the *HOMO* and the *LUMO* are not applicable anymore. However, one of the approaches to calculate the band gap utilizes exact same bands in the vicinity of the chemical potential. At finite temperatures, the electronic band with an energy right below the chemical potential is not fully occupied, and the first band with an energy above the chemical potential has a non-zero occupation. This method to describe the band gap is called *HOMO-LUMO* in this thesis. It averages the energy difference between the two electronic bands about the chemical potential. The electronic bands are either evaluated for every time step of a DFT-MD simulation¹³⁷ or a few atomic snapshots from DFT-MDs with subsequent DFT calculations at a higher \mathbf{k} -point sampling.¹³⁹ The *HOMO-LUMO* approach appears to give consistent results for dense hydrogen.²²⁷ However, at least with the VASP code, this is not the case for helium.²²⁸ The *broadened* approach records the band energies from snapshots and creates a histogram of the band energies. It shifts the band energies by the chemical potential of every snapshot or every time step of the DFT-MD, respectively. Then, it multiplies the resulting density of states (DOS) with a Gaussian function that has 1% of the valence band width.¹³⁸ The *shifted histogram* method also records the histogram of the shifted band energies but omits the process of broadening the DOS. The *histogram* method additionally omits the shifting by the chemical potential. At 0 K it is identical to the DOS of the *shifted histogram* approach, albeit displaced

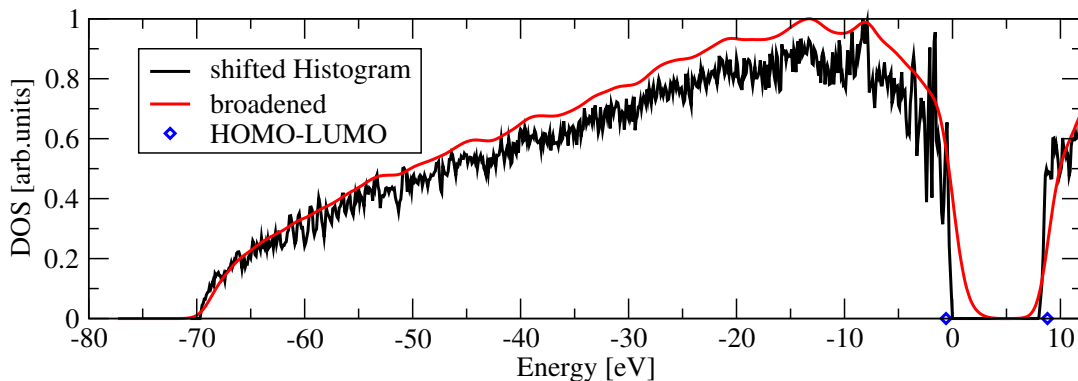


Figure 2.8.: The DOS at $T = 0$ K and $\rho = 10$ g/cm³ with the *shifted histogram* (black) and the *broadened* method (red). The band energies relevant for the *HOMO-LUMO* method are the blue diamonds, whose width gives the uncertainties of the respective band energies.

in the simulation cell and a sampling of $25 \times 25 \times 25$ \mathbf{k} -points. The *HOMO-LUMO* approach gives an upper bound of the *histogram* results. The DOS of the *broadened* method is smeared out compared to the sharp features of the DOS of the *histogram* technique, resulting in a smaller band gap of the *broadened* approach compared to the other methods.

At temperatures above absolute zero, the statistical fluctuations due to thermal excitation induce uncertainties in the resulting band gaps for every technique under discussion. The thermal effects require a thorough investigation of the band gap

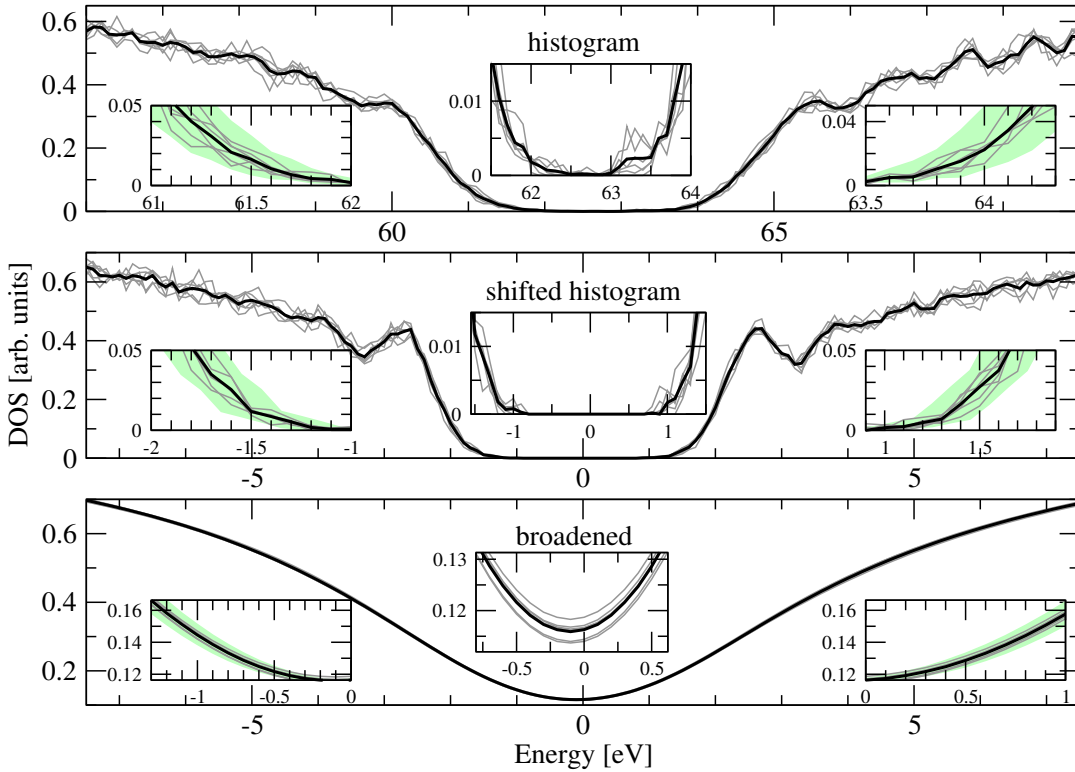


Figure 2.9.: The mean DOS (bold black line) averaged from the DOS of six uncorrelated DFT-MD simulations (thin grey lines) at $T = 20\,000$ K and $\rho = 7$ g/cm³. The green areas indicate the area of uncertainty due to thermal effects.

Normalizing all DOS to the highest occupation of the valence band enables the comparison of different methods to calculate the band gap. While there is no strict definition of the electronic band gap at finite temperatures, the following *a priori* definition ensures robust results for the band gap in the presence of thermal noise: The band gap is closed when the DOS in the energy around the chemical potential is less than 1% of the maximum value of the valence band for all band gap approaches

that derive the band gap directly from the DOS.

The common approach to calculate the band gap is similar to the calculation of the DC conductivity, the reflectivity, and the ionization degree. It utilizes uncorrelated atomic configurations from DFT-MD simulations to calculate the respective property of interest in combination with a more involved \mathbf{k} -point sampling, whenever necessary for convergence. However, the common approach does not give converged results for the band gap of dense helium with VASP. Instead, only the extensive statistical data from DFT-MD simulations ensure converged band gaps in dense helium. Fig. 2.10 demonstrates the convergence behavior of the band gap from

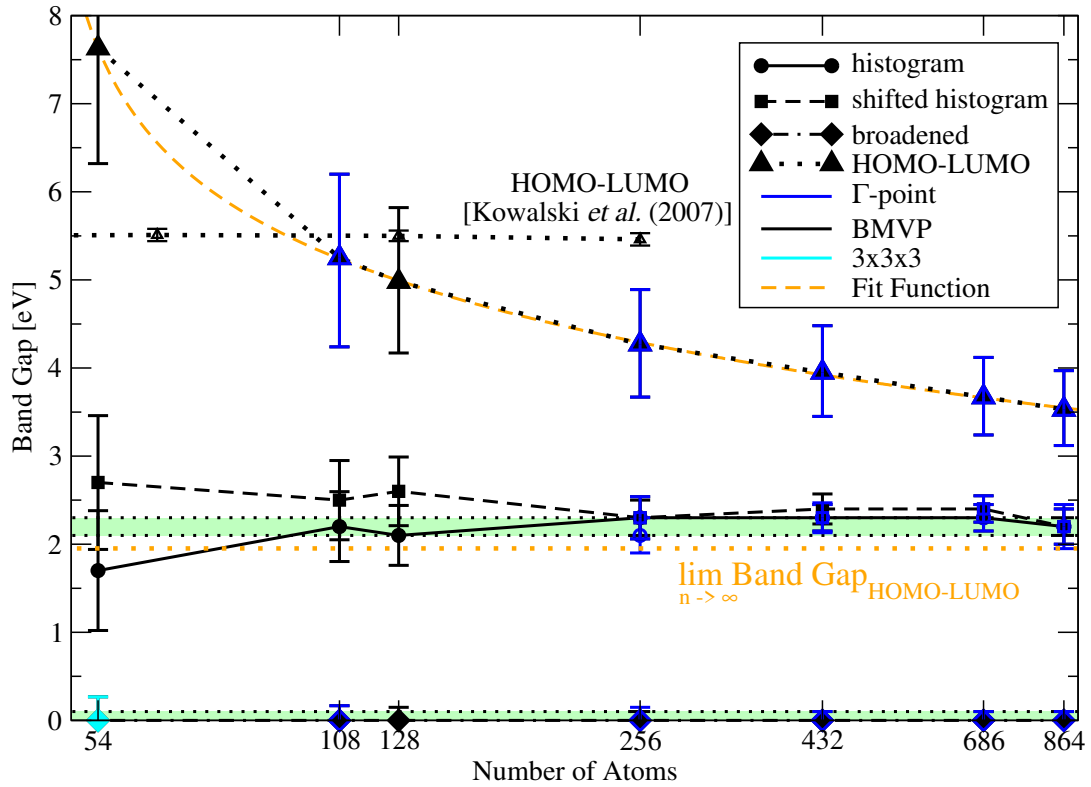


Figure 2.10.: The convergence of different approaches to the band gap at $T = 20\,000$ K and $\rho = 7$ g/cm³. The color code indicates the convergence with respect to the \mathbf{k} -point set. The symbols and corresponding line types indicate the different methods for the calculation of the band gap. Green areas indicate convergence with respect to the most demanding settings. The dashed orange line depicts a fit function to the results of the *HOMO-LUMO* approach, while the dotted orange line is the extrapolation of the *HOMO-LUMO* results to an infinite number of atoms. Small open triangles depict the convergence results of Kowalski *et al.*¹³⁷

to thermal fluctuations, as displayed in Fig. 2.9 and discussed above. They depend on the number of atoms and the width of the energy bins in the calculation of the histogram-based and the broadened approaches and on the fluctuations of the two bands evaluated in the *HOMO-LUMO* definition of the band gap.

The *shifted histogram* approach reproduces the band gaps of the *histogram* method for a high number of atoms. Therefore, the different values of the two *histogram* techniques for the band gap at low atom numbers appear to be a finite-size effect. The popular *HOMO-LUMO* definition does not result in converged results with respect to the number of atoms, at least for high-density helium and with the VASP code. Interestingly, Kowalski *et al.*¹³⁷ employed the ABINIT code^{181–183} and demonstrated good convergence of the *HOMO-LUMO* band gaps. The fourth publication (see Sec. 4.4) used the VASP code as well as *HOMO-LUMO* approach and obtained converged band gaps in dense hydrogen.

At the beginning of a given simulation, the mean value of the band gap fluctuates until the statistical data is sufficient to result in constant values of the band gap. Fig. 2.11 demonstrates the trend of the mean value of the band gap for every approach under discussion during an exemplary DFT-MD simulation. Please note

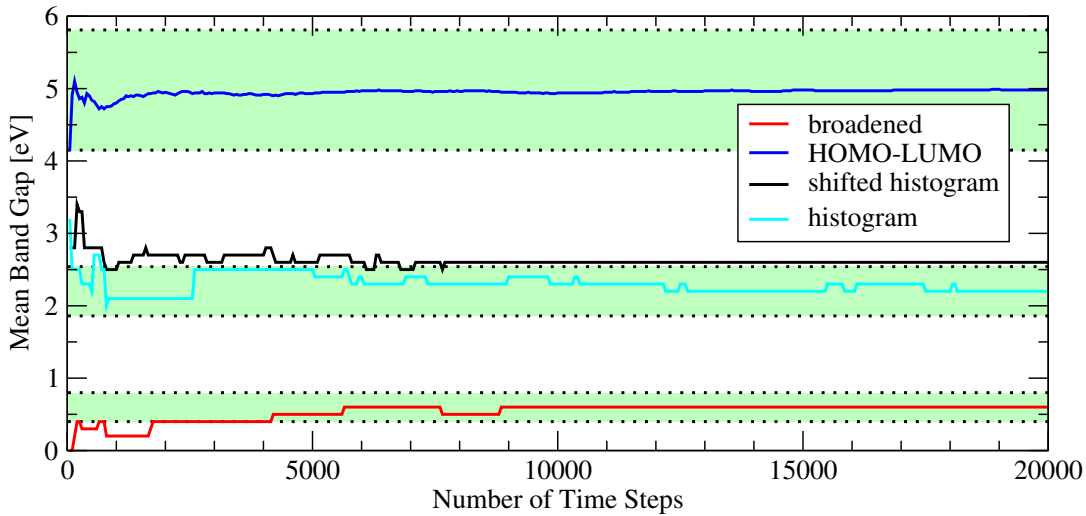


Figure 2.11.: The mean values of the band gap during a DFT-MD simulation at $T = 20\,000$ K and $\rho = 7$ g/cm³ over the number of time steps. The colored bold lines denote the approach to calculate the band gap and the dotted lines and green areas indicate the uncertainties of the converged values. For the sake of clarity, the figure does not feature the area corresponding to converged values of the *shifted histogram* method.

The band gap values of the different methods in Fig. 2.11 reproduce the trends of Fig. 2.10: The *broadened* approach results in the smallest band gaps, followed by the *histogram*, the *shifted histogram*, and the *HOMO-LUMO* definition. The latter

converges after the least number of time steps. At the sample condition and as long as more than 2 000 time steps are evaluated, every method under consideration reproduces the reference values within the uncertainties. Throughout this thesis, all DFT-MD calculations of the band gap employed at least 4 000 time steps.

All the tests above demonstrate a scheme to calculate reliable band gaps from DFT-MD simulations at finite temperatures. The third publication (see Sec. 4.3) employs this method in order to resolve the band gap closure, i.e., the nonmetal-to-metal of liquid helium in the warm dense matter regime, and to predict the thermophysical properties discussed in Sec. 2.2 around the band gap closure.

3. Results

The overall aim of this thesis is to study the nonmetal-to-metal phase transition in fluid helium with DFT-MD by calculating the band gap and the thermophysical properties discussed in Sec. 2.2. To date, no experimental data on helium exists in the temperature-pressure regime in which the most recent publications predicted the PPT.^{138;139} It is therefore not possible to benchmark the theoretical methods in this regime against experimental results. However, a replication of all high-pressure results that do exist would increase the probability that the application of the theoretical methods at more extreme conditions is justified and leads to reliable results in that domain.

Fig. 3.1 shows the status of the helium phase diagram before this work, adopted from W. Lorenzen.¹⁵⁰

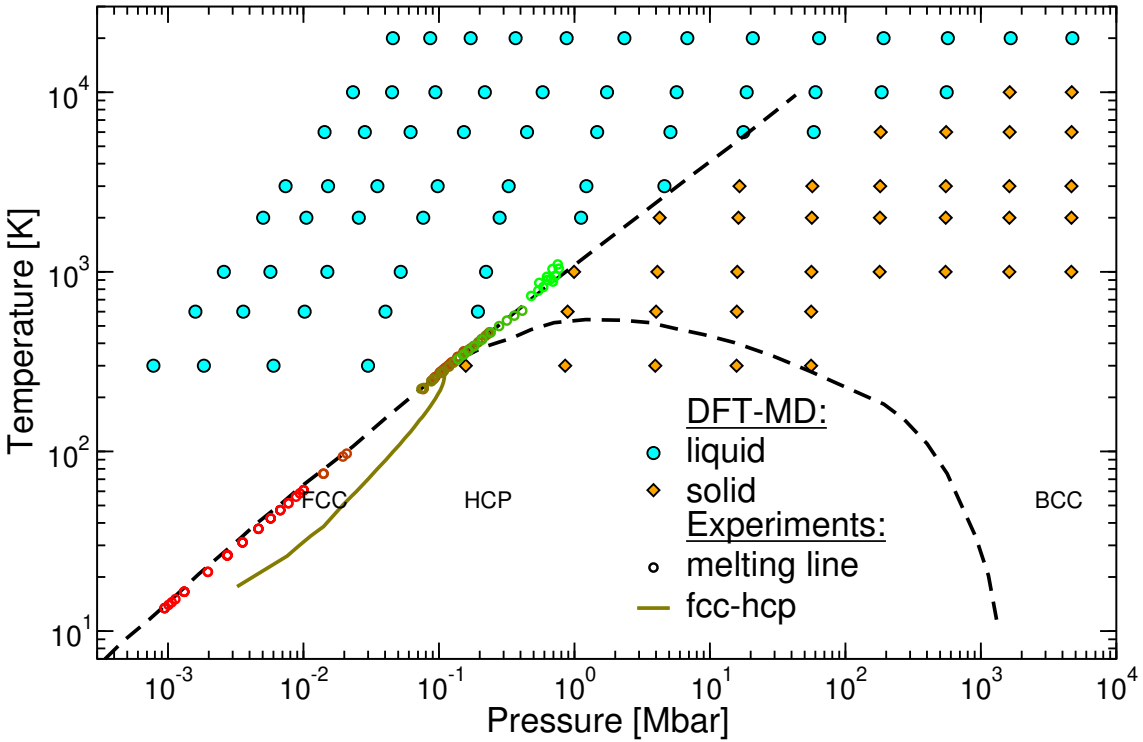


Figure 3.1.: The helium phase diagram (temperature over pressure), after Lorenzen.¹⁵⁰ The dashed black lines denote the hypothetical coexistence lines of Ref. 229.

The first publication (Sec. 4.1) benchmarks the results of DFT-MD concerning

the EOS, the DC conductivity, and the optical reflectivity with a multitude of experiments. It also investigates the influence of different XC functionals regarding the properties mentioned above.

The second publication (Sec. 4.2) tests different two-phase simulation approaches to calculate an accurate melting line from DFT-MD. It predicts the helium melting line to a maximum temperature of 10 000 K and a maximum pressure of 35 TPa using the PBE and the vdW-DF1 XC functional. The results of this publication pave the way for a self-consistent calculation of the metallization in the fluid.

The third publication (Sec. 4.3) explores the three most recent approaches calculating the band gap at finite temperatures. It displays predictions of the band gap closure for eight temperatures between $T = 10\,000$ K and $50\,000$ K, as well as the EOS, the DC conductivity, the optical reflectivity, and the ionization degree, within a density interval $\pm 40\%$ around the density where the band gap closes.

The co-authored fourth publication (Sec. 4.4) evaluates the influence of different XC functionals on the EOS, the DC conductivity, and the band gap of dense hydrogen and deuterium. It benchmarks the results against one of the pioneering experiments regarding the dissociation of molecular hydrogen in the warm dense matter regime.^{127;230} The study finds that the observed differences in DC conductivity and the band gap of the different XC functionals largely arise from the predicted pressures.

Appendix A additionally contains convergence details of all aforementioned first-authored publications.

3.1. Benchmark of the tools against a wide range of experiments

Due to advances in experimental techniques, the last two decades saw a multitude of experiments on compressed helium.^{64;99;100;121;128;231–239} Some of the experiments followed a static approach by compressing helium in diamond anvil cells.^{100;231;233} Especially the higher-pressure experiments employed shockwaves to drive the sample, i.e., helium, to extreme states.^{64;99;121;128;232;234–239} Single-shock experiments can produce high temperatures, while setups with a pre-compressed sample and multiple shockwaves can access high densities at lower temperatures^{99;121;240} due to their quasi-isentropic nature. According to recent theoretical studies,^{137–139} the nonmetal-to-metal phase transition presumably takes place at conditions beyond the reach of today’s experimental capabilities.

The first publication aims to confirm the applicability of the tools discussed in Sec. 2.2 with a wide range of experimental data. A focus of this study is the performance of different XC functionals that describe vdW interactions (vdW-DF1²⁴¹ and vdW-DF2²⁴²) compared to standard XC functionals like the PBE¹⁵⁸ and the HSE^{156;243} XC functional.

The wide range of experimental parameters requires convergence tests of the EOS, the DC conductivity, and the optical reflectivity before the calculations could be performed. 128 atoms for the EOS, up to 256 atoms for the DC conductivity, and 27 atoms for the reflectivity lead to converged results within this study’s density and temperature range; see Appendix A.2 for an in-depth discussion of the convergence of the DC conductivity and the reflectivity.

At zero temperature, the vdW-DF1 XC functional yields higher pressures than the PBE functional, while the vdW-DF2 functional reproduces the results of the PBE XC functional. The vdW-DF1 and vdW-DF2 XC functionals predict lower pressures than the PBE XC functional at higher temperatures.

Fig. 3.2 displays the results of the two existing experiments on the Hugoniot curve of helium^{121;122} and compares the experimental results with data from DFT-MD simulations that employ different XC functionals, namely the PBE, the vdW-DF1, and the vdW-DF2 XC functional.

While all the XC functionals in this study reproduce the experimental trends, increasing temperatures diminish the XC functionals’ differences. The reason for this behavior is the weakening significance of the XC component of the internal energy with increasing temperatures,²⁴⁴ which confirms the choice of the PBE XC functional for the remaining EOS calculations of the publication. However, the extent of the experimental uncertainties does not allow for a clear distinction of XC functionals, which remains a task for future high-precision experiments and subsequent benchmarks of XC functionals.

In the course of the multiple-shock experiment of Eggert *et al.*,¹²¹ the optical reflectivities of the shocked helium samples were measured as well, published by Celliers *et al.*⁹⁹ Later, Brygoo *et al.*²⁴⁵ reanalyzed the reflectivity results with an

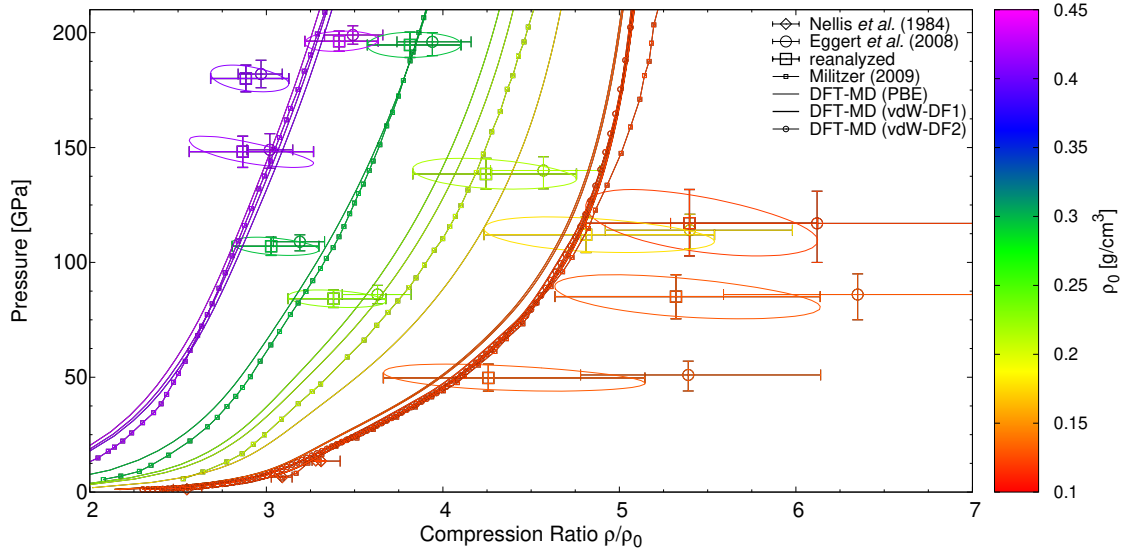


Figure 3.2.: The Hugoniot curve of helium, shown as pressure over the compression rate with colorcoded densities: symbols with error bars mark the results of the two experiments to date.^{121;122} All the other lines and symbols represent the results of DFT-MD simulations that reproduce the experimental values irrespective of the underlying XC functional.

updated pressure standard. The first publication benchmarks three conceptionally different XC functionals against the reanalyzed reflectivities: the GGA functional PBE; the vdW-DF1 XC functional, which enhances a GGA description of the electronic system by including vdW-forces; the hybrid functional HSE, see Tab. 2.1 and the subsequent discussion for further details on the classes of XC functionals. The results are shown in Fig. 3.3.

The results of the different XC functionals exhibit a systematic behavior. The PBE XC functional yields the highest reflectivities, followed by the vdW-DF1 and the HSE XC functional. While the *ab initio* simulations reproduce the experimental trends, the error bars of the experimental data inhibit a comparison of the efficacy of the XC functionals.

Accurate measurements of the DC conductivity in the warm dense matter regime are challenging. Ternovoi *et al.*²³² employed reverberating shock waves to compress cryogenic helium samples while simultaneously measuring the electrical resistance with electrodes as well as the optical emission. They then inferred the DC conductivity from the obtained resistance values. While this approach represents a way to measure the electrical resistance directly, applying the electrodes into the sample chamber further complicates the setup procedure and the actual measurements. The study calculated the temperature, pressure, and density of the final shocked state with a one-dimensional hydrodynamics code that employs the chemical picture as well as a hard-sphere approximation. Both approaches are known to fail in the warm dense matter regime. The first publication attempts to estimate the

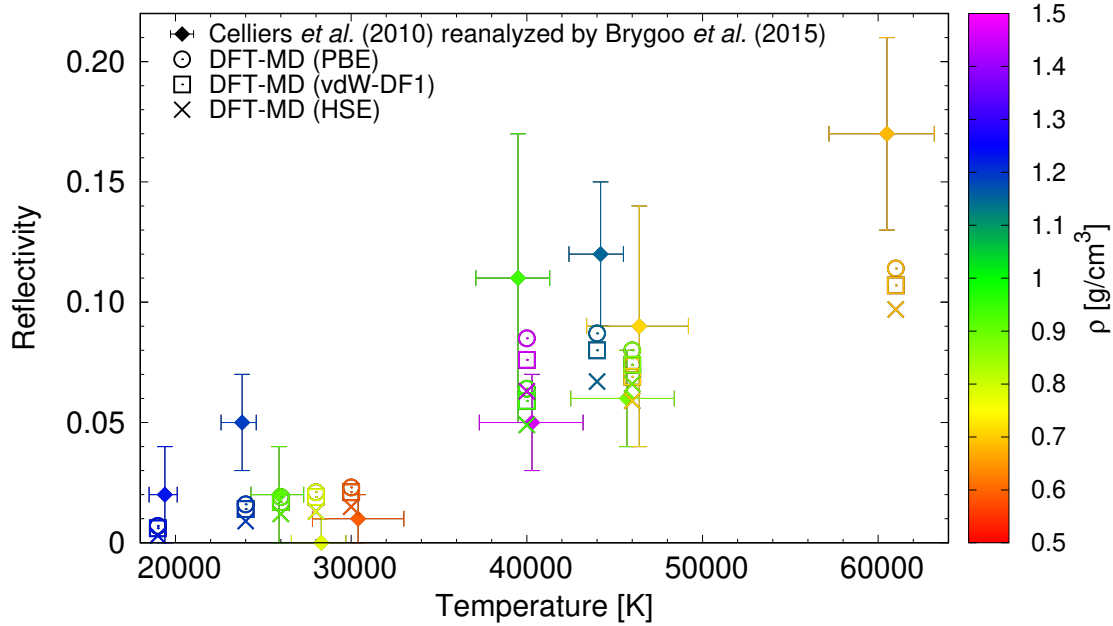


Figure 3.3.: The reflectivity over the temperature with colorcoded densities. Diamonds denote experimental data.²⁴⁵ The PBE, the vdW-DF1, and the HSE XC functional (circles, squares, and crosses, respectively) reproduce the experimental trends.

temperature in this experiment by calculating the DC conductivity at experimental densities and different temperatures and XC functionals. It predicts an increase of the experimental temperature from about 10 000 K to above 30 000 K, extending the temperature range of 15 000 to 25 000 K reported in Ref. 232.

After the publication of the experiment of Eggert *et al.*¹²¹ on the Hugoniot curve, two follow-up publications by Celliers *et al.*⁹⁹ and Soubiran *et al.*¹²⁹ inferred the corresponding DC conductivity by fitting the measured reflectivities with a Drude model. The first publication compared the behavior of the Drude model with the dynamic electrical conductivity from DFT calculations. While the models could reproduce the DC conductivity, their predictions at higher frequencies did not reproduce the dynamic electrical conductivity of the *ab initio* data. However, the DC conductivities of the *ab initio* simulations reproduced the trends of the DC conductivities that were obtained from the Drude models. Similar to the results regarding the Hugoniot curve as discussed above, more precise experiments are required to discern the applicability of different XC functionals in this regime.

Fig. 3.4 displays the DC conductivity from the *ab initio* calculations with the PBE, the vdW-DF1, and the HSE XC functionals and compares them to the results of Ternovoi *et al.*²³² and the Drude models from Celliers *et al.*⁹⁹ and Soubiran *et al.*¹²⁹

The *ab initio* results of the DC conductivity exhibit a systematic behavior. The PBE XC functional yields the highest DC conductivities, followed by the vdW-DF1,

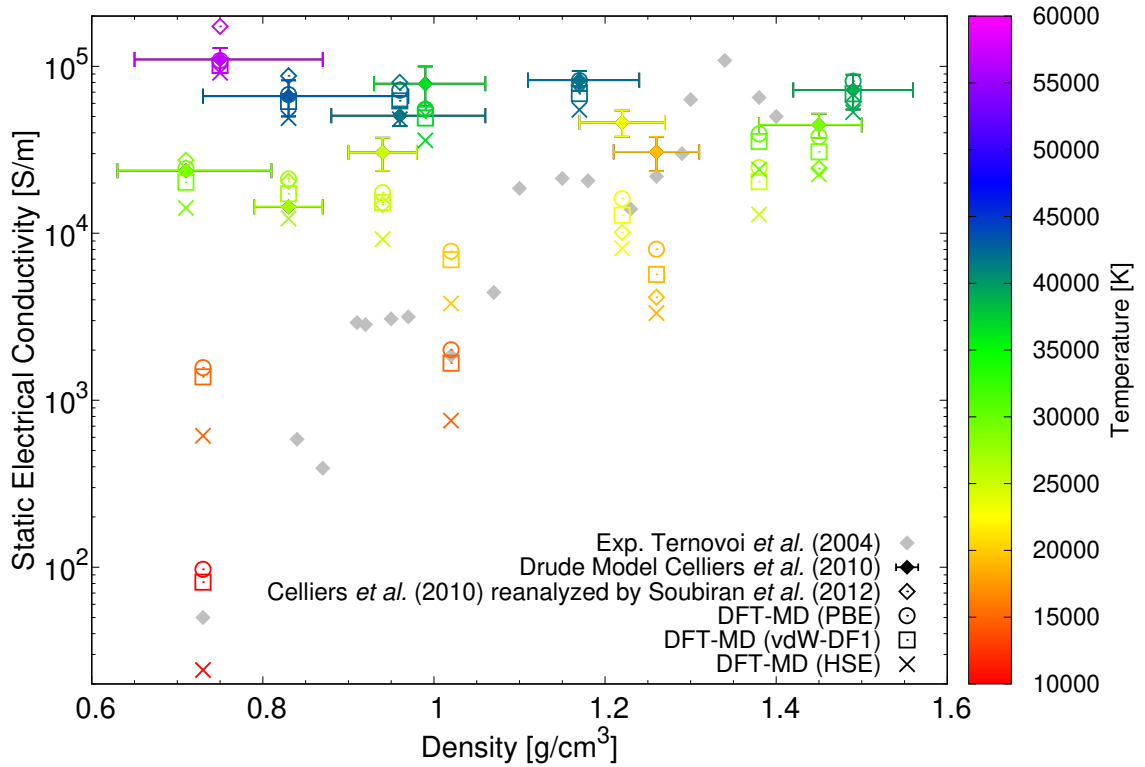


Figure 3.4.: The static electrical conductivity over the density with colorcoded temperatures. Diamonds denote experimental data.^{99;128;129} The PBE, the vdW-DF1, and the HSE XC functional (circles, squares, and crosses, respectively) reproduce the experimental trends.

and the HSE XC functional, respectively.

All XC functionals under consideration reproduce the trends of the experiments. The cause of this accordance is the magnitude of the experimental uncertainties that are significantly greater than the differences in the EOS, reflectivity, and DC conductivity obtained with the XC functionals under study. This encourages more precise experiments, which would lay the foundation on which the viability of the XC functionals under experimental conditions could be tested. It is not possible to perform such benchmarks of the PBE, vdW-DF1, and HSE XC functional with the current magnitude of uncertainty in the experiments. This justifies the use of the PBE functional in the wide range of conditions and properties investigated in this study, which decreases the computational costs compared to the vdW-DF1 and the HSE XC functional.

3.2. Calculation of the high-pressure melting line

Knowledge of the high-pressure melting line paves the way for a consistent calculation of the metallization of dense fluid helium and is relevant in the modeling of dense astrophysical objects, see Secs. 1.2 and 1.3. There are different approaches and methods to calculate points on the melting line. Some publications calculate the Gibbs free energy of the solid and the liquid and then identify the melting points as the points where the Gibbs free energy of the two phases is equivalent.^{246;247} Other publications compute the solid and the liquid in the same simulation box, a technique called two-phase simulation (TPS).^{215;216;218;248–252}

This publication, see Sec. 4.2, tests different approaches to TPSs and the respective convergence with DFT-MD. The literature is not consistent with regards to details such as the spacing between the phases^{219;251;253;254} and the setup of the phases before the two-phase simulations.^{215–222;255–257}

Extensive convergence calculations with respect to the setup of the liquid and solid parts of the two-phase simulation box, the number of atoms, and the \mathbf{k} -point set ensure reliable results, see Sec. A.1.

Among the many ways to set up a TPS cell, a cell containing a perfect crystal configuration and a random liquid distribution provides identical results as more elaborate setup procedures. Additional compression of the solid part counteracts the different pressures between a liquid and a solid at identical temperatures and densities. The higher the number of atoms, the less significant the setup procedure. While more elaborate TPS configurations require only 256 atoms for convergence with respect to TPSs with 2048 atoms, the setup with a perfect crystal and a random liquid part demands 500 atoms.

At the highest densities, a \mathbf{k} -point sampling at the Γ -point is not sufficient. Instead, a single \mathbf{k} -point reproduces the result of a much more involved $2 \times 2 \times 2$ sampling with the computational cost of the Γ -point. The location of this \mathbf{k} -point is $(0 \ 1/3 \ 0)$ relative to the basis vectors $(1 \ 0 \ 0)$, $(-1/2 \ \sqrt{3}/2 \ 0)$, and $(0 \ 0 \ 2\sqrt{8/3})$ of a unit cell consisting of two perfect hcp cells stacked in z -direction.

The standard PAW pseudopotential does not suffice for EOS calculations at the most extreme conditions of this study; see Fig. 3.5 and the subsequent discussion. However, converged TPS results do not require a harder PAW pseudopotential, which greatly reduces the computation time.

On a given isotherm, TPSs provide the density of the melting point. Melting is a first-order phase transition and therefore accompanied by a metastable density region. Tests revealed the extend of this region to be 3.5% in density. In principle, the TPSs could also provide the corresponding melting pressures by continuing the simulations until they have reached thermodynamic equilibrium. However, this is not efficient due to the high number of atoms involved. Instead, EOS calculations with 128 atoms provide the pressures of the melting points at a greatly decreased computational cost. The pressures under investigation range from 15 GPa up to 35 TPa, which demands the use of a harder PAW pseudopotential at the highest pressures and densities; see Fig. 3.5.

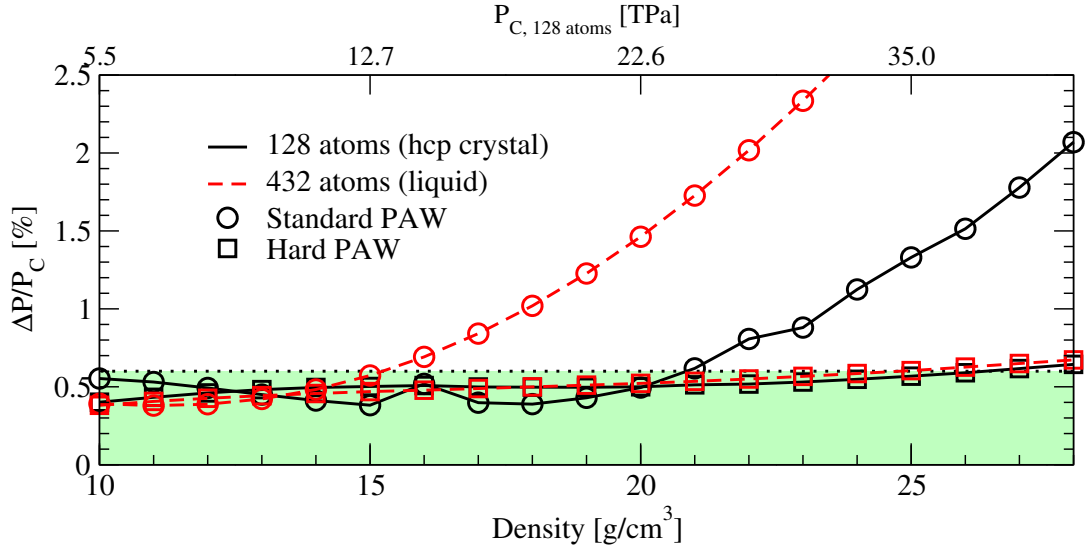


Figure 3.5.: The pressure difference between the full Coulomb potential (baseline), the PAW, and the hard PAW pseudopotential (circles and squares, respectively) over the density. Densities over 14 g/cm^3 require the hard PAW potential for a convergence of better than 0.6% with respect to the Coulomb potential.

At densities below 15 g/cm^3 , the standard PAW pseudopotential reproduces the results of the full Coulomb potential. Higher densities require a harder PAW pseudopotential with greater cutoff energy to obtain convergence within 0.6%.

This study employs the PBE as well as the vdW-DF1 XC functional in order to be consistent with Ref. 90. The previous work²⁵⁸ displayed significant differences in pressures between the results of the PBE and vdW-DF1 XC functional. This raised expectations of significant differences in the resulting TPS melting lines. Instead, as Fig. 3.6 shows, the PBE melting line reproduces the vdW-DF1 melting line within the uncertainties.

The vdW-DF1 XC functional predicts lower densities for each melting point compared to PBE. At the same time, vdW-DF1 results in higher pressures at a given density compared to PBE. The two effects effectively compensate each other, which in turn results in melting points that are virtually identical for both XC functionals. See also Sec. 4.4 for further discussion on the implications of the different pressures predicted by the PBE and the vdW-DF1 XC functional for warm dense hydrogen and deuterium.

The fit function of the melting line reproduces all the available experimental data for the melting line of helium within the respective error bars.^{39;100;119;231;259–261} Its slope is slightly downward, which is contrary to the fit function to the latest experimental data of Santamaría-Pérez *et al.*¹⁰⁰ However, said fit function was never intended to predict the melting line in the terapascal regime.

The fit function of Ref. 100 predicted solid helium in Jupiter and Saturn. In con-

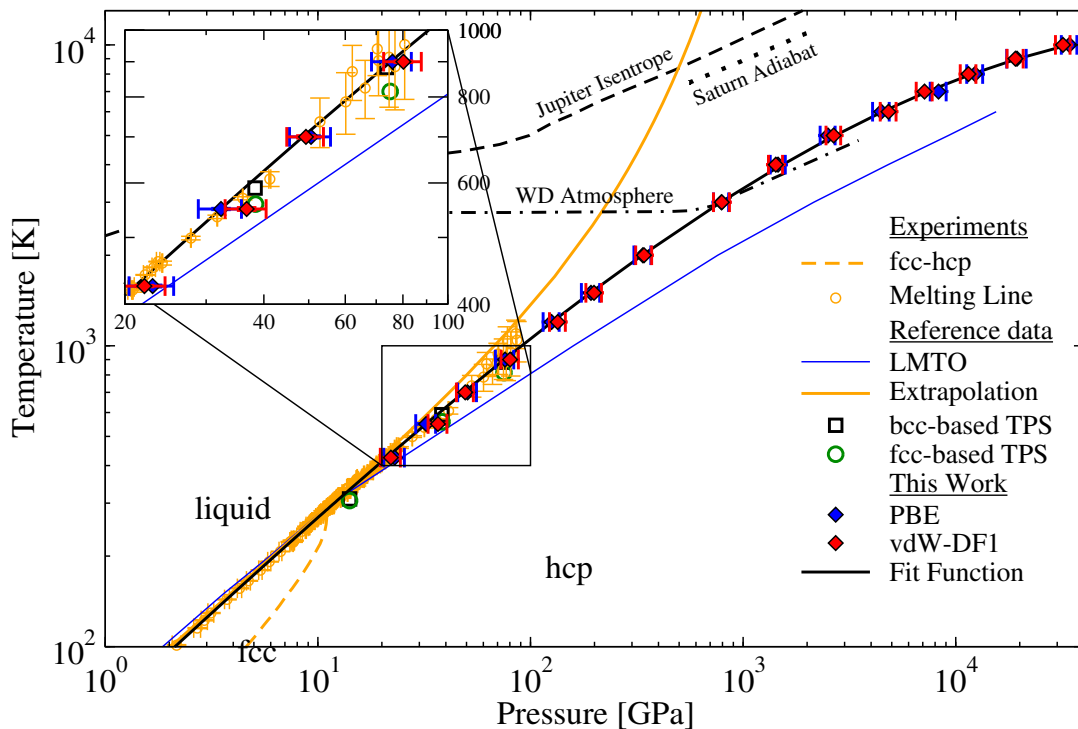


Figure 3.6.: The phase diagram of helium with the PBE (blue diamonds) and the vdW-DF1 (red diamonds) XC functional, and a fit (solid black line) to the melting line from DFT-MD. Orange elements mark experimental data^{39;100;119;231;259–261} and extrapolations.¹⁰⁰ Other black lines denote conditions of astrophysical objects.^{97;101;262}

trast, the Jupiter isentrope¹⁰¹ and the coldest possible helium layer around Saturn’s core⁹⁷ lie above the TPS melting line of this publication. Therefore, the behavior of solid helium is predicted not to influence the interior processes of the gas giant planets of our solar system, in which helium is liquid.

The TPS melting line intersects the P-T conditions of interior simulations of old and cool white dwarfs²⁶² and is therefore relevant for modeling this type of astrophysical object, see also Sec. 1.2. White dwarfs do not generate heat via fusion processes. They instead radiate internal heat and slowly cool over time. The cooling rate strongly depends on the interior structure of the respective WD: In a solid layer, phonons transport heat in an insulating solid, while electron transport provides an additional heat transfer mechanism in a metallic solid. In a liquid, however, convection provides the main heat transport mechanism in the insulating case, with additional electron transport in the case of a metallic liquid. The increased heat transport in a liquid vs. a solid-state and a metallic vs. a nonmetallic phase therefore greatly affects the cooling rate of a WD. As the luminosities of WDs are often used to infer the age of a cosmic region, the results of this study affect the projected ages of helium-rich WDs and their surrounding region.

3.3. Band gap closure at high pressures

The previous publication established the location of the fluid regime of dense helium. This allows the consistent calculation of the location of the nonmetal-to-metal phase transition. This third publication, see Sec. 4.3, aims to identify the order of the PPT and to predict several material properties within a certain density range around the PPT. Should the nonmetal-to-metal transition be of first order, the band gap, the EOS, the DC conductivity, the optical reflectivity, and the ionization degree would exhibit discontinuities at the transition points. If all those properties are continuous, the identification of the PPT location is via the band gap closure. In any case, the prediction of accurate band gaps was necessary. After extensive convergence tests, reported in the supplemental material²⁶³ of this publication, DFT-MD simulations at eight isotherms ranging from 10 000 to 50 000 K at densities between 1 and 22 g/cm³ provided the raw data.

The band gap is ill-defined for temperatures $T > 0$ K. However, there are three phenomenological methods to compute the band gap at finite temperatures in the literature on dense helium: the *HOMO-LUMO*,^{137;139} the *histogram*,²¹⁴ and the *broadened*¹³⁸ approach.

The *HOMO-LUMO* method evaluates the energies below the chemical potential (HOMO) and above (LUMO). At least with the VASP code and in dense liquid helium, this technique always results in finite band gaps. However, for unknown reasons, this is neither the case with the ABINIT code¹³⁷ nor for liquid hydrogen and deuterium, see Sec. 4.4.

A second method, labeled *histogram*, records histograms of the band energies and calculates the band gap from the resulting DOS.

The third technique, labeled *broadened*, shifts the band energies by the chemical potential and then broadens the resulting DOS with a Gaussian function. The width of the Gaussian function depends on the width of the valence band. As increasing densities lead to a wider valence band, the corresponding broadening leads to band gap closures at lower densities compared to the other approaches to the band gap. Sec. 2.4 provides further details regarding the calculation of band gaps with DFT-MD and Fig. 2.8 therein contains a visual representation of the different approaches to the band gap. Fig. 3.7 compares the band gaps, calculated with the three methods discussed above, with the corresponding literature values.

While the results of all techniques for the calculation of the band gap reproduced the literature values, none displayed the discontinuities that are characteristic for a first-order phase transition. As discussed above, the *broadened* approach gave the smallest band gaps of all methods under consideration for every temperature and density. The results of the *histogram* technique demonstrated a systematic behavior. The lack of results of the *histogram* method in liquid helium in the literature prevented a comparison. All the trends of the literature values of the *HOMO-LUMO* approach could be reproduced. However, this technique does not result in closed band gaps in liquid helium, even at the highest densities under consideration, and is therefore unable to predict the corresponding band gap closure.

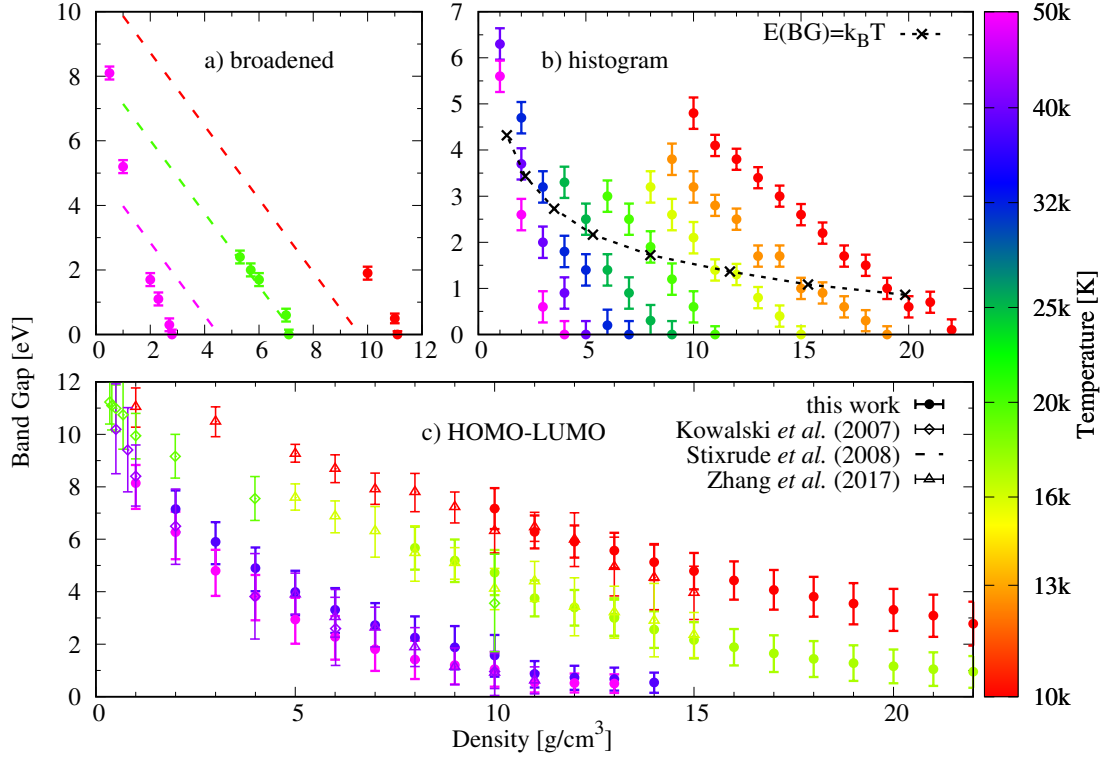


Figure 3.7.: The band gap over the density for all colorcoded temperatures under consideration in the respective study. The panels compare the different approaches: panel a) displays the results of the *broadened*, panel b) of the *histogram*, and panel c) of the *HOMO-LUMO* method. The data of this study is shown as filled circles, while the literature values are dashed lines,¹³⁸ open diamonds,¹³⁷ and open triangles,¹³⁹ respectively.

Not only the band gaps did not demonstrate signs of a first-order phase transition, but this was also the case for the results of the EOS, the DC conductivity, the optical reflectivity, and the ionization degree. Due to the lack of experimental data in this density-temperature regime of fluid helium, the previous studies on the theoretical description of the metallization in fluid helium^{137–139} provided data to compare the results to. Fig. 3.8 displays the results for the DC conductivity representing the lack of signs for a first-order phase transition in all quantities of this study.

Aside from the lowest temperature considered in Ref. 139, the DC conductivities of this study and the literature values gave a consistent picture. The thermal activation of the band gap close to the minimum Mott conductivity leads to features in the DC conductivities at the lower temperatures of this study. The DC conductivities from Ref. 129 and the corresponding DFT values of the first publication, see also Sec. 3.1, provided low-density data that continued the trends of the high-density results.

The third publication employed a novel self-consistent way to calculate the ionization degree within DFT pioneered by M. Bethkenhagen *et al.*²⁰⁸ Sec. 2.2.5 provides

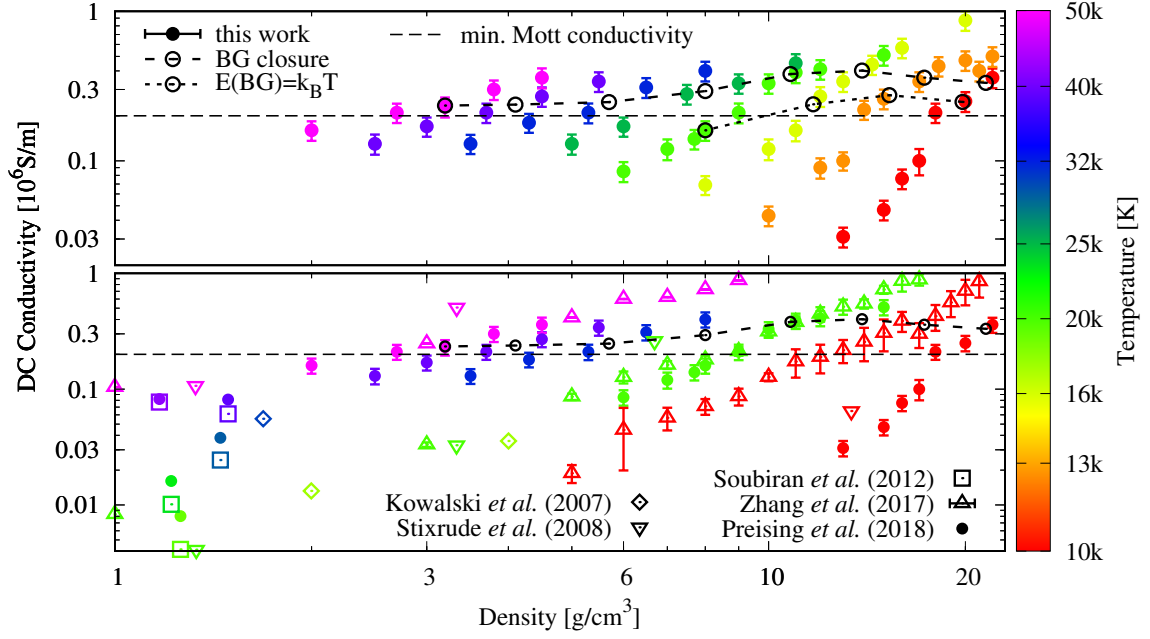


Figure 3.8.: The DC conductivity over the density for all the isotherms of this study (upper panel). The lower panel compares selected isotherms to results from the literature.^{129;137–139;258}

an outline of this approach. It applies the dynamic electrical conductivity and the Thomas-Reiche-Kuhn sum rule to calculate the effective number of electrons that contribute to the electronic transitions within the conduction band;^{209–212} see Sec. 2.2.5. The conventional method calculates the number of electrons at energies above the band gap from an integration over the DOS and equates the result with the number of free electrons. Fig. 3.9 shows the results for the ionization degree.

The method that employs the sum rule predicted a steady pressure ionization from under 10% ionization at 2 g/cm³ to more than 99% ionization at 22 g/cm³ and almost no temperature dependency. In contrast, integrating over the DOS resulted in less than 15% ionization and exhibited a relatively strong temperature effect with no systematic influence on the density. Therefore, the description of the ionization degree with an integration over the DOS seems to be unable to describe the pressure ionization of dense helium.

The wide range of densities required extensive convergence tests (see Sec. A.2) of the DC conductivity, the reflectivity, and the ionization degree at the most extreme densities and temperatures of this publication. The ionization degree, in particular, displayed a great sensitivity with respect to the (pseudo-)potential and demanded the full Coulomb potential for converged results of the ionization degree. In contrast, the DC conductivity required the PAW pseudopotential, while the reflectivity demanded the use of the hard PAW pseudopotential at all densities under consideration.

Neither the results of the pressure, the internal energy, the DC conductivity, the

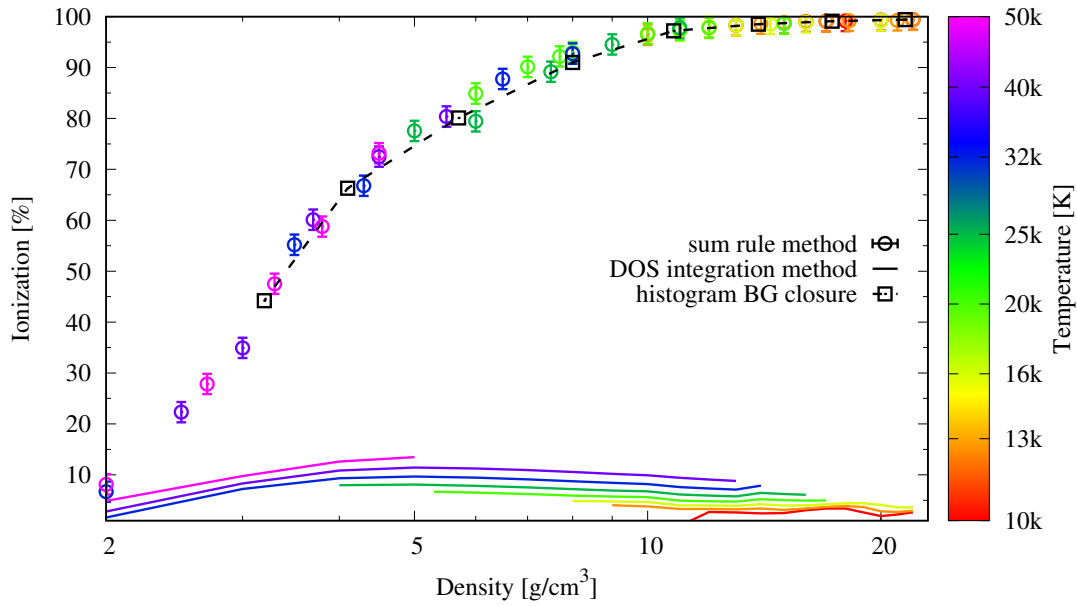


Figure 3.9.: The ionization degree, calculated with two different methods over the density for all temperatures under consideration.

optical reflectivity, the ionization degree, or the band gap demonstrated signs of a first-order phase transition from the nonmetallic fluid to the metallic fluid. Therefore, the nonmetal-to-metal phase transition seems to be continuous or of higher order.

This third publication predicted quantities in a temperature-density range yet unexplored by experiments on fluid helium. Future measurements of the EOS, the DC conductivity, and the reflectivity under the reported conditions would provide a benchmark of the theoretical framework under those extreme conditions. The results of this study can serve as an input for planetary and stellar modeling, and for future experiments, and, hopefully, spark a renewed interest in the behavior of warm dense helium.

3.4. Influence of different XC functionals on the location of the dissociation of hydrogen and deuterium

While the previous publications concern the properties of warm dense helium, this publication²²⁷ describes the dissociation and subsequent metallization of warm dense hydrogen and deuterium; see Sec. 4.4.

Similar to the metallization of helium, the so-called plasma phase transition (PPT) of hydrogen and its isotopes has been predicted in the advent of quantum theory.^{264–266} Recent advantages in the theoretical description of warm dense matter beyond chemical models as well as in experimental capabilities lead to a lively discussion of the PPT of hydrogen. As discussed in Sec. 1.3, the dissociation of hydrogen acts as a catalyst for the demixing of hydrogen and helium under planetary interior conditions.⁸⁹ Therefore, the exact location of the PPT has a significant impact on the processes in giant planets.^{267;268}

After the pioneering experiment on the metallization of hydrogen by Weir, Mitchell, and Nellis (WMN),^{127;230} this transition has been probed by many more,^{88;269–271} yielding results with a pressure difference of a factor around three between the lowest²⁷⁰ and highest pressures⁸⁸ obtained in the experiments. The results of *ab initio* methods display roughly the same discrepancy, depending on the method.^{88;272;273} While *ab initio* calculations accompanied the more recent experiments, this is not the case for the very first one, where the computational demand of DFT-MD calculations was not yet feasible.

WMN measured the electrical conductivity and the impact velocity in gas gun experiments using reverberating shocks. The reported pressures, densities, and temperatures at maximum compression resulted from calculations based on the Kerley²⁷⁴ and Ross^{275–277} EOS. They used two methods to infer the final temperatures and densities, described as different but equivalent. However, only one method described the thermodynamic path of the experiment correctly, while the other method neglected the entropy increase due to the multiple shocks in the experiment. Based on an updated and well-accepted version of the Kerley EOS, labeled Kerley03,²⁷⁸ this publication recalculated the pressures and temperatures of this experiment and found substantial differences of about 20-30% to the reported data.

The energy gap of WMN resulted from a semiconductor model that was linear in density. In order to reproduce the reported conductivities, this model requires negative energy gaps above a certain density. An updated model incorporates the reported saturated DC conductivity and reproduces the conductivity values of WMN, while maintaining energy gaps $E_g \geq 0$ eV. The publication demonstrates that the original model underestimated the energy gap by about 1 eV.

WMN inferred the pressures in the experiment independent from the EOS of hydrogen or deuterium. In the respective region of the phase diagram, the pressures more strongly depend on the density than the temperature. Therefore, the pressures are more strongly constrained than the temperatures.

Accordingly, the DFT-MD calculations of the fourth publication were performed at the reported temperatures of WMN. The calculations then iteratively found the densities that reproduced the reported pressures with the PBE,¹⁵⁸ the vdW-DF1,¹⁵⁷ and the vdW-DF2²⁴² XC functionals. Fig. 3.10 compares the resulting densities for hydrogen.

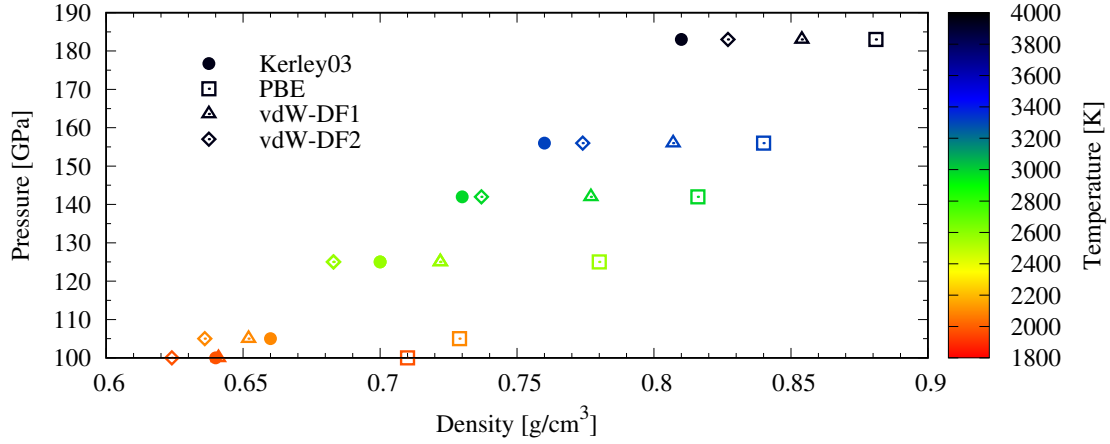


Figure 3.10.: The pressure over the density with colorcoded temperatures of hydrogen for the Kerley03 EOS²⁷⁸ (circles), and the PBE (squares), the vdW-DF1 (triangles), and the vdW-DF2 (diamonds) XC functional.

The PBE XC functional resulted in the highest densities, which are systematically larger than those of the Kerley03 EOS by around 9-12%. The nonlocal vdW XC functionals yielded densities below (above) those of the Kerley03 EOS at lower (higher) pressures and therefore reproduced the Kerley03 predictions better than the PBE XC functional. Among the nonlocal functionals, the vdW-DF1 XC functional resulted in systematically higher densities than the vdW-DF2 XC functional.

The differences in the predicted densities have profound implications for the inferred DC conductivity, see Fig. 3.11.

Compared to the vdW-DF1 and the vdW-DF2 XC functionals, the PBE functional appears to overestimate the DC conductivity in this regime. It predicts a metallic conductivity under all experimental conditions, while the nonlocal functionals reproduce the onset of the metallization as observed in the experiment. However, when plotted as a function of density instead of pressure, all functionals reproduce the experimental trends. In general, the PBE XC functional gives the highest DC conductivities, followed by the vdW-DF1 and the vdW-DF2 XC functional. At least for the PBE and the vdW-DF1 XC functional, the corresponding DC conductivities in warm dense helium reproduce this trend; see Fig. 3.4 and the discussion in Sec. 3.1.

Calculations of the DOS of hydrogen displayed a correlating behavior. The PBE functional predicts closed band gaps under all conditions of the WMN experiment, while the band gaps from the nonlocal functionals close upon increasing pressure

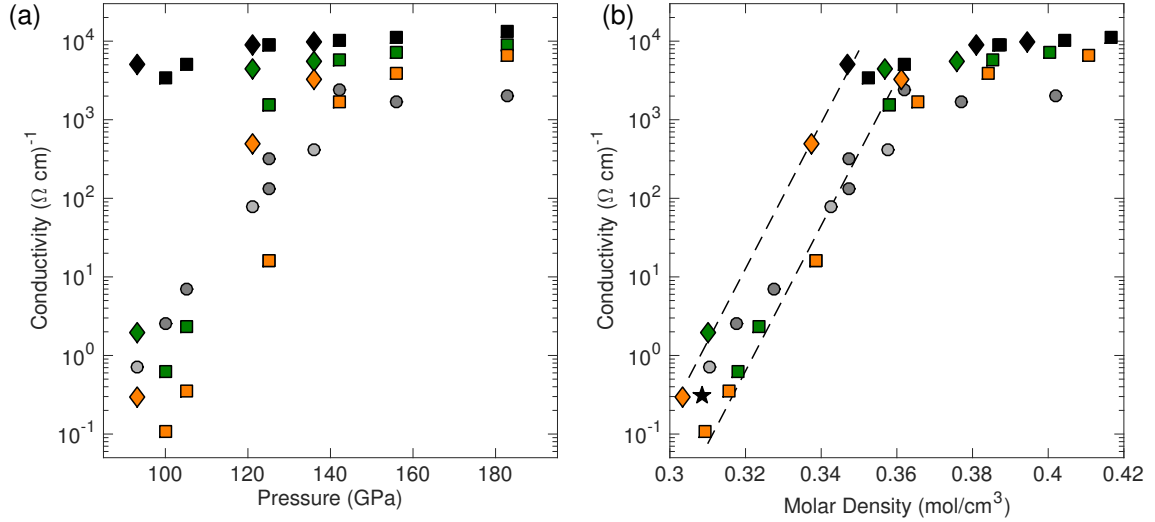


Figure 3.11.: The DC conductivity over the pressure (panel (a)) and the molar density (panel (b)). The circles represent the measured conductivities for hydrogen (dark gray) and deuterium (light gray) of WMN.^{127;230} The squares denote calculated DC conductivities for hydrogen (squares) and deuterium (diamonds). Black, green, and orange symbols indicate the PBE, the vdW-DF1, and the vdW-DF2 XC functional, respectively. Dashed lines guide the eye and the star is an additional PBE calculation at lower molar density.

and temperature, with vdW-DF2 resulting in larger energy gaps than the vdW-DF1 XC functional.

The corresponding band gaps are closed under all conditions for the PBE XC functional, while the band gaps of the nonlocal functionals resemble the energy gaps of the updated semiconductor model discussed above. However, when plotted as a function of molar density instead of pressure, all XC functionals follow the same trend, see Fig. 3.12. This behavior is analogous to the one displayed in Fig. 3.11.

The band gaps resulted from the *HOMO-LUMO* approach discussed in Sec. 2.4 and applied to warm dense helium in the third publication, see Secs. 3.3 and 4.3. Identical to the third publication, the VASP code performed the calculations. However, contrary to the results in warm dense helium, the band gap of warm dense hydrogen closes with the *HOMO-LUMO* method and gives converged results with 40 snapshots. The *HOMO-LUMO* technique in warm dense helium required the statistical data of thousands of DFT-MD time steps to converge; see Ref. 263. This discrepancy deserves future attention.

Additional calculations reviewed whether the observed behavior of the PBE XC functional with respect to the DC conductivity and the band gap resulted from the decision to fix the temperature and vary the density instead of fixing the density and varying the temperature to reproduce the pressures of the WMN experiment. However, the resulting states exhibited metallic behavior as well as closed band gaps,

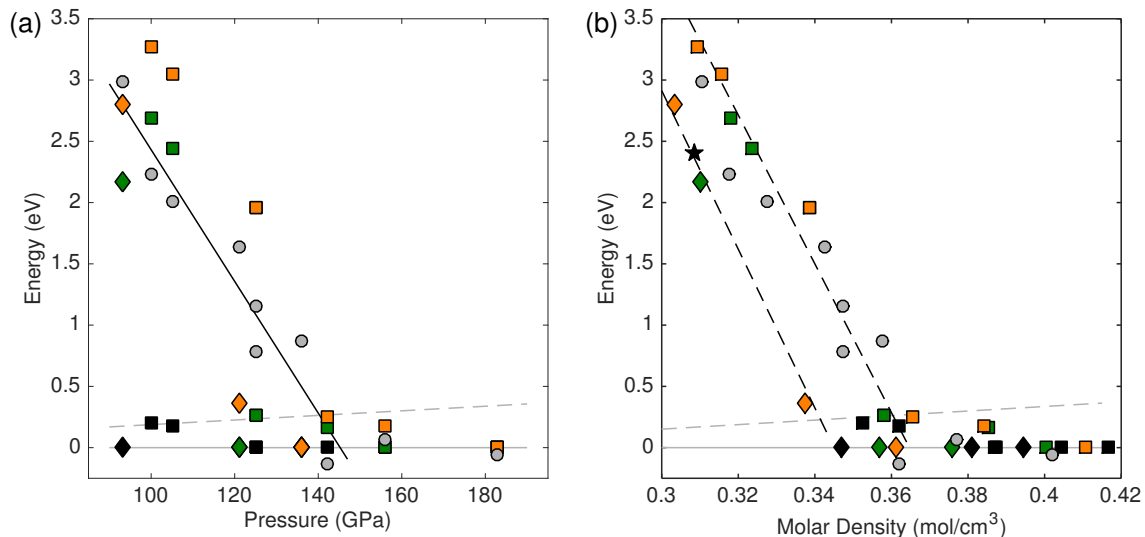


Figure 3.12.: The band gap over the pressure (panel (a)) and the molar density (panel (b)). Gray circles represent the results of the updated semiconductor model described above. The notation of the other symbols is identical to that of Fig. 3.11. The dashed gray line indicates the temperature of the system in eV. The solid gray line represents a closed band gap, while the solid black line denotes a fit to data with a band gap larger than the thermal energy. Dashed black lines display the trends in the case of hydrogen and deuterium, resulting in an offset of about 1 eV.

independent of the fixed quantity. Therefore, irrespective of the method to reach the desired pressures, the results by the PBE XC functional are inconsistent with measured data.

An examination of the measured and calculated DC conductivities as a function of the band gap evaluated the temperature dependence of the conductivities. After normalizing all conductivities to the one observed at the lowest temperature, the DC conductivities increase linearly with decreasing band gaps. Here, the nonlocal XC functionals follow the results of the updated semiconductor model, while the PBE XC functional exhibits closed band gaps and metallic conductivities under all the experimental conditions, as discussed above.

The PBE and the nonlocal XC functionals exhibit significant differences with respect to the EOS, the band gaps, and the DC conductivities in warm dense hydrogen and deuterium. The underlying cause appears to be the higher pressures resulting from the PBE XC functional,^{279;280} which underestimate the pressures for the dissociation. The underprediction of the dissociation pressures has profound consequences. It leads to exaggerated DC conductivities and underestimated band gaps, inconsistent with the results of the WMN experiments. This finding is consistent with earlier studies.⁸⁸ However, other experiments report a coincidence of their results with calculations using the PBE XC functional.^{269–271;281} The respective re-

sults are under lively debate.^{88;282;283}

3.5. Conclusion

In this work, high-pressure properties of helium have been studied and predicted within an *ab initio* DFT-MD framework. The verification of the theoretical foundations with experimental data increased the confidence in the results of the computational methods. This allowed applying the method in regions of the helium phase diagram that have yet to be explored experimentally. The focus was a knowledge gain concerning the high-pressure phase diagram of helium. Extensive two-phase simulations over a wide range of densities resulted in the *high-pressure melting line* of helium. The knowledge of the melting line allowed for a consistent calculation of the nonmetal-to-metal phase transition in liquid helium that has been discussed for decades.

A variety of experiments on dense helium have produced a rich experimental data set. In the first publication²⁵⁸ (Sec. 4.1), *ab initio* simulations demonstrated very good agreement with various experimental results concerning the equation of state, the static electrical conductivity, and the reflectivity. A test of different exchange-correlation functionals within DFT-MD confirmed that the popular PBE functional provides a sufficient description of all the quantities under study, at least within the parameter range of this publication and the experimental uncertainties in the literature.

The second publication²¹³ (Sec. 4.2) employed *two-phase simulations* to calculate the high-pressure melting line of helium. For the sake of consistency with respect to previous calculations on the demixing of hydrogen-helium mixtures, this publication used the PBE and the vdW-DF1 exchange-correlation functional. Although quite different in nature, the two functionals reproduced each other's melting lines within the uncertainties. The results of all the experimental data to date could be reproduced within the experimental error bars. Further simulations at higher pressures and densities allowed for a prediction of the helium melting line to pressures of up to 35 TPa and temperatures of 10 000 K. The conditions inside the giant gas planets of the solar system, Jupiter and Saturn, do not intersect the resulting melting line according to recent models and helium is fluid in those giant planets. Instead, the helium melting line is relevant for models of astrophysical objects with lower temperatures like old and cool white dwarfs.

On the foundations of the first publications, the third publication²²⁸ (Sec. 4.3) studied a wide range of high-density properties of fluid helium. The literature is not conclusive with respect to the method to calculate the band gap in helium. An in-depth review of the different approaches to the band gap and their convergence implicated that the most reliable method relies on histograms of the band energies during DFT-MD simulations. Besides the band gap and the closure thereof, the study contains results for the pressure, the internal energy, the static electrical conductivity, the optical reflectivity, and the ionization degree. The latter was calculated self-consistently with a novel method that utilizes the Thomas-Reiche-Kuhn sum rule. Neither of the quantities displayed any signs of a first-order phase transition. Instead, the nonmetal-to-metal transition seems to be continuous with a

static electrical conductivity of around the minimum Mott conductivity of 0.2 MS/m and reflectivity of around 35%. The ionization degree increases from below 10% at low densities to above 99% at high densities and displays no strong dependency on the temperature within the uncertainties. The results are relevant for models of brown dwarfs, white dwarfs, and the class of exoplanets called hot Jupiters.

The results of the second and third publication culminate in an updated version of the helium phase diagram of Fig. 3.1, see Fig. 3.13.

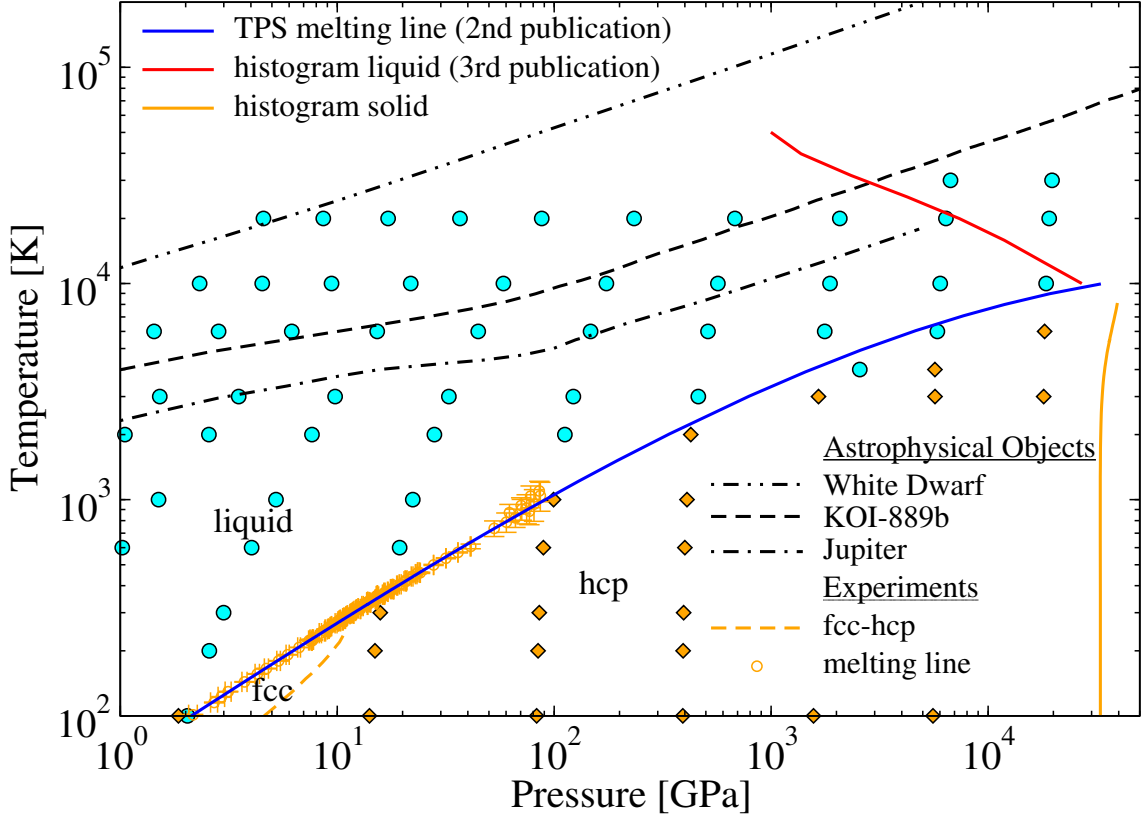


Figure 3.13.: The updated helium phase diagram (temperature over pressure). Additional to the data of Fig. 3.1, the blue line denotes the two-phase melting line of the second publication, the red line is the band gap closure of the histogram method in the liquid of the third publication, and the orange line is the band gap closure in the solid of Ref. 214. The black lines show isentropes of astrophysical objects from Refs. 101;111;284. The resulting phases that were a byproduct of the calculation of the He-REOS.3¹¹⁰ are the cyan circles (liquid) and the orange diamonds (solid), taken from Ref. 150.

Although it was never the intention of the calculations that were performed for the He-REOS.3,¹¹⁰ the resulting liquid and solid EOS points are in good accordance with the TPS melting line of the second publication. This highlights the quality and consistency of the He-REOS.3 and the TPS melting line.

The fourth publication²²⁷ (Sec. 4.4) studied the efficacy of the semilocal PBE and the nonlocal vdW-DF1 and vdW-DF2 XC functionals to describe the EOS, the DC conductivity, and the band gap in warm dense hydrogen and deuterium. It benchmarked the results against pioneering multiple-shock experiments and demonstrated and corrected inconsistencies in the subsequent analysis of the experimental data. The PBE XC functional appeared to predict higher pressures than the nonlocal XC functionals, which manifests in underestimating the dissociation pressure and the band gap and overestimating the DC conductivity. The results of the nonlocal XC functionals, however, were in good agreement with the corrected experimental data. This finding suggests that the PBE XC functional is unsuitable to describe the dissociation of hydrogen and deuterium in the warm dense matter regime, which has a profound impact on the analysis of future and past experiments.

3.6. Outlook

Future work will expand the band gap calculations toward lower densities and other exchange-correlation functionals such as the vdW-DF1²⁴¹ and the hybrid HSE functional,^{156;243} and the GW method^{285–287} for the computation of very accurate band gaps. This would allow for more precise models of planetary dynamos of young and hot giant gas planets such as the so-called Hot Jupiters.

Lower pressures at higher temperatures are more easily achieved in experiments compared to low temperatures and high pressures. Experiments in the region of the low-density band gap closure would provide a benchmark for the quality of different exchange-correlation functionals. Especially the results of the third publication for the static electrical conductivity and the optical reflectivity, as well as a comparison to future experiments, allow for a discussion of the predictive power of the theoretical methods. While the results of different exchange-correlation functionals merge at increasing temperatures,²⁴⁴ highly precise experiments in this regime might still provide valuable information on the efficacy of different functionals.

The novel description of the ionization degree²⁰⁸ with the TRK sum rule will provide further insight into the behavior of matter under extreme conditions. This method is very fast and accurate. It could potentially resolve the critical point of the molecular and atomic liquid in dense hydrogen. Of course, the TRK sum rule method would also yield insight into the behavior of other elements.

This thesis demonstrates the accuracy of the DFT-MD method and predicts properties beyond present experimental capabilities. Hopefully, a renewed interest in warm dense helium leads to high-precision experiments which would help to further refine theoretical descriptions as well as our understanding of astrophysical properties.

4. Publications

This chapter contains three peer-reviewed first-author publications^{213;228;258} and one publication as a co-author.²²⁷ An overview prior to every publication lists the authors and their respective contributions to the publication.

4.1. Equation of state and optical properties of warm dense helium

Author contributions

M.P. Preparation of the manuscript, all calculations for the cold curve, calculations for the hugoniot, all calculations for the density of states, the reflectivity, the static and the dynamic electrical conductivity.

W.L. Preparation of the manuscript, calculations for the hugoniot.

A.B. Preparation of the manuscript, calculations for the temperature-pressure relations along the hugoniot, calculations for the isentropic compression experiments.

R.R. Supervision of the project, preparation of the manuscript.

M.K. Supervision of the project, preparation of the manuscript, calculations for the hugoniot.

M.D. Supervision of the project, preparation of the manuscript.

Equation of state and optical properties of warm dense helium

Cite as: Phys. Plasmas **25**, 012706 (2018); <https://doi.org/10.1063/1.5011650>

Submitted: 01 November 2017 . Accepted: 21 December 2017 . Published Online: 08 January 2018

Martin Preising, Winfried Lorenzen, Andreas Becker, Ronald Redmer, Marcus D. Knudson, and Michael P. Desjarlais



View Online



Export Citation



CrossMark

ARTICLES YOU MAY BE INTERESTED IN

[Directly calculated electrical conductivity of hot dense hydrogen from molecular dynamics simulation beyond Kubo-Greenwood formula](#)

Phys. Plasmas **25**, 012707 (2018); <https://doi.org/10.1063/1.5013631>

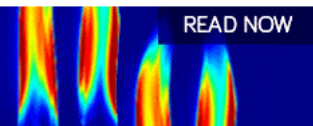
[Multi-charge-state molecular dynamics and self-diffusion coefficient in the warm dense matter regime](#)

Phys. Plasmas **25**, 012701 (2018); <https://doi.org/10.1063/1.5000757>

[A comprehensive alpha-heating model for inertial confinement fusion](#)

Phys. Plasmas **25**, 012703 (2018); <https://doi.org/10.1063/1.4991405>

AIP Advances
Fluids and Plasmas Collection



Phys. Plasmas **25**, 012706 (2018); <https://doi.org/10.1063/1.5011650>

25, 012706

© 2018 Author(s).



Equation of state and optical properties of warm dense helium

Martin Preising,¹ Winfried Lorenzen,¹ Andreas Becker,¹ Ronald Redmer,¹ Marcus D. Knudson,² and Michael P. Desjarlais³

¹*Institut für Physik, Universität Rostock, D-18051 Rostock, Germany*

²*Institute for Shock Physics, Washington State University, Pullman, Washington 99164-2816, USA*

³*Pulsed Power Sciences Center, Sandia National Laboratories, Albuquerque, New Mexico 87185, USA*

(Received 1 November 2017; accepted 21 December 2017; published online 8 January 2018)

We used molecular dynamics simulations based on density functional theory to study the thermophysical properties of warm dense helium. The influence of different exchange-correlation (XC) functionals was analyzed. We calculated the equation of state at high pressures up to several Mbar and temperatures up to 100 000 K in order to reconstruct recent static, single shock, and quasi-isentropic compression experiments. Furthermore, we calculated the dynamic electrical conductivity and determined the reflectivity and DC conductivity. We compared our results with experimental data and found good agreement between our calculations and the high-pressure experiments. The different XC functionals give similar results in the equation of state calculations, but have a strong impact on the reflectivity and the DC conductivity. *Published by AIP Publishing.* <https://doi.org/10.1063/1.5011650>

I. INTRODUCTION

Helium, the second most abundant element in the universe, is of paramount interest for a variety of problems in astrophysics, e.g., the interior structure and evolution of stars, brown dwarfs, and giant planets. Matter exists under extreme conditions inside these objects with pressures varying from a few bars in the atmosphere up to several tens of Mbar in the core of giant planets and hundreds of Gbar in that of Brown Dwarfs. Although many properties of these objects are dominated by the behavior of hydrogen, the most abundant element by far, the influence of helium cannot be neglected. Therefore, detailed theoretical and experimental efforts have been made to determine the equation of state (EOS) as well as the optical properties of helium, albeit to a lesser extent than for hydrogen. While the low-temperature regime (i.e., up to about 1000 K) is accessible by static diamond anvil cell (DAC) experiments,^{1–5} the high-temperature region of the phase diagram can only be explored using dynamic shock-wave experiments that utilize, e.g., gas guns⁶ or high explosives.^{7–9} A novel technique is the combination of DACs and laser-driven shock waves to generate higher densities at lower temperatures compared with single-shock experiments.^{10–12}

On the theoretical side, various techniques have been applied to study warm dense helium. For instance, chemical models^{13–20} lead to approximate but useful results for a large domain of temperatures and pressures. However, in the ionization regime from a dense neutral fluid to a fully ionized plasma, the assumptions of chemical models on the stability of bound states and on the validity of effective two-particle interactions between the species become questionable. For instance, two first-order phase transitions, one for each ionization stage, have been proposed for helium¹⁴ similar to the plasma phase transition in hydrogen. Recent studies on hydrogen have shown that chemical models tend to substantially overestimate the density jumps for the first-order liquid-liquid phase transition connected with the nonmetal-to-

metal transition, compared with *ab initio* simulations.^{21–26} Therefore, *ab initio* simulations based on the physical picture were also performed for helium, e.g., using a combination of classical molecular dynamics simulations for the ions and density functional theory for the electrons (DFT-MD).^{27–30} Extended quantum Langevin MD simulations within the DFT framework were performed recently.³¹ A reliable method for high temperatures is the path-integral Monte Carlo (PIMC) simulation,^{32,33} or diffusion quantum Monte Carlo (DMC) for solid helium,³⁴ i.e., low temperatures. As a noble gas, the interaction between helium atoms is dominated by van-der-Waals (vdW) forces. These long-range correlations are not taken into account by local [Local Density Approximation (LDA)], semi-local [Perdew, Burke and Ernzerhof (PBE),³⁵ Armiento and Mattsson (AM05),³⁶ and rPW86³⁷ or hybrid [Heyd, Scuseria and Ernzerhof (HSE)^{38,39}] exchange-correlation (XC) functionals. A serious problem in DFT-based methods is the underestimation of the band gap of helium,^{28,29,31,34} which should have an influence on the EOS data in the ionization regime and a strong impact on optical properties like the reflectivity.

In this work, we performed extensive DFT-MD simulations and determined a broad spectrum of thermophysical properties, e.g., thermodynamic (EOS, Hugoniot curve, isentropes), optical (reflectivity), and transport properties (electrical conductivity), in order to get a comprehensive overview of the high-pressure behavior of dense helium with a special focus on the transformations induced by density and temperature changes. We cover the region of static and dynamic experiments performed in the solid and liquid phase of helium which represent parameters ranging from ambient conditions up to extreme pressures of 5 TPa and temperatures of 100 000 K. In particular, our study is motivated by the reflectivity measurements of Eggert *et al.*¹¹ along the principal Hugoniot curve. We reanalyze their data by using the improved quartz standard of Knudson and Desjarlais^{40–42} which shifts the Hugoniot curve systematically towards lower compressions as in the case of hydrogen. This was also shown

by Brygoo *et al.*⁴³ for laser-driven shock wave experiments on precompressed hydrogen⁴⁴ and helium samples.¹¹ Furthermore, we calculate isentropic compression paths up to 5 TPa as recently reported by Mochalov *et al.*⁹ In addition, we determine the reflectivity and electrical conductivity of warm dense helium by evaluating the Kubo-Greenwood formula.^{45,46} Our results are then compared with the experimental data of Eggert *et al.*¹¹ and Ternovoi *et al.*⁷

In order to test the efficacy of the XC functionals, we perform DFT-MD simulations using various XC functionals and compare the results. In particular, to estimate the influence of vdW forces on the EOS of helium, we calculated the 0 K isotherm in the solid regime with all vdW implementations contained in VASP version 5.3.5. More demanding DFT-MD simulations were performed at lower densities and 300 K in the fluid regime employing some representatives of the aforementioned vdW implementations. As we find mostly negligible deviations between PBE and most vdW functionals in the EOS calculations, we use PBE for all non-optical computations. The optical and transport properties are then calculated using the PBE, HSE, and vdW-DF1 XC functionals.

Our paper is organized as follows: In Sec. II, we briefly outline details of the DFT-MD simulations. The results for the EOS are presented in Sec. III and those for the optical properties in Sec. IV. At the end, we give a summary and an outlook.

II. THEORETICAL METHOD

A. DFT-MD simulations

We perform DFT-MD simulations based on a combination of DFT^{47,48} for the electrons and classical MD for the ions to calculate EOS data. We use the plane wave code VASP,^{49,50} employing the PBE³⁵ XC functional and Plane Augmented Wave (PAW) potentials⁵¹ with an energy cutoff of 800 eV for high pressures (i.e., high densities and/or temperatures), and a cutoff of up to 1400 eV for low pressures, ensuring a convergence of better than 1% for all calculations, and better than 0.25% for most of the results. The Brillouin zone is evaluated at the Baldereschi mean value point,⁵² which yields results that coincide with those using higher \mathbf{k} point sets (i.e., $3 \times 3 \times 3$) within the error bars. All simulations relevant for the Hugoniot data were performed with 108 helium atoms (i.e., 216 electrons). The number of bands which are occupied according to the Fermi-Dirac statistics at the current temperature was chosen in such a manner that the occupation of the highest bands is less than 5×10^{-5} , usually much less than that. The temperature of the ions is controlled with a Nosé-Hoover thermostat. To adjust the Nosé frequency as well as the time step of the simulations, the power spectrum was calculated. Only time steps smaller than 1/30 of the maximum “phonon” frequency were used, while the Nosé frequency was adjusted to be within this power spectrum.

B. Electrical conductivity and reflectivity

Each result of the electrical conductivity is calculated from 20 to 40 snapshots of a simulation using the Kubo-Greenwood formula^{45,46,53,54}

$$\sigma_1(\omega) = \frac{2\pi e^2}{3\omega\Omega} \sum_{\mathbf{k}} W(\mathbf{k}) \sum_{j=1}^N \sum_{i=1}^N \sum_{\alpha=1}^3 [F(\epsilon_{i,\mathbf{k}}) - F(\epsilon_{j,\mathbf{k}})] \times |\langle \Psi_{j,\mathbf{k}} | \mathbf{v} | \Psi_{i,\mathbf{k}} \rangle|^2 \delta(\epsilon_{j,\mathbf{k}} - \epsilon_{i,\mathbf{k}} - \hbar\omega), \quad (1)$$

where e is the electron charge and m is its mass. The summations over i and j run over N discrete bands are considered in the electronic structure calculation for the supercell volume Ω . The three spatial directions are averaged by the α sum. $F(\epsilon_{i,\mathbf{k}})$ describes the occupation of the i th band corresponding to the energy $\epsilon_{i,\mathbf{k}}$ and the wavefunction $\Psi_{i,\mathbf{k}}$ at wavenumber \mathbf{k} .

The calculations were performed using 128–256 atoms evaluating the Baldereschi mean value point. The number of bands was adjusted so that at least 50 bands are unoccupied in every setting. We then average over the snapshots in order to obtain the real part of the dynamic conductivity $\sigma_1(\omega)$. The reflectivity is calculated via the Fresnel formula

$$R(\omega) = \frac{[n_0(\omega) - n(\omega)]^2 + [k_0(\omega) - k(\omega)]^2}{[n_0(\omega) + n(\omega)]^2 + [k_0(\omega) + k(\omega)]^2}, \quad (2)$$

where $n + ik$ denotes the complex index of refraction; n_0 and k_0 refer to the material at the reflecting boundary. The complex index of refraction is determined via the complex dielectric function according to

$$n(\omega) + ik(\omega) = \sqrt{\epsilon_1(\omega) + i\epsilon_2(\omega)}, \quad (3)$$

$$\epsilon_1(\omega) = 1 - \frac{4\pi}{\omega} \sigma_2(\omega), \quad (4)$$

$$\epsilon_2(\omega) = \frac{4\pi}{\omega} \sigma_1(\omega), \quad (5)$$

where the real part of the dynamic conductivity $\sigma_1(\omega)$ is given by the Kubo-Greenwood formula (1) and its imaginary part $\sigma_2(\omega)$ is obtained from $\sigma_1(\omega)$ using a Kramers-Kronig relation; details can be found in Refs. 55–59. These calculations were performed with the PBE,³⁵ the vdW-DF1,⁶⁰ and the HSE^{38,39} functional, the latter yields improved band gaps, cf. Figure 6. In testing the convergence of our calculations relative to a reference calculation with 108 atoms, a $3 \times 3 \times 3$ k point set, and 40 snapshots, we found that the reflectivity remained converged at the 0.5% level until backing off the simulation to as few as 27 atoms in the supercell, the Brillouin zone evaluated only at the Γ -Point, and 20 snapshots.

III. RESULTS FOR THE EOS

We have calculated the EOS of warm dense helium for a wide range of densities and temperatures in order to compare our *ab initio* results with recent static and dynamic compression experiments.

A. Cold curve

The first step is the calculation of the initial states of helium for the shock-compression experiments of Eggert *et al.*¹¹ using precompressed targets, i.e., along the 300 K

isotherm. An important issue is the neglect of long-range vdW interactions when using the PBE XC functional in the DFT calculations. To estimate the effect of vdW forces, we calculated the same isotherm with various vdW XC functionals: vdW-DF1,⁶⁰ vdW-DF2,⁶³ and using the additive Tkatchenko-Scheffler (TS) method⁶⁴ based on PBE. The results for the pressure along the 300 K isotherm are shown in Fig. 1. The experimental data are reproduced by all XC functionals employed; none of the vdW-implementations yields a significantly better agreement with the experiments. The lower the density, the lower the pressure of vdW-DF1 and the higher the one of vdW-DF2 compared to PBE and PBE + TS. The higher the density, the higher the pressure of vdW-DF1 and the lower the one of vdW-DF2 compared to the other XC functionals employed. While the TS-correction on PBE yields systematically lower pressures than just PBE, the agreement with experimental data is comparable.

At higher pressures, the liquid phase solidifies into the fcc structure. The calculations for 0 K without phonons shown in Fig. 2 were performed with 8 atoms, a $5 \times 5 \times 5$ Monkhorst-Pack \mathbf{k} point set, and an energy cutoff of 1500 eV with all vdW implementations available in VASP version 5.3.5. For comparison, we performed additional calculations with the LDA, PBE, AM05, rPW86, and HSE XC functional. The PBE-based wide-range equation of state He-REOS.3⁶⁵ is plotted as a representative for the difference of DFT-MD and pure DFT. In addition, one can estimate the influence of finite temperatures on the pressures by inspecting the differences between the He-REOS.3 isotherms at 60 and 300 K.

The overall agreement between our DFT-MD results and the experimental values is very good, only at higher densities the DFT-MD pressures are too high. Our results show that the PBE + TS results give a slightly lower pressure below 0.3 g/cm^3 , while at higher densities vdW-DF2 yields the lowest pressure. The vdW-optB86b agrees with the PBE functional. Considering the pure electronic calculations, the vdW-DF1 XC functional yields systematically the highest

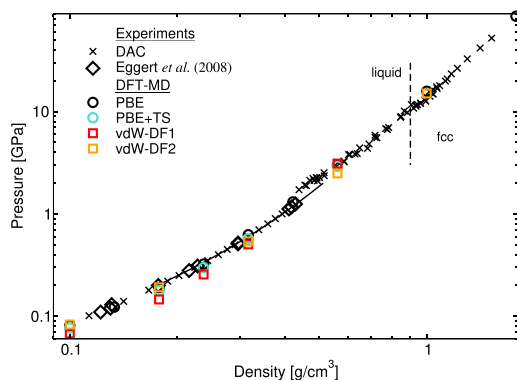


FIG. 1. Pressure in helium along the 300 K isotherm. Shown are the results for the initial states in the precompressed targets as used by Eggert *et al.*¹¹ (black diamonds), together with other DAC results^{1,11,61,62} (black crosses and the black line) and DFT-MD results (circles) with different XC functionals: PBE (black), PBE + TS [cyan, vdW-DF1 (red), and vdW-DF2 (orange)].

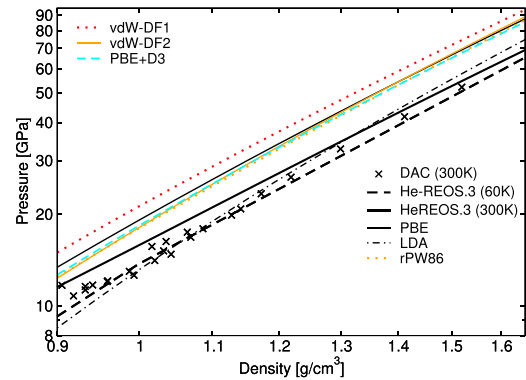


FIG. 2. Pressure in helium as a function of density at 0 K. Experimental results at 300 K are identical to those shown in Fig. 1. Conventional XC functionals (PBE and LDA) are shown as black thin line and black dash-dotted line. Results of the additional vdW corrected D3 method are represented by the dashed cyan line. XC functionals with a modified correlation part are drawn as red dots and bold orange line (vdW-DF1 and vdW-DF2, respectively). The vdW-DF2 XC functional is based on the rPW86 functional, which is shown as orange dots. He-REOS.3 pressure lines⁶⁵ are represented by the bold dashed black line (60 K) and the bold solid black line (300 K). The following XC functionals and methods yield almost the same results as PBE and are, therefore, not shown: AM05, PBE + TS, PBE + TS-SCS, vdW-optB86b, vdW-optB88, and vdW-optPBE. The results for HSE and PBE + D3 almost coincide; therefore, the HSE results are not shown.

pressures, while the LDA yields the lowest of all functionals and methods under study. At lower densities, vdW-DF2, rPW86, HSE, and PBE + D3⁶⁶ give a systematically lower pressure compared to PBE. This effect vanishes at densities above 1.3 g/cm^3 . The other vdW-implementations reproduce the PBE results and are not shown in Fig. 2 for the sake of clarity. As the vdW-DF2 functional is based on rPW86-exchange, the influence of vdW-forces on the pressure can be observed directly. For densities between 0.9 and 0.95 g/cm^3 , the vdW-forces decrease the pressure, while for higher densities the effect is opposite.

Since the difference between vdW-implementations and the PBE XC functional is rather small, we decided to use PBE for all remaining EOS calculations, except for an additional test on the Hugoniot curves (see Fig. 3) where we examine the temperature-dependent behavior of the vdW-DF1 and vdW-DF2 XC functionals. Isotherms at higher temperatures were calculated on a roughly logarithmic grid up to 100 000 K at the relevant densities.

B. Hugoniot curve

Using the extended data set for the EOS of dense helium based on DFT-MD simulations, the Hugoniot relation was evaluated for each of the experimental starting points. The resulting Hugoniot curves are shown in Fig. 3 together with the original data of Eggert *et al.*¹¹ and the reanalyzed results. As can be seen, the reanalyzed results show a smaller compression ratio compared with the original data and thus, a better agreement with our theoretical results. A systematic shift towards lower compressions due to an improved quartz

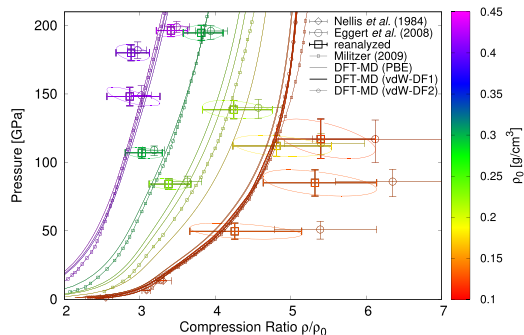


FIG. 3. Helium Hugoniot curve for various experimental starting points: Nellis *et al.*⁶ (diamonds), Eggert *et al.*¹¹ (circles), and our reanalyzed results (squares). For comparison, we show our DFT-MD results obtained with the PBE, the vdW-DF1, and the vdW-DF2 XC functional. The PBE results agree with DFT-MD calculations of Militzer.³³ The color code indicates the density of the initial state.

standard has already been found for hydrogen^{40–42} and later for precompressed samples of hydrogen and helium.⁴³

In Sec. III A, we employed a number of XC functionals at 0 and 300 K. For calculations of the Hugoniot, significantly higher temperatures are needed. Therefore, we recalculated a representative Hugoniot curve with the vdW-DF1 and the vdW-DF2 XC functional at an initial density of 0.123 g/cm³. While we see significant differences between the Hugoniot curves using the PBE and these XC functionals at lower temperatures (see Sec. III A), the discrepancies disappear for higher temperatures. The reason for this behavior is the decreasing XC component of the internal energy at higher temperatures.⁶⁷ This confirms the choice of PBE for the remaining EOS calculations.

The deviations between our results and the Hugoniot of Militzer³³ are probably due to convergence issues: While our Hugoniot curves were calculated with 108 atoms and the Brillouin zone was evaluated at the Baldereschi mean value point (see Sec. II A), the ones in Ref. 33 were determined with only 32 atoms at the Γ point. For 32 atoms, the deviations between the Γ and a better Brillouin zone sampling as performed here can amount up to 8%. Additionally, two different codes were used in Ref. 33, VASP with PAW and Car-Parrinello MD (CPMD) with Troullier-Martins norm-conserving pseudopotentials.

Figure 4 illustrates the temperature-pressure plane for the Hugoniot experiments of Celliers *et al.*¹² (filled circles) and the reverberating shock wave experiments of Ternovoi *et al.*⁷ (colored squares). The predictions for these experiments according to our EOS data are displayed in the same color code. For the principal Hugoniot with an initial density of $\rho_0 = 0.123$ g/cm³, we obtain an agreement between the experimental and theoretical data within the error bars; the DFT results are systematically above the experimental data points.

In contrast to the single-shock experiments along the Hugoniot, the reverberating shock wave technique, as used by Ternovoi *et al.*,⁷ yields a quasi-isentropic compression. The pressures and densities reported for these compression paths were derived from hydrodynamic simulations using

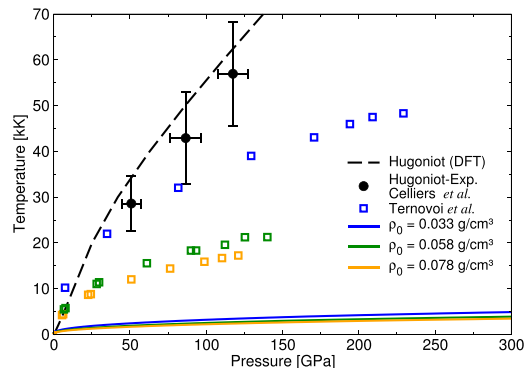


FIG. 4. Temperature-pressure relations along the principal Hugoniot curve of helium with experiments of Celliers *et al.*¹² Theoretical DFT-MD isentropes starting from three initial densities as used in the reverberating shock wave experiments of Ternovoi *et al.*⁷ for which we have determined the electrical conductivity, see Sec. IV C are also shown.

the experimental temperatures, impactor velocities, and a model EOS, see Ref. 7 for details. Assuming isentropic compression, we are able to reconstruct the thermodynamic paths of these experiments for given initial conditions by solving the differential equation:

$$\left(\frac{\partial T}{\partial \rho}\right)_s = \frac{T}{\rho^2} \left(\frac{\partial P}{\partial T}\right)_\rho \left(\frac{\partial u}{\partial T}\right)_\rho^{-1}. \quad (6)$$

If we know the thermal EOS $P(\rho, T)$ and the specific caloric EOS $u(\rho, T)$, the thermodynamic states (ρ, P, T) can be determined. Equation (6) is solved by using the PBE-based wide-range equation of state He-REOS.3;⁶⁵ the results are shown in Fig. 4. For three different initial densities with an initial temperature of 78 K, the hydrodynamic results of Ternovoi *et al.* (colored squares) are significantly above our corresponding isentropes (solid curves). The deviations can be traced back directly to the EOS used by Ref. 7, which is based on the simple Debye and a hard sphere model. These approximations are of limited validity at high densities. Another reason for the discrepancies in the $P-T$ plane is that the experimental compression path follows a Hugoniot within the first shock and an isentrope for the subsequent reverberating shocks. Thus, our pure isentropic path according to Eq. (6) gives a lower limit for the temperatures at given pressures at the experimental conditions.

C. Isentropic compression experiments

Contrary to single shock experiments along the Hugoniot curve, quasi-isentropic compression experiments are able to probe thermodynamic states at lower temperatures and high pressures. Novel experimental setups^{9,68–71} utilized a spherical compression of helium driven by high explosives which reached pressures up to 5 TPa. The compression of the samples in those experiments, i.e., the density, has been monitored via x-ray backlighting. Pressures

and temperatures were obtained from one-dimensional gas-dynamic calculations using a model EOS for helium, see Ref. 70 for details.

The results are shown in Fig. 5 along with the initial conditions of the isentropes as reported in the respective publications. Solid curves represent our isentropes that were calculated according to Eq. (6) using He-REOS.3.⁶⁵ We compare them with the pressures obtained from their gas-dynamic calculations at the densities measured in the experiment (same color code). One of the Mochalov *et al.* experiments⁶⁹ predicts significantly higher pressures at the measured density than we have derived from our DFT-MD simulations. A further discrepancy is the strikingly higher temperatures as predicted by their model EOS. For example, starting from an initial density of 0.008 g/cm^3 at 301.65 K, as in the experiment of Ref. 71 (orange diamond and curve), we obtain from our DFT-MD isentropes a final pressure of 1.56 TPa at 4.6 g/cm^3 and 30 000 K, in contrast to 3 TPa at 101 000 K at the same density. For the highest compression at 8.4 g/cm^3 (magenta square and solid curve) starting from an initial density of 0.038 g/cm^3 at 300 K, we obtain 4.64 TPa at 23 600 K compared to 4.75 TPa at 74 000 K as given in Refs. 9 and 69. Similar results are known for the quasi-isentropic compression of hydrogen, see Ref. 72 for details.

IV. RESULTS FOR THE OPTICAL PROPERTIES

Besides the EOS data, the optical properties, including the DC conductivity, can be analyzed in order to study the behavior of dense helium in more detail, especially the changes in the electronic properties along the compression path. We performed another series of DFT-MD simulations for the experimental conditions employing the PBE, vdW-DF1, and HSE XC functionals using the Kubo-Greenwood formula (1) as discussed in Sec. II B.

Celliers *et al.*¹² launched strong shock waves in precompressed samples (DAC) by using high-power lasers so that helium was compressed up to densities of 1.5 g/cm^3 and temperatures up to 60 000 K. The reflectivity for photons of

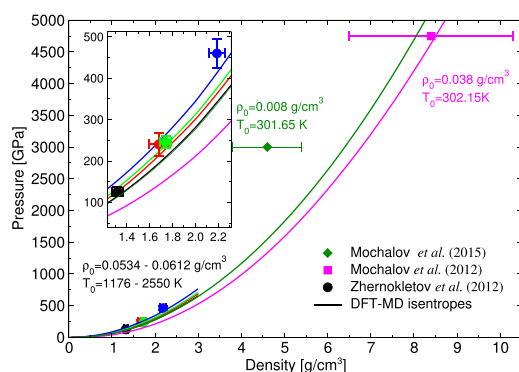


FIG. 5. Quasi-isentropic compression of helium as performed by Mochalov *et al.* (Ref. 69 magenta square, Ref. 71 green diamond), and Zhernokletov *et al.* (Ref. 68 blue, green, red, and black dots), in comparison with the isentropes derived from DFT-MD shown as solid curves with the same color code.

532 nm wavelength and the temperature were measured. The DC conductivity was inferred from a temperature-independent Drude model. Soubiran *et al.*²⁹ revisited the data of Celliers *et al.* using a temperature-dependent gap energy model that was fitted to *ab initio* data obtained by Kowalski *et al.*⁷³ As the Kowalski *et al.* calculations were performed only up to temperatures of 3 eV ($\sim 35 \text{ kK}$), extrapolation to higher temperatures was performed. In contrast to a strong density dependence of the conductivity as found by Celliers *et al.*, Soubiran *et al.* found a dominant temperature effect based on their model.

A. Density of states

The different XC functionals have an impact on the resulting density of states (DOS) as can be seen in Fig. 6. There we show an exemplary DOS for helium at 0.73 g/cm^3 and 10 000 K using the PBE, HSE, and vdW-DF1 XC functionals by creating a histogram of the occupied band energies with a bin size of 0.1 eV. We then broaden this histogram with a Gaussian of 0.1 eV width and normalize the area under the graph to 1. We infer the largest band gap for HSE, while PBE and vdW-DF1 yield almost the same but smaller band gap compared to HSE. The employed XC functionals also yield different DOS for the conduction and valence band. Both results, the different band gaps and the different slope of the DOS, will influence the optical properties and the DC conductivity.

B. Reflectivity

We performed calculations with the PBE, vdW-DF1, and HSE XC functionals for conditions of the experiment of Celliers *et al.*¹² As discussed in Sec. I, the new quartz standard lowers the compression ratio as shown in Fig. 3 and by Brygoo *et al.*⁴³ so that we computed the reflectivity for the revised experimental conditions. The results are shown in Fig. 7 and listed in Table I.

The coincidence between the revised data points and our results is significantly better than with the unrevised ones. Over the whole parameter range, the relative deviations between the

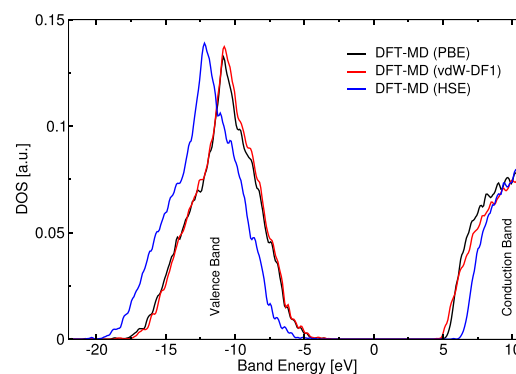


FIG. 6. Electronic density of states as resulting from the PBE, HSE, and vdW-DF1 XC functional for helium at 0.73 g/cm^3 and 10 000 K.

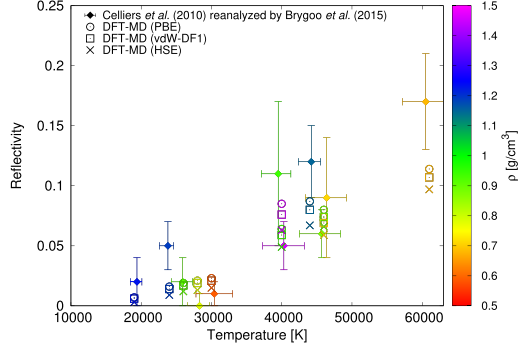


FIG. 7. Reflectivity data for helium. Shown are the experimental data of Brygoo *et al.*⁴³ and our DFT-MD results with the PBE, the vdW-DF1, and the HSE XC functional (circles, squares, and crosses, respectively).

employed XC functionals decrease with increasing temperature. The reasons are the same as discussed in Sec. III B.

While we see the onset of metallization in the increasing reflectivity at higher temperatures, we cannot identify a plateau. In addition, our DFT-MD reflectivity is well below the reflectivity value of over 0.55 that Zhang *et al.*³¹ identify with the nonmetal-to-metal transition. The reported densities of this transition, in the temperature range as relevant to the data of Celliers *et al.*, lie above 6 g/cm^3 , which is far more dense than the experimental values. The band gap closure as reported by Stixrude and Jeanloz²⁸ occurs at pressures between $\sim 1.4 \text{ TPa}$ and above 6 TPa and temperatures between $\sim 70\,000 \text{ K}$ and $\sim 7\,000 \text{ K}$. The pressures we extracted from our DFT-MD simulations at experimental conditions are well below 300 GPa and do not exceed $57\,000 \text{ K}$.

C. Electrical conductivity

Ternovoi *et al.*⁷ measured the optical emission and electrical resistance of multiply shock compressed helium. Using the EOS of Young *et al.*,⁷⁴ the shock processes were simulated employing a 1D hydrodynamic code in the framework of a chemical plasma model.⁷⁵ From these data, Ternovoi *et al.* calculated the electrical conductivity which shows a

TABLE I. Our results for the optical reflectivity under conditions as reported by Brygoo *et al.*⁴³

ρ (g/cm^3)	T (K)	R_{PBE} (%)	$R_{\text{vdW-DF1}}$ (%)	R_{HSE} (%)
0.59	30 000	2.3	2.1	1.5
0.68	61 000	11.4	10.7	9.7
0.71	46 000	7.4	6.9	5.9
0.78	28 000	2.1	1.9	1.3
0.88	46 000	8.0	7.4	6.6
0.91	26 000	1.9	1.7	1.2
0.94	40 000	6.4	5.9	4.9
1.15	44 000	8.7	8.0	6.7
1.19	24 000	1.6	1.4	0.9
1.23	19 000	0.7	0.6	0.3
1.46	40 000	8.5	7.6	6.3

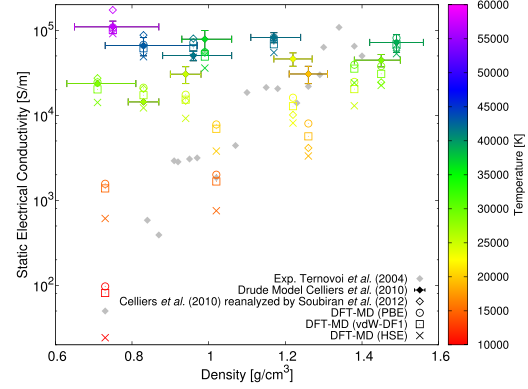


FIG. 8. DC electrical conductivity as reported by Ternovoi *et al.*⁷ (filled grey diamonds), Celliers *et al.*¹² (filled and color coded diamonds), the revisited Celliers *et al.* data by Soubiran *et al.*²⁹ (open diamonds), and our DFT-MD results (circles are PBE, squares are vdW-DF1, and crosses are HSE).

strong increase between 0.8 g/cm^3 and 1.4 g/cm^3 , indicating a strong increase in the ionization degree as typical of a continuous nonmetal-to-metal transition.

In Fig. 8, the DC conductivities derived from the reflectivity data of Celliers *et al.*¹² and the Celliers data revisited by Soubiran *et al.*²⁹ that employ a temperature-dependent Drude model are shown. Furthermore, we display the data of Ternovoi *et al.*⁷ and our DFT-MD results using the PBE, vdW-DF1, and HSE XC functionals. Notice that the present PBE results associated with the Ternovoi *et al.* data are an update of the data reported earlier by Kietzmann *et al.*²⁷ with only a slight change toward a lower conductivity at the lowest temperature.

In Table II, the corresponding values for the DC conductivity are shown.

TABLE II. Our results for the DC conductivity under conditions as reported by Ternovoi *et al.*⁷ (denoted as superscript a at the corresponding densities and temperatures) and Celliers *et al.*¹² (superscript b).

ρ (g/cm^3)	T (K)	σ_{PBE} ($1/\Omega\text{m}$)	$\sigma_{\text{vdW-DF1}}$ ($1/\Omega\text{m}$)	σ_{HSE} ($1/\Omega\text{m}$)
0.73 ^a	10 000 ^a	97.2	81.4	24.2
0.73 ^a	15 000 ^a	1569	1382	613
1.02 ^a	15 000 ^a	2004	1669	755
1.02 ^a	20 000 ^a	7815	6954	3799
1.38 ^a	25 000 ^a	24 765	20 364	12 958
1.38 ^a	30 000 ^a	39 426	35 492	24 103
0.71 ^b	29 000 ^b	24 442	20 215	14 183
0.75 ^b	57 000 ^b	108 390	101 170	91 488
0.83 ^b	27 000 ^b	21 174	17 257	12 250
0.83 ^b	43 000 ^b	67 701	61 579	48 926
0.94 ^b	25 000 ^b	17 519	15 297	9220
0.96 ^b	42 000 ^b	71 912	62 062	48 199
0.99 ^b	37 000 ^b	55 325	49 075	36 025
1.17 ^b	42 000 ^b	82 142	68 604	54 895
1.22 ^b	23 000 ^b	16 135	12 833	8132
1.26 ^b	19 000 ^b	8028	5668	3327
1.45 ^b	29 000 ^b	37 972	30 774	22 547
1.49 ^b	39 000 ^b	81 453	68 464	53 173

The HSE functional yields systematically the lowest conductivity, while PBE and vdW-DF1 give higher conductivities. This is consistent with the behavior of the band gap as shown in Fig. 6.

Comparing our DFT-MD results with the data of Ternovoi *et al.*, we infer that the temperature in the experiments should rise from below 10 000 K at the lowest density to above 30 000 K according to the PBE and vdW-DF1 calculations. Since the hybrid HSE functional gives larger band gaps and thus, significantly lower conductivities, the corresponding temperatures must be higher than those predicted by PBE and vdW-DF1 in order to match the experimental data. The presented temperature range can narrow down the temperature uncertainty as discussed in Sec. III B and as shown in Fig. 4.

Our DFT-MD results are in good agreement with the Celliers *et al.*¹² data for the DC conductivity. The relative discrepancies between the different XC functionals and the Drude models of Celliers *et al.* and Soubiran *et al.* tend to decrease with increasing temperatures and decreasing densities. In the parameter range of the results of Soubiran *et al.*, the differences between the conductivity results for the different functionals tend to decrease with increasing temperature and decreasing density. This effect cannot be observed with the Celliers *et al.* model, where the relative differences between the XC functionals remain constant over all densities and temperatures. The differences between the XC functionals among themselves decrease with increasing temperatures and decreasing densities. This effect of groundstate XC functionals to give matching results in the high-temperature limit was reported by Smith *et al.*⁶⁷ first and has already been discussed in Sec. III B.

We compare the dynamic electrical conductivity derived from our DFT-MD simulations with the Drude models of Celliers *et al.* and Soubiran *et al.* and find that the agreement is purely coincidental, as the shape of the dynamic electrical conductivity from our DFT-MD simulations is Drude-like only at low energies. This is shown for 0.83 g/cm³ and 27 000 K in Fig. 9. The Celliers and Soubiran models assume

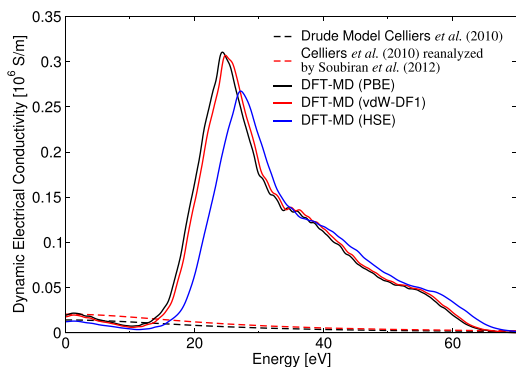


FIG. 9. Comparison of the dynamic electrical conductivity at 0.83 g/cm³ and 27 000 K: The Drude models by Celliers *et al.*¹² and Soubiran *et al.*²⁹ are shown as dashed black and red lines, respectively, and are compared to our DFT-MD results [straight lines in black (PBE), red (vdW-DF1), and blue (HSE)].

much larger ionization states as evidenced by the area under the curve and the corresponding sum rule for the nearly free component. Correspondingly, the characteristic electron relaxation time τ is also much smaller in those models in order to preserve approximately the same DC limit. Both models use an effective electron mass multiplier γ of 0.62. Here, electrons are thermally excited above a large band gap in a disordered liquid and the density of states is approximately ideal. An effective mass multiplier less than one drives towards smaller τ and larger ionization. We therefore conclude that simple Drude models are not reliable for helium under these conditions without additional insight into the electronic properties that first-principles methods such as DFT provide.

The metallization conductivity as reported by Zhang *et al.*³¹ is in the range of 7×10^5 to 1.3×10^6 S/m, typical of a good conductor compared to other low-Z fluids with a conductivity of 2×10^5 S/m. In the experimental density range, the minimum Mott conductivity lies between 2×10^4 and 2.8×10^4 S/m according to Stixrude and Jeanloz.²⁸ However, they find that band gap closure occurs at much higher densities of 4 g/cm³ at 50 000 K to over 10 g/cm³ at 0 K. The highest conductivity we obtain is $\sim 1.1 \times 10^5$ S/m at 0.75 g/cm³ and 57 000 K. This conductivity value is well above the minimum Mott conductivity according to Stixrude and Jeanloz and well below the reported metallization conductivity of Zhang *et al.* Similar to the reflectivity results, we see no saturation but increasing conductivities with increasing temperatures and densities. This is consistent with the onset of a metallization and the Zhang *et al.* results. As already discussed in Sec. IV B, the pressures we extract from our DFT-MD simulations at experimental conditions are well below 300 GPa and do not exceed 57 000 K. These conditions are far below the metallization parameters reported by Stixrude and Jeanloz and Zhang *et al.*

V. CONCLUSION

We have presented EOS, conductivity, and reflectivity data for warm dense helium based on extensive DFT-MD simulations. All XC-functionals employed yield different cold curves, yet the difference between vdW-implementations and the PBE XC functional is rather small. Therefore, only the latter was used for most of the subsequent EOS calculations. As shown for hydrogen earlier, the new quartz standard⁴⁰ shifts also the helium Hugoniot curve systematically to smaller compressions; see Ref. 43. Analogous to the cold curve, the deviations between the PBE XC functional and vdW-implementations are negligible. Based on our DFT-MD data, we recalculate quasi-isentropic compression experiments presented in Refs. 68, 69, and 71 and get substantially lower pressures compared with their hydrodynamic calculations using a model EOS. The band gap problem in DFT is addressed with different XC functionals (PBE, vdW-DF1, HSE). We derive reflectivity and DC conductivity data which show the onset of a nonmetal-to-metal transition at high pressures and temperatures. We observe that the reflectivities and DC conductivities obtained with PBE exceed those of vdW-DF1 which are in turn greater than those of the HSE XC functional. We consider the results using the HSE XC functional

as reliable since the corresponding band gaps are most suitable. In the future, we will investigate whether or not the non-metal-to-metal transition is of first order below a critical temperature, as predicted by chemical models,¹⁴ similarly to recent work on dense liquid hydrogen.⁷⁶

ACKNOWLEDGMENTS

We thank M. French, F. Soubiran, P. Celliers, S. Brygoo, L. Shulenburg, and M. Schöttler for helpful discussions. This work was supported by the Deutsche Forschungsgemeinschaft within the SFB 652 and the Project No. RE 882/11, by the North German Supercomputing Alliance (HLRN), the ITMZ of the University of Rostock, and the Sandia National Laboratories.

- ¹R. L. Mills, D. H. Liebenberg, and J. C. Bronson, *Phys. Rev. B* **21**, 5137 (1980).
- ²H. K. Mao, R. J. Hemley, Y. Wu, A. P. Jephcoat, L. W. Finger, C. S. Zha, and W. A. Bassett, *Phys. Rev. Lett.* **60**, 2649 (1988).
- ³W. L. Vos, M. G. E. van Hinsberg, and J. A. Schouten, *Phys. Rev. B* **42**, 6106 (1990).
- ⁴F. Datchi, P. Loubeyre, and R. L. Toullec, *Phys. Rev. B* **61**, 6535 (2000).
- ⁵D. Santamaría-Pérez, G. D. Mukherjee, B. Schwager, and R. Boehler, *Phys. Rev. B* **81**, 214101 (2010).
- ⁶W. J. Nellis, N. C. Holmes, A. C. Mitchell, R. J. Trainor, G. K. Governo, M. Ross, and D. A. Young, *Phys. Rev. Lett.* **53**, 1248 (1984).
- ⁷V. Y. Ternovoi, A. S. Filimonov, A. A. Pyalling, V. B. Mintsev, and V. E. Fortov, *AIP Conf. Proc.* **620**, 107 (2002).
- ⁸M. Zhemokletov, V. Arinin, V. Buzin, Y. Grigorieva, N. Davydov, and V. Khrustalev, *AIP Conf. Proc.* **1426**, 1411 (2012).
- ⁹M. A. Mochalov, R. I. Il'kaev, V. E. Fortov, A. L. Mikhailov, V. A. Raevskii, V. A. Ogorodnikov, A. A. Yukhimchuk, A. I. Davydov, N. N. Anashkin, V. A. Arinin, A. O. Blikov, A. Y. Baurin, N. B. Davydov, V. A. Komrakov, A. I. Logvinov, S. F. Manachkin, A. V. Ryzhkov, B. I. Tkachenko, A. V. Fedorov, S. A. Finyushin, D. A. Kalashnikov, E. A. Chudakov, E. A. Pronin, and E. A. Bakulina, *JETP* **119**, 146 (2014).
- ¹⁰R. Jeanloz, P. M. Celliers, G. W. Collins, J. H. Eggert, K. K. M. Lee, R. S. McWilliams, S. Brygoo, and P. Loubeyre, *Proc. Natl. Acad. Sci.* **104**, 9172 (2007).
- ¹¹J. Eggert, S. Brygoo, P. Loubeyre, R. S. McWilliams, P. M. Celliers, D. G. Hicks, T. R. Boehly, R. Jeanloz, and G. W. Collins, *Phys. Rev. Lett.* **100**, 124503 (2008).
- ¹²P. M. Celliers, P. Loubeyre, J. H. Eggert, S. Brygoo, R. S. McWilliams, D. G. Hicks, T. R. Boehly, R. Jeanloz, and G. W. Collins, *Phys. Rev. Lett.* **104**, 184503 (2010).
- ¹³M. Ross and D. A. Young, *Phys. Lett. A* **118**, 463 (1986).
- ¹⁴A. Förster, T. Kahlbaum, and W. Ebeling, *Laser Part. Beams* **10**, 253 (1992).
- ¹⁵T. Kahlbaum and A. Förster, *Fluid Phase Equilib.* **76**, 71 (1992).
- ¹⁶D. Saumon, G. Chabrier, and H. M. van Horn, *Astrophys. J. Suppl. Ser.* **99**, 713 (1995).
- ¹⁷V. Schwarz, H. Juranek, and R. Redmer, *Phys. Chem. Chem. Phys.* **7**, 1990 (2005).
- ¹⁸C. Winisdoerffer and G. Chabrier, *Phys. Rev. E* **71**, 026402 (2005).
- ¹⁹Q. Chen, Y. Zhang, L. Cai, Y. Gu, and F. Jing, *Phys. Plasmas* **14**, 012703 (2007).
- ²⁰M. Ross, F. Rogers, N. Winter, and G. Collins, *Phys. Rev. B* **76**, 020502 (2007).
- ²¹B. Holst, R. Redmer, and M. P. Desjarlais, *Phys. Rev. B* **77**, 184201 (2008).
- ²²W. Lorenzen, B. Holst, and R. Redmer, *Phys. Rev. B* **82**, 195107 (2010).
- ²³R. Redmer and B. Holst, in *Metal-to-Nonmetal Transitions. Springer Series in Material Sciences*, edited by R. Redmer, B. Holst, and F. Hensel (Springer, Berlin, 2010), Vol. 132, pp. 63–84.
- ²⁴M. A. Morales, C. Pierleoni, and D. M. Ceperley, *Phys. Rev. E* **81**, 021202 (2010).
- ²⁵M. A. Morales, C. Pierleoni, E. Schwegler, and D. M. Ceperley, *Proc. Natl. Acad. Sci. U.S.A.* **107**, 12799 (2010).
- ²⁶J. M. McMahon, M. A. Morales, C. Pierleoni, and D. M. Ceperley, *Rev. Mod. Phys.* **84**, 1607 (2012).
- ²⁷A. Kietzmann, B. Holst, R. Redmer, M. P. Desjarlais, and T. R. Mattsson, *Phys. Rev. Lett.* **98**, 190602 (2007).
- ²⁸L. Stixrude and R. Jeanloz, *Proc. Natl. Acad. Sci. U.S.A.* **105**, 11071 (2008).
- ²⁹F. Soubiran, S. Mazevet, C. Winisdoerffer, and G. Chabrier, *Phys. Rev. B* **86**, 115102 (2012).
- ³⁰Z.-G. Li, Y. Cheng, Q.-F. Chen, and X.-R. Chen, *Phys. Plasmas* **23**, 052701 (2016).
- ³¹W. Zhang, Z. Li, Z. Fu, J. Dai, Q. Chen, and L. Cai, *Sci. Rep.* **7**, 41885 (2017).
- ³²B. Militzer, *Phys. Rev. Lett.* **97**, 175501 (2006).
- ³³B. Militzer, *Phys. Rev. B* **79**, 155105 (2009).
- ³⁴S. A. Khairallah and B. Militzer, *Phys. Rev. Lett.* **101**, 106407 (2008).
- ³⁵J. P. Perdew, K. Burke, and M. Ernzerhof, *Phys. Rev. Lett.* **77**, 3865 (1996).
- ³⁶R. Armiento and A. E. Mattsson, *Phys. Rev. B* **72**, 085108 (2005).
- ³⁷É. D. Murray, K. Lee, and D. C. Langreth, *J. Chem. Theory Comput.* **5**, 2754 (2009).
- ³⁸J. Heyd, G. E. Scuseria, and M. Ernzerhof, *J. Chem. Phys.* **118**, 8207 (2003).
- ³⁹J. Heyd, G. E. Scuseria, and M. Ernzerhof, *J. Chem. Phys.* **124**, 219906 (2006).
- ⁴⁰M. D. Knudson and M. P. Desjarlais, *Phys. Rev. Lett.* **103**, 225501 (2009).
- ⁴¹M. D. Knudson and M. P. Desjarlais, *Phys. Rev. B* **88**, 184107 (2013).
- ⁴²M. P. Desjarlais, M. D. Knudson, and K. R. Cochrane, *J. Appl. Phys.* **122**, 035903 (2017).
- ⁴³S. Brygoo, M. Millot, and P. Loubeyre, *J. Appl. Phys.* **118**, 195901 (2015).
- ⁴⁴P. Loubeyre, S. Brygoo, J. Eggert, P. M. Celliers, D. K. Spaulding, J. R. Rygg, T. R. Boehly, G. W. Collins, and R. Jeanloz, *Phys. Rev. B* **86**, 144115 (2012).
- ⁴⁵R. Kubo, *J. Phys. Soc. Jpn.* **12**, 570 (1957).
- ⁴⁶D. A. Greenwood, *Proc. Phys. Soc.* **71**, 585 (1958).
- ⁴⁷P. Hohenberg and W. Kohn, *Phys. Rev.* **136**, B864 (1964).
- ⁴⁸W. Kohn and L. J. Sham, *Phys. Rev.* **140**, A1133 (1965).
- ⁴⁹G. Kresse and J. Furthmüller, *Phys. Rev. B* **54**, 11169 (1996).
- ⁵⁰J. Hafner, *J. Comput. Chem.* **29**, 2044 (2008).
- ⁵¹P. E. Blöchl, *Phys. Rev. B* **50**, 17953 (1994).
- ⁵²A. Baldereschi, *Phys. Rev. B* **7**, 5212 (1973).
- ⁵³M. P. Desjarlais, J. D. Kress, and L. A. Collins, *Phys. Rev. E* **66**, 025401(R) (2002).
- ⁵⁴B. Holst, M. French, and R. Redmer, *Phys. Rev. B* **83**, 235120 (2011).
- ⁵⁵D. B. Melrose and R. C. McPhedran, *Electromagnetic Processes in Dispersive Media* (Cambridge University Press, Cambridge, 1991).
- ⁵⁶S. Mazevet, J. D. Kress, L. A. Collins, and P. Blottiau, *Phys. Rev. B* **67**, 054201 (2003).
- ⁵⁷S. Mazevet, M. P. Desjarlais, L. A. Collins, J. D. Kress, and N. H. Magee, *Phys. Rev. E* **71**, 016409 (2005).
- ⁵⁸M. Gajdoš, K. Hummer, G. Kresse, J. Furthmüller, and F. Bechstedt, *Phys. Rev. B* **73**, 045112 (2006).
- ⁵⁹M. French and R. Redmer, *Phys. Plasmas* **24**, 092306 (2017).
- ⁶⁰J. Klimeš, D. R. Bowler, and A. Michaelides, *J. Phys.: Condens. Matter* **22**, 022201 (2010).
- ⁶¹A. Dewaele, J. H. Eggert, P. Loubeyre, and R. Le Toullec, *Phys. Rev. B* **67**, 094112 (2003).
- ⁶²M. Lallemand and D. Vidal, *J. Chem. Phys.* **66**, 4776 (1977).
- ⁶³K. Lee, E. D. Murray, L. Kong, B. L. Lundquist, and D. C. Langreth, *Phys. Rev. B* **82**, 081101 (2010).
- ⁶⁴A. Tkatchenko and M. Scheffler, *Phys. Rev. Lett.* **102**, 073005 (2009).
- ⁶⁵A. Becker, W. Lorenzen, J. Fortney, N. Nettelmann, M. Schöttler, and R. Redmer, *Astrophys. J. Suppl. Ser.* **215**, 21 (2014).
- ⁶⁶S. Grimme, J. Antony, S. Ehrlich, and H. Krieg, *J. Chem. Phys.* **132**, 154104 (2010).
- ⁶⁷J. C. Smith, F. Sagredo, and K. Burke, "Warming up density functional theory," in *Frontiers of Quantum Chemistry* (Springer, 2017), pp. 249–271.
- ⁶⁸M. Zhemokletov, V. Gryaznov, V. Arinin, V. Buzin, N. Davydov, R. Il'kaev, I. Iosilevskiy, A. Mikhailov, M. Novikov, V. Khrustalev, and V. Fortov, *JETP Lett.* **96**, 432 (2012).
- ⁶⁹M. A. Mochalov, R. I. Il'kaev, V. E. Fortov, A. L. Mikhailov, V. A. Arinin, A. O. Blikov, A. Y. Baurin, V. A. Komrakov, V. A. Ogorodnikov, A. V. Ryzhkov, and A. A. Yukhimchuk, *JETP Lett.* **96**, 158 (2012).
- ⁷⁰M. A. Mochalov, R. I. Il'kaev, V. E. Fortov, A. L. Mikhailov, Y. M. Makarov, V. A. Arinin, A. O. Blikov, A. Y. Baurin, V. A. Komrakov, V. A. Ogorodnikov, A. V. Ryzhkov, E. A. Pronin, and A. A. Yukhimchuk, *J. Exp. Theor. Phys.* **115**, 614 (2012).




- ⁷¹M. A. Mochalov, R. I. Il'kaev, V. E. Fortov, A. L. Mikhailov, V. A. Arinin, A. O. Blikov, V. A. Komrakov, A. V. Ryzhkov, V. A. Ogorodnikov, and A. A. Yukhimchuk, *JETP Lett.* **101**, 519 (2015).
- ⁷²A. Becker, N. Nettelmann, B. Holst, and R. Redmer, *Phys. Rev. B* **88**, 045122 (2013).
- ⁷³P. M. Kowalski, S. Mazevet, D. Saumon, and M. Challacombe, *Phys. Rev. B* **76**, 075112 (2007).
- ⁷⁴D. A. Young, A. K. McMahan, and M. Ross, *Phys. Rev. B* **24**, 5119 (1981).
- ⁷⁵V. Fortov and I. Iakubov, *Physics of Nonideal Plasma* (Hemisphere Publishing, 1990).
- ⁷⁶M. D. Knudson, M. P. Desjarlais, A. Becker, R. W. Lemke, K. R. Cochrane, M. E. Savage, D. E. Bliss, T. R. Mattsson, and R. Redmer, *Science* **348**, 1455 (2015).

4.2. The high-pressure melting line of helium

Author contributions

M.P. Preparation of the manuscript, all calculations.

R.R. Supervision of the project, preparation of the manuscript.

High-pressure melting line of helium from *ab initio* calculationsMartin Preising  and Ronald Redmer *Institut für Physik, Universität Rostock, D-18051 Rostock, Germany* (Received 1 June 2018; revised manuscript received 16 July 2019; published 13 November 2019)

We applied two-phase simulations to directly calculate the high-pressure melting line of helium from 425 to 10 000 K and from 15 GPa to 35 TPa by using molecular dynamics based on density-functional theory. The implementation of the two-phase simulation method and the relaxation of the simulation to an equilibrium state was studied in detail, as well as its convergence with respect to particle number. We performed extensive two-phase simulations with the Perdew, Burke and Ernzerhof and the van der Waals density functional exchange-correlation functional and found almost identical results.

DOI: [10.1103/PhysRevB.100.184107](https://doi.org/10.1103/PhysRevB.100.184107)**I. INTRODUCTION**

Experimental data for the melting line of helium are currently available for pressures up to 80 GPa [1–7]. However, knowledge of the high-pressure melting line up to the TPa region is important to astrophysics, e.g., for the determination of the region of hydrogen-helium phase separation as predicted in the interior of gas giants like Saturn and Jupiter [8–12].

The phase diagram of solid helium was studied in depth in diamond anvil cell experiments. For instance, Mao *et al.* [13] observed a hexagonal close-packed (hcp) structure along the 300 K isotherm with x-ray diffraction experiments. Loubeyre *et al.* [14] extended the experimental range and detected a stable face-centered cubic (fcc) area embedded in the hcp structure at the melting line below 300 K.

Theoretical approaches for the calculation of the melting line start from the free energies of the solid (s) and liquid (l) phase in equilibrium and determine the melting point (p, T) from the equality of the corresponding Gibbs free energies, $G_l(p, T) = G_s(p, T)$, see Refs. [15,16].

An alternative method to determine the melting line directly is to treat the solid and the liquid in coexistence within two-phase simulations (TPSs). Pioneering work was performed by Belonoshko [17–20] and later by Alfè *et al.* [21] by combining a simulation box that contains a crystal with a box containing a liquid and subsequently relaxing the total system to an equilibrium state. When the number of atoms N , the simulation box volume V , and the internal energy E is fixed, the equilibrium pressure and temperature result in a point on the melting line, while the simulation box contains liquid and solid parts [22]. If the temperature is fixed, instead of the internal energy, the melting of the solid part of the box or the crystallization of the liquid part will occur. The location of the melting line can then be found in an iterative manner by changing the simulation parameters.

The first TPSs for helium were performed by Koči *et al.* [23] who reproduced the melting line as it was measured by Loubeyre *et al.* [4]. Belonoshko *et al.* [24] calculated the melting points of body-centered cubic (bcc) and fcc helium at about 14, 40, and 75 GPa with TPSs. The hcp phase was not considered. Nevertheless, the experimental melting line was

reproduced. The two studies employed classical molecular dynamics (MD) for the ions.

While the TPS method is very intuitive, its implementation poses several problems. For instance, a spacing between the solid and the liquid part is crucial to avoid particle overlap and excessive potential energies [23,25–27]. A possible starting point would be a crystal configuration in the simulation box at temperatures exceeding the melting temperature [28,29]. As soon as a liquid configuration is established, it is brought into contact with the initial crystal configuration. This implies a spacing of half of the lattice distance. To ensure density conservation, one or both parts of the supercell have to be compressed or expanded if the spacing is not equal to half of the lattice distance. However, a spacing of half of the lattice distance might not be enough to avoid excessive potential energies and could require other methods to achieve similar potential energies in the different phases of the supercell. For instance, one can remove atoms from the liquid part of the cell to equilibrate the pressure difference between the constituents [30]. In any case, the choice of the spacing is somewhat arbitrary. An alternative to the introduction of a spacing of an arbitrary size is the application of constant-pressure MD. Here, the size of the box in the direction orthogonal to the solid-liquid interface is allowed to change according to the pressure in the solid part.

Furthermore, there is no consensus on how both parts are to be set up in the first place. If a perfect crystal and a random liquid configuration are combined without previous relaxation, the results could be distorted. In some cases, the crystalline and the liquid part were relaxed prior to the TPS [22,27,30–32] and in some cases they were not [17,33,34].

References [27,35] performed tests on the influence of the joint surface plane and found no difference in the melting temperature, if the number of atoms is sufficiently large. Reference [24] performed calculations in which the solid part was either bcc or fcc. The experimental melting line was reproduced irrespective of the underlying solid structure that was simulated. This indicates that the influence of the crystal structure on the TPS results of helium is small in the temperature-density range that was examined in Ref. [24]. This is not necessarily the case for other densities and

temperatures. The influence of nuclear quantum effects (NQE) on the melting line was calculated by Ref. [36] and was found to be $\sim 5\%$ for high-pressure lithium. However, for systems with strong chemical bonds like hydrogen, the impact of NQE on the melting line can be significant, as Chen *et al.* [37] have demonstrated. Due to the very weak chemical bonds in helium, we chose to neglect NQE.

Many calculations of the melting line [23,38–41] were performed with classical methods and empirical potentials. Young *et al.* [38] were the first to predict the melting line of helium up to temperatures of 6000 K. They employed linear muffin-tin orbital-calculations.

In this paper, we calculated the high-pressure melting line of helium with TPSs up to extreme pressures of 35 TPa and temperatures of 10 000 K. In particular, we studied how details in the setup of the simulation box for the TPS are affecting the results. As helium is a noble gas, it is very well suited for a case study, as there are no further chemical processes involved and the small number of electrons speeds up the electronic-structure calculations.

II. DFT-MD SIMULATIONS

In our simulations, we employed density-functional theory (DFT) [42,43] to treat the electrons, while the ions were propagated with classical MD. We used the implementation of the plane wave code VASP [44–48]. Due to the finite temperature, the electronic bands were occupied according to Fermi-Dirac statistics. The number of bands as well as the size of the time step were chosen individually for each temperature and density, as documented in Ref. [49]. A Nosé-Hoover thermostat [50–52] controlled the temperature of the ions.

To ensure a suitable choice of the pseudopotential, we performed static calculations of a perfect hcp helium crystal with 128 atoms and a random liquid configuration with 432 atoms with three different pseudopotentials: The standard projector-augmented wave (PAW) pseudopotential, [53] a “harder” PAW pseudopotential with a smaller cutoff radius than the standard one, and the full Coulomb potential. The Coulomb potential we employed for helium does not have a cutoff radius, in contrast to the PAW potentials. The cutoff energy corresponding to the Coulomb potential in this paper defines the number of plane waves that modeled the strongly oscillating wave functions around the nuclei. We assured convergence with respect to the number of plane waves for each of the potentials individually. The potentials require a maximum plane-wave energy (cutoff energy) of 800 eV (standard PAW), 2500 eV (harder PAW), and 15 000 eV (Coulomb) for a pressure convergence of better than 0.2% relative to calculations with cutoff energies of 3000 eV, 2500 eV, and 50 000 eV (PAW, harder PAW, and Coulomb, respectively). The harder PAW potential displayed a divergence of the internal energy above cutoff energies of 2500 eV. We therefore chose to discard the results that were obtained with higher cutoff energies. The Brillouin zone was sampled at the Baldereschi mean value point [54] (BMVP) for a cubic box (liquid) and with a $3 \times 3 \times 3$ k -point set (hcp solid). The pressure of the hcp crystal and the pressure of the liquid are converged to within 0.1% with respect to calculations with a $3 \times 3 \times 3$ and a $5 \times 5 \times 5$ k -point set, respectively.

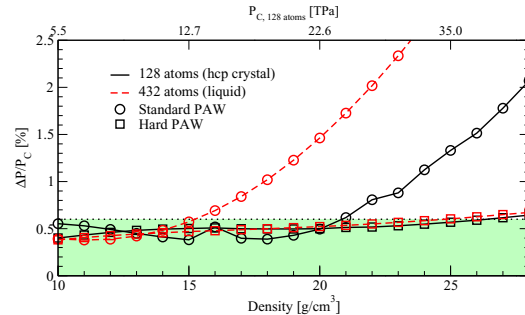


FIG. 1. Pressure deviations between the PAW pseudopotentials and the Coulomb potential. The pressure that was obtained for the perfect hcp crystal with the full Coulomb potential is shown on the upper x axis. The horizontal dotted line guides the eye.

The exchange-correlation (XC) functional was Perdew, Burke and Ernzerhof (PBE) [55] in all convergence tests. For these tests, we chose high densities to ensure the convergence of the Coulomb potential, which is very demanding at lower densities. The density region under consideration is also the region in which the PAW pseudopotentials are expected to give unphysical results as soon as the interatomic distance approaches the cutoff radius [56]. Figure 1 shows the pressure deviations ΔP between the pseudopotentials relative to the pressure P_C that was obtained with the Coulomb potential. As Lorenzen [56] demonstrated, the forces on the ions are converged when the resulting pressures are converged.

The correspondence of the standard PAW potential with the full Coulomb potential is better than 0.6% at densities up to 15 g/cm^3 . The hard PAW potential reproduces the pressure obtained with the Coulomb potential within 0.6% for densities below 25 g/cm^3 . For densities below 14 g/cm^3 , we utilized the standard PAW potential with an energy cutoff of 900 eV and switched to the harder PAW potential with an energy cutoff of 2500 eV for densities of 14 g/cm^3 and above. Only the PBE calculations of the melting point at 10 000 K exceed 24 g/cm^3 and are therefore converged to within 0.65%. Therefore, we utilized only the standard and the hard PAW potential.

When we decrease the size of the simulation box, the size of the cell in reciprocal space increases. Therefore, a Brillouin zone sampling that is sufficient at low densities might not be at very high densities. We studied densities from 1 to 30 g/cm^3 and analyzed the convergence of a perfect hcp crystal with 128 atoms. We switched to the hard PAW potential at densities higher than 14 g/cm^3 . The pressures of the calculations with the perfect hcp crystal are converged to within 0.4% with the BMVP compared to $5 \times 5 \times 5$ for all the densities under consideration.

III. TWO-PHASE SIMULATIONS

To ensure fully converged TPS results, we performed extensive test calculations, mostly for a density of 1.6 g/cm^3 . At this density, the PBE XC functional results in pressures below 80 GPa in the temperature range in which experimental

data [7] for the melting line of helium are available. We also verified the convergence of the TPS calculations at 17 and 20 g/cm³. Please note that we did not relax the cell shape but employed the perfect c/a ratio. When we relaxed the cell at the lowest and the highest density, the box vectors were identical to the perfect ones within 2.2%. This resulted in pressure deviations of less than 0.16% between the relaxed and the perfect hcp cells. This deviation is negligible. As discussed in Sec. II, the forces on the ions are converged if the pressures are converged.

A. Setup of the simulation box

Our setup scheme was similar to that of Ref. [30]. To set up the solid subdomain before the TPS was performed, we chose a temperature T_s of around 70% of the experimental melting temperature. At this temperature, a perfect hcp crystal was relaxed for 5 ps. The resulting atomic configuration and its velocity vectors were used as the input for the next calculation, in which the crystal was heated with a rate of 50 K/ps until melting occurred at T_s^m . After every picosecond of this heating process, the ionic positions and the corresponding velocity vectors were recorded. Every snapshot was then further relaxed at its respective temperature for an additional 2 ps.

In the exact same manner, the ionic configuration and velocity vectors of the liquid subdomain were obtained as the result of a relaxation at a temperature T_l above the experimental melting temperature followed by a cooling procedure with a rate of 50 K/ps until the starting temperature of the solid was reached. The resulting snapshots were relaxed for 2 ps.

From the ionic configurations and their velocity vectors, the TPS boxes were constructed. The results of the setup procedure depicted above were TPS boxes at a density of 1.6 g/cm³ and temperatures between T_s and T_s^m or T_l , depending on which is lower. The temperature difference between these TPS boxes is 50 K. The interface of the solid and the liquid phase was [0001]. References [27,35] found that the influence of the joint surface plane is negligible provided that the number of atoms is sufficient (96 atoms in Ref. [27], 108 atoms in Ref. [35]). We therefore chose not to perform tests on the joint interface plane.

The problem of excess potential energies at the construction of the TPS boxes can be avoided by using three methods. The first method employs constant pressure MD during the TPS. In this method, the shape of the liquid part of the box can change in the direction perpendicular to the interface. The second method evaluates the pressure of the solid part and removes atoms from the liquid part until the pressures of both parts are comparable. Then the boxes are brought into contact and the TPS is conducted with a spacing of half the lattice distance between the constituents. We call this method *equilibrated TPS (e-TPS)*. However, with this method, the formation of a crystal without defects is not possible due to the fact that there are atoms missing. The third method compresses the solid in such a way that the excess pressure of the liquid is compensated. We call this method *compressed TPS (c-TPS)*. These methods can also be combined by relaxing the liquid and the solid part prior to the compression of the solid part. We call this *compressed relaxed TPS (cr-TPS)*.

The TPS boxes were simulated in the NVT ensemble until the crystal melted or the liquid froze. These processes were monitored with the radial distribution function, the mean-square displacement, the pressure, and internal energy during the simulation, and direct visualization of the atomic configurations with the visual molecular dynamics tool [57].

B. Influence of the atom number

As solid helium exists in an hcp structure [13] in the regime we are interested in, the number of atoms for the crystal is restricted to $2n^3$, where n is the number of periodic images of the unit cell per space dimension. The TPS cells with 256 atoms were obtained with four unit cells in every direction in the solid and the liquid, respectively. In the same way, the TPS box with 500 atoms was constructed from five unit cells in every direction and the box with 864 atoms from six unit cells in every direction. Note that due to the hcp basis cell, the box is not cubic. We did not relax the cell parameters prior to the TPS calculations, as mentioned above. By applying the heating/cooling scheme as described above with just 54 atoms in the box, the liquid crystallized at 1300 K, while the crystal melted above 1100 K. As there was no temperature overlap in which we could perform TPS, we concluded that the number of 54 atoms for each constituent and 108 in the TPS is not sufficient. We achieved a sufficient temperature overlap with 128 and more atoms and calculated the melting temperature with 256, 500, and 864 atoms in the TPS box with the setup procedure as it was described above for cr-TPS. The c-TPS ansatz, i.e., a compressed perfect crystal and a random liquid configuration in the simulation cell, was tested with 256, 500, 864, and 2048 atoms in the simulation cell, as well as the e-TPS ansatz with 254, 495, and 856 atoms, see Fig. 2. We employed a \mathbf{k} -point sampling at the Γ -point and performed additional calculations with a \mathbf{k} -point at 0 1/3 0 and a Monkhorst-Pack set of 2 x 2 x 2.

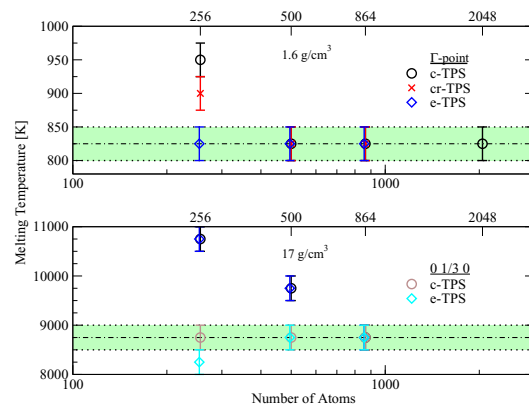


FIG. 2. Convergence of the melting temperature with respect to the number of atoms at a density of 1.6 and 17 g/cm³. Shown are results for c-TPS (circles), cr-TPS (crosses), and e-TPS (diamonds). The lower panel demonstrates the necessity to change the \mathbf{k} -point sampling at higher densities, see the discussion below.

For the calculations at 1.6 g/cm^3 , we can see systematic behavior of the c-TPS and the cr-TPS. The e-TPS seems to be converged with 254 atoms already. The convergence of the different TPS methods with respect to the number of atoms is consistent with the results of Refs. [30,34,37]. At 17 g/cm^3 , a \mathbf{k} -point sampling at the Γ -point is not sufficient for converged TPS calculations with 500 atoms. Instead, a more precise sampling has to be employed.

The smaller the number of atoms in the simulation box, the higher the impact of the initial velocity vector distribution. With an increasing number of atoms, the crystal lattice becomes more and more stable as the random lattice errors induced by the velocity vector initialization average out. We therefore concluded that 500 atoms are sufficient to obtain well-converged results irrespective of the TPS method. We chose c-TPS, which drastically simplifies the setup procedure compared to the cr-TPS and the e-TPS scheme. The latter was also employed by Ref. [30].

The simulation box of the TPS configuration is a hcp cell that is elongated in the z -direction. The intuitive choice of a \mathbf{k} -point sampling has less \mathbf{k} -points in the direction of the elongation. When we employ a sampling of $2 \times 2 \times 2$ (12 \mathbf{k} -points) or better, the maximum deviations in pressure between those more accurate samplings are within the numerical noise. Some special points in the Brillouin zone of the hexagonal cell, given by Ref. [58], result in a pressure convergence of better than 0.05% over a density range of 1 to 30 g/cm^3 compared to the more demanding sampling mentioned above. For the TPS, we employ the Γ -point for densities below 7 g/cm^3 and a \mathbf{k} -point at $0 \frac{1}{3} 0$ in reciprocal space for higher densities.

For a density of 17 and 20 g/cm^3 , we studied the influence of the choice of the pseudopotential as well as the choice of \mathbf{k} -point sampling. As described above, we expected a significant difference between the standard and the hard PAW potential above 14 g/cm^3 . However, when we calculated the melting temperature at 20 g/cm^3 with a \mathbf{k} -point sampling at the Γ -point, a Monkhorst-Pack set of $2 \times 2 \times 2$, and a \mathbf{k} -point at $0 \frac{1}{3} 0$, we obtained no difference between the pseudopotentials. The corresponding melting temperatures at 20 g/cm^3 were $10\,750 \pm 250 \text{ K}$ for the Γ -point calculations and $9750 \pm 250 \text{ K}$ with the \mathbf{k} -point at $0 \frac{1}{3} 0$ and $2 \times 2 \times 2$. The respective melting temperatures at 17 g/cm^3 were 1000 K lower than those at 20 g/cm^3 . Again, the melting points obtained with the hard PAW potential and a Monkhorst-Pack set of $2 \times 2 \times 2$ result in the same melting temperature as the standard PAW potential and a single \mathbf{k} -point at $0 \frac{1}{3} 0$ at high densities. We therefore employ the standard PAW potential throughout this study for the TPS calculations, except for the melting points at 10 000 K that exceeded 20 g/cm^3 . Here, we employed the hard PAW potential for the TPS calculations.

C. Influence of the spacing

In the considered region of the helium phase diagram, the pressure in a liquid part is greater than that in a solid part, if the box volume and temperature are equivalent. This causes the atoms of the liquid part of the TPS box to expand into the solid, which subsequently begins to melt, if no spacing between the constituents is introduced. To circumvent this

well-known problem, we compressed the crystal in such a way that the liquid part was attached to the solid at a certain fraction of the lattice distance $b = a\sqrt{3}/2$. Here, a is the smaller lattice constant of an hcp lattice. The compression increases the pressure in the solid. At the beginning of the TPS, the excess pressures in each part of the box are decreased by the expansion of both parts into the void between them. To benchmark the influence of the spacing size on the result, we set up TPS boxes with 500 atoms and identical liquid and solid parts but different fractions of b from 95% to 108%. Each of these TPS boxes was then simulated with the PBE XC functional at 7000 K and densities of 9.70, 9.88, 9.92, 9.96, 10.00, 10.04, 10.08, 10.12, 10.30, 10.47, and 10.54 g/cm^3 . We found no dependency of the results on the spacing. However, at the greatest and the smallest spacings under consideration and therefore a smaller or bigger compression of the solid part, the solid part showed increasing oscillations perpendicular to the interface. We limited our calculations to parameters in which this unphysical behavior did not occur. We found that as long as the spacing size is within this range, the choice of b is arbitrary. We chose a spacing of 100%. The liquid part is therefore attached to the solid part where the next crystal plane would be in the compressed solid.

D. Influence of the metastable region

The melting of a solid is a first-order phase transition. When we performed TPS calculations at various densities, we encountered a region of higher density in which all TPS calculations yielded solid results and a region of lower density in which all TPS calculations gave liquid results. The density region in between is metastable and can result in either a solid or a liquid. The sampling of this metastable region was a byproduct of the study of the influence of the spacing. The simulations demonstrated that the mean size of the metastable region is 3.4% in density. We therefore infer a typical error of 3.5% in density for the EOS calculations that follow the TPS, see Sec. IV. This statistical behavior can be utilized to resolve the pressure and temperature during the melting transition with fewer atoms but a greater number of TPS simulations [35].

The final TPS calculations were performed with 500 atoms, a spacing of b , a Brillouin zone sampling with the Γ point at densities below 7 g/cm^3 , and with a \mathbf{k} -point at $0 \frac{1}{3} 0$ for higher densities, and with the PBE and the van der Waals density functional (vdW-DF1) [59] XC functionals to be consistent with recent hydrogen-helium demixing calculations [12,60,61]. As Monserrat *et al.* [62] found the hcp structure to be the most stable at pressures between 10 and 20 TPa and no contradicting experimental results nor other predictions from random structure search algorithms exist, we assumed solid helium to remain in the hcp structure throughout the entire pressure range considered here, i.e., from 15 GPa to 35 TPa. However, the extreme high-pressure phase of helium is considered to be bcc. [63] The TPS results of Belonoshko *et al.* [24] that were obtained with the fcc and bcc structure are in good agreement with the experimental melting line, where the underlying crystal structure is hcp. This indicates that the underlying crystal configuration might not be essential for the

reproduction of the helium melting line, at least in the part of the phase diagram that was investigated by Ref. [24].

IV. CALCULATION OF THE MELTING LINE

The high number of atoms that is required for converged TPSs is neither necessary nor computationally feasible for converged pressures as the pressure obtained with 128 atoms is identical to the pressure with a greater number of atoms within 0.15%. The pressure inside a TPS box drops if the resulting phase is solid, but several thousand additional time steps would be required for the pressure to fluctuate around the solid equilibrium pressure at the given density and temperature T . The same applies for rising pressures and liquid TPS results. To save computation time, we performed calculations of the solid or liquid phase with 128 atoms for at least 5 ps. To ensure the integrity of the hcp structure, we heated a perfect hcp crystal within 5 ps from a temperature of $0.8T$ to T prior to the relaxation process described above. However, the densities at which converged pressures were calculated with 128 atoms are the result of TPS with 500 atoms.

As discussed above, the lowest possible solid density at a given temperature cannot be determined exactly with TPS. Therefore, we made a conservative estimate of an error of 3.5% in density based on the results of Sec. III. First, we performed TPS simulations on a density grid with a width of less than 2% for every temperature under consideration. Then, the pressure P_s of the lowest density ρ_s at which the TPS results in a solid at a given temperature was calculated with 128 atoms, as well as the pressure P_l that corresponds to the highest density with a liquid TPS result and $\rho_l < \rho_s$. The mean pressure $|P_s - P_l|/2$ yielded the melting pressure p_m .

To account for the uncertainties due to the density jump along the first-order phase transition, we also calculated the pressure of a solid at a density that is 3.5% smaller than ρ_s . The pressure deviation of the two solid configurations is the uncertainty we added to the pressure difference $|P_s - P_l|$ to estimate the error of the melting pressure p_m , as discussed above. We chose to perform the calculations at constant temperatures to provide the melting points at the exact temperatures that were required by Ref. [12]. The solid pressures were calculated in a hexagonal cell, while the pressures of the liquid were obtained with cubic simulation boxes.

The algorithm for the calculation of one point of the melting line can be summarized as follows:

- (i) At a fixed temperature, iteratively find the density where melting occurs with 500 atoms and TPS until the difference in density between the least dense solid ρ_s and the most dense liquid result ρ_l is $< 2\%$.
- (ii) Calculate the pressures P_s and P_l corresponding to ρ_s and ρ_l with 128 atoms.
- (iii) Calculate the pressure P'_s corresponding to $\rho'_s = 0.965\rho_s$ with 128 atoms.
- (iv) Calculate the melting pressure $P_m = (P_s + P_l)/2$.
- (v) Calculate the error in pressure $dP_m = |P'_s - P_s|$.

The final results for the high-pressure melting line of helium obtained with TPSs are displayed in Fig. 3.

The different XC functionals resulted in the same melting line within the error bars and reproduced the available experimental data very well. The vdW-DF1 functional resulted

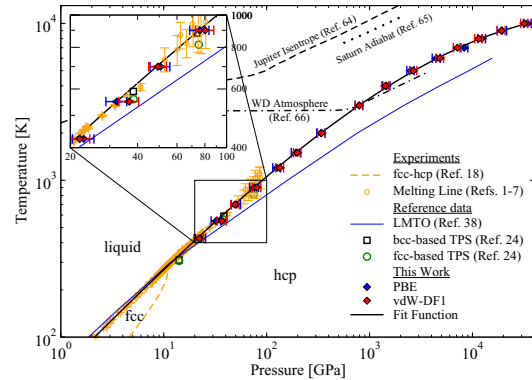


FIG. 3. Helium phase diagram with the TPS results (diamonds) that employed the PBE (blue) and vdW-DF1 (red) XC functional compared with experimental data (orange) [1–7]. Note that we plotted the data of Ref. [7] as corrected by Ref. [24]. The previous melting line predictions (blue line, black squares, and red circles) [24,38], the coldest Jupiter adiabat of the preliminary Jupiter model of Hubbard and Militzer [64], the coldest possible adiabatic layer of helium around Saturn’s core of Püstow *et al.* [65], and the coldest P-T profile of white dwarfs of Ref. [66] are displayed as well. The inset shows a magnification of the melting line between 400 and 1000 K. The fit function to our TPS results is depicted as a bold black line.

in systematically lower densities for the melting points than the PBE functional at the same temperature. However, the vdW-DF1 functional also yielded higher pressures than the PBE functional at the same density and temperature. These two effects canceled each other out, which resulted in identical pressures within the error bars. Different XC functionals can give different pressures at identical densities due to the construction of the XC functionals and their parameters, respectively. The enhancement factor of revPBE, the exchange functional that underlies vdW-DF1, over the reduced gradient has a steeper slope than that of PBE. This results in a stronger repulsion of the ions and therefore in higher pressures, see Ref. [67]. The TPS melting line lies above the linear-muffin-tin-orbital results of Ref. [38]. The melting line shows a slight downward curvature at higher pressures but not as pronounced as was predicted by Young [38].

In Saturn and possibly Jupiter, the demixing of hydrogen and helium into a helium-rich and a helium-poor component might act as an additional heat source, which could explain the high luminosity of Saturn [8–10,12,60,65]. The accurate location of the melting line of helium is relevant to the helium-rich side of the miscibility diagram of hydrogen and helium, in particular when the demixing temperatures approach the helium melting line for high helium concentrations [12]. Note that our melting line is located well below the isentropes of Jupiter [64] and Saturn [65]. Therefore, if a helium-rich layer is formed due to H-He demixing, it is still liquid. Prior to our investigations, the possibility of solid helium in the giant planets of the solar system could not be estimated. Models of very old and cool white dwarf atmospheres that consisted of pure helium [66] predicted a P-T profile that intersects

our TPS melting line. This is important for accurate interior models of white dwarfs. The knowledge of the melting line paves the way for consistent wide-range equation of states calculated with DFT-MD like the He-REOS.3 [68], which can be applied in planetary physics.

We could not find a Simon-Glatzel [69] or Kechin equation [70] that reproduces all of the experimental data as well as our averaged TPS results with $p(T)_{\text{Melt}} = (p(T)_{\text{Melt, PBE}} + p(T)_{\text{Melt, vdW-DF1}})/2$. Therefore, we chose a fit function of the type

$$T(P) = \exp[a + b \ln P + c(\ln P)^2 - d(\ln P)^3], \quad (1)$$

with $a = 4.11633$, $b = 0.649134$, $c = 4.13856 \cdot 10^{-5}$, and $d = 1.48182 \cdot 10^{-3}$. The Kechin equation of Ref. [7] predicts an upward curvature of the melting line in Fig. 3, which is not reproduced by our TPS results. Please note that we therefore did not include the data of Ref. [7] in the fitting procedure.

V. CONCLUSION

We calculated the high-pressure melting line of helium with the two-phase approximation with DFT-MD by using the PBE and the vdW-DF1 XC functional. The different function-

als resulted in the same melting line within the error bars. The results for the experimental melting line up to 100 GPa were reproduced. The calculations span a temperature range of one magnitude and a pressure range of three magnitudes, i.e., from 425 K to 10 000 K and from 15 GPa to 35 TPa. We find that the high-pressure melting line exhibits a slight downward curvature. The implementation of the TPS cell and the calculation of the melting pressure in this paper were developed to minimize the computational effort that is required for the setup procedure of the TPS cell and the calculation of the melting pressure. Its general applicability has to be demonstrated.

ACKNOWLEDGMENTS

We thank M. French, C. Kellermann, N. Nettelmann, M. Schöttler, and F. Tamm for helpful discussions and remarks. We thank the anonymous referees for helpful comments. This work was supported by the Deutsche Forschungsgemeinschaft within the Sonderforschungsbereich 652, by the North German Supercomputing Alliance (HLRN) and the ITMZ of the University of Rostock.

-
- [1] J. S. Dugdale and D. K. C. MacDonald, *Phys. Rev.* **89**, 832 (1953).
 - [2] R. K. Crawford and W. B. Daniels, *J. Chem. Phys.* **55**, 5651 (1971).
 - [3] R. L. Mills, D. H. Liebenberg, and J. C. Bronson, *Phys. Rev. B* **21**, 5137 (1980).
 - [4] P. Loubeyre, J. M. Besson, J. P. Pinceaux, and J. P. Hansen, *Phys. Rev. Lett.* **49**, 1172 (1982).
 - [5] W. L. Vos, M. G. E. van Hinsberg, and J. A. Schouten, *Phys. Rev. B* **42**, 6106 (1990).
 - [6] F. Datchi, P. Loubeyre, and R. Le Toullec, *Phys. Rev. B* **61**, 6535 (2000).
 - [7] D. Santamaría-Pérez, G. D. Mukherjee, B. Schwager, and R. Boehler, *Phys. Rev. B* **81**, 214101 (2010).
 - [8] D. J. Stevenson, *Phys. Rev. B* **12**, 3999 (1975).
 - [9] D. J. Stevenson and E. E. Salpeter, *Astrophys. J. Suppl. Ser.* **35**, 221 (1977).
 - [10] J. J. Fortney and W. B. Hubbard, *Astrophys. J.* **608**, 1039 (2004).
 - [11] J. J. Fortney, *Science* **305**, 1414 (2004).
 - [12] M. Schöttler and R. Redmer, *Phys. Rev. Lett.* **120**, 115703 (2018).
 - [13] H. K. Mao, R. J. Hemley, Y. Wu, A. P. Jephcoat, L. W. Finger, C. S. Zha, and W. A. Bassett, *Phys. Rev. Lett.* **60**, 2649 (1988).
 - [14] P. Loubeyre, R. LeToullec, J. P. Pinceaux, H. K. Mao, J. Hu, and R. J. Hemley, *Phys. Rev. Lett.* **71**, 2272 (1993).
 - [15] D. Alfè, L. Vočadlo, G. Price, and M. Gillan, *J. Phys.: Condens. Matter* **16**, S973 (2004).
 - [16] G. Robert, P. Legrand, P. Arnault, N. Desbiens, and J. Clérouin, *Phys. Rev. E* **91**, 033310 (2015).
 - [17] A. B. Belonoshko, *Geochim. Cosmochim. Acta* **58**, 4039 (1994).
 - [18] A. B. Belonoshko and L. S. Dubrovinsky, *Geochim. Cosmochim. Acta* **59**, 1883 (1995).
 - [19] A. Belonoshko and R. Ahuja, *Phys. Earth Planet. Inter.* **102**, 171 (1997).
 - [20] A. B. Belonoshko, R. Ahuja, and B. Johansson, *Phys. Rev. Lett.* **84**, 3638 (2000).
 - [21] D. Alfè, M. J. Gillan, and G. D. Price, *J. Chem. Phys.* **116**, 6170 (2002).
 - [22] J. R. Morris, C. Z. Wang, K. M. Ho, and C. T. Chan, *Phys. Rev. B* **49**, 3109 (1994).
 - [23] L. Koči, R. Ahuja, A. B. Belonoshko, and B. Johansson, *J. Phys.: Condens. Matter* **19**, 016206 (2007).
 - [24] A. B. Belonoshko, L. Koči, and A. Rosengren, *Phys. Rev. B* **85**, 012503 (2012).
 - [25] L. Koči, R. Ahuja, and A. B. Belonoshko, *Phys. Rev. B* **75**, 214108 (2007).
 - [26] J. Bouchet, F. Bottin, G. Jomard, and G. Zérah, *Phys. Rev. B* **80**, 094102 (2009).
 - [27] Y. Usui and T. Tsuchiya, *J. Earth Sci.* **21**, 801 (2010).
 - [28] J. R. Morris and X. Song, *J. Chem. Phys.* **116**, 9352 (2002).
 - [29] D. Alfè, *Phys. Rev. B* **68**, 064423 (2003).
 - [30] S. Root, L. Shulenburger, R. W. Lemke, D. H. Dolan, T. R. Mattsson, and M. P. Desjarlais, *Phys. Rev. Lett.* **115**, 198501 (2015).
 - [31] A. B. Belonoshko and L. S. Dubrovinsky, *Am. Mineral.* **81**, 303 (1996).
 - [32] H. L. Tepper and W. J. Briels, *J. Chem. Phys.* **115**, 9434 (2001).
 - [33] R. Ahuja, A. B. Belonoshko, and B. Johansson, *Phys. Rev. E* **57**, 1673 (1998).
 - [34] A. B. Belonoshko, R. Ahuja, O. Eriksson, and B. Johansson, *Phys. Rev. B* **61**, 3838 (2000).
 - [35] Q.-J. Hong and A. van de Walle, *J. Chem. Phys.* **139**, 094114 (2013).

- [36] Y. Feng, J. Chen, D. Alfé, X.-Z. Li, and E. Wang, *J. Chem. Phys.* **142**, 064506 (2015).
- [37] J. Chen, X.-Z. Li, Q. Zhang, M. I. J. Probert, C. J. Pickard, R. J. Needs, A. Michaelides, and E. Wang, *Nat. Commun.* **4**, 2064 (2013).
- [38] D. A. Young, A. K. McMahan, and M. Ross, *Phys. Rev. B* **24**, 5119 (1981).
- [39] D. Lévesque, J.-J. Weis, and M. L. Klein, *Phys. Rev. Lett.* **51**, 670 (1983).
- [40] P. Loubeyre and J.-P. Hansen, *Phys. Rev. B* **31**, 634 (1985).
- [41] M. Ross and D. A. Young, *Phys. Lett. A* **118**, 463 (1986).
- [42] P. Hohenberg and W. Kohn, *Phys. Rev.* **136**, B864 (1964).
- [43] W. Kohn and L. J. Sham, *Phys. Rev.* **140**, A1133 (1965).
- [44] G. Kresse and J. Hafner, *Phys. Rev. B* **47**, 558 (1993).
- [45] G. Kresse and J. Hafner, *Phys. Rev. B* **49**, 14251 (1994).
- [46] G. Kresse and J. Furthmüller, *Phys. Rev. B* **54**, 11169 (1996).
- [47] G. Kresse and J. Furthmüller, *Comput. Mater. Sci.* **6**, 15 (1996).
- [48] J. Hafner, *J. Comput. Chem.* **29**, 2044 (2008).
- [49] M. Preising, W. Lorenzen, A. Becker, R. Redmer, M. D. Knudson, and M. P. Desjarlais, *Phys. Plasmas* **25**, 012706 (2018).
- [50] S. Nosé, *J. Chem. Phys.* **81**, 511 (1984).
- [51] S. Nosé, *Prog. Theor. Phys. Suppl.* **103**, 1 (1991).
- [52] D. M. Bylander and L. Kleinman, *Phys. Rev. B* **46**, 13756 (1992).
- [53] P. E. Blöchl, *Phys. Rev. B* **50**, 17953 (1994).
- [54] A. Baldereschi, *Phys. Rev. B* **7**, 5212 (1973).
- [55] J. P. Perdew, K. Burke, and M. Ernzerhof, *Phys. Rev. Lett.* **77**, 3865 (1996).
- [56] W. Lorenzen, Phase transitions in hydrogen-helium mixtures, Ph.D. thesis, University of Rostock, 2012.
- [57] W. Humphrey, A. Dalke, and K. Schulten, *J. Mol. Graph.* **14**, 33 (1996).
- [58] R. A. Evarestov and V. P. Smirnov, *Phys. Status Solidi (b)* **119**, 9 (1983).
- [59] J. Klimeš, D. R. Bowler, and A. Michaelides, *J. Phys.: Condens. Matter* **22**, 022201 (2010).
- [60] W. Lorenzen, B. Holst, and R. Redmer, *Phys. Rev. Lett.* **102**, 115701 (2009).
- [61] W. Lorenzen, B. Holst, and R. Redmer, *Phys. Rev. B* **84**, 235109 (2011).
- [62] B. Monserrat, N. D. Drummond, C. J. Pickard, and R. J. Needs, *Phys. Rev. Lett.* **112**, 055504 (2014).
- [63] H. Niki, H. Nagara, H. Miyagi, and T. Nakamura, *Physics Letters A* **79**, 428 (1980).
- [64] W. B. Hubbard and B. Militzer, *Astrophys. J.* **820**, 80 (2016).
- [65] R. Püstow, N. Nettelmann, W. Lorenzen, and R. Redmer, *Icarus* **267**, 323 (2016); the data for the dotted curve in Fig. 4 were provided by N. Nettelmann.
- [66] P. Bergeron, D. Saumon, and F. Wesemael, *Astrophys. J.* **443**, 764 (1995).
- [67] J. Klimeš, D. R. Bowler, and A. Michaelides, *Phys. Rev. B* **83**, 195131 (2011).
- [68] A. Becker, W. Lorenzen, J. J. Fortney, N. Nettelmann, M. Schöttler, and R. Redmer, *Astrophys. J. Suppl. Series* **215**, 21 (2014).
- [69] F. Simon and G. Glatzel, *Z. Anorg. Allg. Chem.* **178**, 309 (1929).
- [70] V. V. Kechin, *J. Phys.: Condens. Matter* **7**, 531 (1995).



4.3. Metallization of Helium at High Densities from *ab initio* Simulations


Author contributions

M.P. Preparation of the manuscript, all calculations.

R.R. Supervision of the project, preparation of the manuscript.

Metallization of dense fluid helium from *ab initio* simulations

Martin Preising  and Ronald Redmer 
Institut für Physik, Universität Rostock, D-18051 Rostock, Germany

 (Received 25 September 2020; accepted 4 December 2020; published 21 December 2020)

We examine the metallization of fluid helium with molecular dynamics simulations based on density functional theory. The insulator-to-metal transition is studied at densities between 1 and 22 g/cm³ and temperatures between 10 000 and 50 000 K. We calculate the equation of state, the band gap dependent on density and temperature by using different definitions, the DC conductivity, the reflectivity, and the ionization degree for which a novel method has been proposed recently [see M. Bethkenhagen *et al.*, *Phys. Rev. Research* **2**, 023260 (2020)]. We find no indication of a first-order phase transition in any of the properties studied here and therefore conclude that the metallization of fluid helium is continuous. For instance, we do not observe jumps in the DC conductivity and/or the reflectivity when the band gap closes. However, the ionization degree increases continuously from below 10% at the lowest to over 99% at the highest densities which reflects the continuous insulator-to-metal transition. The increase is almost exclusively driven by pressure ionization and shows only a weak temperature dependency. We discuss the high-pressure phase diagram of helium and the implications of our results on the structure of astrophysical objects like gas giant planets and brown dwarfs.

DOI: [10.1103/PhysRevB.102.224107](https://doi.org/10.1103/PhysRevB.102.224107)

I. INTRODUCTION

Helium is generated by primordial nucleosynthesis in the early universe [1] or by hydrogen burning in stars [2]. After hydrogen, it is the second most abundant element and makes up about 23% of the baryon density in the universe. For a comprehensive understanding of many astrophysical processes the properties of hydrogen and helium have to be known for a wide range of densities and temperatures. Especially, this is the case for the formation and evolution as well as for the structure and composition of astrophysical objects like stars, brown dwarfs, and gas giant planets, where hydrogen and helium typically amount to about 98% of their mass. Of particular importance are the equation of state (EOS) data, optical properties like absorption, and the DC conductivity. The latter is a key input in dynamo simulations for the structure of the magnetic fields of these objects [3].

Therefore, the behavior of hydrogen and helium under extreme conditions has been in the focus of plasma, astro- and high-pressure physics for decades; for reviews, see Refs. [4–7]. Both hydrogen and helium are insulators at ambient conditions. The prediction of an insulator-to-metal transition (IMT) at high pressures, i.e., the *metallization* of molecular hydrogen and of atomic helium represents an intriguing problem in this context: How can their metallic-like electrical conductivities be traced back to their atomic properties? How do these change along the transformation pathway from ambient conditions to pressures of several megabar? These questions have inspired fundamental contributions to early quantum theory and solid state physics by, e.g., Herzfeld [8] and Mott [9]; for a review, see Ref. [10].

Wigner and Huntington [11] were the first to predict the transition from insulating molecular solid hydrogen to

metallic atomic solid hydrogen at 25 GPa at $T = 0$ K in 1935. Since then, enormous progress in understanding dense hydrogen has been made. Yet, the exact location of the IMT in the pressure-temperature diagram and the character of this transition is not precisely known, neither for the solid [6,12] nor the fluid domain [13–15]. A full understanding of the IMT in hydrogen still poses a great challenge, both for high-pressure experiments (e.g., measurement of temperature, interpretation of an increased reflectivity as signature for metallization) and *ab initio* simulations (e.g., treatment of nuclear quantum effects and of latent heat; see Ref. [16]). However, it is now consistently predicted to occur at few megabars (1 Mbar=100 GPa); see, e.g., Refs. [12,17] for recent surveys.

Consequently, the assumption that helium transforms to a metal upon sufficient compression has triggered many studies, although by far not as many as for hydrogen, see Refs. [18–21]. While the band gap (BG) of solid helium at zero temperature has been calculated with various approaches [22–25], ionization in dense helium plasmas has been treated within chemical models since the late 1980s [26–30]. Landau and Zeldovich [31] evaluated such ionization phenomena first. They concluded that the phase transition might be of first-order in a certain region of the phase diagram. This so-called *plasma phase transition (PPT)* would be connected with latent heat and a density jump between the two phases. Since then, a lot of effort has been made towards the prediction of the slope of the coexistence line of the PPT and the location of its critical point for hydrogen and other elements and compounds; see, e.g., Ref. [21]. Some of the models for helium predict two distinct phase transitions at high pressures: the first due to the ionization of neutral helium to He⁺, the second one due to a subsequent ionization of He⁺ to He²⁺. For instance, Förster *et al.* [26] locate the

critical point for the corresponding coexistence curve between the neutral and singly ionized fluids at around 35 000 K and 620 GPa (first PPT). They further predict a coexistence curve between the singly and twofold ionized fluids (second PPT) which ends in a second critical point at 114 000 K and 9 100 GPa.

Since the mid 2000s, the application of density functional theory (DFT) allowed for a more intricate description of the metallization transition in solid helium [32]. DFT coupled with classical molecular dynamics (MD) led to further investigations of the metallization transition of fluid helium in the physical picture [19,33–35]. Those studies could reach densities that are beyond the range of the most recent experiments on dense helium [20,36,37]. However, they did not exhibit any features of a thermodynamic instability, i.e., a PPT, that was predicted by chemical models as mentioned above.

In this study, we examine the metallization of fluid helium with DFT-MD and calculate the EOS, the DC conductivity, the reflectivity, and the ionization state for a broad range of densities (1–22 g/cm³ and temperatures (10 000–50 000) K. In particular, we study the evolution of the electronic BG and of the ionization degree as function of density and temperature. We search for jumps in the EOS, the DC conductivity, and the optical reflectivity, indicative of a first-order phase transition. The ionization degree is calculated with a novel method proposed recently [38]. Furthermore, we investigate whether or not metallic helium can exist at the extreme conditions in the interior of gas giant planets like Jupiter or in brown dwarfs like KOI 889b. We then discuss further implications of our results for astrophysics.

Our paper is organized as follows. In Sec. II, we introduce the computational methods for the EOS, the band gaps, the DC conductivity, the reflectivity, and the ionization degree. We then display and discuss the results in the same order in Sec. III, outline implications on the high-pressure phase diagram of helium and illustrate consequences for the behavior of dense helium in astrophysical objects.

II. METHODS

We apply a consistent approach for the calculation of the thermophysical properties of dense helium by treating the electrons with DFT [39,40] and combining this quantum-statistical description with classical MD for the ions. We employ the plane wave code VASP (*Vienna ab initio simulation package*) [41–45], in which the electronic bands are occupied according to Fermi-Dirac statistics. We adjust the number of bands as well as the size of the time step for each density and temperature under consideration in the same way as documented in Preising *et al.* [46]. We control the temperature of the ions with a Nosé-Hoover thermostat [47–49] and sample the Brillouin zone with different \mathbf{k} -point sets: the Γ point, the Baldereschi Mean Value Point (BMVP) [50], or a more elaborate Monkhorst-Pack set [51]. We use the Perdew-Burke-Ernzerhof (PBE) exchange-correlation (XC) functional [52] and employ pseudopotentials in the plane augmented wave (PAW) description [53] as well as the full Coulomb potential where necessary. The PAW pseudopotentials both treat two valence electrons. The difference between

the standard PAW and the hard PAW potential is the distance at which the augmentation of the wavefunction begins; it is smaller for the hard PAW (0.6 Å) than for the standard PAW (1.1 Å). Most important for the determination of precise thermophysical properties are careful checks of the convergence of the DFT-MD simulations; details are outlined in Ref. [54].

A. EOS

The pressure and internal energy are evaluated from DFT-MD runs after they have achieved thermodynamic equilibrium. We ensure that the total simulation time is at least 5 ps at every density and temperature grid point in this study.

B. Band gaps

It is known that DFT-based methods underestimate the band gap systematically depending on the number of atoms and the XC functional [30,34,35,55]. Nevertheless, we can gain valuable insight in the evolution of the BG dependency on density and temperature.

We examine and compare different definitions of the BG that were used in recent work on the behavior of dense helium, namely the *HOMO-LUMO* definition [33,35], the *broadened* method [34], and the *histogram* technique [32]. The latter is from our perspective best suited to identify the BG. Details of these methods are outlined in Ref. [54] (see, also, Refs. [26,27 and 32] therein).

C. DC conductivity

The dynamic electrical conductivity is calculated with the Kubo-Greenwood formula [56–60]:

$$\sigma^{\text{tot}}(\omega) = \frac{2\pi e^2}{3\omega\Omega} \sum_{\mathbf{k}} W(\mathbf{k}) \sum_{j=1}^N \sum_{i=1}^N \sum_{\alpha=1}^3 [F(\epsilon_{i,\mathbf{k}}) - F(\epsilon_{j,\mathbf{k}})] \times |(\Psi_{j,\mathbf{k}}|\mathbf{v}|\Psi_{i,\mathbf{k}})|^2 \delta(\epsilon_{j,\mathbf{k}} - \epsilon_{i,\mathbf{k}} - \hbar\omega). \quad (1)$$

Here, the Fermi-Dirac occupation $F(\epsilon_{i,\mathbf{k}})$ of the i th band that corresponds to the energy $\epsilon_{i,\mathbf{k}}$ and the wave function $\Psi_{i,\mathbf{k}}$ at \mathbf{k} -point \mathbf{k} is summed up over the spatial directions α and the bands i and j . The prefactor contains the electron charge e , the frequency ω , and the supercell volume Ω .

The DC conductivity is the low-frequency limit of the dynamic electrical conductivity:

$$\sigma_{\text{DC}} = \lim_{\omega \rightarrow 0} \sigma^{\text{tot}}(\omega). \quad (2)$$

D. Reflectivity

We calculate the reflectivity R at 532 nm as in Preising *et al.* [46] via the Fresnel formula,

$$R(\omega) = \frac{[n_0(\omega) - n(\omega)]^2 + [k_0(\omega) - k(\omega)]^2}{[n_0(\omega) + n(\omega)]^2 + [k_0(\omega) + k(\omega)]^2}, \quad (3)$$

with the complex index of refraction, $n + ik$. The subscript 0 denotes the material at the reflecting boundary. The complex index of refraction results from the complex dielectric

function $\varepsilon(\omega) = \varepsilon_1(\omega) + i\varepsilon_2(\omega)$ as

$$n(\omega) + ik(\omega) = \sqrt{\varepsilon(\omega)}, \quad (4)$$

$$\varepsilon_1(\omega) = \frac{\sigma_2(\omega)}{\varepsilon_0\omega}, \quad (5)$$

$$\varepsilon_2(\omega) = 1 - \frac{\sigma_1(\omega)}{\varepsilon_0\omega}. \quad (6)$$

Here, we obtain the real part of the dynamic conductivity $\sigma_1(\omega)$ from the Kubo-Greenwood formula (1) and calculate the imaginary part $\sigma_2(\omega)$ from $\sigma_1(\omega)$ with a Kramers-Kronig relation; see Refs. [58,60–63] for further details. The testing regime for the optical reflectivity at 532 nm was identical with that of the DC conductivity.

E. Ionization

Bethkenhagen *et al.* [38] proposed a new method to calculate the ionization degree of high-density plasmas via the dynamic electrical conductivity obtained from DFT-MD simulations and an evaluation of the Kubo-Greenwood formula, Eq. (1). Former work instead relied on the DOS to analyze the ionization degree [64–66]. We provide a brief summary of the approach; for details, see Refs. [38,54].

The dynamic electrical conductivity has to satisfy the Thomas-Reiche-Kuhn (TRK) sum rule [67–70],

$$Z^{\text{tot}} = \frac{N_e^{\text{tot}}}{N_i} = \frac{2m\Omega}{\pi e^2 N_i} \int_0^\infty d\omega \sigma^{\text{tot}}(\omega), \quad (7)$$

with the total charge state Z^{tot} , the total number of electrons N_e^{tot} and ions N_i , and the dynamic electrical conductivity $\sigma^{\text{tot}}(\omega)$. For helium, Eq. (7) is fulfilled if $Z^{\text{tot}} = 2$. We then partition the TRK sum rule into different electronic contributions and calculate the ionization state α from the number of electrons of each contribution as

$$\alpha = \frac{Z^{\text{c-c}}}{Z^{\text{tot}}}, \quad (8)$$

where $Z^{\text{c-c}}$ is the effective number of electrons per ion that contributes to electronic transition within the conduction band.

III. RESULTS

If the IMT of helium is a first-order phase transition we should observe discontinuities in the thermodynamic functions due to latent heat. The IMT should then be accompanied by BG closure and abrupt changes (jumps) of the DC conductivity, the reflectivity, and the ionization degree. Similar studies on the metallization in dense fluid hydrogen have shown that the discontinuities are generally more pronounced at lower temperatures [71–73].

In order to constrain our study to the fluid regime we only consider temperatures starting from 10 000 K and densities below the corresponding melting density of (21.3 ± 0.7) g/cm³; see Ref. [74].

A. EOS

We calculate pressures P and internal energies u for given densities ρ and temperatures T from the DFT-MD runs. In

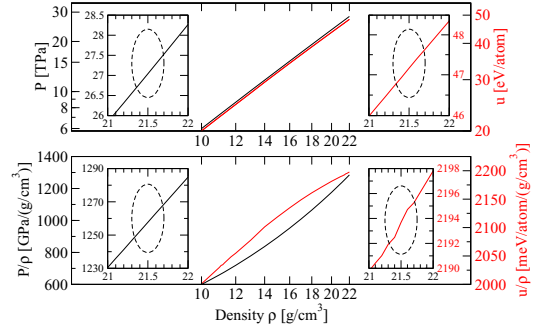


FIG. 1. (Top) Pressure P (black, left y axis) and internal energy per atom u (red, right y axis) for fluid helium at 10 000 K as function of density ρ . (Bottom) P/ρ (black, left y axis) and u/ρ (red, right y axis). The insets depict P and u over the density range where the BG closes according to the *histogram* method. The density range of interest is further highlighted by dashed ellipses.

case of a first-order phase transition, we should observe a plateau in P (density jump) and a jump in u (latent heat). The upper panel of Fig. 1 displays the pressure P and internal energy u at the lowest temperature considered here, i.e., 10 000 K. In order to illuminate the influence of correlation effects which should change considerably at the IMT, we show P/ρ and u/ρ in the lower panel. The insets left and right zoom into the density region where metallization occurs.

We do not observe a plateau-like structure in P or a jump in u in the entire density range but find some faint features in the raw data of u/ρ in the density range where the BG closes according to the *histogram* approach. However, the statistical fluctuations of u/ρ under these conditions are larger than ± 4 eV/atom/(g/cm³) in our MD runs. We therefore conclude that no noticeable behavior of P , u , P/ρ , and u/ρ occurs when the BG closes in fluid helium at 10 000 K. Furthermore, we do not find any features at higher temperatures or at densities where the BG closes according to the *broadened* method.

B. Band gaps

In order to determine the location of the band gap closure, we calculate isotherms at $T_x = 10^x$ with $x=4, 4.1, \dots, 4.7$ at a density grid of 1 g/cm³ width. By progressively decreasing the density interval we iteratively find the density at which the BG closes within 0.1 g/cm³ according to the *histogram* and *broadened* method. We then compare our results for the BG with values from Refs. [33–35] in Fig. 2.

While we reproduce the results of the *broadened* method of Ref. [34] at 20 000 K, we obtain different results at higher and lower temperatures. The reason for this discrepancy is most likely due to the use of a different XC functional. While Ref. [34] performed the DFT-MD simulations with the PBE [52] XC functional, they then determined the BGs using snapshots and the PW91 [75] XC functional. We performed all calculations with the PBE XC functional and used data from MDs to calculate the BG.

Our results reproduce the *HOMO-LUMO* results of Refs. [33,35] for all conditions of our study within the error

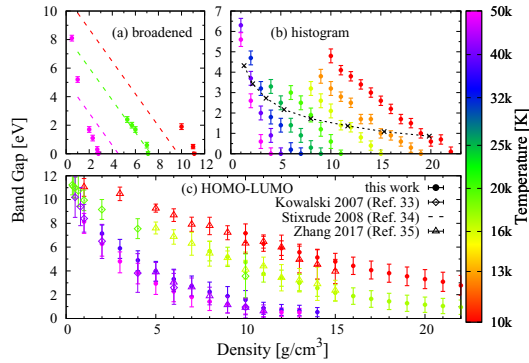


FIG. 2. Evolution of the BG with density for a set of isotherms (color-coded). Results of this work are always depicted as closed circles. (a) on the upper left shows the results of the *broadened* method of Ref. [34] as dashed lines as well as the *broadened* results of this work. (b) on the upper right displays the results of the *histogram* approach of this work. The dashed line represents the conditions where the BG is equal to $k_B T$. (c) compares results of this work with those of Refs. [33,35] within the *HOMO-LUMO* approach to the BG as open diamonds and upper triangles, respectively.

bars. However, as we discuss in Ref. [54], we could not obtain converged results with the snapshot-based methods of Refs. [33,35], even with a greater number of atoms and better \mathbf{k} -point sampling. Essentially, the BG results with the *HOMO-LUMO* method can be shifted by an arbitrary energy offset, depending on the chosen number of atoms, see Fig. S4 in Ref. [54]. Our calculations show that converged BGs in dense helium can only be obtained via MD simulations and by using the *histogram* or *broadened* technique, see Ref. [54].

C. DC conductivity

The DC conductivity σ_{DC} has been calculated from the Kubo-Greenwood formula, Eq. (1), for every isotherm and at least five corresponding densities. We increased the number of density points at lower temperatures, see Fig. 3. For the determination of σ_{DC} , we averaged over up to 20 ionic snapshots of the MD simulations; see Ref. [54] for further details. Due to the results of Sec. III B, we know the densities at which the BG closes according to the *histogram* method, see Fig. 2. If necessary, we interpolate σ_{DC} between the two most close-lying points and include this interpolated DC conductivity at conditions where the BG closes in Fig. 3. In a similar fashion, we interpolate the density where $k_B T$ is identical to the BG for every isotherm. We then interpolate the σ_{DC} at these densities in order to study whether the slope of the band gap over density changes when $k_B T$ approaches the BG. Additionally, we compare to the minimum metallic Mott conductivity $\sigma_{Mott} = 0.2 \times 10^6$ S/m and to values given in Refs. [33–35,55].

At the lowest temperatures, we observe a strong increase of the DC conductivity with the density that tends to become more flattened out at densities above the BG closure, i.e., in the metallic region. We do not see this feature in the results of

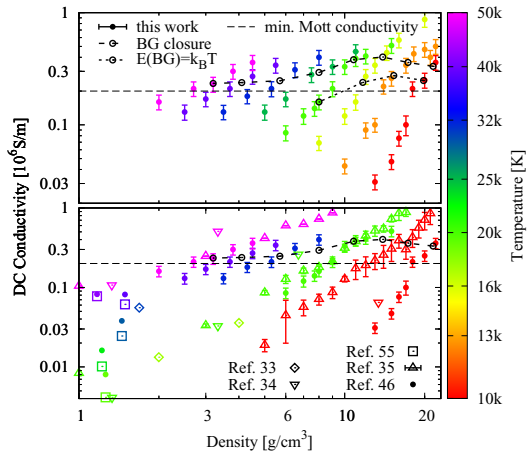


FIG. 3. DC conductivity as a function of density for different isotherms (color-coded). The upper panel shows the results of this work as filled circles. Open black symbols along the dashed line denote the interpolated DC conductivity at conditions where the BG closes according to the *histogram* method. Open black symbols along the dotted line denote the interpolated DC conductivity at conditions where the BG equals the thermal energy $k_B T$, see Fig. 2(b). The thin dashed line represents the minimum Mott conductivity at $T = 0$ K [10]. The lower panel compares our results (filled circles) for selected isotherms with the results of Kowalski *et al.* [33], Stixrude *et al.* [34], Soubiran *et al.* [55], Zhang *et al.* [35], and Preising *et al.* [46] that are denoted as open diamonds, lower triangles, squares, upper triangles, and filled circles without error bars, respectively.

Ref. [35]. The strong increase with density does not correlate strongly with the BG closure. Instead, it more strongly correlates with the conditions where the thermal energy approaches the value of the BG and the minimum Mott conductivity of 0.2×10^6 S/m given in Ref. [10]. This indicates that thermal excitations in this region lower the electronic resistance significantly and therefore increase the conductivity. Furthermore, the increase of the DC conductivity becomes less pronounced with increasing temperature due to these thermal effects. Note that the behavior of the DC conductivity of dense fluid helium as a function of density and temperature is very similar to earlier results for the continuous nonmetal-to-metal transition observed in expanded fluid metals [76,77] and noble gases [78,79].

We do not see jumps of the electrical conductivity in any of the isotherms, contrary to the results obtained for the metallization of dense fluid hydrogen [71,72]. In conjunction with the results for the EOS shown in Fig. 1 this clearly indicates that the metallization of dense fluid helium is a continuous transition of higher order.

While we reproduce the results of Ref. [35] at higher temperatures within the error bars, the strong increase of our DC conductivity at 10 000 K occurs at higher densities compared to Ref. [35]. This is likely due to the different implementations and codes used in Ref. [35] and in this study. At low

temperatures, the results of Ref. [35] seem to exhibit a similar change of slope around the minimum Mott conductivity, although the change is not as pronounced compared to our results. The low-density trends of our results reproduce all the available literature values to the best of our knowledge. At higher densities where no experimental results are available to date, we concur with the results of Ref. [33]. The high-density results of Ref. [34] are shifted toward higher DC conductivities compared to our results and those of Ref. [35]. We attribute this difference to the use of different XC functionals and finite size effects. Reference [35] employed the PW91 XC functional and 64 atoms, we used PBE and at least 128 atoms.

The DC conductivity at which the BG closes according to the *histogram* method (0.2–0.6 MS/m, see Fig. 3) is smaller than the DC conductivity at which the BG closes according to the *HOMO-LUMO* definition in Ref. [35] (0.7–1.0 MS/m). This trend is reasonable considering the differences of the results obtained for the *HOMO-LUMO* and the *histogram* approach displayed in Fig. 2 as well as in Fig. S4 of Ref. [54]. We emphasize again in this context that the BG of the *HOMO-LUMO* technique cannot be converged with respect to the number of atoms; see Ref. [54].

D. Reflectivity

We calculate the optical reflectivity at 532 nm for every isotherm at the same densities as in Sec. III C and perform the same interpolations as we did for the DC conductivity shown in Fig. 3. In a previous study [46], we calculated the reflectivity with different XC functionals under the conditions reported in Ref. [80]. We compare our results to Refs. [33,35,80], and the results of the PBE XC functional of Ref. [46], see Fig. 4.

Similar to the results for the DC conductivity (Fig. 3), we obtain a strong increase of the reflectivity with the density at the lowest temperatures that tends to become more flattened out at densities above the BG closure. As with our results for the DC conductivity, the strong increase with the density does not correlate strongly with BG closure and instead correlates more strongly with the conditions where $k_B T$ approaches the value of the BG. The reason for this correlation is most likely due to thermal excitation, see the discussion in Sec. III C.

Our low-density reflectivity trends reproduce the results of Refs. [33,80] as well as the results of Ref. [35] within the error bars. Similar to the discussion of Fig. 3 the reflectivity at which the BG according to the *histogram* method closes (30% to 40%) is smaller than the DC conductivity at which the BG according to the *HOMO-LUMO* closes in Ref. [35] (45% to 60%). In Ref. [35], the reflectivity at the BG closure increases systematically with decreasing density, from 45% at 24 g/cm³ over 55% at 15 g/cm³ to somewhere below 60% at 7 g/cm³, while our corresponding results fluctuate between 33% and 41%.

E. Ionization

We utilize the TRK sum rule method and the DOS integration approach as discussed in Sec. II E to calculate the ionization degree α via Eq. (8). Results are shown in Fig. 5.

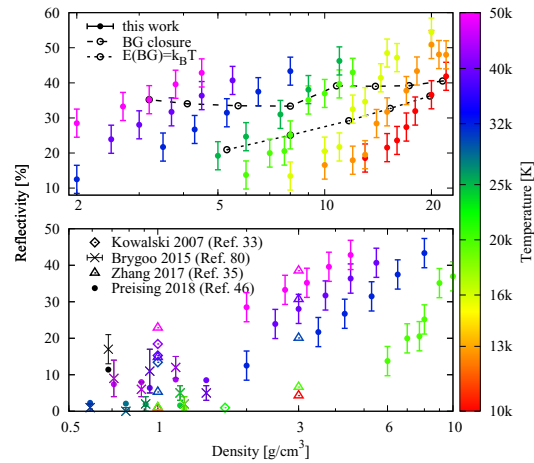


FIG. 4. Reflectivity at 532 nm as a function of density for different isotherms (color-coded). Note that the highest temperature of Ref. [80] is greater than the highest temperature considered here. For the sake of completeness, we added the corresponding data in black. The upper panel shows the results of this work: filled circles are our reflectivity results, open black symbols along the dashed line denote the interpolated reflectivity at which the BG according to the *histogram* method closes. Open black symbols along the dotted line show the interpolated reflectivity at which the BG equals $k_B T$. The lower panel compares the reflectivity of selected isotherms with the results of Refs. [33,35,46,80], denoted as open diamonds, crosses, upper triangles, and filled circles without error bars, respectively.

Consistent with our previous results, the ionization degree obtained via the TRK sum rule method shows pressure ionization, i.e., a significant increase from below 10% at 2 g/cm³ to more than 99% at the highest densities. The exact values seem to be virtually independent of temperature within our error bars and mostly depend on density. The interpolated α

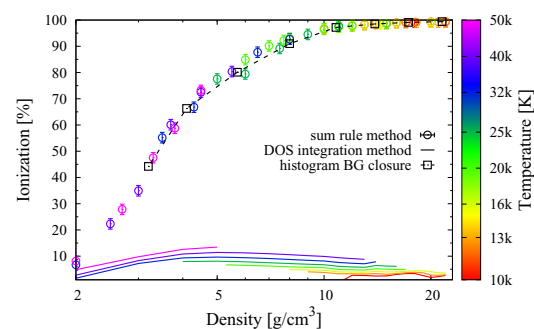


FIG. 5. Ionization degree α as a function of density at different isotherms (color-coded). Open circles with error bars show the results of the TRK sum rule method, while solid lines denote the results of the DOS integration method. Open black symbols along the dashed line show the interpolated α values at which the BG closes according to the *histogram* approach.

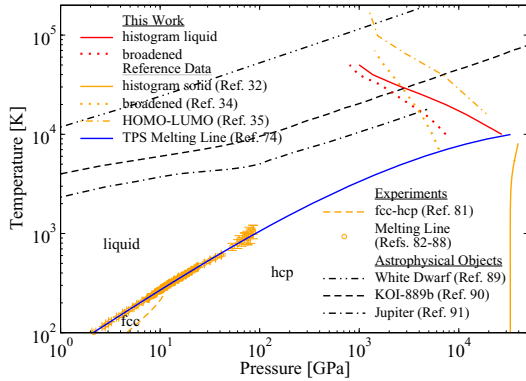


FIG. 6. Phase diagram of helium in the temperature-pressure plane: the melting line from *ab initio* simulations of Preising *et al.* [74] (bold blue line) and experimental data (dashed orange line and symbols) of Refs. [81–88]. Shown are the P - T conditions where the BG closes in fluid helium according to the *broadened* method (dotted lines, results of Ref. [34] in orange and of this work in red), the *histogram* technique of this work for the fluid (bold red line) and that of Ref. [32] for the solid (bold orange line), and the *HOMO-LUMO* definition of Ref. [35] (orange dash-dotted line). The black lines display exemplarily P - T conditions for astrophysical objects which contain substantial fractions of helium: an old white dwarf [89], the brown dwarf KOI-889b [90], and the gas giant planet Jupiter [91].

at which the BG closes according to the *histogram* technique therefore closely resembles the course of α over the density. In contrast, the results of the DOS integration approach are more temperature-dependent. The most striking result in this context is that the DOS integration method fails to show pressure ionization: the ionization degree is less than 15% for all considered densities and temperatures. Actually, the ionization seems to decrease slightly at the highest densities. We therefore conclude that the DOS integration method is not at all suited for the description of pressure ionization, at least in high-density fluid helium.

Note that the ionization degree derived from the TRK sum rule confirms the general trends predicted by chemical models, see, e.g., Ref. [26]: low ionization degree at low densities though increasing with temperature, full ionization at high densities. Note that we do not find any evidence for an instability region (PPT) inbetween as characteristic of chemical models.

F. High-pressure phase diagram of helium

Our results of neither the EOS, the DC conductivity, the reflectivity or the ionization degree demonstrate hints where the nonmetal-to-metal phase transition takes place. We instead use the *histogram* BG closure as a marker for the IMT. We summarize our findings for the IMT in dense fluid helium and propose a new high-pressure phase diagram in Fig. 6, with special emphasis on the region where the BG closes.

We consider the *histogram* method as most reliable in order to locate the BG closure and the corresponding IMT in dense fluid helium in P - T space. Therefore, the bold red line in

Fig. 6 separates the nonmetallic (left) from the metallic fluid (right) according to our extensive DFT-MD simulations and evaluations outlined in detail in Secs. III A to III E.

The IMT in solid helium from the *histogram* method in Ref. [32] intersects the melting line of Ref. [74] at a few tens of terapascals. Disorder as well as the movement of the atoms shift the metallization transition in the fluid toward lower pressures. Therefore our result for the IMT in the fluid with the *histogram* approach is consistent with the corresponding IMT of Ref. [32] in the solid. This agreement further increases our confidence in the *histogram* technique for the prediction of reliable BGs.

According to the *broadened* method, the BG closure occurs at lower densities than predicted by the *histogram* approach. This is expected as the BG of the *broadened* technique is smaller than that of the *histogram* method at high densities, see Fig. 2 and Ref. [54]. At lower pressures, however, the pressure difference between the BG closure as predicted by the two methods decreases.

Our result derived from the *broadened* approach (dotted lines) is quite similar to that of Ref. [34]. The origin of the different slopes for the BG closure curves is most likely due to the use of different XC functionals and numbers of atoms. We used PBE and at least 128 atoms, while Ref. [34] used PW91 and 64 atoms.

The BG closure according to the *histogram* method is located between the *HOMO-LUMO* results of Ref. [35] and our results using the *broadened* approach. This behavior is expected and reproduces the trends shown in Fig. 2.

Based on our results, we can infer consequences for the interior composition of astrophysical objects like gas giant planets, brown dwarfs, or the atmosphere of old and cool white dwarfs which contain large fractions of helium. For instance, the P - T conditions inside Jupiter [91], the largest gas giant planet in our Solar System, do not intersect our results for BG closure according to the *histogram* method (bold red line in Fig. 6) which we consider as most reliable. Therefore Jupiter probably does not contain metallic helium in its deep interior. Since hydrogen is metallic under these conditions [5,71], the consequences for H-He demixing, the solubility of heavier elements in H-He (core erosion), and its actual structure near the core have to be studied, see Refs. [7,92] for recent surveys. However, extrasolar gas giant planets that are larger and hotter than Jupiter (hot Jupiters) [93] reach more extreme P - T conditions in their interior and could, therefore, contain metallic helium. This has consequences for the calculation of their interior profiles, evolution scenarios, and magnetic field structure [3]. The brown dwarf KOI-889b intersects the metallization lines of all methods shown in Fig. 6 and therefore probably contains metallic helium in its deep interior. The representative white dwarf model [89] has a higher temperature than the scope of this study. However, unless the slope of the band gap closure lines changes drastically, this particular white dwarf should contain metallic helium.

The higher-order nature of the nonmetal-to-metal phase transition in dense fluid helium results in a continuous behavior of all properties under study. Around the *histogram* BG closure the DC conductivity fluctuates around 0.4×10^6 S/m, the reflectivity is within 30 to 40%, and the ionization degree

increases continuously from below 10% at the lowest density to more than 99% at the highest densities.

IV. CONCLUSION

We simulated dense fluid helium with DFT-MD simulations in order to investigate the metallization transition in detail. We were especially interested whether the metallization leads to a first-order phase transition as predicted earlier [26,27]. Hence, we calculated the EOS, the BG closure with different methods, the DC conductivity, the optical reflectivity, and the ionization degree from the DFT-MD simulations for a wide range of densities and temperatures. We found no indications for jumps or discontinuities in any of our results. In particular, the ionization calculated from the TRK sum rule method clearly shows a continuous transition to full ionization of 2.0, see Fig. 5. Therefore, we conclude that the metallization transition in dense fluid helium is driven by BG closure and continuous or of higher order, see Fig. 6.

The conventional DOS integration method for the calculation of the ionization degree did not capture pressure

ionization, contrary to the TRK sum rule method. We therefore recommend to use the TRK sum rule method for the calculation of the ionization degree in high-density plasmas where pressure ionization is significant.

In a future study, we will investigate whether the DC conductivity, the reflectivity, and the ionization degree obtained from the TRK sum rule can reproduce temperature ionization at densities below the scope of this study. It is known that the DOS integration method describes temperature ionization reasonably well, in contrast to the pressure ionization that we investigated in this study. We will also employ different XC functionals in order to study their influence on the evolution of the BG.

ACKNOWLEDGMENTS

We thank M. French, C. Kellermann, L. Stixrude, M. Schöttler, M. Bethkenhagen, and M. Schörner for helpful discussions. This work was supported by the North German Supercomputing Alliance (HLRN) and the ITMZ of the University of Rostock as well as by the Deutsche Forschungsgemeinschaft (DFG) via the Research Unit FOR 2440.

-
- [1] K. A. Olive, G. Steigman, and T. P. Walker, *Phys. Rep.* **333-334**, 389 (2000).
- [2] E. G. Adelberger, A. Garcia, R. G. Robertson, K. A. Snover, A. B. Balantekin, K. Heeger, M. J. Ramsey-Musolf, D. Bemmerer, A. Junghans, C. A. Bertulani, J. W. Chen, H. Costantini, P. Prati, M. Couder, E. Uberseder, M. Wiescher, R. Cyburt, B. Davids, S. J. Freedman, M. Gai, D. Gazit, L. Gialanella, G. Imbriani, U. Greife, M. Hass, W. C. Haxton, T. Itahashi, K. Kubodera, K. Langanke, D. Leitner, M. Leitner, P. Vetter, L. Winslow, L. E. Marcucci, T. Motobayashi, A. Mukhamedzhanov, R. E. Tribble, K. M. Nollett, F. M. Nunes, T. S. Park, P. D. Parker, R. Schiavilla, E. C. Simpson, C. Spitaleri, F. Strieder, H. P. Trautvetter, K. Suemmerer, and S. Typel, *Rev. Mod. Phys.* **83**, 195 (2011).
- [3] T. Gastine, J. Wicht, L. D. V. Duarte, M. Heimpel, and A. Becker, *Geophys. Res. Lett.* **41**, 5410 (2014).
- [4] H.-k. Mao and R. J. Hemley, *Rev. Mod. Phys.* **66**, 671 (1994).
- [5] J. M. McMahon, M. A. Morales, C. Pierleoni, and D. M. Ceperley, *Rev. Mod. Phys.* **84**, 1607 (2012).
- [6] A. Goncharov, *Low Temp. Phys.* **46**, 97 (2020).
- [7] R. Helled, G. Mazzola, and R. Redmer, *Nat. Rev. Phys.* **2**, 562 (2020).
- [8] K. F. Herzfeld, *Phys. Rev.* **29**, 701 (1927).
- [9] N. F. Mott, *Proc. Phys. Soc. A* **62**, 416 (1949).
- [10] P. P. Edwards, M. T. J. Lodge, F. Hensel, and R. Redmer, *Philos. Trans. R. Soc. A* **368**, 941 (2010).
- [11] E. Wigner and H. B. Huntington, *J. Chem. Phys.* **3**, 764 (1935).
- [12] P. Loubeyre, F. Occelli, and P. Dumas, *Nature (London)* **577**, 631 (2020).
- [13] S. T. Weir, A. C. Mitchell, and W. J. Nellis, *Phys. Rev. Lett.* **76**, 1860 (1996).
- [14] M. D. Knudson, M. P. Desjarlais, A. Becker, R. W. Lemke, K. R. Cochran, M. E. Savage, D. E. Bliss, T. R. Mattsson, and R. Redmer, *Science* **348**, 1455 (2015).
- [15] P. M. Celliers, M. Millot, S. Brygoo, R. S. McWilliams, D. E. Fratanduono, J. R. Rygg, A. F. Goncharov, P. Loubeyre, J. H. Eggert, J. L. Peterson, N. B. Meezan, S. Le Pape, G. W. Collins, R. Jeanloz, and R. J. Hemley, *Science* **361**, 677 (2018).
- [16] M. P. Desjarlais, M. D. Knudson, and R. Redmer, *Phys. Rev. B* **101**, 104101 (2020).
- [17] H. Y. Geng, Q. Wu, M. Marqués, and G. J. Ackland, *Phys. Rev. B* **100**, 134109 (2019).
- [18] V. Y. Ternovoi, A. S. Filimonov, A. A. Pyalling, V. B. Mintsev, and V. E. Fortov, *AIP Conf. Proc.*, **620**, 107 (2002).
- [19] A. Kietzmann, B. Holst, R. Redmer, M. P. Desjarlais, and T. R. Mattsson, *Phys. Rev. Lett.* **98**, 190602 (2007).
- [20] P. M. Celliers, P. Loubeyre, J. H. Eggert, S. Brygoo, R. S. McWilliams, D. G. Hicks, T. R. Boehly, R. Jeanloz, and G. W. Collins, *Phys. Rev. Lett.* **104**, 184503 (2010).
- [21] V. Fortov, *Thermodynamics and Equations of State for Matter* (World Scientific, Singapore, 2016).
- [22] C. A. T. Seldam, *Proc. Phys. Soc. Sect. A* **70**, 97 (1957).
- [23] L. N. Simcox and N. H. March, *Proc. Phys. Soc.* **80**, 830 (1962).
- [24] D. Brust, *Phys. Lett. A* **40**, 255 (1972).
- [25] D. A. Young, A. K. McMahan, and M. Ross, *Phys. Rev. B* **24**, 5119 (1981).
- [26] A. Förster, T. Kahlbaum, and W. Ebeling, *Laser Part. Beams* **10**, 253 (1992).
- [27] T. Kahlbaum and A. Förster, *Fluid Phase Equilib.* **76**, 71 (1992).
- [28] D. Saumon, G. Chabrier, and H. M. van Horn, *Astrophys. J. Suppl. Ser.* **99**, 713 (1995).
- [29] C. Winisdoerffer and G. Chabrier, *Phys. Rev. E* **71**, 026402 (2005).
- [30] S. A. Khairallah and B. Militzer, *Phys. Rev. Lett.* **101**, 106407 (2008).
- [31] L. Landau and J. Zeldovich, *Acta Physicochim. USSR* **18**, 194 (1943).

- [32] B. Monserrat, N. D. Drummond, C. J. Pickard, and R. J. Needs, *Phys. Rev. Lett.* **112**, 055504 (2014).
- [33] P. M. Kowalski, S. Mazevet, D. Saumon, and M. Challacombe, *Phys. Rev. B* **76**, 075112 (2007).
- [34] L. Stixrude and R. Jeanloz, *Proc. Natl. Acad. Sci. U.S.A.* **105**, 11071 (2008).
- [35] W. Zhang, Z. Li, Z. Fu, J. Dai, Q. Chen, and L. Cai, *Sci. Rep.* **7**, 41885 (2017).
- [36] J. Eggert, S. Brygoo, P. Loubeyre, R. S. McWilliams, P. M. Celliers, D. G. Hicks, T. R. Boehly, R. Jeanloz, and G. W. Collins, *Phys. Rev. Lett.* **100**, 124503 (2008).
- [37] R. S. McWilliams, D. A. Dalton, Z. Konôpková, M. F. Mahmood, and A. F. Goncharov, *Proc. Natl. Acad. Sci.* **112**, 7925 (2015).
- [38] M. Bethkenhagen, B. B. L. Witte, M. Schörner, G. Röpke, T. Döppner, D. Kraus, S. H. Glenzer, P. A. Sterne, and R. Redmer, *Phys. Rev. Research* **2**, 023260 (2020).
- [39] P. Hohenberg and W. Kohn, *Phys. Rev.* **136**, B864 (1964).
- [40] W. Kohn and L. J. Sham, *Phys. Rev.* **140**, A1133 (1965).
- [41] G. Kresse and J. Hafner, *Phys. Rev. B* **47**, 558 (1993).
- [42] G. Kresse and J. Hafner, *Phys. Rev. B* **49**, 14251 (1994).
- [43] G. Kresse and J. Furthmüller, *Phys. Rev. B* **54**, 11169 (1996).
- [44] G. Kresse and J. Furthmüller, *Comput. Mater. Sci.* **6**, 15 (1996).
- [45] J. Hafner, *J. Comput. Chem.* **29**, 2044 (2008).
- [46] M. Preising, W. Lorenzen, A. Becker, R. Redmer, M. D. Knudson, and M. P. Desjarlais, *Phys. Plasmas* **25**, 012706 (2018).
- [47] S. Nosé, *J. Chem. Phys.* **81**, 511 (1984).
- [48] S. Nosé, *Prog. Theor. Phys. Suppl.* **103**, 1 (1991).
- [49] D. M. Bylander and L. Kleinman, *Phys. Rev. B* **46**, 13756 (1992).
- [50] A. Baldereschi, *Phys. Rev. B* **7**, 5212 (1973).
- [51] H. J. Monkhorst and J. D. Pack, *Phys. Rev. B* **13**, 5188 (1976).
- [52] J. P. Perdew, K. Burke, and M. Ernzerhof, *Phys. Rev. Lett.* **77**, 3865 (1996).
- [53] P. E. Blöchl, *Phys. Rev. B* **50**, 17953 (1994).
- [54] See Supplemental Material at <http://link.aps.org/supplemental/10.1103/PhysRevB.102.224107> for an in-depth discussion of the calculation of the ionization degree, the band gap approaches and their convergence as well as the convergence of the EOS, the DC conductivity, the reflectivity, and the ionization degree.
- [55] F. Soubiran, S. Mazevet, C. Winisdoerffer, and G. Chabrier, *Phys. Rev. B* **86**, 115102 (2012).
- [56] R. Kubo, *J. Phys. Soc. Jpn.* **12**, 570 (1957).
- [57] D. A. Greenwood, *Proc. Phys. Soc.* **71**, 585 (1958).
- [58] M. Gajdoš, K. Hummer, G. Kresse, J. Furthmüller, and F. Bechstedt, *Phys. Rev. B* **73**, 045112 (2006).
- [59] B. Holst, M. French, and R. Redmer, *Phys. Rev. B* **83**, 235120 (2011).
- [60] M. French and R. Redmer, *Phys. Plasmas* **24**, 092306 (2017).
- [61] D. B. Melrose and R. C. McPhedran, *Electromagnetic Processes in Dispersive Media* (Cambridge University Press, Cambridge, 1991).
- [62] S. Mazevet, J. D. Kress, L. A. Collins, and P. Blottiau, *Phys. Rev. B* **67**, 054201 (2003).
- [63] S. Mazevet, M. P. Desjarlais, L. A. Collins, J. D. Kress, and N. H. Magee, *Phys. Rev. E* **71**, 016409 (2005).
- [64] S. M. Vinko, O. Ciricosta, and J. S. Wark, *Nat. Commun.* **5**, 3533 (2014).
- [65] S. X. Hu, *Phys. Rev. Lett.* **119**, 065001 (2017).
- [66] K. P. Driver, F. Soubiran, and B. Militzer, *Phys. Rev. E* **97**, 063207 (2018).
- [67] W. Thomas, *Naturwissenschaften* **13**, 627 (1925).
- [68] F. Reiche and W. Thomas, *Z. Phys.* **34**, 510 (1925).
- [69] W. Kuhn, *Z. Phys.* **33**, 408 (1925).
- [70] M. P. Desjarlais, J. D. Kress, and L. A. Collins, *Phys. Rev. E* **66**, 025401(R) (2002).
- [71] W. Lorenzen, B. Holst, and R. Redmer, *Phys. Rev. B* **82**, 195107 (2010).
- [72] W. Lorenzen, B. Holst, and R. Redmer, *Phys. Rev. B* **84**, 235109 (2011).
- [73] M. A. Morales, C. Pierleoni, E. Schwegler, and D. M. Ceperley, *Proc. Natl. Acad. Sci. U.S.A.* **107**, 12799 (2010).
- [74] M. Preising and R. Redmer, *Phys. Rev. B* **100**, 184107 (2019).
- [75] J. P. Perdew and Y. Wang, *Phys. Rev. B* **45**, 13244 (1992).
- [76] R. Redmer, *Phys. Rev. E* **59**, 1073 (1999).
- [77] S. Kuhlbrodt and R. Redmer, *Phys. Rev. E* **62**, 7191 (2000).
- [78] S. Kuhlbrodt, R. Redmer, H. Reinholz, G. Röpke, B. Holst, V. B. Mintsev, V. K. Gryaznov, N. S. Shilkin, and V. E. Fortov, *Contrib. Plasma Phys.* **45**, 61 (2005).
- [79] J. R. Adams, H. Reinholz, R. Redmer, V. B. Mintsev, N. S. Shilkin, and V. K. Gryaznov, *Phys. Rev. E* **76**, 036405 (2007).
- [80] S. Brygoo, M. Millot, P. Loubeyre, A. E. Lazicki, S. Hamel, T. Qi, P. M. Celliers, F. Coppari, J. H. Eggert, D. E. Fratanduono, D. G. Hicks, J. R. Rygg, R. F. Smith, D. C. Swift, G. W. Collins, and R. Jeanloz, *J. Appl. Phys.* **118**, 195901 (2015).
- [81] P. Loubeyre, R. LeToullec, J. P. Pinceaux, H. K. Mao, J. Hu, and R. J. Hemley, *Phys. Rev. Lett.* **71**, 2272 (1993).
- [82] J. S. Dugdale and D. K. C. MacDonald, *Phys. Rev.* **89**, 832 (1953).
- [83] R. K. Crawford and W. B. Daniels, *J. Chem. Phys.* **55**, 5651 (1971).
- [84] R. L. Mills, D. H. Liebenberg, and J. C. Bronson, *Phys. Rev. B* **21**, 5137 (1980).
- [85] P. Loubeyre, J. M. Besson, J. P. Pinceaux, and J. P. Hansen, *Phys. Rev. Lett.* **49**, 1172 (1982).
- [86] W. L. Vos, M. G. E. van Hinsberg, and J. A. Schouten, *Phys. Rev. B* **42**, 6106 (1990).
- [87] F. Datchi, P. Loubeyre, and R. Le Toullec, *Phys. Rev. B* **61**, 6535 (2000).
- [88] D. Santamaría-Pérez, G. D. Mukherjee, B. Schwager, and R. Boehler, *Phys. Rev. B* **81**, 214101 (2010).
- [89] E. Y. Chen and B. M. S. Hansen, *Mon. Not. R. Astron. Soc.* **413**, 2827 (2011).
- [90] A. Becker, M. Bethkenhagen, C. Kellermann, J. Wicht, and R. Redmer, *Astron. J.* **156**, 149 (2018).
- [91] W. B. Hubbard and B. Militzer, *Astrophys. J.* **820**, 80 (2016).
- [92] F. Debras and G. Chabrier, *Astrophys. J.* **872**, 100 (2019).
- [93] D. P. Thorngren and J. J. Fortney, *Astron. J.* **155**, 214 (2018).

4.4. Evaluation of exchange-correlation functionals with multiple-shock conductivity measurements in hydrogen and deuterium at the molecular-to-atomic transition

Author contributions

- M.K.** Preparation of the manuscript, all the calculations that are not concerning the DC conductivity and the band gaps.
- M.D.** Supervision of the project, calculations of the DC conductivity and the band gaps of deuterium.
- M.P.** Supervision of the project, calculations of the DC conductivity of hydrogen, the band gaps of hydrogen, and the density of states of hydrogen.
- R.R.** Supervision of the project, preparation of the manuscript.

Evaluation of exchange-correlation functionals with multiple-shock conductivity measurements in hydrogen and deuterium at the molecular-to-atomic transition

M. D. Knudson*

Institute for Shock Physics, Washington State University, Pullman, Washington 99164, USA

M. P. Desjarlais

Sandia National Laboratories, Albuquerque, New Mexico 87185-1195, USA

M. Preising and R. Redmer

Institute of Physics, University of Rostock, Rostock, Germany

(Received 16 August 2018; published 26 November 2018)

The temperature (T) and density (ρ) conditions at which hydrogen undergoes a molecular-to-atomic (MA) transition is crucial to our understanding of the gas-giant planets such as Jupiter and Saturn. First-principles (FP) calculations suggest that this transition is coincident with metallization and acts as a catalyst for hydrogen-helium demixing, which has significant consequences for models of planetary interiors. Prediction of this transition boundary has proven to be difficult using FP methods. In particular, detailed comparisons of finite temperature density functional theory (FT-DFT) calculations of the MA transition in both the high- T , low- ρ regime, where the transition is largely T driven, and the low- T , high- ρ regime, where the transition is largely ρ driven, suggest that the transition is very sensitive to the exchange-correlation (xc) functional used in the calculation. Here we present a detailed comparison of previous multiple-shock electrical conductivity measurements with FT-DFT calculations employing various xc functionals to probe a regime where both T and ρ play an important role in the transition. The measurement results are found to be inconsistent with the semilocal xc functional PBE and are in much better agreement with the nonlocal xc functionals vdW-DF1 and vdW-DF2. Furthermore, we show that the inconsistency with PBE likely stems from pressure errors associated with the PBE xc functional, resulting in calculated pressures that are too low at these T and ρ conditions. Together with previous comparisons at high- T , low- ρ and low- T , high- ρ these results provide a consistent picture for the MA transition over a wide T and ρ range. This picture may also provide insight into differences in experimental observations of the metallization of liquid hydrogen and deuterium in the low- T regime.

DOI: [10.1103/PhysRevB.98.174110](https://doi.org/10.1103/PhysRevB.98.174110)

I. INTRODUCTION

The question of precisely how and at what pressure (P) hydrogen metallizes at low temperature (T) has become one of the longest-standing open questions of high-pressure physics [1]. Also of great interest, due to its relevance to planetary science [2,3], is the analogous molecular insulator to atomic metal transition in the liquid at low T , just above the melt boundary. First-principles (FP) calculations suggest that hydrogen metallization is coincident with a molecular-to-atomic (MA) transition and acts as a catalyst for hydrogen-helium demixing [4]. Thus the location of the MA transition in the low- T liquid could provide a constraint for the low- P boundary of the region of hydrogen-helium immiscibility and justification for the presence of a layer boundary in the interior of gas-giant planets, a necessary feature of the often-used three-layer model [5], which has shown reasonable success in describing observables of Jupiter and Saturn [6].

Hydrogen, as one of the simplest elemental systems, has also been a model system in the development of advanced FP simulation techniques including finite temperature density functional theory (FT-DFT) and quantum Monte Carlo (QMC) methods [1]. However, prediction of the MA transition using FP methods has proven to be very sensitive to the framework used. Recent work [7] comparing FT-DFT methods to the deuterium Hugoniot—the locus of end states achievable through compression by large amplitude shock waves—concluded that no one exchange-correlation (xc) functional adequately describes the MA transition. In this high- T (~ 5 – 10 kK), low-density (ρ) regime where dissociation is largely T driven the P onset of the MA transition, as evidenced by first-shock ρ and reshock P measurements, is underestimated by the semilocal xc functional PBE [8] and is best described by nonlocal functionals, such as vdW-DF1 [9] and vdW-DF2 [10]. However, the P width over which dissociation occurs is likely overestimated by these vdW functionals and is in better agreement with PBE.

Differences between functionals become even more pronounced in the low- T (~ 1 – 2 kK), high- ρ regime where the MA transition appears to be largely ρ driven. In this regime the predicted transition P and ρ are extremely sensitive to

*Present address: Sandia National Laboratories, Albuquerque, New Mexico 87185-1195, USA; mdknuds@sandia.gov

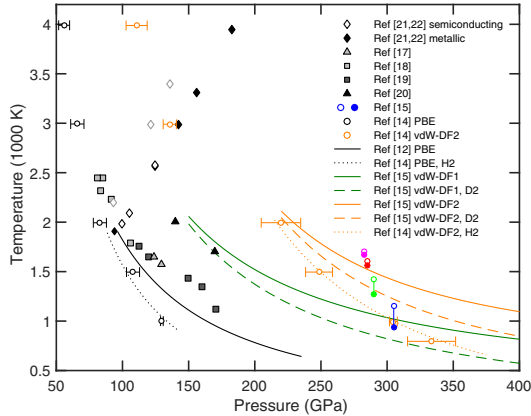


FIG. 1. T - P phase diagram showing experimental and theoretical estimates for the metallization of hydrogen/deuterium. Experiment: open (closed) diamonds [21,22], semiconducting (metallic) states from multiple-shock experiments with corrected T (see Sec. II); gray triangle [17], gray square [18], black square [19], and black triangle [20], static high- P and pulsed heated experiments; colored open and closed circles [15], dynamic compression experiments. Theory: open black (orange) circles [14], calculations of $\sigma = 2000$ ($\Omega \text{ cm}$) $^{-1}$ for PBE (vdW-DF2) with nuclear (hydrogen) treatment for the ions; solid [12] and dotted [14] black lines, first-order MA transition boundary for PBE with classical and nuclear (hydrogen) treatment for the ions, respectively; solid and dashed green lines [15], transition boundary for vdW-DF1 with classical and nuclear (deuterium) treatment for the ions, respectively; solid [15], dotted [14], and dashed [15] orange lines, transition boundary for vdW-DF2 with classical, nuclear (hydrogen), and nuclear (deuterium) treatment of the ions, respectively.

the xc functional. For PBE, vdW-DF1, and vdW-DF2 the predicted transition P differs by ~ 200 – 300 GPa (see Fig. 1) and the ρ at the transition ranges from ~ 0.75 – 1.2 g/cm 3 for hydrogen and ~ 1.5 – 2.4 g/cm 3 for deuterium [11–15]. Experimental determination of the MA transition in this regime also spans a large range in P . Dynamic compression experiments [15] on liquid deuterium in the ~ 1 – 2 kK regime performed at the Sandia Z machine [16] revealed an abrupt MA transition, as evidenced by a sudden increase in reflectivity between ~ 280 and 305 GPa, in reasonable agreement with the nonlocal vdW-DF2 xc functional. Static high- P and pulsed heated experiments [17–20] on hydrogen and deuterium in a similar T regime suggest the MA transition occurs at ~ 75 to 170 GPa, based on observation of T plateaus in the heating curves and increases in reflectivity, seemingly in better agreement with the semilocal xc functional PBE.

The first experiments [21,22] to address the MA transition in liquid hydrogen and deuterium were performed roughly 20 years ago using gas-gun techniques. In that study multiple-shock compression, achieved through a wave reverberation technique, was used to attain successively higher P and T states in liquid hydrogen and deuterium. Measurement of the electrical conductivity (σ) in the peak state revealed saturation at ~ 2000 ($\Omega \text{ cm}$) $^{-1}$, a value consistent with minimum

metallic conductivity, at a P of ~ 140 GPa and an estimated T of ~ 2600 K. This set of experiments provides another very good test of FP methods in a regime in which both T and ρ (or P) play an important role in the MA transition. However, while indirect comparisons between the measured σ and FP calculations have been made, to the best of our knowledge no one has performed a detailed comparison of these experimental results with FP calculations.

Here we present a detailed comparison of the measured σ from multiple-shock compression experiments [21,22] with FT-DFT calculations using both semilocal (PBE) and nonlocal (vdW-DF1 and vdW-DF2) xc functionals. We show that the measured results are inconsistent with PBE predictions. Similar to both the T -driven and ρ -driven regime, PBE appears to underestimate the P conditions necessary for dissociation. In contrast, the MA transition appears to be better described by the vdW xc functionals. Furthermore, we show that the inconsistency with PBE likely stems from P errors associated with the PBE xc functional, resulting in calculated P that are too low at these T and ρ conditions. These results, along with the previous studies comparing the various xc functionals in the T -driven [7] and ρ -driven [15] regimes, provide a consistent picture for the MA transition over a wide P and T range and raise questions about the recent static high- P and pulsed heated studies [17–20] that appear to be in agreement with predictions from PBE.

Section II summarizes the multiple-shock experiments [21,22] and includes a reanalysis of the results. The original study included inconsistencies in both the inferred T states reached and in the fit to a semiconductor model used to interpret the measured σ . Correction of both of these inconsistencies is important with respect to comparisons with the FP calculations. Section III describes the FT-DFT calculations performed to determine σ and the energy gap for the various xc functionals and compares these with the experimental measurements. The results are discussed in Sec. IV. The main findings are summarized in Sec. V.

II. REANALYSIS OF MULTIPLE-SHOCK CONDUCTIVITY EXPERIMENTS

The first experiments [21,22] to address the MA transition in hydrogen and deuterium were performed roughly 20 years ago by Nellis, Weir, and Mitchell (NWM) using gas-gun techniques. A layer of liquid hydrogen or deuterium was compressed by multiple shocks using a wave reverberation technique; this minimized the entropy increase, thereby minimizing the temperature (T) in the peak state. The sample was contained within a cell between two sapphire anvils and cooled to cryogenic temperatures. The sample cell was impacted by a metal anvil (either aluminum or copper) resulting in a strong shock wave that reverberated between the relatively stiff sapphire anvils, driving the sample to high pressure (P) and density (ρ) and relatively low T . The impact velocity (v_f) was measured using a flash x-ray technique [23]. The peak P of the sample was determined from the known equations of state (EOS) of aluminum, copper, and sapphire and the measured v_f (in the reverberation configuration the peak P is only a function of the confining anvils and does not depend upon the EOS of hydrogen or deuterium). The electrical

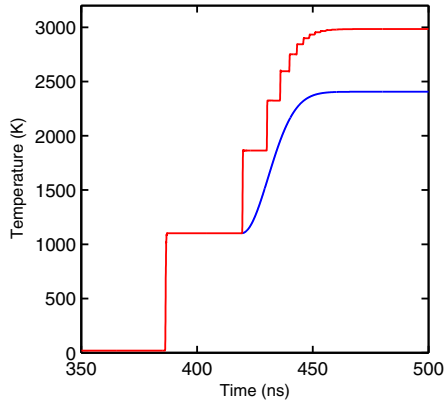


FIG. 2. Comparison of the two methods used by NWM to infer T in the multiple-shock experiments on hydrogen and deuterium. Red line: hydrodynamic simulation accounting for the full multiple-shock nature of the experiment (in this case SLDMS12- H_2). Blue line: hydrodynamic simulation with the same magnitude first shock followed by ramp compression to the same peak P (in this case 142 GPa). Both simulations used the Kerley03 [28] EOS for hydrogen (a modern revision of the Kerley [24] EOS used by NWM).

conductivity (σ) was measured at the peak state using either a constant-voltage, two-probe method [$\sigma < 10 (\Omega \text{ cm})^{-1}$] or a constant-current, four-probe method [$\sigma > 10 (\Omega \text{ cm})^{-1}$]. We note that v_f and σ were the only quantities measured in these experiments.

To estimate the T and ρ of the sample in the peak state two different EOS models for hydrogen and deuterium were considered; a tabular EOS denoted as Kerley [24] and an analytical EOS denoted as Ross [25–27]. Because only one of these EOS models (Kerley) was in a tabular format, conducive for use in hydrodynamic simulations, two different methods were used to infer T and ρ ; these two methods were described by NWM as being different but equivalent. Method 1, used for the Kerley EOS, inferred T and ρ from hydrodynamic simulations of the impact experiments and therefore fully accounted for the multiple-shock nature of the experiments. Method 2, used for the Ross EOS, inferred T and ρ by determining $T(P_{\text{max}})$ and $\rho(P_{\text{max}})$ along an isentropie centered at the first shocked state of the hydrogen or deuterium (P_1 , T_1 , and ρ_1), where P_{max} was the peak P reached in the experiment. In other words, method 2 only accounted for the entropy increase due to the first shock and treated the subsequent compression as isentropic.

These two methods are, in fact, not equivalent; method 2 fails to account for the non-negligible increase in entropy that results from the subsequent shocks during the reverberation. The difference in these two methods is illustrated in Fig. 2, which shows two different hydrodynamic simulations using the same EOS for hydrogen, Kerley03 [28], a modern revision of the Kerley EOS used by NWM. The red line represents a simulation accounting for the full multiple-shock nature of the experiment (method 1). The blue line represents a simulation with the same magnitude first shock followed by ramp compression to the same peak P (method 2). In these simulations

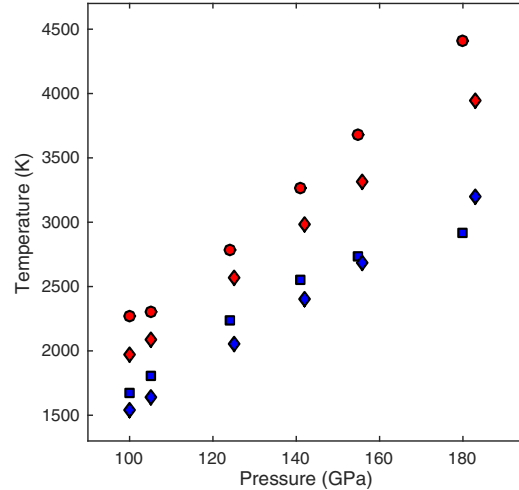


FIG. 3. Comparison of the inferred T for the NWM hydrogen experiments. The colors and symbols denote the method used to infer T and the EOS model, respectively: Red and blue correspond to method 1 and 2, respectively; squares, circles, and diamonds correspond to the Ross [25–27], Kerley [24], and Kerley03 [28] EOS, respectively.

EOS models 3325 [29,30], 3700 [31,32], and 7411 [33] were used to model copper, aluminum, and sapphire, respectively. As can be seen in the figure, T in the peak state for these two simulations differs by over 500 K. This is completely explained by the difference in entropy of the final states for the two different methods used by NWM. As a result, the T in the peak states inferred by NWM using the Kerley EOS with method 1 and the Ross EOS with method 2 were considerably different.

The differences in inferred T for the subset of hydrogen experiments performed by NWM are shown graphically in Fig. 3 and listed in Table I. The colors and symbols denote the method used to infer T and the EOS model, respectively: Red and blue correspond to method 1 and 2, respectively; squares, circles, and diamonds correspond to the Ross, Kerley, and Kerley03 EOS, respectively. As can be seen in Fig. 3 the largest difference in inferred T is due to the method used, not the EOS model. In particular, the red and blue diamonds represent inferred T for the same EOS model (Kerley03) using the two different methods outlined above. The T difference ranges from ~ 440 – 750 K (~ 20 – 30%) with an average T difference of ~ 550 K over the entire P range. In contrast, differences in inferred T between various models for the same calculation method are noticeably smaller.

NWM interpreted the large T difference arising from the two calculation methods as being due to differences in the Kerley and Ross EOS models with respect to dissociation. They concluded that the Kerley EOS neglected dissociation at the conditions reached in their experiments and therefore resulted in higher inferred T as compared to the Ross EOS. They therefore chose to use the T and ρ values inferred from the Ross EOS (using method 2) to estimate the states reached

TABLE I. Inferred P , T , and ρ states reached in the multiple-shock experiments [21,22] on hydrogen and deuterium performed by NWM. The first four columns list the experiment designation, impactor material, measured impact velocity, and measured σ , respectively. The subsequent columns list the inferred P , T , and ρ reported by NWM (using the Ross EOS and method 2) and the inferred P , T , and ρ obtained using method 1 and the Kerley03 [28] and Saumon [34] EOS. The subsequent analysis performed in this work uses the values inferred from the Kerley03 EOS.

Experiment	Impactor	v_f (km/s)	σ ($\Omega \text{ cm}^{-1}$)	NWM			Kerley03			Saumon		
				P (GPa)	T (K)	ρ (g/cm^3)	P (GPa)	T (K)	ρ (g/cm^3)	P (GPa)	T (K)	ρ (g/cm^3)
SLDMS4-D ₂	Aluminum	5.59	0.71	93	2090	1.17	93	2204	1.25	93	2197	1.26
SLDMS5-D ₂	Aluminum	6.76	77	121	2760	1.29	121	2987	1.38	121	2998	1.39
SLDMS8-D ₂	Aluminum	7.33	417	135	3090	1.35	136	3397	1.44	136	3476	1.45
SLDMS6-H ₂	Aluminum	5.90	2.6	100	1670	0.61	100	1978	0.64	100	1867	0.66
SLDMS13-H ₂	Aluminum	6.10	7.1	105	1810	0.62	105	2093	0.66	105	1976	0.67
SLDMS7-H ₂	Aluminum	6.90	135	124	2230	0.66	125	2567	0.70	125	2430	0.72
SLDMS9-H ₂	Aluminum	6.91	313	124	2230	0.66	125	2573	0.70	125	2436	0.72
SLDMS12-H ₂	Copper	5.58	2380	141	2560	0.69	142	2984	0.73	142	2889	0.76
SLDMS10-H ₂	Copper	5.96	1670	155	2730	0.72	156	3310	0.76	156	3253	0.79
SLDMS11-H ₂	Copper	6.65	2000	180	2910	0.77	183	3951	0.81	183	3848	0.84

in their experiments. However, due to the error in method 2, these conditions do not accurately reflect the T states reached. We contend that the T obtained by method 1 using the Kerley03 EOS are a better representation. We note that a similar analysis performed with a revised EOS for hydrogen and deuterium by Saumon [34] resulted in very similar T and ρ states (see Table I), lending confidence in these inferred values. Also, we note that Kerley03 is a widely-used EOS model and was used to infer T and ρ (along with the vdW-DF2 xc functional) in the low- T , high- ρ metallization study [15]. Finally, we acknowledge that EOS models based on FT-DFT calculations are available [35,36]. However, at the P , T , and ρ conditions relevant here these models rely primarily on FT-DFT calculations using the PBE [8] xc functional. As shown here and elsewhere [1,7], PBE systematically underestimates the P conditions necessary for dissociation, which can result in isentropes that exhibit $-dT/dP$ at P below where saturation in σ was observed in the NWM experiments. Perhaps even more problematic, we show in Sec. IV that PBE exhibits P errors that results in a calculated P that is too low at a given T and ρ condition, or equivalently, a ρ that is too high at a given P and T condition. For these reasons we do not consider these PBE based EOS tables in estimating the conditions reached in the NWM experiments.

To infer an energy gap as a function of ρ from their measurements of σ , NWM appealed to a simplified semiconductor model. The data were fit to

$$\sigma = \sigma_0 \exp[-E_g(\rho)/2k_B T], \quad (1)$$

where σ_0 is the limiting value of conductivity, k_B is Boltzmann's constant, and $E_g(\rho)$ is the energy gap, assumed to be linear in ρ and independent of T . The result of a least-squares fit was reported to be

$$E_g(\rho) = 20 - 62.6\rho, \quad (2)$$

where E_g is in units of eV, ρ is the molar density in units of mol/cm^3 , and $\sigma_0 = 90 (\Omega \text{ cm})^{-1}$. NWM suggested this fit was reasonable, noting that a value of $\sigma_0 = 200\text{--}300 (\Omega \text{ cm})^{-1}$ is typical of liquid semiconductors.

However, this value for the limiting conductivity requires a negative energy gap to reproduce the measured σ for molar densities above $\sim 0.32 \text{ mol/cm}^3$ (using the Ross EOS and method 2 to infer ρ), which is inconsistent with the requirement that $E_g \geq 0$. If one uses the same model but instead constrains σ_0 to be the average of the measured σ at saturation, $\sigma_0 = 1850 (\Omega \text{ cm})^{-1}$, a physically reasonable result is obtained. In this case

$$E_g(\rho) = 18.3 - 49.8\rho \quad (3)$$

and the gap closes at $\sim 0.37 \text{ mol/cm}^3$ (using the Kerley03 EOS and method 1 to infer ρ), consistent with the observed saturation in σ .

These two fits are displayed graphically in Fig. 4(a). The black and gray circles are the energy gap values obtained from Eq. (1) using the T and ρ values inferred from the Ross EOS using method 2 and the T and ρ values inferred from the Kerley03 EOS using method 1, respectively. The dashed and solid black lines are the corresponding fits [Eq. (2) and Eq. (3), respectively]. The dashed gray line denotes the temperature of the system in eV ($k_B T$ as a function of ρ). This figure clearly shows the inconsistent behavior that arises from setting the limiting conductivity value at $\sigma_0 = 90 (\Omega \text{ cm})^{-1}$. The estimated energy gap reaches a value equal to $(k_B T)$ at $\sim 0.32 \text{ mol/cm}^3$, significantly lower than the ρ at which a minimum metallic conductivity was reached in the experiments. In order to match the measured σ at higher ρ a negative energy gap is required. The more reasonable value of $\sigma_0 = 1850 (\Omega \text{ cm})^{-1}$ results in an energy gap that is systematically larger by ~ 2 eV, reaching zero at $\sim 0.37 \text{ mol/cm}^3$, in agreement with observations.

We note that ρ was not measured in the experiments performed by NWM; the quantity in the peak state that was most tightly constrained is the peak P . We therefore also considered the inferred energy gap as a function of P , as shown in Fig. 4(b). Again, the estimated energy gap using the T and ρ values inferred by NWM using $\sigma_0 = 90 (\Omega \text{ cm})^{-1}$ is systematically low, reaching a value equal to $(k_B T)$ at ~ 120 GPa, roughly 20 GPa lower than the P at which a minimum

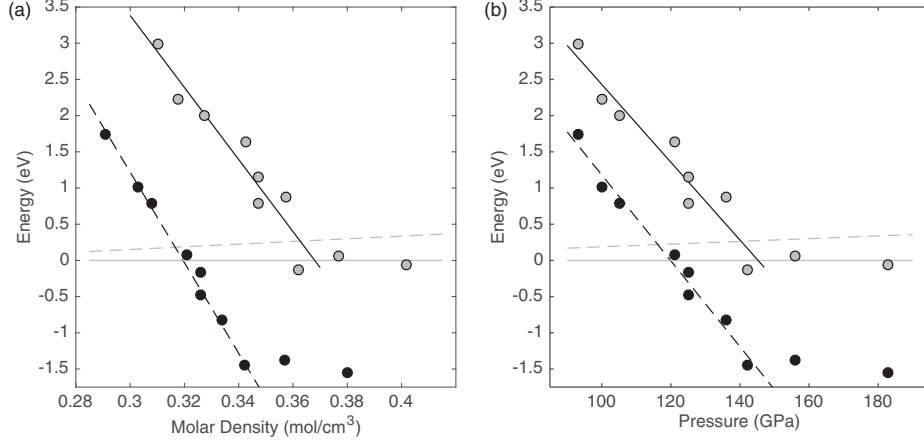


FIG. 4. Energy gap as a function of (a) molar density and (b) P . The black and gray circles are the energy gap values obtained from Eq. (1) using $\sigma_0 = 90 \text{ } (\Omega \text{ cm})^{-1}$ with T and ρ values inferred from the Ross [25–27] EOS using method 2 and those obtained from Eq. (1) using $\sigma_0 = 1850 \text{ } (\Omega \text{ cm})^{-1}$ with T and ρ values inferred from the Kerley03 [28] EOS using method 1, respectively. The dashed and solid black lines are the corresponding fits [Eq. (2) and Eq. (3), respectively]. The dashed gray line denotes the temperature of the system in eV ($k_B T$ as a function of ρ or P).

metallic conductivity was reached in the experiments. However, because of the difference in inferred ρ between the Ross and Kerley03 EOS, the systematic difference in the energy gap when viewed as a function of P is ~ 1 eV. Thus the error in the NWM fit to the semiconductor model [with $\sigma_0 = 90 \text{ } (\Omega \text{ cm})^{-1}$] underestimates the energy gap by ~ 1 eV as a function of P as compared to the same semiconductor model with a more reasonable value of σ_0 . In the subsequent section we will compare the results of first-principles simulations to this semiconductor model.

III. COMPARISON WITH FIRST-PRINCIPLES CALCULATIONS

First-principles (FP) calculations of the electrical conductivity (σ) and the energy gap at conditions consistent with the multiple-shock compression experiments [21,22] performed by NWM were carried out within the framework of finite temperature density functional theory (FT-DFT). Both semilocal (PBE [8]) and nonlocal (vdW-DF1 [9] and vdW-DF2 [10]) exchange and correlation (xc) functionals were considered. FP molecular dynamics simulations were performed using the Vienna *ab initio* simulation package (VASP), a plane-wave DFT code developed at the Technical University of Vienna [37–39]. The density was fixed by the total volume of the cubic supercell and the ion temperature was regulated with a Nosé-Hoover thermostat [40–42]. A total 256 atoms were included in the supercell, with a plane-wave cutoff energy of 1200 eV. Simulations were performed in the canonical ensemble and typically covered a few to several picoseconds of real time. The thermodynamic quantities were taken as averages over an equilibrated portion of the cumulative averages.

The electrical conductivity was calculated by averaging over 40 randomly selected snapshots for a given temperature (T) and density (ρ) configuration using the Kubo-Greenwood

[43,44] formula

$$\sigma(\omega) = \frac{2\pi e^2}{3Vm_c^2\omega} \sum_{\mathbf{k}\nu\mu} |(\mathbf{k}\nu|\hat{\mathbf{p}}|\mathbf{k}\mu)|^2 (f_{\mathbf{k}\nu} - f_{\mathbf{k}\mu}) \delta(E_{\mathbf{k}\mu} - E_{\mathbf{k}\nu} - \hbar\omega), \quad (4)$$

where ω is the frequency, V is the volume of the supercell, e and m_e are the charge and mass of electrons, respectively, and $f_{\mathbf{k}\mu}$ is the Fermi occupation number for a given temperature. The eigenvalues $E_{\mathbf{k}\mu}$ for the Bloch states $|\mathbf{k}\mu\rangle$ are computed within each step of the FT-DFT simulation so that the dipole matrix elements $(\mathbf{k}\nu|\hat{\mathbf{p}}|\mathbf{k}\mu)$ are determined with the momentum operator. The imaginary part of the electrical conductivity can be obtained from a Kramers-Kronig transformation. For these calculations the Brillouin zone was sampled by a $5 \times 5 \times 5$ Monkhorst-Pack \mathbf{k} -point grid [45].

The density of states (DOS) was obtained from the same set of 40 randomly selected snapshots. For each given T and ρ configuration a histogram of the eigenvalues of the band energies was created from the collection of snapshots and smoothed with a gaussian of width 0.2 eV. The energy gaps were extracted directly from the simulations. For each time step eigenvalues in the vicinity of the fermi energy were extracted. These eigenvalues were then averaged. The energy gap was obtained from the energy difference of the averaged eigenvalues. The precision to which the energy gap can be directly computed from the simulations is set by the local separation of eigenvalue energies on either side of the gap. Eigenvalue averages for adjacent eigenstates indicate these local differences to be ~ 0.15 eV; states with energy gap values on the order of 0.15 eV or less were assumed to have a closed gap and the energy gap was set to zero.

As described in Sec. II, the measured quantities in the multiple-shock experiments of NWM were the impact velocity (v_f) and σ . The peak P in the experiment was

TABLE II. Predicted σ from various xc functionals for the estimated P , T , and ρ states reached in the multiple-shock experiments [21,22] on hydrogen and deuterium performed by NWM. The first two columns list the experimental designation and the measured σ , respectively. The next three columns list the T , P , and ρ states reached as inferred using the Kerley03 [28] EOS. The subsequent columns list the predicted σ and ρ at the inferred P and T for the PBE, vdW-DF1, and vdW-DF2 xc functionals.

Experiment	σ ($\Omega \text{ cm}^{-1}$) ⁻¹	Kerley03			PBE		DF1		DF2	
		P (GPa)	T (K)	ρ (g/cm ³)	σ ($\Omega \text{ cm}^{-1}$) ⁻¹	ρ (g/cm ³)	σ ($\Omega \text{ cm}^{-1}$) ⁻¹	ρ (g/cm ³)	σ ($\Omega \text{ cm}^{-1}$) ⁻¹	ρ (g/cm ³)
SLDMS4-D ₂	0.71	93	2204	1.25	4989	1.397	1.99	1.249	0.30	1.222
SLDMS5-D ₂	77	121	2987	1.38	8919	1.534	4518	1.437	493	1.359
SLDMS8-D ₂	417	136	3397	1.44	9970	1.589	5461	1.514	3234	1.455
SLDMS6-H ₂	2.6	100	1978	0.64	3456	0.710	0.62	0.641	0.11	0.624
SLDMS13-H ₂	7.1	105	2093	0.66	4990	0.729	2.32	0.652	0.35	0.636
SLDMS7-H ₂	135	125	2567	0.70	9034	0.780	1546	0.722	16.2	0.683
SLDMS9-H ₂	313	125	2573	0.70	9034	0.781	1546	0.722	16.2	0.683
SLDMS12-H ₂	2380	142	2984	0.73	10410	0.816	5671	0.777	1693	0.737
SLDMS10-H ₂	1670	156	3310	0.76	11290	0.840	7061	0.807	3880	0.774
SLDMS11-H ₂	2000	183	3951	0.81	13180	0.881	8907	0.854	6551	0.827

determined from the measured v_f and the known EOS of the impactor (copper or aluminum), baseplate (aluminum), and anvils (sapphire). In the reverberation geometry used in these experiments the P in the peak state is independent of the EOS of hydrogen or deuterium and is therefore well constrained. In contrast, T and ρ in the peak state are calculated and are therefore dependent upon the particular model used for hydrogen or deuterium. For the reasons discussed in Sec. II, we used the Kerley03 [28] EOS to estimate the T and ρ conditions at the corresponding peak P (see Table II).

To perform a detailed comparison of the NWM experiments with FP calculations we first had to determine how best to equate the peak state of the system. In general, the EOS surfaces of different models are not coincident. Thus, in comparing two models one can only match two of the three variables P , T , and ρ that define a particular state of

the system. Since the peak P in these experiments does not depend upon the hydrogen or deuterium EOS, P is an obvious choice for one of the variables to equate. The second variable to equate is less obvious. However, in exploring the EOS surface it was found that in this P , T , and ρ regime P depends much more strongly on ρ than T . For example, at ~ 100 GPa a $\sim 10\%$ increase in P required only a $\sim 5\%$ increase in ρ , while the same increase in P required roughly a factor of two increase in T . Thus for the comparisons presented here, T is a more appropriate second variable to equate than ρ . We therefore chose to fix the T in the FT-DFT simulations and vary the ρ until the experimentally inferred P was reached.

The resulting P , T , and ρ states obtained in this way using PBE, vdW-DF1, and vdW-DF2 xc functionals are listed in Table II (for each functional P and T are the same as those listed under Kerley03). As expected, systematic differences

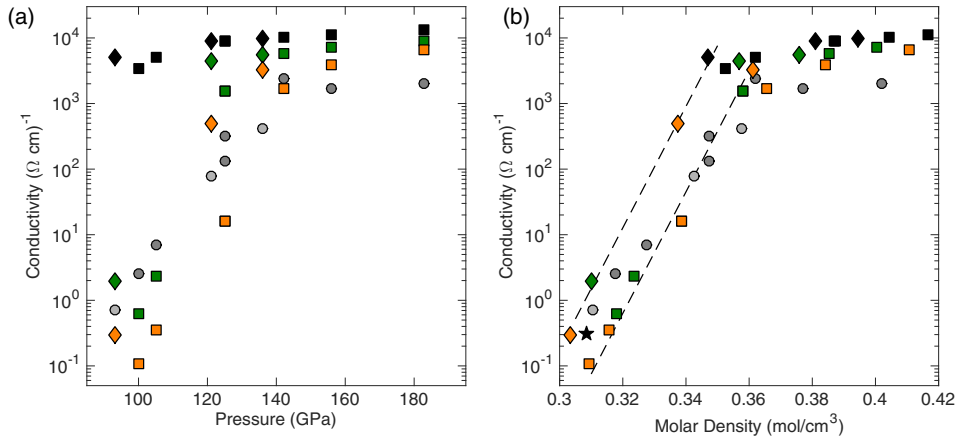


FIG. 5. Conductivity as a function of (a) P and (b) molar density. Dark (light) gray circles, measured [21,22] σ for hydrogen (deuterium). Black, green, and orange squares (diamonds), calculated σ of hydrogen (deuterium) using PBE [8], vdW-DF1 [9], and vdW-DF2 [10] xc functionals, respectively, at the conditions listed in Table II. The black star is an additional calculated conductivity using PBE at a lower molar density described in Sec. IV. Dashed lines in (b) are guides to the eye that are offset by one order of magnitude in σ .

in the inferred ρ were observed. In particular, the ρ inferred using the PBE xc functional were found to be significantly larger ($\sim 9\text{--}12\%$) than the values obtained from Kerley03. In contrast, both of the nonlocal vdW xc functionals resulted in ρ values that were in better agreement with the Kerley03 EOS. For both functionals the ρ was found to be lower than Kerley03 at low P (-0.1% and -2.2% for vdW-DF1 and vdW-DF2, respectively) and higher than Kerley03 at high P ($+5.4\%$ and $+2.1\%$ for vdW-DF1 and vdW-DF2, respectively). These ρ differences and their effect on the calculated σ will be discussed in more detail in the next section.

The calculated σ for the various xc functionals at these P , T , and ρ conditions are listed in Table II and plotted as a function of P in Fig. 5(a). This comparison suggests that PBE significantly overestimates σ in this P , T , and ρ regime. In particular, calculations using the PBE xc functional predict that a minimum metallic conductivity should have been observed in all experiments performed by NWM. In contrast, the overall trend of the experimental data is captured reasonably well by the two nonlocal vdW functionals. However, when σ is plotted as a function of molar density, as in Fig. 5(b), all three functionals appear to adequately reproduce the experimental results. In particular, the predicted σ for the two sets of calculations (hydrogen and deuterium) collapse onto linear trend lines in $\log(\sigma)$ vs ρ (dashed lines in Fig. 5). These trend lines are systematically offset by one order of magnitude in σ . We note that given the higher shock impedance of deuterium, those experiments reached ~ 400 K higher T at a similar P and molar density as compared to hydrogen. These isotopic differences will be explored further in the next section.

Similar behavior is exhibited in the inferred energy gaps extracted from FP calculations of the DOS. Figure 6 shows the calculated DOS for the conditions reached in the subset of hydrogen experiments performed by NWM. Energy gap values obtained for the various xc functionals at the T and ρ conditions listed in Table II are plotted in Fig. 7 as functions of both P and molar density. Also shown in the figure for reference are the inferred energy gap values obtained from the measured σ using Eq. (1) with $\sigma_0 = 1850$ ($\Omega\text{ cm})^{-1}$ and the T and ρ values inferred from the Kerley03 EOS. As was the case for σ , PBE appears to significantly underestimate the energy gap in this P , T , and ρ regime, while the nonlocal vdW functionals are in reasonable agreement with the energy gap values inferred from the simple semiconductor model described in Sec. II. However, again, when viewed as a function of molar density, all three functionals appear to exhibit very similar results; the extracted energy gaps for the two sets of calculations (hydrogen and deuterium) collapse onto linear trend lines (dashed lines in Fig. 7). These trend lines are offset in energy, with the deuterium trend line being systematically ~ 1 eV lower than that of hydrogen. Again, these isotopic differences will be explored further in the next section.

IV. DISCUSSION

The comparisons shown in Figs. 5 and 7 suggest that the most important parameter in determining the location of the MA transition for the various xc functionals is the molar density, at least in this P , T , and ρ regime. Given this

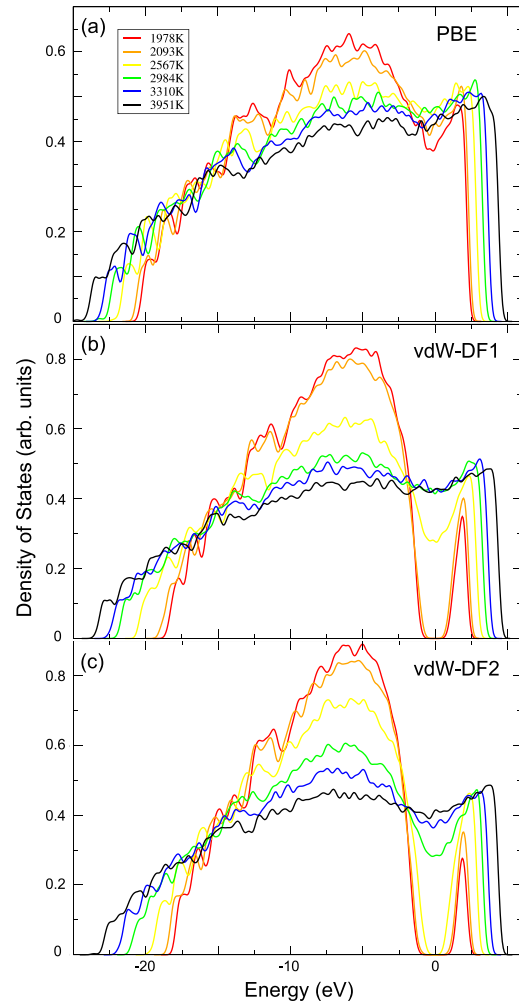


FIG. 6. Density of states extracted from FP calculations for (a) PBE, (b) vdW-DF1, and (c) vdW-DF2 at the P , T , and ρ conditions (listed in Table II) reached in the multiple-shock experiments [21,22] on hydrogen performed by NWM.

observation, and the significantly larger ρ predicted by PBE at the P and T conditions considered here, one must ask the question whether the comparison of the NWM experiments with PBE is biased by our choice to equate the P and T in the peak state as opposed to the P and ρ . To investigate this we performed several more FP calculations of experiment SLDMS13- H_2 (one of the lower P hydrogen experiments) using the PBE xc functional.

Fixing the T and ρ at 2093 K and 0.66 g/cm^3 (conditions estimated by the Kerley03 EOS) results in a P of 88 GPa for the PBE xc functional, $\sim 16\%$ lower than the experimentally inferred P of 105 GPa. An increase of $\sim 10\%$

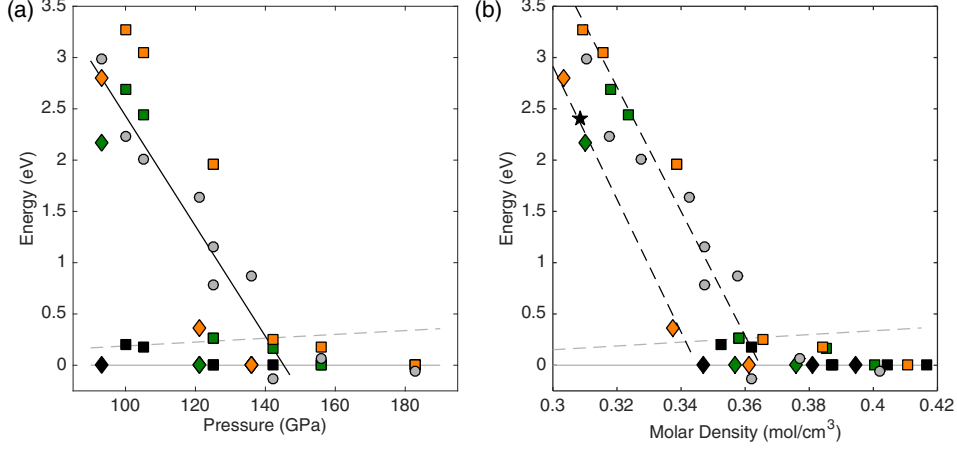


FIG. 7. Energy gap as a function of (a) P and (b) molar density. The gray circles are the energy gap values obtained from Eq. (1) using $\sigma_0 = 1850$ ($\Omega \text{ cm}$) $^{-1}$ with the T and ρ values inferred from the Kerley03 [28] EOS (see Table II). The dashed gray line denotes the temperature of the system in eV ($k_B T$ as a function of P or ρ); the solid black line is a fit to data where the inferred gap was greater than the temperature of the system. Black, green, and orange squares (diamonds), calculated energy gap of hydrogen (deuterium) using PBE [8], vdW-DF1 [9], and vdW-DF2 [10] xc functionals, respectively, at the conditions listed in Table II. The black star is an additional calculated energy gap using PBE at a lower molar density described in Sec. IV. Dashed lines in (b) are guides to the eye and indicate an offset of ~ 1 eV between hydrogen and deuterium.

in ρ (to 0.729 g/cm^3) was required to increase the P to 105 GPa. These were the P , T , and ρ values used in the calculations described in the previous section (see Table II). Here, we instead fixed the ρ at 0.66 g/cm^3 and varied the T . A T increase to 5800 K (a factor of ~ 2.8) was required to match the experimentally inferred P of 105 GPa. The resulting state was found to exhibit metallic behavior, with $\sigma = 7500$ ($\Omega \text{ cm}$) $^{-1}$ and no energy gap. We performed a similar exercise at an intermediate ρ of 0.689 g/cm^3 . In this case, a T increase to 4200 K (a factor of ~ 2) was required to reach the experimentally inferred P of 105 GPa. Again, this state was found to exhibit metallic behavior, with $\sigma = 7600$ ($\Omega \text{ cm}$) $^{-1}$ and no energy gap. It seems clear that for the PBE xc functional no matter what T and ρ combination one uses to match the experimentally inferred P of 105 GPa, the calculated σ will be much too high, by roughly three orders of magnitude. The same conclusions would be reached for the higher P experiments performed by NWM. From this exercise we conclude that regardless of how one tries to equate the P states reached in the NWM experiments, predictions using the PBE xc functional are inconsistent with the measured σ .

To further explore the trends observed in σ and energy gap with molar density, we also performed calculations with the PBE xc functional at lower P . The Kerley03 EOS was used to estimate the T that would be reached in a ~ 80 GPa multiple-shock experiment. These P and T conditions, 80 GPa and 1500 K, respectively, correspond to a molar density of 0.3085 g/cm^3 with the PBE xc functional. At these conditions PBE predicts $\sigma = 0.31$ ($\Omega \text{ cm}$) $^{-1}$ and an energy gap of 2.4 eV [shown as black stars in Figs. 5(b) and 7(b)]. While these results do reasonably follow the trends exhibited by the nonlocal vdW xc functionals, PBE does appear to display gap closure at a slightly lower molar density. However,

we note the T for this PBE calculation is considerably lower (1500 K) than the other calculations considered here.

To evaluate the relative effect of T on the FP calculations we consider σ as a function of band gap energy, shown in Fig. 8. The as calculated values (listed in Table II) are plotted in Fig. 8(a). Also plotted as triangles and squares are the experimentally measured σ as a function of inferred energy gap as determined by NWM and reanalyzed in this work, respectively; dark and light gray correspond to hydrogen and deuterium, respectively. As expected, the FP calculations, particularly with the nonlocal vdW xc functionals, are in reasonable agreement with the experimental measurements and the reanalyzed energy gaps, showing a small scatter about a common trend line. These σ values were then normalized to a common T of 1978 K (the lowest inferred experimental T) using the semiconductor model:

$$\sigma_n = \sigma_1 \exp \left[\frac{-E_{g_1}}{2k_B T_1} \left(\frac{T_1}{1978} - 1 \right) \right], \quad (5)$$

where σ_1 at T_1 and E_{g_1} has been normalized to σ_n at T of 1978 K and the same energy gap E_{g_1} . The normalized experimental and calculated σ_n are plotted as a function of energy gap in Fig. 8(b). We see that the small scatter apparent in Fig. 8(a) can be explained by the corresponding T differences. In particular, the low value for σ obtained for the 1500 K PBE calculation is largely due to the correspondingly low thermal excitation. These results do suggest a small isotopic difference for FP calculations of hydrogen and deuterium; σ for deuterium appears to be systematically lower than that of hydrogen by a factor of 2–3. While the source of this small isotopic difference is not entirely clear, it suggests the energy gap is both a function of T and ρ in this regime, as one might expect.

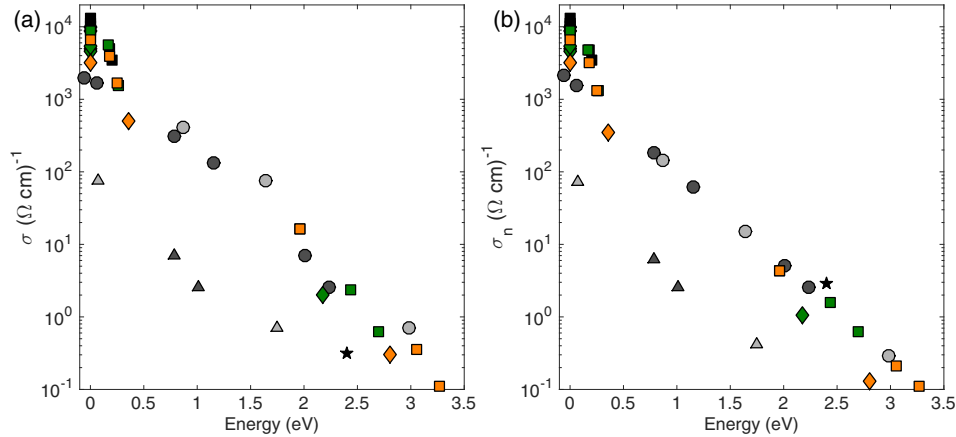


FIG. 8. Conductivity as a function of energy gap. (a) Dark and light gray circles (triangles) are the results for hydrogen and deuterium, respectively, from experiments [21,22] performed by NWM where the energy gap was inferred from the modified (original) semiconductor model described in Sec. II. Black, green, and orange squares (diamonds) are calculations for hydrogen (deuterium) using PBE [8], vdW-DF1 [9], and vdW-DF2 [10] xc functionals, respectively, at the conditions listed in Table II. The black star is the additional PBE calculation performed at lower molar density. (b) Same as (a) but with the conductivity values normalized [Eq. (5)] to a common T (1978 K, corresponding to the lowest T NWM experiment) as described in the text.

These comparisons suggest that the significant differences in σ and the energy gap exhibited by the various xc functionals when viewed as a function of P , as in Figs. 5(a) and 7(a), are largely tied to differences in the predicted P for the xc functionals at similar T and ρ conditions. We note that the various functionals considered here have recently been carefully evaluated with respect to quantum Monte Carlo (QMC) calculations by Clay *et al.* [46]. They explored the accuracy of the various functionals in comparison to QMC calculations for both liquid and solid hydrogen structures. The vdW functionals, particularly vdW-DF1, were found to provide a very good description of the global and local energetics as compared to QMC but exhibited larger differences in P than PBE relative to the QMC calculations. The P obtained from all of the xc functionals were higher than QMC (by ~ 5 – 10% in the relevant ρ regime), with PBE and vdW-DF2 being the lowest and highest, respectively.

This trend in P differences observed by Clay *et al.*, which is consistent with the trend observed in this study, would seem to suggest that the P determined by the vdW functionals is too high rather than the P determined by PBE being too low. However, this conclusion is refuted by the incompatibility of PBE with the measured σ from the NWM experiments. We note that the calculations by Clay *et al.* were carried out in liquid structures with Wigner-Seitz radii (r_s) of 1.30, 1.45, and 1.60 (1.23, 0.88, and 0.66 g/cm^3 in hydrogen, respectively) at $T = 1000$ K. The ρ range considered here corresponds to an r_s of 1.5–1.6, within the range evaluate by Clay *et al.*, however, the T range considered here (2–4 kK) is higher. At higher T , thermal population of electrons into the excited states is not insignificant. This thermal occupation of electronic orbitals has direct consequences on the liquid structure and the forces but is not included in the QMC calculations.

Similar observations were made in a recent evaluation of the various xc functionals with high-precision Hugoniot and reshock measurements on liquid deuterium [7], which probed the MA transition in the largely T -driven regime. In that study the same trend in P was observed for the MA transition along the principal Hugoniot; dissociation, as evidenced by a transient drop in the slope of the shock velocity relative to the particle velocity behind the shock front, occurred at a lower P for PBE than for the vdW functionals. Furthermore, the experimentally determined P onset of dissociation was found to be bounded from below by PBE (~ 3 GPa lower than experiment) and above by the vdW functionals (~ 1 GPa higher than experiment). This conclusion was corroborated by measurements of the reshock P from Hugoniot states near peak compression. Those measurements suggest that the reshock P determined by the vdW functionals are too low by a few percent. In contrast, the P difference for vdW-DF1 relative to QMC at those conditions is on the order of $+2$ – 4% . Again, while the trend in P was found to be the same as that determined by Clay *et al.*, comparison with the MA transition along the Hugoniot suggests that the P for dissociation is in better agreement with the vdW xc functionals and that PBE underestimates the P necessary for dissociation.

Finally, we note that there are conflicting experimental results for the MA transition in the low- T , high- ρ regime where the transition appears to be largely ρ driven (see Fig. 1). Dynamic compression experiments [15] on liquid deuterium in the ~ 1 – 2 kK regime performed at the Sandia Z machine revealed an abrupt MA transition, as evidenced by a rapid increase in reflectivity, between ~ 280 and 305 GPa. Similar to the T -driven regime probed by the Hugoniot and the intermediate regime probed by the σ measurements of NWM, the dynamic compression experimental results are in

reasonable agreement with the nonlocal vdW xc functionals and suggest that the PBE xc functional underestimates the P onset of the MA transition. In contrast, static high- P and pulsed heated experiments [17–20] on hydrogen and deuterium in a similar T regime suggest the MA transition occurs at ~ 75 to 170 GPa, based on observation of T plateaus in the heating curves and increases in reflectivity, in apparent agreement with PBE. However, these conditions are consistent with the onset of strong optical absorption in the dynamic compression experiments, which lead to alternative interpretations of those data [11, 15, 47]. Furthermore, we have shown that the predictions of PBE are inconsistent with the σ measurements of NWM. This raises questions about the static high- P and pulsed heated studies, particularly given that the MA transition in those studies is reported to be in a very similar P but even lower T range than the multiple-shock σ experiments examined here.

V. CONCLUSION

A detailed comparison of the measured σ from multiple-shock compression experiments [21, 22] with FT-DFT calculations using both semilocal (PBE) and nonlocal (vdW-DF1 and vdW-DF2) xc functionals was performed. As a part of this comparison, the multiple-shock σ experiments were reanalyzed; the original study included inconsistencies in both the inferred T states reached in the experiments and in the fit to a semiconductor model used to interpret the measured σ . Due to the method used to infer the T , which only accounted for the entropy increase from the first shock and treated subsequent compression as isentropic, the T states reported by NWM are systematically low by ~ 440 – 750 K (~ 20 – 30%). Also, due to a low $\sigma_0 = 90$ ($\Omega \text{ cm}$) $^{-1}$, the energy gap inferred from a simple semiconductor model is underestimated by ~ 1 eV as a function of P as compared to the same semiconductor model with a more reasonable $\sigma_0 = 1850$ ($\Omega \text{ cm}$) $^{-1}$.

Using P and T conditions inferred from the Kerley03 EOS for the peak states, FP calculations with PBE, vdW-DF1, and vdW-DF2 xc functionals were performed to directly compare with the NWM experiments. Calculations of σ using the PBE xc functional predict that a minimum metallic conductivity should have been observed in all of the experiments performed

by NWM. It was also shown that regardless of how one tries to equate the P states reached in the NWM experiments, predictions using the PBE xc functional are inconsistent with the measured σ . In contrast, the overall trend of the experimental data is captured reasonably well by the two vdW xc functionals. Similar behavior was exhibited in the inferred energy gaps extracted from FP calculations of the DOS.

This study, along with previous studies comparing the various xc functionals with recent Hugoniot experiments [7] on deuterium that probed the MA transition in the high- T and low- ρ regime and dynamic compression experiments [15] on deuterium that probed the MA transition in the low- T and high- ρ regime, provides a consistent picture for the MA transition over a wide P and T range. Over this entire range the P onset of the MA transition is captured reasonably well by the nonlocal vdW xc functionals, while PBE appears to underestimate the P conditions necessary for dissociation. This likely stems from P errors associated with the PBE xc functional, resulting in calculated P that are too low at these T and ρ conditions. This raises questions about recent static high- P and pulsed heated studies [17–20] that appear to be in agreement with predictions from PBE, particularly given that the MA transition in those studies is reported to be in a very similar P but even lower T range than the multiple-shock σ experiments examined here.

ACKNOWLEDGMENTS

This work was supported in part by the US Department of Energy, National Nuclear Security Administration under Award No. DE-NA0002007. Sandia National Laboratories is a multimission laboratory managed and operated by National Technology and Engineering Solutions of Sandia, LLC., a wholly owned subsidiary of Honeywell International, Inc., for the US Department of Energy’s National Nuclear Security Administration under Contract No. DE-NA0003525. This paper describes objective technical results and analysis. Any subjective views or opinions that might be expressed in the paper do not necessarily represent the views of the US Department of Energy or the United States Government. M.P. and R.R. thank the Deutsche Forschungsgemeinschaft (DFG) for support via the SFB 652.

- [1] J. M. McMahon, M. A. Morales, C. Pierleoni, and D. M. Ceperley, *Rev. Mod. Phys.* **84**, 1607 (2012).
- [2] R. Smoluchowski, *Nature (London)* **215**, 691 (1967).
- [3] E. E. Salpeter, *Astrophys. J.* **181**, L83 (1973).
- [4] W. Lorenzen, B. Holst, and R. Redmer, *Phys. Rev. B* **84**, 235109 (2011).
- [5] T. Guillot, *Science* **286**, 72 (1999).
- [6] N. Nettelmann, A. Becker, B. Holst, and R. Redmer, *Astrophys. J.* **750**, 52 (2012).
- [7] M. D. Knudson and M. P. Desjarlais, *Phys. Rev. Lett.* **118**, 035501 (2017).
- [8] J. P. Perdew, K. Burke, and M. Ernzerhof, *Phys. Rev. Lett.* **77**, 3865 (1996).
- [9] M. Dion, H. Rydberg, E. Schröder, D. C. Langreth, and B. I. Lundqvist, *Phys. Rev. Lett.* **92**, 246401 (2004).
- [10] K. Lee, E. D. Murray, L. Kong, B. I. Lundqvist, and D. C. Langreth, *Phys. Rev. B* **82**, 081101 (2010).
- [11] I. Tamblyn and S. A. Bonev, *Phys. Rev. Lett.* **104**, 065702 (2010).
- [12] M. A. Morales, C. Pierleoni, E. Schwegler, and D. M. Ceperley, *Proc. Natl. Acad. Sci. USA* **107**, 12799 (2010).
- [13] W. Lorenzen, B. Holst, and R. Redmer, *Phys. Rev. B* **82**, 195107 (2010).
- [14] M. A. Morales, J. M. McMahon, C. Pierleoni, and D. M. Ceperley, *Phys. Rev. Lett.* **110**, 065702 (2013).
- [15] M. D. Knudson, M. P. Desjarlais, A. Becker, R. W. Lemke, K. R. Cochrane, M. E. Savage, D. E. Bliss, T. R. Mattsson, and R. Redmer, *Science* **348**, 1455 (2015).
- [16] M. K. Matzen, M. A. Sweeney, R. G. Adams, J. R. Asay, J. E. Bailey, G. R. Bennett, D. E. Bliss, D. D. Bloomquist, T. A.

- Brunner, R. B. Campbell, G. A. Chandler, C. A. Coverdale, M. E. Cuneo, J.-P. Davis, C. Deeney, M. P. Desjarlais, G. L. Donovan, C. J. Garasi, T. A. Haill, C. A. Hall, D. L. Hanson, M. J. Hurst, B. Jones, M. D. Knudson, R. J. Leeper, R. W. Lemke, M. G. Mazarakis, D. H. McDaniel, T. A. Mehlhorn, T. J. Nash, C. L. Olson, J. L. Porter, P. K. Rambo, S. E. Rosenthal, G. A. Rochau, L. E. Ruggles, C. L. Ruiz, T. W. L. Sanford, J. F. Seamen, D. B. Sinars, S. A. Slutz, I. C. Smith, K. W. Struve, W. A. Stygar, R. A. Vesey, E. A. Weinbrecht, D. F. Wenger, and E. P. Yu, *Phys. Plasmas* **12**, 055503 (2005).
- [17] V. Dzyabura, M. Zaghoo, and I. F. Silvera, *Proc. Natl. Acad. Sci. USA* **110**, 8040 (2013).
- [18] K. Otha, K. Ichimaru, M. Einaga, S. Kawaguchi, K. Shimizu, T. Matsuoka, N. Hirao, and Y. Ohishi, *Sci. Rep.* **5**, 16560 (2015).
- [19] M. Zaghoo, A. Salamat, and I. F. Silvera, *Phys. Rev. B* **93**, 155128 (2016).
- [20] M. Zaghoo and I. F. Silvera, *Proc. Nat. Acad. Sci. USA* **114**, 11873 (2017).
- [21] S. T. Weir, A. C. Mitchell, and W. J. Nellis, *Phys. Rev. Lett.* **76**, 1860 (1996).
- [22] W. J. Nellis, S. T. Weir, and A. C. Mitchell, *Phys. Rev. B* **59**, 3434 (1999).
- [23] A. C. Mitchell and W. J. Nellis, *Rev. Sci. Instrum.* **52**, 347 (1981).
- [24] G. I. Kerley, *Molecular-based study of fluids* (American Chemical Society, Washington, 1983), p. 107.
- [25] N. C. Holmes, M. Ross, and W. J. Nellis, *Phys. Rev. B* **52**, 15835 (1995).
- [26] M. Ross, *Phys. Rev. B* **54**, R9589 (1996).
- [27] M. Ross, *Phys. Rev. B* **58**, 669 (1998).
- [28] G. Kerley, Sandia National Laboratories Report No. SAND2003-3613 (Sandia National Laboratories, 2003).
- [29] J. H. Carpenter (private communication, 2014).
- [30] K. R. Cochrane, R. W. Lemke, Z. Riford, and J. H. Carpenter, *J. Appl. Phys.* **119**, 105902 (2016).
- [31] G. I. Kerley, *Int. J. Impact Eng.* **5**, 441 (1987).
- [32] G. Kerley, Kerley Publishing Services Report No. KPS98-1 (Kerley Publishing Services, 1998).
- [33] J. F. Barnes and S. P. Lyon, Los Alamos Technical Report No. LA-11058-MS (Los Alamos National Laboratory, 1987).
- [34] D. Saumon (private communication, 2018).
- [35] L. Caillabet, S. Mazevet, and P. Loubeyre, *Phys. Rev. B* **83**, 094101 (2011).
- [36] B. Holst, R. Redmer, and M. P. Desjarlais, *Phys. Rev. B* **77**, 184201 (2008).
- [37] G. Kresse and J. Hafner, *Phys. Rev. B* **47**, 558 (1993).
- [38] G. Kresse and J. Hafner, *Phys. Rev. B* **49**, 14251 (1994).
- [39] G. Kresse and J. Furthmüller, *Phys. Rev. B* **54**, 11169 (1996).
- [40] S. Nosé, *Mol. Phys.* **52**, 255 (1984).
- [41] S. Nosé, *J. Chem. Phys.* **81**, 511 (1984).
- [42] W. G. Hoover, *Phys. Rev. A* **31**, 1695 (1985).
- [43] R. Kubo, *J. Phys. Soc. Jpn.* **12**, 570 (1957).
- [44] D. A. Greenwood, *Proc. Phys. Soc.* **71**, 585 (1958).
- [45] H. J. Monkhorst and J. D. Pack, *Phys. Rev. B* **13**, 5188 (1976).
- [46] R. C. Clay, J. Mcminis, J. M. McMahon, C. Pierleoni, D. M. Ceperley, and M. A. Morales, *Phys. Rev. B* **89**, 184106 (2014).
- [47] R. S. McWilliams, D. A. Dalton, M. F. Mahmood, and A. F. Goncharov, *Phys. Rev. Lett.* **116**, 255501 (2016).

A. Appendix

A.1. Convergence of the TPS method

The most conservative way to obtain a TPS box at a given density is to slowly heat up a crystal configuration and cool down a liquid simulation box. This creates a temperature overlap where the solid is not yet molten and the liquid is not yet frozen. The melting temperature then has to be within the temperature overlap. After establishing the temperature overlap, simulations of the liquid and the solid part ensure the relaxation of the future constituents of the TPS box. Finally, the TPS box at a given temperature results from a combination of the corresponding liquid and the solid simulation cells.

However, at a fixed density, a solid has a lower pressure compared to a liquid of the same density. A way to resolve this pressure difference is to employ constant-pressure MD. Another method removes atoms from the liquid part until the pressure of the liquid part matches that of the solid. This *equilibrated TPS (e-TPS)*, however, leads to imperfections within a possible solid result of a TPS due to the missing atoms. In contrast, the *compressed relaxed TPS (cr-TPS)* does not remove atoms from the liquid but instead slightly compresses the solid and matches the pressures in this manner. While all the previous methods rely on some kind of relaxation of the liquid and the solid part, *compressed TPS (c-TPS)* utilizes a random liquid configuration and a perfect crystal in combination with a slight compression of the crystalline part. Due to the missing relaxation processes, the computational demand of the c-TPS approach decreases significantly compared to the other methods. Of course, the different approaches should reproduce each other, given a sufficient number of atoms.

k-point sampling and the choice of the pseudopotential

The forces on the ions govern the melting process. Converged forces require converged pressures.¹⁵⁰ Therefore, Fig. A.1 demonstrates the convergence of the pressure of a sample TPS box with 500 atoms with respect to the \mathbf{k} -point sampling at different densities.

While Fig. A.1 shows only a few representative \mathbf{k} -point samplings, the convergence tests employed many more. However, the resulting convergence behavior is comparable for different sampling types: A $1 \times 1 \times n$ grid with an arbitrary number $n > 1$ reproduces the results of the Γ -point. Automatic meshes, a $2 \times 2 \times n$ grid and more involved \mathbf{k} -point meshes give identical results within numerical noise. Furthermore, special points¹⁷⁸ of the Brillouin zone replicate those complex \mathbf{k} -point meshes within

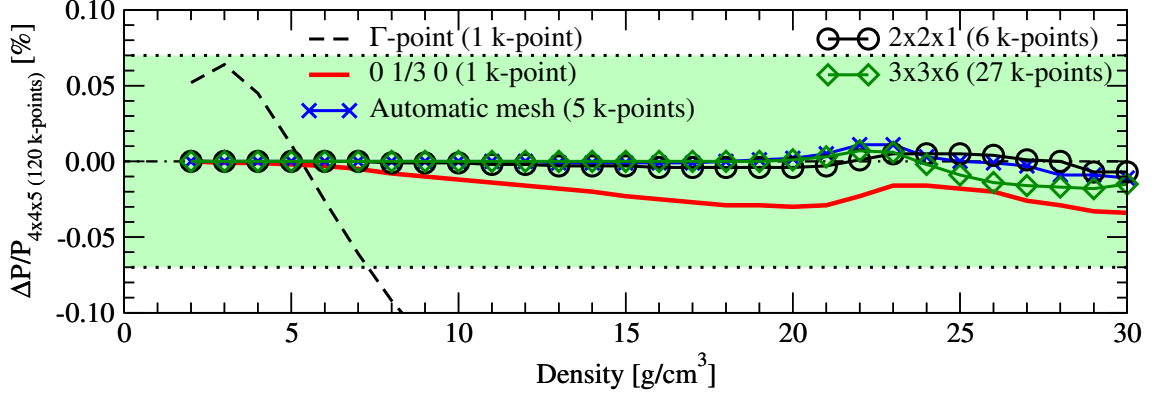


Figure A.1.: Pressure convergence of a TPS cell with 500 atoms over the density with different \mathbf{k} -point samplings compared to a \mathbf{k} -point mesh of $4 \times 4 \times 5$.

less than 0.05% deviation in pressure with only one \mathbf{k} -point. Therefore, a single \mathbf{k} -point is sufficient for a pressure convergence of 0.05% with respect to calculations with 120 \mathbf{k} -points up to densities of 30 g/cm^3 .

In order to confirm the convergence of TPS with respect to the \mathbf{k} -point sampling and the pseudopotential, actual TPS may reveal further valuable insights. A pure test of pressure convergence might not translate into the intricacies of TPS, as the \mathbf{k} -point sampling and the choice of pseudopotential might correlate. This assumption led to a test that combines different \mathbf{k} -point samplings, the standard PAW, and the hard PAW at 17 cm^3 and 20 g/cm^3 , see Fig. A.2. The TPS cells contained 500 atoms in c-TPS configurations.

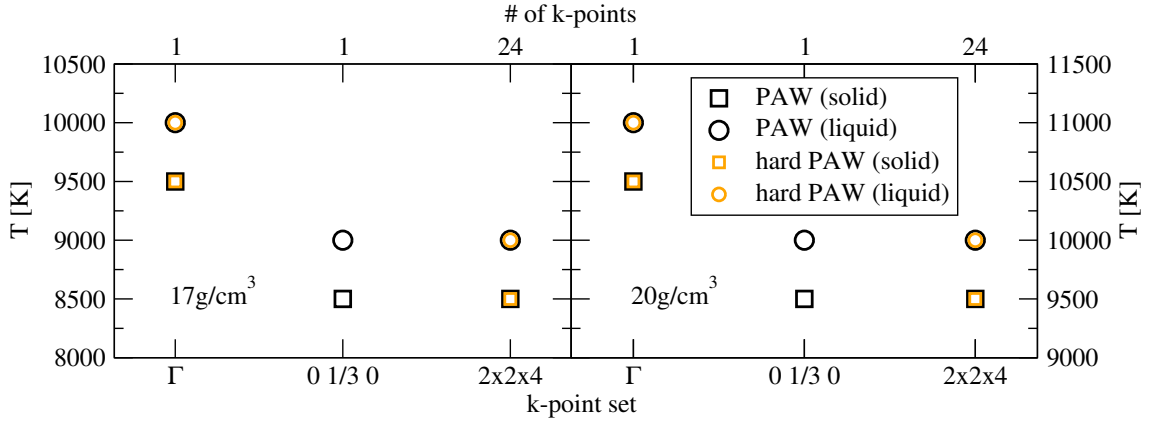


Figure A.2.: Results of TPS with the standard PAW (black) and the hard PAW potential (orange) at different \mathbf{k} -point sets and densities of 17 g/cm^3 (left panel) and 20 g/cm^3 (right panel). The alternate x-axis shows the number of \mathbf{k} -points. Circles denote a liquid state at the end of the TPS, squares denote a solid.

The standard and the hard PAW result in identical final states in the TPS, even at

the extreme densities of Fig. A.2. In contrast, the \mathbf{k} -point set has a great influence on the TPS convergence. The Γ -point is not sufficient at any of those high densities, while a single \mathbf{k} -point at $0\ 1/3\ 0$ reproduces \mathbf{k} -point grids of $2 \times 2 \times n$. This result confirms the findings of Fig. A.1. The second publication therefore employed a \mathbf{k} -point at $0\ 1/3\ 0$ for the sampling of the Brillouin zone in the TPS at densities above $7\ \text{g/cm}^3$. At lower densities, the Γ -point gives converged results, as Fig. A.1 demonstrates.

Different approaches to TPS

The previous tests validated the choice of the standard PAW pseudopotential, the use of a \mathbf{k} -point at $0\ 1/3\ 0$, and a total of 500 atoms in the TPS cell. However, a sampling at the Γ -point should still suffice at the lowest densities, as lower densities result in larger simulation cells. This translates to smaller Brillouin zones in reciprocal space, which leads to a sufficient sampling at the Γ -point for any geometry. While the \mathbf{k} -point-sampling at low densities does not play an important role, the actual setup procedure of the TPS box plays a major role. Fig. A.3 therefore tests the performance of different approaches to TPS at densities of $1.6\ \text{g/cm}^3$ and $17\ \text{g/cm}^3$, as well as the convergence with respect to the number of atoms.

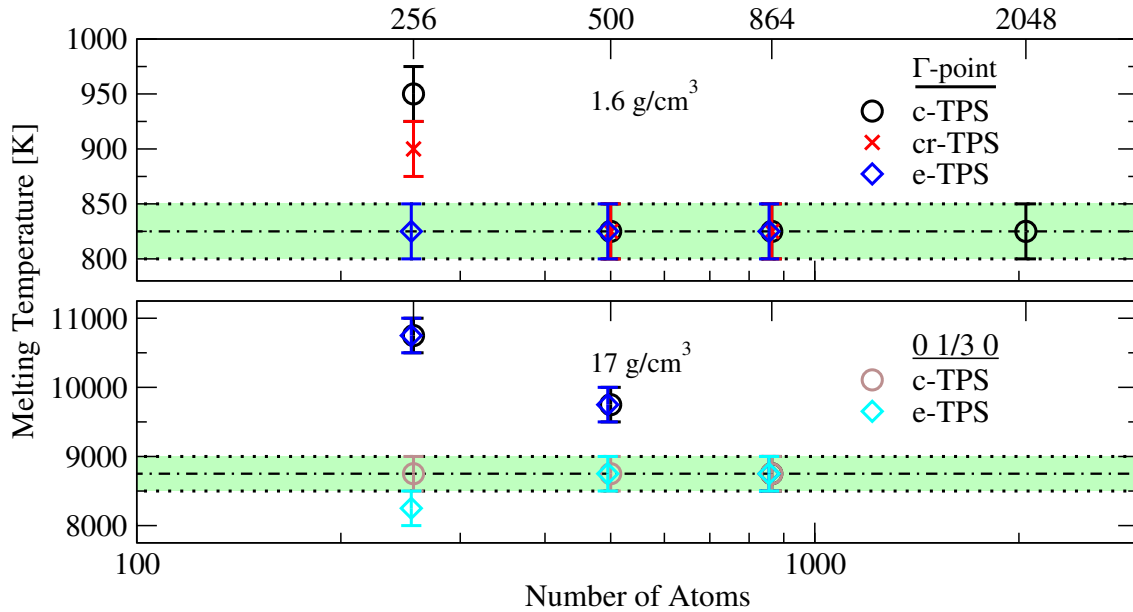


Figure A.3.: The results of the c-TPS (circles), the cr-TPS (crosses), and the e-TPS (diamonds) at $1.6\ \text{g/cm}^3$ (upper panel) and $17\ \text{g/cm}^3$ (lower panel) over the number of atoms. The darker symbols correspond to results with a sampling at the Γ -point, while the lighter colored symbols denote a \mathbf{k} -point at $0\ 1/3\ 0$. The light green area marks the converged area. The corresponding dotted and dash-dotted lines guide the eye.

When the number of atoms suffices, the three TPS approaches reproduce the same melting temperature of 825 ± 25 K at 1.6 g/cm^3 with a Brillouin zone sampling at the Γ -point. The results of the c-TPS method reproduce those of the much more demanding cr- and e-TPS approaches, as long as the TPS cell contains at least 500 atoms. At 17 g/cm^3 , the different implementations of TPS reproduce each other for each number of atoms with a sampling at the Γ -point. However, TPS at the Γ -point require at least 864 atoms in order to reproduce the results of the more adequate sampling at $0 \ 1/3 \ 0$. The Brillouin zone sampling at $0 \ 1/3 \ 0$ requires at least 500 atoms in order to give identical results with all TPS implementations. In conclusion, the c-TPS approach and 500 atoms suffice for converged TPS calculations. As established above, the Γ -point is not sufficient for all densities. Instead, the study employed a \mathbf{k} -point at $0 \ 1/3 \ 0$ for all TPS at densities above 7 g/cm^3 .

Size of the metastability region and the spacing

The solid-liquid phase transition is accompanied by a density jump at any given temperature. The density jump translates into a metastable density region, where the TPS stochastically result in either a solid or a liquid. All TPS at higher densities will give a solid, while all TPS at lower densities will result in a liquid state. The extend of the metastable region determines the uncertainties of the TPS melting line. 154 TPS with 500 atoms around the melting point at $7 \ 000$ K and a density of about 10 g/cm^3 ensured a sufficient amount of statistical data with reasonable computation time due to the comparatively high density. It is not possible to conduct this tests under every condition as the computational demand increases exponentially with decreasing densities, especially with the comparatively great number of 500 atoms. The results of Fig. A.4 therefore only represent one snapshot on the density-temperature plane.

The left panel of Fig. A.4 illustrates the influence of the spacing on the result of the TPS within a certain range of spacing sizes. Greater or smaller spacing sizes result in shock waves that travel through the simulation box due to the expansion of the solid and the liquid into the empty space between them. A spacing size between 95% to 108% of the lattice distance b of a hcp cell demonstrates no such behavior. The spacing size has to be within this range to avoid unphysical oscillations but the exact value of the spacing is of no apparent importance for the result of the TPS. The study employed a spacing of 100%.

The right panel of Fig. A.4 summarizes the left panel and illustrates the extend of the metastable region: The fit of the fraction of solid results intersects the y-axis at about $\rho_1 = 9.9 \text{ g/cm}^3$ on the left and at about $\rho_2 = 10.45 \text{ g/cm}^3$ on the right, which implies a density range of $\Delta\rho = |\rho_1 - \rho_2|/\rho_{1 \text{ or } 2} \approx 5.5\%$ for the metastable region. In the final TPS, the density difference between the two points above and below the melting line was a maximum of 2% for each isotherm. This value combined with the inferred additional uncertainty due to the metastable region of 3.5% in the accounts for the density range $\Delta\rho = 5.5\%$ of the metastable region. In a similar way, a large number of TPS at one condition with a smaller particle number have

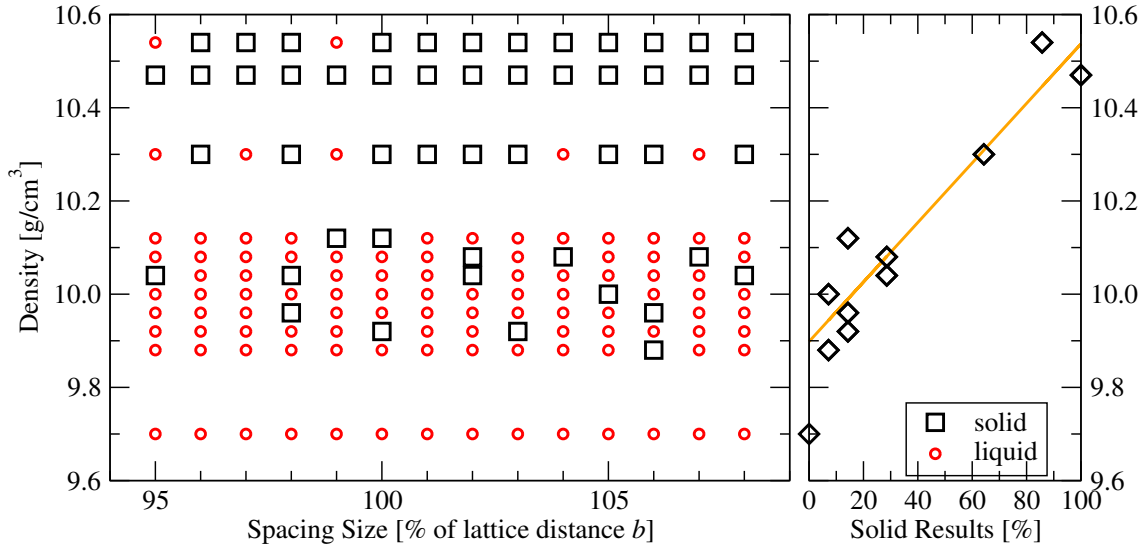


Figure A.4.: Left panel: The results of 154 TPS in total with a solid outcome marked as black squares and a liquid marked as red circle. The x-axis denotes the size of the spacing, see text. Right panel: The fraction of TPS that resulted in a solid configuration (black diamonds) and a linear regression through the data points (orange line).

been performed by Hong *et al.*,²⁵⁷ which allows for an evaluation of the pressure and temperature during the melting. However, this was not the scope of this work.²¹³

Convergence of the pressure over a wide range of densities

While converged TPS require 500 atoms, a pure calculation of the pressure already converges with 128 atoms.²⁵⁸ The study therefore first predicted the density of the melting point at a given temperature and then calculated the corresponding pressure with 128 atoms in order to save computation time, without sacrificing accuracy. However, this requires \mathbf{k} -point convergence for a wide range of densities for the liquid and the solid. Therefore, the calculations have been performed on either a perfect hcp crystal with 128 atoms to represent the solid or a random liquid configuration with a greater number of atoms (432) in order to capture the statistical distribution of atoms in the liquid phase. The greater the number of atoms the lower the number of \mathbf{k} -points that are necessary for convergence. In order to account for this aspect, the convergence criterion of the hcp crystal with 128 atoms is a reproduction of the pressures obtained with a $5 \times 5 \times 5$ \mathbf{k} -point grid within 0.4%. The convergence criterion for the liquid cell with 432 atoms is 0.05%, compared to the results of a $3 \times 3 \times 3$ grid. Fig. A.5 displays the results of convergence tests over a wide range of densities.

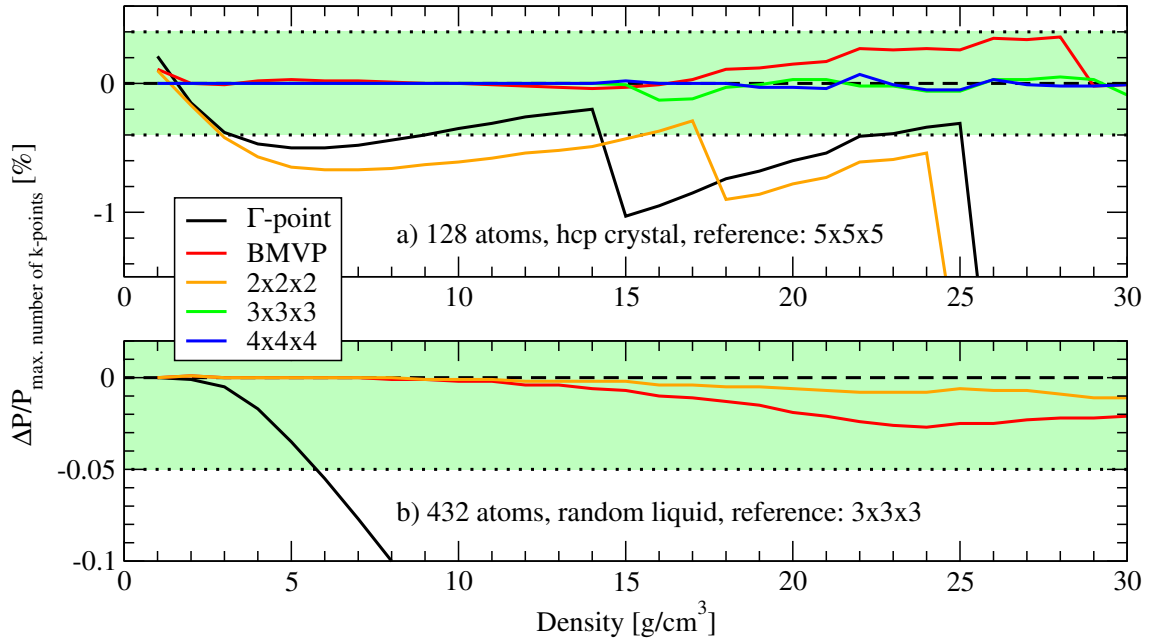


Figure A.5.: Pressure convergence of a perfect hcp crystal (upper panel) and a random liquid configuration (lower panel) at different color-coded \mathbf{k} -point sets over the density.

Neither the Γ -point nor a sampling with a $2 \times 2 \times 2$ grid result in converged pressures in case of the perfect hcp crystal. In the liquid cell, all samplings apart from the Γ -point give converged results. However, the BMVP meets all the convergence criteria discussed above across the range of densities in this test and irrespective of the phase. All the EOS calculations of the respective study therefore employ the BMVP.

A.2. Convergence of high-pressure properties around the band closure of helium

The resolution of very small effects requires a convergence that is much better than the presumed magnitude of the effect. None of the previous calculations of helium demonstrated signs of a first-order nonmetal-to-metal phase transition. Therefore, in order to resolve a small-scale effect, all properties under study have to be calculated when they are very well converged.

This section touches on the convergence of the band gap which has been extensively discussed in the supplemental material²⁶³ of the respective study. Furthermore, it focuses on the convergence details of the DC conductivity (Sec. A.2.1), the reflectivity (Sec. A.2.2), and the ionization degree (Sec. A.2.3).

A test grid of two temperatures, 10 000 and 60 000 K, and three densities, 1, 10, and 24 g/cm³, and subsequent calculations of the optical properties thereon, provided all the necessary information. An in-depth discussion of all convergence parameters is not the focus of this section. Instead, it will review the convergence with respect to the number of atoms, the choice of the potential, and the number of bands per atom. A \mathbf{k} -point sampling at the BMVP suffices for all conditions on the test grid.

Although Ref. 150 studied the convergence of some of the quantities under discussion, the wide range of densities of this work required further tests.

A.2.1. DC conductivity

The DC conductivity is sensitive with respect to the number of atoms, the energy cutoff of the potential, the choice of the potential itself, the \mathbf{k} -point sampling, the number of snapshots, and the number of bands per atoms at every density and temperature. Densities of 10 g/cm^3 and above require a Brillouin zone sampling at the BMVP and 20 atomic snapshots, while the Γ -point and 10 snapshots suffice for lower densities.

DC conductivity: number of atoms

Fig. A.6 shows the convergence of the low-frequency part of the dynamic electric conductivity with respect to the number of atoms.

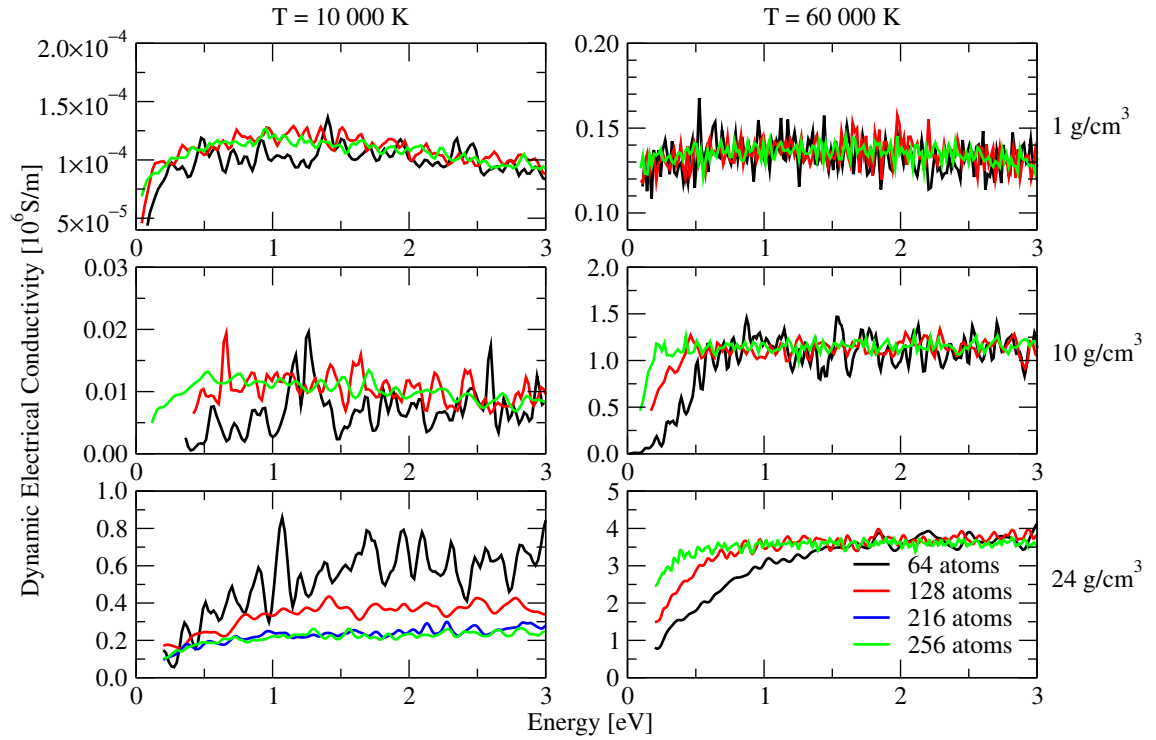


Figure A.6.: The low-frequency part of dynamic electrical conductivity over the energy at 10 000 K (left panels) and 60 000 K (right panels) at 1 g/cm^3 (upper panels), 10 g/cm^3 (panels in the middle), and 24 g/cm^3 (lower panels), respectively. The colorcode denotes the number of atoms.

While all the low-frequency dynamic electrical conductivities at 60 000 K achieve convergence with 64 atoms, a temperature of 10 000 K requires 128 atoms for convergence at 1 and 10 g/cm^3 , and 216 atoms at 24 g/cm^3 . A lower number of atoms results higher energies at which the linear regression for the calculation of the low-frequency limit can begin, see Sec. 2.2.3. The study used 216 atoms for densities above 10 g/cm^3 and 128 atoms at 10 g/cm^3 and below.

DC conductivity: choice of the (pseudo-)potential and energy cutoff

The treatment of the electronic system within DFT strongly depends on the choice of the (pseudo-)potential. At the lowest densities and temperatures, the standard PAW pseudopotential reproduces all relevant parts of the electronic structure. Higher densities require a harder PAW pseudopotential with a greater energy cutoff, while the highest densities call for the full Coulomb potential. Fig. A.7 compares the DC conductivity of different potentials on the ρ - T grid established above, at different energy cutoffs.

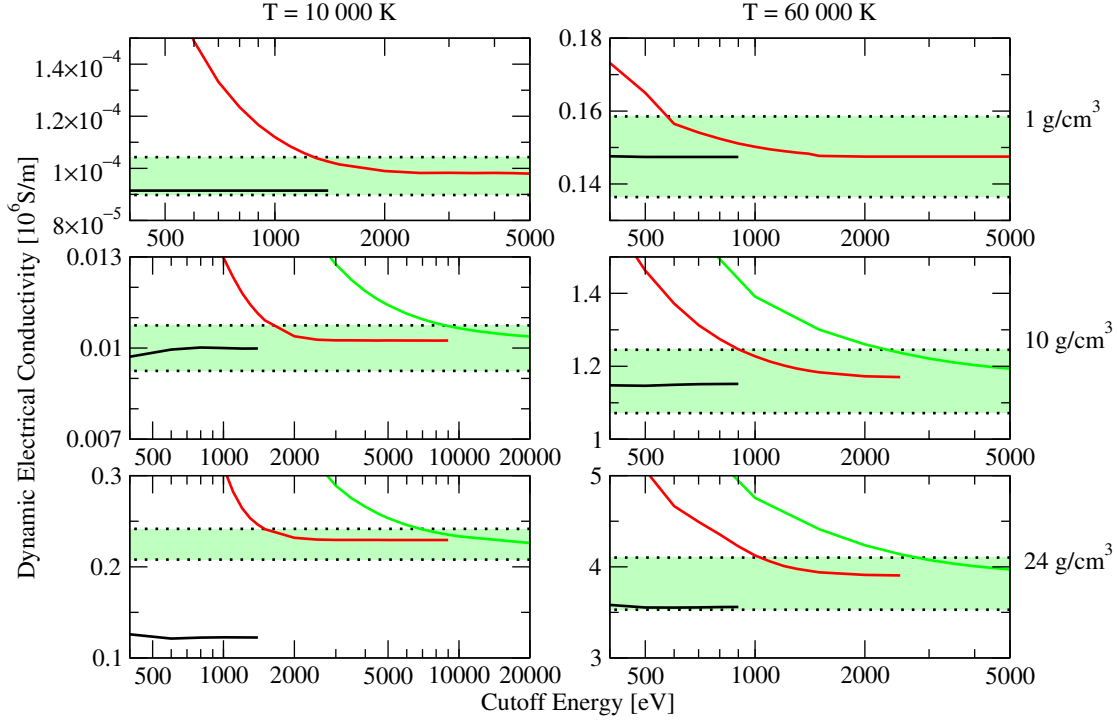


Figure A.7.: The convergence of the DC conductivity with the cutoff energy. The panels denote different ρ - T conditions. Results for the PAW pseudopotential are shown in black, the ones for the hard PAW pseudopotential in red, and the full Coulomb potential in green. The light green areas indicate $\pm 7.5\%$ convergence with respect to the Coulomb potential at densities above 1 g/cm^3 and the hard PAW at 1 g/cm^3 .

Absolute convergence of the Coulomb is not possible at 10 g/cm^3 and lower densities. Therefore, a fit of the form $\sigma = a + \frac{b}{(E+c)^d}$ to the DC conductivity results of the Coulomb potential, and a subsequent extrapolation to infinite energies provided the reference value of the DC conductivity for the Coulomb potential at 10 g/cm^3 . In the fit equation, σ is the DC conductivity, E denotes the cutoff energy, and a , b , c , and d are the fit parameters. At densities below 10 g/cm^3 , the hard PAW pseudopotential provides the reference values as the Coulomb potential is computationally not feasible at those comparatively low densities. At densities of up to 10 g/cm^3 , the

results of the standard PAW pseudopotential with a cutoff energy of at least 400 eV agree with the reference values. However, higher densities require the use of the hard PAW pseudopotential with at least 1 500 eV cutoff energy for converged DC conductivities. The respective study used the hard PAW pseudopotential with an energy cutoff of 2 000 eV for all the DC conductivity calculations.

DC conductivity: number of bands per atom

A greater number of bands results in a physical dynamic electrical conductivity $\sigma(\omega)$ to higher energies, see Fig. 2.5 for a representation of $\sigma(\omega)$ to very high energies. However, the DC conductivity σ_{DC} is the low-frequency limit of $\sigma(\omega)$. Therefore, converged values of σ_{DC} require less bands per atoms than other optical properties, see the following sections. Fig. A.8 displays the convergence of the DC conductivity with the number of bands per atom.

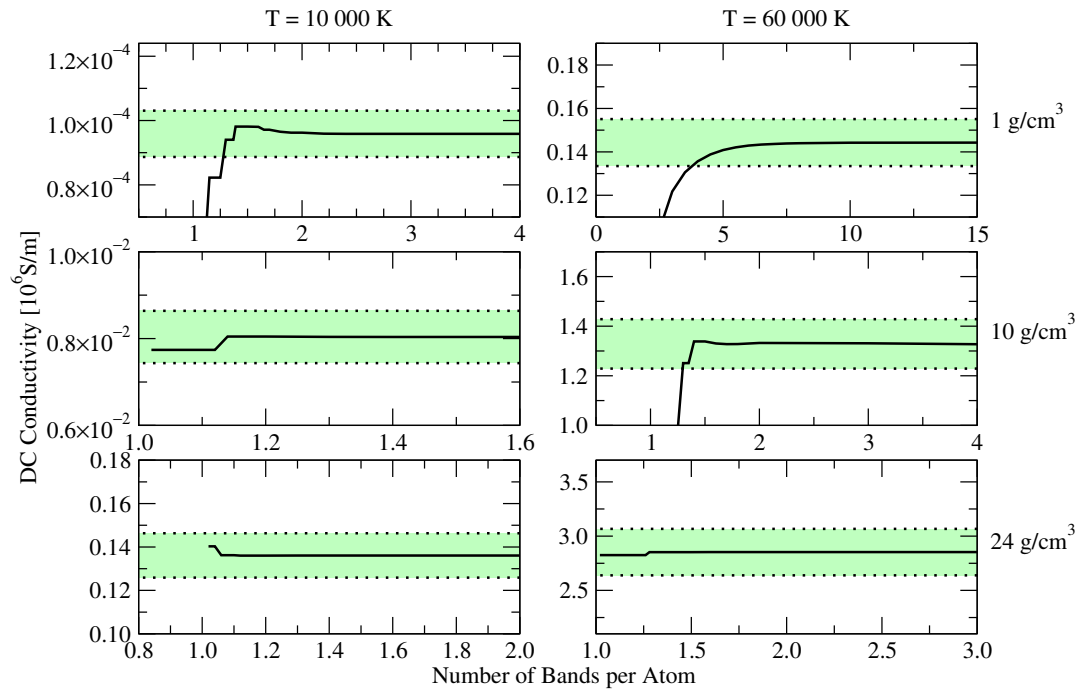


Figure A.8.: The convergence of the DC conductivity with the number of bands per atoms. The panels denote different ρ - T conditions. The light green areas indicate $\pm 7.5\%$ convergence with respect to the highest number of bands per atom at every condition.

The required number of bands increases with temperature and decreases with density. However, 1.3 bands per atoms are sufficient for 10 000 K, while 60 000 K require at least four bands per atom at the lowest density. The third publication employed five bands per atoms.

A.2.2. Reflectivity

The optical reflectivity is sensitive to the same parameters as the DC conductivity. Therefore, the same testing procedure applies. A Brillouin zone sampling at the Γ -point suffices compared to more involved \mathbf{k} -point samplings. Densities of 5 g/cm^3 and below require 20 snapshots. Higher densities demand 10 snapshots for a convergence of 0.01 compared to 40 snapshots.

Reflectivity: number of atoms

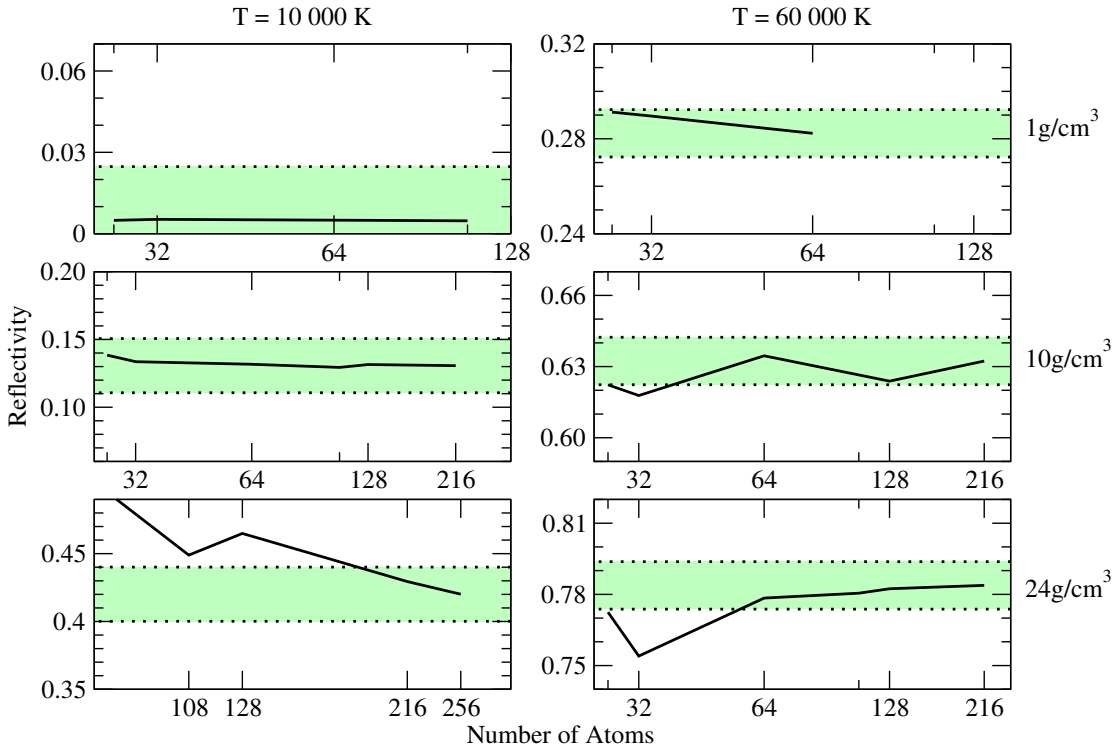


Figure A.9.: The reflectivity over the number of atoms. The panels denote different ρ - T conditions. The light green areas indicate ± 0.02 convergence with respect to the highest number of atoms.

Higher temperatures and higher densities demand a greater number of atoms to achieve a convergence of ± 0.02 at $T = 10\,000 \text{ K}$ and ± 0.01 at $T = 60\,000 \text{ K}$. The third publication employed 128 atoms for densities of 10 g/cm^3 and less, and 216 atoms for higher densities.

As the reflectivity at 1 g/cm^3 and $10\,000 \text{ K}$ is within numerical noise, further convergence tests of the reflectivity will not evaluate this condition.

Reflectivity: choice of the (pseudo-)potential and energy cutoff

Figure A.10.: The convergence of the reflectivity with the cutoff energy. The panels denote different ρ - T conditions. Results for the PAW pseudopotential are shown in black, the ones for the hard PAW pseudopotential in red, and the full Coulomb potential in green, identical to Fig. A.7.

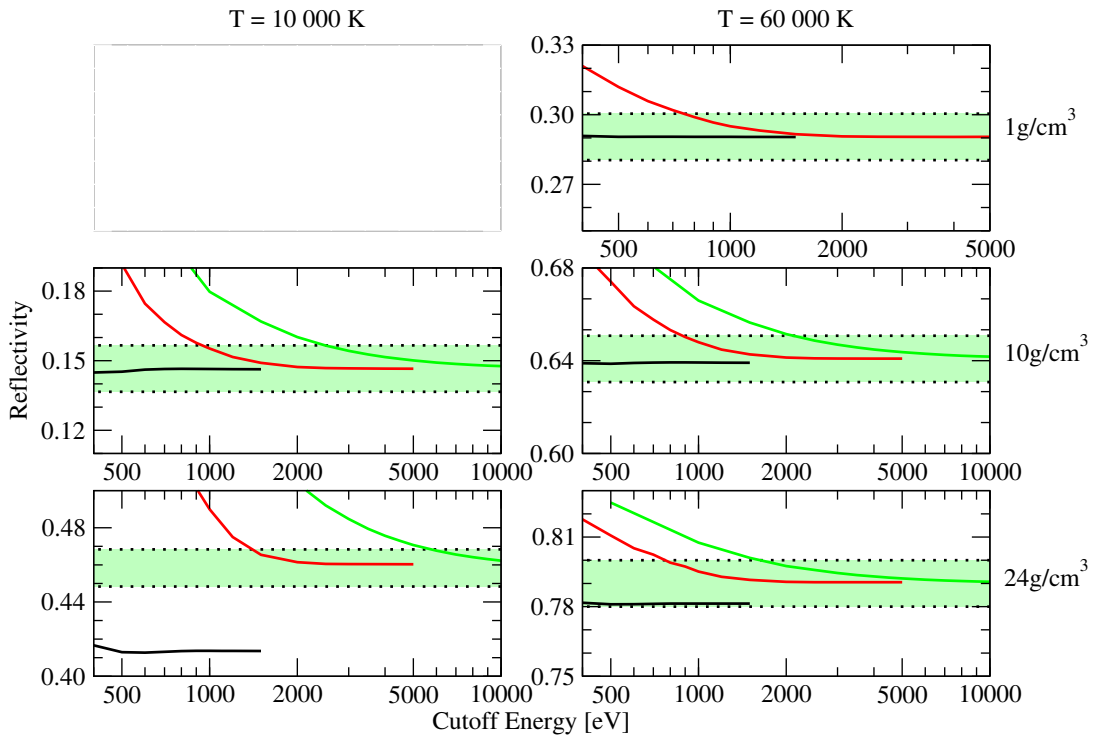


Figure A.10.: The convergence of the reflectivity with the cutoff energy. The panels denote different ρ - T conditions. Results for the PAW pseudopotential are shown in black, the ones for the hard PAW pseudopotential in red, and the full Coulomb potential in green, identical to Fig. A.7. The light green areas indicate ± 0.01 convergence with respect to the Coulomb potential at densities above 1 g/cm³ and the hard PAW at 1 g/cm³.

At densities below 10 g/cm³, the hard PAW pseudopotential provides the reference value. At densities of up to 10 g/cm³, the results of the standard PAW pseudopotential with a cutoff energy of at least 400 eV agree with the reference values. However, higher densities require the use of the hard PAW pseudopotential with at least 1 500 eV cutoff energy for converged reflectivities. The respective study used the hard PAW pseudopotential with an energy cutoff of 2 000 eV for all the reflectivity calculations.

Reflectivity: number of bands per atom

Converged values for the reflectivity require a converged dynamic electrical conductivity. Figure A.11 shows the convergence of the DC conductivity. Figure A.11 shows the convergence of the

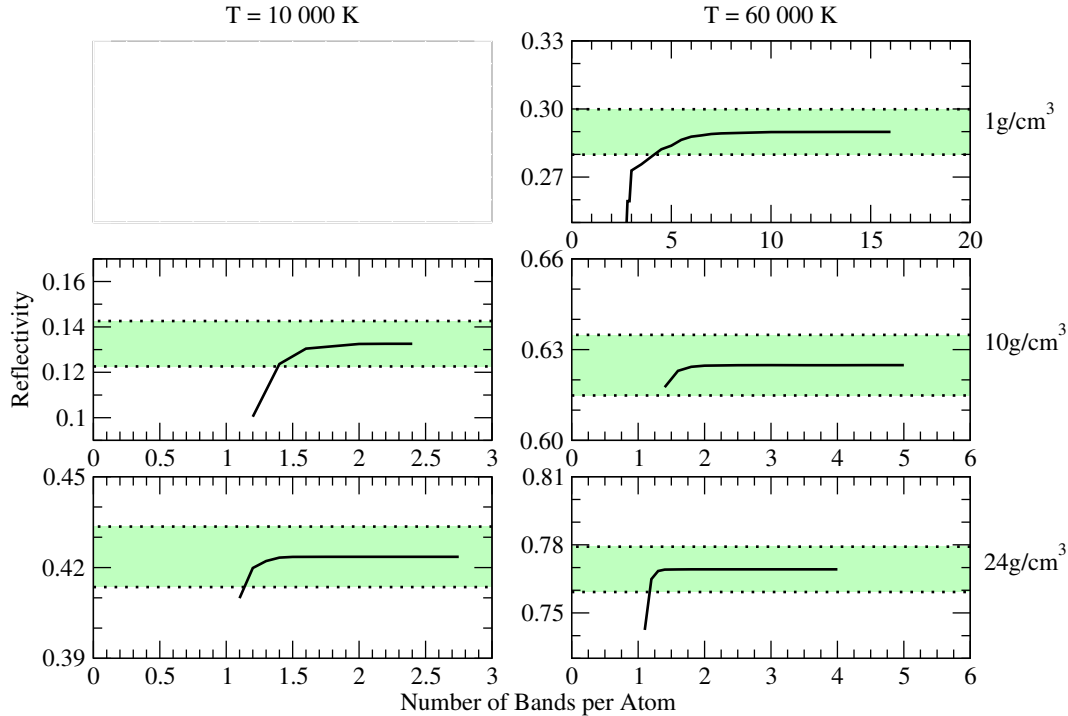


Figure A.11.: The convergence of the reflectivity with the number of bands per atoms. The panels denote different ρ - T conditions. The light green areas indicate ± 0.01 convergence with respect to the highest number of bands per atom at every condition.

Just like for the DC conductivity, discussed in Sec. A.2.1, the required number of bands for converged reflectivities increases with temperature and decreases with density. However, 1.5 bands per atoms are sufficient for 10 000 K. 60 000 K require at least 4.5 bands per atom. The third publication employed five bands per atoms.

A.2.3. Ionization degree

The ionization is sensitive to the same parameters as the DC conductivity and the reflectivity. Therefore, the same testing procedure applies. At densities below 4 g/cm^3 , a Brillouin zone sampling at the BMVP suffices, while higher densities require a Monkhorst-Pack set of $2 \times 2 \times 2$. A single snapshot gives converged ionization degrees under all conditions under consideration.

Ionization degree: number of atoms

Fig. A.12 shows the convergence of the ionization degree with respect to the number of atoms. Please note that the ionization degree is zero for $\rho = 1 \text{ g/cm}^3$ and $T = 10\,000 \text{ K}$, and 100% at $\rho = 24 \text{ g/cm}^3$ and $T = 60\,000 \text{ K}$ for all numbers of atoms in this test. The corresponding graphs are therefore not shown for clarity, both here and in the following tests.

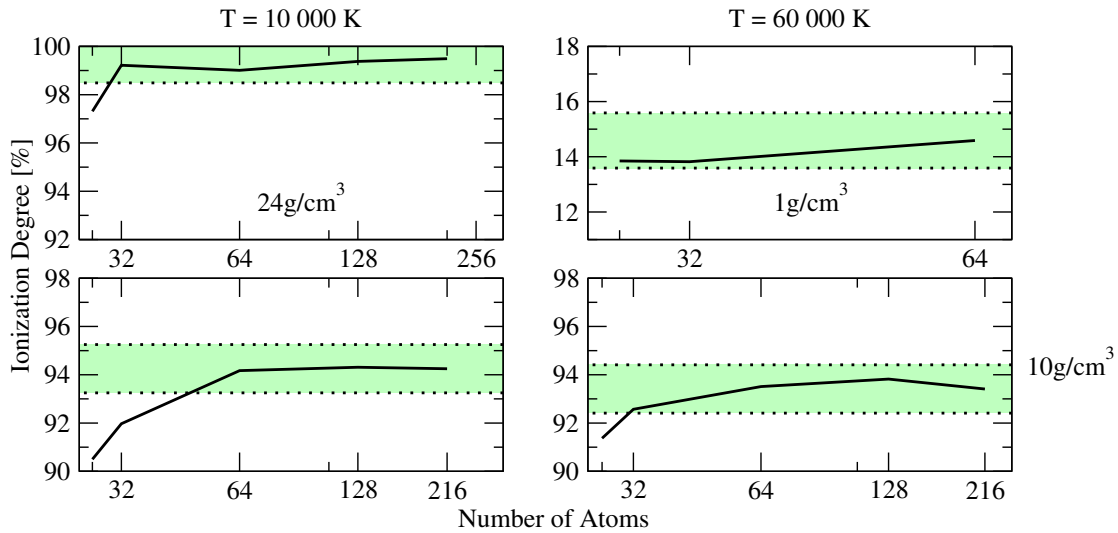


Figure A.12.: The ionization degree over the number of atoms. The panels denote different ρ - T conditions. The light green areas indicate $\pm 1\%$ convergence with respect to the highest number of atoms.

The required number of atoms for a convergence of $\pm 1\%$ decreases with increasing temperature. Compared to the DC conductivity and the reflectivity, the ionization degree requires a significantly smaller number of atoms, demonstrating convergence with 64 atoms under all conditions under consideration. The third publication employed 128 atoms for densities of 10 g/cm^3 and less, and 216 atoms for higher densities.

Ionization degree: choice of the (pseudo-)potential and energy cutoff

Figure A.13.: The convergence of the ionization degree with the cutoff energy. The panels denote different ρ - T conditions. Results for the PAW pseudopotential are shown in black, the ones for the hard PAW pseudopotential in red, and the full Coulomb potential in green, identical to Fig. A.7. The light green areas indicate $\pm 1\%$ convergence with respect to the Coulomb potential at densities above 1 g/cm^3 and the hard PAW at 1 g/cm^3 .

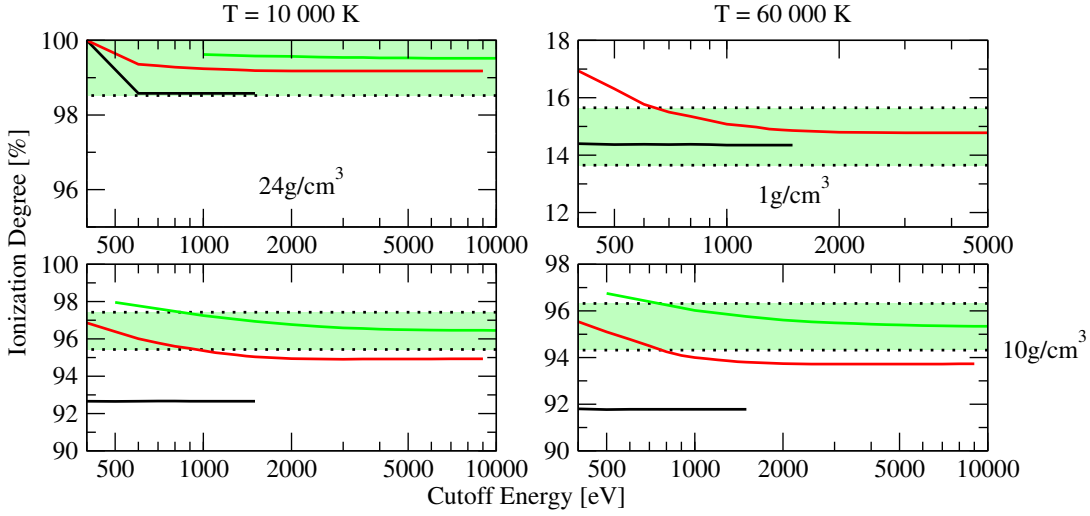


Figure A.13.: The convergence of the ionization degree with the cutoff energy. The panels denote different ρ - T conditions. Results for the PAW pseudopotential are shown in black, the ones for the hard PAW pseudopotential in red, and the full Coulomb potential in green, identical to Fig. A.7. The light green areas indicate $\pm 1\%$ convergence with respect to the Coulomb potential at densities above 1 g/cm^3 and the hard PAW at 1 g/cm^3 .

At densities below 10 g/cm^3 , the hard PAW pseudopotential provides the reference value. At a density of 1 g/cm^3 , the results of the standard PAW pseudopotential with a cutoff energy of at least 400 eV agree with the reference values. However, higher densities require the use of the full Coulomb potential with at least $1\,000 \text{ eV}$ cutoff energy for converged ionization degrees. The third publication studied densities starting from 2 g/cm^3 , which would require the full Coulomb potential according to Fig. A.13, which is not computationally feasible. Therefore, additional tests at densities between 2 and 9 g/cm^3 and $T = 39\,000 \text{ K}$ provided further insight, see Fig. A.14. After ensuring that every (pseudo-)potential was converged, the figure compares the results of the highest energy cutoffs of every (pseudo-)potential at different densities.

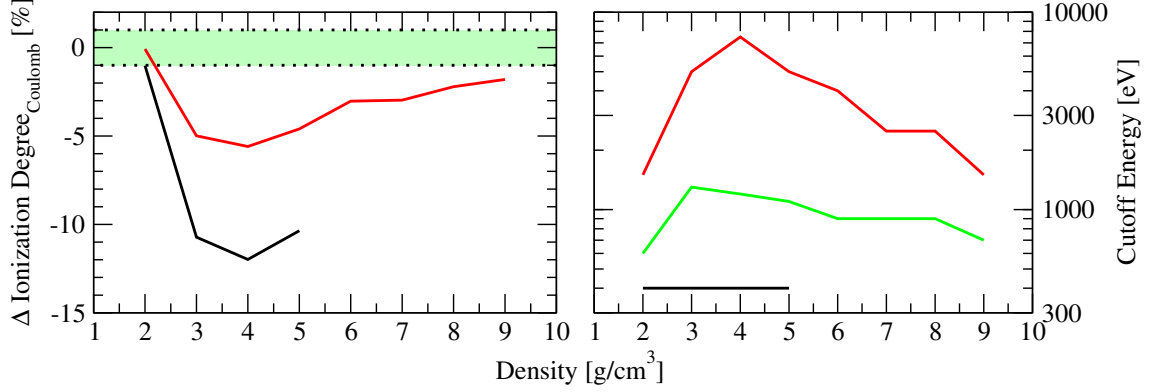


Figure A.14.: Convergence of the PAW (black) and the hard PAW (red) pseudopotential, and the Coulomb potential (green) at about $T = 39\,000$ K over the density. Left panel: The convergence of the ionization degree over the density. The light green area indicate $\pm 1\%$ convergence with respect to the results of the Coulomb potential. Right panel: The cutoff energy required for $\pm 1\%$ convergence with respect to the highest cutoff energies under consideration for all (pseudo-)potentials.

At $\rho = 2$ g/cm³, the results of the PAW pseudopotential for the ionization degree closely resemble the lower convergence boundary of the ionization degree at this condition. The ionization degrees calculated with the hard PAW pseudopotential reproduce the ones obtained with the Coulomb potential. Therefore, calculations of the ionization degree up to a density of 2 g/cm³ employed the hard PAW pseudopotential in this thesis. Upon further compression to $\rho = 4$ g/cm³, however, the results of the PAW pseudopotentials increasingly deviate and the ones of the hard PAW pseudopotential do not reproduce those of the Coulomb potential anymore. This deviation decreases at densities above 4 g/cm³, until all the (pseudo-)potentials reproduce each other's results at $\rho = 24$ g/cm³, see the upper left panel in Fig. A.13. In order to consistently obtain converged results, the third study employed the full Coulomb potential at densities above 2 g/cm³.

The different (pseudo-)potentials require different cutoff energies in order to give converged results, depending on the density. While the PAW pseudopotential requires a cutoff energy of 400 eV independent of the density, the hard PAW pseudopotential demands up to 1 300 eV, which increases to 7 500 eV for the Coulomb potential. The third study employed the full Coulomb potential with a cutoff energy of 7 500 eV for densities above 2 g/cm³.

Ionization degree: number of bands per atom

Converged values for the ionization degree require a dynamic electrical conductivity $\sigma(\omega)$ to higher energies than the DC conductivity and the reflectivity. Fig. A.15 displays the convergence of the ionization degree with the number of bands per atom.

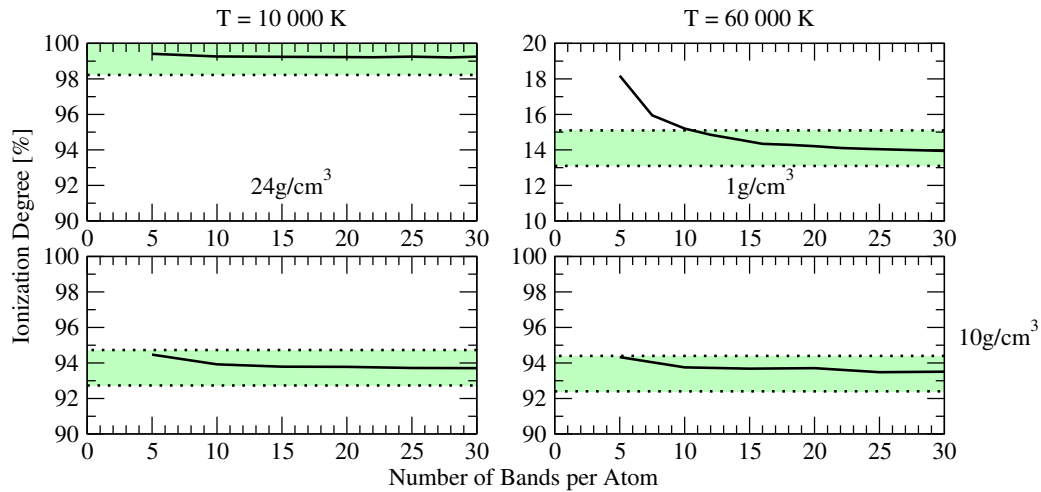


Figure A.15.: The convergence of the ionization degree with the number of bands per atoms. The panels denote different ρ - T conditions. The light green areas indicate $\pm 1\%$ convergence with respect to the highest number of bands per atom at every condition.

Just like for the DC conductivity, discussed in Sec. A.2.1, the required number of bands for converged ionization degrees decrease with density. However, 5 bands per atoms are sufficient for 10 000 K. A temperature of 10 000 K demands 5 bands per atom, while 60 000 K require at least 12 bands per atom at a density of 1 g/cm³. However, at a density of 10 g/cm³, 5 bands per atom suffice. The third publication employed 12 bands per atom at densities below 10 g/cm³, while calculations at higher densities used five bands per atom.

B. Bibliography

- [1] R. A. Alpher, H. Bethe, and G. Gamow, *Phys. Rev.* **73**, 803 (1948).
- [2] H. A. Bethe, *Phys. Rev.* **55**, 434 (1939).
- [3] M. Turner, in *Bulletin of the American Astronomical Society*, Vol. 15 (1983) p. 681.
- [4] A. Burrows and J. Liebert, *Rev. Mod. Phys.* **65**, 301 (1993).
- [5] I. Baraffe, G. Chabrier, F. Allard, and P. H. Hauschildt, *Astrophys. J.* **446**, L35 (1995).
- [6] S. R. Kulkarni, *Science* **276**, 1350 (1997).
- [7] K. Lodders, H. Palme, and H.-P. Gail, *Landolt-Börnstein - Group VI Astronomy and Astrophysics* (Springer-Verlag Berlin Heidelberg, 2009).
- [8] U. von Zahn, D. M. Hunten, and G. Lehmacher, *J. Geophys. Res.* **103**, 0148 (1998).
- [9] B. J. Conrath and D. Gautier, *Icarus* **144**, 124 (2000).
- [10] B. Conrath, D. Gautier, R. Hanel, G. Lindal, and A. Marten, *J. Geophys. Res.* **92**, 15003 (1987).
- [11] W. B. Hubbard, *Science* **275**, 1279 (1997).
- [12] R. Barron and T. Jackson, *Cryogenic Systems* (Oxford University Press, 1985).
- [13] F. A. Staas, A. P. Severijns, and H. C. M. Van der Waerden, *Phys. Lett. A* **53**, 327 (1975).
- [14] C. A. M. Castelijns, J. G. M. Kuerten, A. T. A. M. de Waele, and H. M. Gijssman, *Phys. Rev. B* **32**, 2870 (1985).
- [15] A. Marx, J. Hoess, and K. Uhlig, “Dry dilution refrigerator for experiments on quantum effects in the microwave regime,” (2014), arXiv:1412.3619 [cond-mat.other] .
- [16] B. van den Brandt, P. Hautle, J. A. Konter, F. M. Piegsa, and J. P. Urrego-Blanco, *J. Phys.: Conf. Ser.* **150**, 012024 (2009).

- [17] O. Kirichek, R. Down, G. Kouzmenko, J. Keeping, D. Bunce, R. Wotherspoon, and Z. Bowden, *Cryogenics* **50**, 666 (2010).
- [18] D. A. Tocher, *Appl. Organomet. Chem.* **14**, 172 (2000).
- [19] X. Dong, A. R. Oganov, A. F. Goncharov, E. Stavrou, S. Lobanov, G. Saleh, G.-R. Qian, Q. Zhu, C. Gatti, V. L. Deringer, R. Dronskowski, X.-F. Zhou, V. B. Prakapenka, Z. Konôpková, I. A. Popov, A. I. Boldyrev, and H.-T. Wang, *Nat. Chem.* **9**, 440 (2017).
- [20] V. B. Efimov, L. P. Mezhov-Deglin, C. D. Dewhurst, A. V. Lokhov, and V. V. Nesvizhevsky, *Adv. High Energy Phys.* (2015).
- [21] P. L. Elliott, C. I. Pakes, L. Skrbek, and W. F. Vinen, *Phys. Rev. B* **61**, 1396 (2000).
- [22] N. Tariq, N. A. Taisan, V. Singh, and J. D. Weinstein, *Phys. Rev. Lett.* **110**, 153201 (2013).
- [23] F. Grandinetti, *Int. J. Mass Spectrom.* **237**, 243 (2004).
- [24] P. Moroshkin and K. Kono, *Phys. Rev. A* **93**, 052510 (2016).
- [25] H. Liu, Y. Yao, and D. D. Klug, *Phys. Rev. B* **91**, 014102 (2015).
- [26] D. Z. Kandula, C. Gohle, T. J. Pinkert, W. Ubachs, and K. S. E. Eikema, *Phys. Rev. Lett.* **105**, 063001 (2010).
- [27] *CRC Handbook of Chemistry and Physics*, 88th ed. (CRC Press, 2007).
- [28] G. D. Considine, *Van Nostrand's Encyclopedia of Chemistry* (John Wiley & Sons, Inc. do, 2005).
- [29] J. A. Stone and A. Stejskal, *Metrologia* **41**, 189 (2004).
- [30] A. Zajac and E. Hecht, *Optics, Fourth Edit* (Pearson Higher Education, 2003).
- [31] J. Wilks, *The Properties of Liquid and Solid Helium* (Clarendon P., 1967).
- [32] H. K. Onnes, "Further experiments with liquid helium. c. on the change of electric resistance of pure metals at very low temperatures etc. iv. the resistance of pure mercury at helium temperatures," in *Through Measurement to Knowledge: The Selected Papers of Heike Kamerlingh Onnes 1853–1926*, edited by K. Gavroglu and Y. Goudaroulis (Springer Netherlands, Dordrecht, 1991).
- [33] T. E. Graedel, *J. Ind. Ecol.* **13**, 154 (2009).
- [34] B. V. Rollin and F. Simon, *Physica* **6**, 219 (1939).

- [35] A. Abrikosov, *J. Phys. Chem. Solids* **2**, 199 (1957).
- [36] E. J. Yarmchuk and R. E. Packard, *J. Low Temp. Phys.* **46**, 479 (1982).
- [37] W. R. Brode, *Science* **164**, 678 (1969).
- [38] F. Pobell, *Matter and Methods at Low Temperatures*, Vol. 3 (Springer-Verlag Berlin Heidelberg, 2007).
- [39] P. Loubeyre, J. M. Besson, J. P. Pinceaux, and J. P. Hansen, *Phys. Rev. Lett.* **49**, 1172 (1982).
- [40] P. Loubeyre, R. LeToullec, J. P. Pinceaux, H. K. Mao, J. Hu, and R. J. Hemley, *Phys. Rev. Lett.* **71**, 2272 (1993).
- [41] H. Niki, H. Nagara, H. Miyagi, and T. Nakamura, *Phys. Lett. A* **79**, 428 (1980).
- [42] O. Penrose and L. Onsager, *Phys. Rev.* **104**, 576 (1956).
- [43] G. V. Chester, *Phys. Rev. A* **2**, 256 (1970).
- [44] C. M. H. Kim E., *Nature* **427**, 225–227 (2004).
- [45] Y. Vekhov and R. B. Hallock, *Phys. Rev. Lett.* **109**, 045303 (2012).
- [46] Z. G. Cheng and J. Beamish, *Phys. Rev. Lett.* **121**, 225304 (2018).
- [47] D. D. Osheroff, R. C. Richardson, and D. M. Lee, *Phys. Rev. Lett.* **28**, 885 (1972).
- [48] D. D. Osheroff, W. J. Gully, R. C. Richardson, and D. M. Lee, *Phys. Rev. Lett.* **29**, 920 (1972).
- [49] A. J. Leggett, *Phys. Rev. Lett.* **29**, 1227 (1972).
- [50] M. Woolfson, *Astron. Geophys* **41**, 1.12 (2000).
- [51] S. Basu and H. Antia, *Phys. Rep.* **457**, 217 (2008).
- [52] E. G. Adelberger, A. García, R. G. H. Robertson, K. A. Snover, A. B. Balantekin, K. Heeger, M. J. Ramsey-Musolf, D. Bemmerer, A. Junghans, C. A. Bertulani, J.-W. Chen, H. Costantini, P. Prati, M. Couder, E. Uberseder, M. Wiescher, R. Cyburt, B. Davids, S. J. Freedman, M. Gai, D. Gazit, L. Gialanella, G. Imbriani, U. Greife, M. Hass, W. C. Haxton, T. Itahashi, K. Kubodera, K. Langanke, D. Leitner, M. Leitner, P. Vetter, L. Winslow, L. E. Marcucci, T. Motobayashi, A. Mukhamedzhanov, R. E. Tribble, K. M. Nollett, F. M. Nunes, T.-S. Park, P. D. Parker, R. Schiavilla, E. C. Simpson, C. Spitaleri, F. Strieder, H.-P. Trautvetter, K. Suemmerer, and S. Typel, *Rev. Mod. Phys.* **83**, 195 (2011).

- [53] M. Salaris and S. Cassisi, *Evolution of Stars and Stellar Populations* (John Wiley & Sons, Ltd, 2005).
- [54] A. Bonanno, H. Schlattl, and L. Paternò, *A&A* **390**, 1115 (2002).
- [55] J. N. Connelly, M. Bizzarro, A. N. Krot, Å. Nordlund, D. Wielandt, and M. A. Ivanova, *Science* **338**, 651 (2012).
- [56] D. Goldsmith and T. Owen, *The Search For Life In The Universe* (University Science Books, 2001).
- [57] R. G. Deupree and R. K. Wallace, *Astrophys. J.* **317**, 724 (1987).
- [58] K.-P. Schröder and R. Connors Smith, *Mon. Not. R. Astron. Soc.* **386**, 155 (2008).
- [59] R. Napiwotzki, *J. Phys. Conf. Ser.* **172**, 012004 (2009).
- [60] G. Fontaine, P. Brassard, and P. Bergeron, *Publ. Astron. Soc. Pac.* **113**, 409 (2001).
- [61] G. Laughlin, P. Bodenheimer, and F. C. Adams, *Astrophys. J.* **482**, 420 (1997).
- [62] J. Liebert, P. Bergeron, D. Eisenstein, H. C. Harris, S. J. Kleinman, A. Nitta, and J. Krzesinski, *Astrophys. J.* **606**, L147 (2004).
- [63] F. D'Antona and I. Mazzitelli, *Annu. Rev. Astron. Astr.* **28**, 139 (1990).
- [64] V. E. Fortov, V. Y. Ternovoi, M. V. Zhernokletov, M. A. Mochalov, A. L. Mikhailov, A. S. Filimonov, A. A. Pyalling, V. B. Mintsev, V. K. Gryaznov, and I. L. Iosilevskii, *J. Exp. Theor. Phys.* **97**, 259 (2003).
- [65] C. Winisdoerffer and G. Chabrier, *Phys. Rev. E* **71**, 026402 (2005).
- [66] C. F. Claver, D. E. Winget, R. E. Nather, and P. J. MacQueen, in *American Astronomical Society Meeting Abstracts*, Vol. 193 (1998).
- [67] L. Ferrario, D. de Martino, and B. T. Gänsicke, *Space Sci. Rev.* **191**, 111 (2015).
- [68] C. F. Hall, *Science* **183**, 301 (1974).
- [69] P. H. Abelson, *Science* **183**, 259 (1974).
- [70] A. G. Opp, *Science* **188**, 447 (1975).
- [71] E. C. Stone and A. L. Lane, *Science* **204**, 945 (1979).
- [72] E. C. Stone and A. L. Lane, *Science* **206**, 925 (1979).

- [73] E. J. Smith, K.-P. Wenzel, and D. E. Page, *Science* **257**, 1503 (1992).
- [74] R. E. Young, *J. Geophys. Res. Planets* **103**, 22775 (1998).
- [75] H. B. Niemann, S. K. Atreya, G. R. Carignan, T. M. Donahue, J. A. Haberman, D. N. Harpold, R. E. Hartle, D. M. Hunten, W. T. Kasprzak, P. R. Mahaffy, T. C. Owen, N. W. Spencer, and S. H. Way, *Science* **272**, 846 (1996).
- [76] J. N. Bahcall and M. H. Pinsonneault, *Astrophys. J. Lett.* **395**, L119 (1992).
- [77] C. R. Proffitt, *Astrophys. J.* **425**, 849 (1994).
- [78] C. J. Hansen, S. J. Bolton, D. L. Matson, L. J. Spilker, and J.-P. Lebreton, *Icarus* **172**, 1 (2004), special Issue: Cassini-Huygens at Jupiter.
- [79] Y. Guo and R. W. Farquhar, *Space Sci. Rev.* **140**, 49 (2008).
- [80] S. J. Bolton, J. Lunine, D. Stevenson, J. E. P. Connerney, S. Levin, T. C. Owen, F. Bagenal, D. Gautier, A. P. Ingersoll, G. S. Orton, T. Guillot, W. Hubbard, J. Bloxham, A. Coradini, S. K. Stephens, P. Mokashi, R. Thorne, and R. Thorpe, *Space Sci. Rev.* **213**, 5 (2017).
- [81] M. H. Acuña and N. F. Ness, *Science* **207**, 444 (1980).
- [82] B. A. Smith, L. Soderblom, R. Beebe, J. Boyce, G. Briggs, A. Bunker, S. A. Collins, C. J. Hansen, T. V. Johnson, J. L. Mitchell, R. J. Terrile, M. Carr, A. F. Cook, J. Cuzzi, J. B. Pollack, G. E. Danielson, A. Ingersoll, M. E. Davies, G. E. Hunt, H. Masursky, E. Shoemaker, D. Morrison, T. Owen, C. Sagan, J. Veverka, R. Strom, and V. E. Suomi, *Science* **212**, 163 (1981).
- [83] B. A. Smith, L. Soderblom, R. Batson, P. Bridges, J. Inge, H. Masursky, E. Shoemaker, R. Beebe, G. B. A. Boyce, J.; Briggs, C. J. J. T. V. M. J. L. Collins, S. A.; Hansen, R. J. Terrile, A. F. Cook, J. Cuzzi, J. B. Pollack, G. E. Danielson, A. P. Ingersoll, M. E. Davies, G. E. Hunt, D. Morrison, T. Owen, C. Sagan, J. Veverka, R. Strom, and V. E. Suomi, *Science* **215**, 504 (1982).
- [84] M. K. Dougherty, N. Achilleos, N. Andre, C. S. Arridge, A. Balogh, C. Bertucci, M. E. Burton, S. W. H. Cowley, G. Erdos, G. Giampieri, K.-H. Glassmeier, K. K. Khurana, J. Leisner, F. M. Neubauer, C. T. Russell, E. J. Smith, D. J. Southwood, and B. T. Tsurutani, *Science* **307**, 1266 (2005).
- [85] R. K. Achterberg and F. M. Flasar, *Planet. Sci. J.* **1**, 30 (2020).
- [86] O. Mousis, D. H. Atkinson, T. Spilker, E. Venkatapathy, J. Poncey, R. Frampton, A. Coustenis, K. Reh, J. P. Lebreton, L. N. Fletcher, R. Hueso, M. J. Amato, A. Colaprete, F. Ferri, D. Stam, P. Wurz, S. Atreya, S. Aslam, D. J. Banfield, S. Calcutt, G. Fischer, A. Holland, C. Keller, E. Kessler, M. Leese,

- P. Levacher, A. Morse, O. Muñoz, J. B. Renard, S. Sheridan, F. X. Schmider, F. Snik, J. H. Waite, M. Bird, T. Cavalié, M. Deleuil, J. Fortney, D. Gautier, T. Guillot, J. I. Lunine, B. Marty, C. Nixon, G. S. Orton, and A. Sánchez-Lavega, *Planet. Space Sci.* **130**, 80 (2016).
- [87] W. Lorenzen, B. Holst, and R. Redmer, *Phys. Rev. B* **82**, 195107 (2010).
- [88] M. D. Knudson, M. P. Desjarlais, A. Becker, R. W. Lemke, K. R. Cochrane, M. E. Savage, D. E. Bliss, T. R. Mattsson, and R. Redmer, *Science* **348**, 1455 (2015).
- [89] W. Lorenzen, B. Holst, and R. Redmer, *Phys. Rev. B* **84**, 235109 (2011).
- [90] M. Schöttler and R. Redmer, *Phys. Rev. Lett.* **120**, 115703 (2018).
- [91] S. K. Atreya, M. H. Wong, T. C. Owen, P. R. Mahaffy, H. B. Niemann, I. de Pater, P. Drossart, and T. Encrenaz, *Planet. Space Sci.* **47**, 1243 (1999).
- [92] H. F. Wilson and B. Militzer, *Phys. Rev. Lett.* **104**, 121101 (2010).
- [93] J. C. Pearl, B. J. Conrath, R. A. Hanel, J. A. Pirraglia, and A. Coustenis, *Icarus* **84**, 12 (1990).
- [94] D. J. Stevenson and E. E. Salpeter, *Astrophys. J. Suppl. Ser.* **35**, 221 (1977).
- [95] J. J. Fortney and W. B. Hubbard, *Astrophys. J.* **608**, 1039 (2004).
- [96] L. Elkins-Tanton, *Jupiter and Saturn* (Facts on File, 2011).
- [97] R. Püstow, N. Nettelmann, W. Lorenzen, and R. Redmer, *Icarus* **267**, 323 (2016).
- [98] T. Gastine, J. Wicht, L. D. V. Duarte, M. Heimpel, and A. Becker, *Geophys. Res. Lett.* **41**, 5410 (2014).
- [99] P. M. Celliers, P. Loubeyre, J. H. Eggert, S. Brygoo, R. S. McWilliams, D. G. Hicks, T. R. Boehly, R. Jeanloz, and G. W. Collins, *Phys. Rev. Lett.* **104**, 184503 (2010).
- [100] D. Santamaría-Pérez, G. D. Mukherjee, B. Schwager, and R. Böhler, *Phys. Rev. B* **81**, 214101 (2010).
- [101] W. B. Hubbard and B. Militzer, *Astrophys. J.* **820**, 80 (2016).
- [102] M. French, A. Becker, W. Lorenzen, N. Nettelmann, M. Bethkenhagen, J. Wicht, and R. Redmer, *Astrophys. J. Suppl. Ser.* **202**, 5 (2012).
- [103] N. Nettelmann, B. Holst, A. Kietzmann, M. French, R. Redmer, and D. Blaschke, *Astrophys. J.* **683**, 1217 (2008).

- [104] N. Nettelmann, A. Becker, B. Holst, and R. Redmer, *Astrophys. J.* **750**, 52 (2012).
- [105] R. Püstow, *Die innere Struktur und Evolution von Saturn*, Diplomarbeit, University of Rostock (2010).
- [106] N. Nettelmann, R. Helled, J. Fortney, and R. Redmer, *Planet. Space Sci.* **77**, 143 (2013).
- [107] N. Nettelmann, K. Wang, J. Fortney, S. Hamel, S. Yellamilli, M. Bethkenhagen, and R. Redmer, *Icarus* **275**, 107 (2016).
- [108] L. Scheibe, N. Nettelmann, and R. Redmer, *Astron. Astrophys.* **632**, A70 (2019).
- [109] R. Helled, N. Nettelmann, and T. Guillot, *Space Sci. Rev.* **216** (2020).
- [110] A. Becker, W. Lorenzen, J. J. Fortney, N. Nettelmann, M. Schöttler, and R. Redmer, *Astrophys. J. Suppl. Ser.* **215**, 21 (2014).
- [111] A. Becker, M. Bethkenhagen, C. Kellermann, J. Wicht, and R. Redmer, *Astron. J.* **156**, 149 (2018).
- [112] A. J. Poser, N. Nettelmann, and R. Redmer, *Atmosphere* **10** (2019).
- [113] Y. Zel'dovich and Y. Raizer, *Physics of Shock Waves and High-Temperature Hydrodynamic Phenomena* (Dover Publications, 2012).
- [114] S. Thunborg, G. E. Ingram, and R. A. Graham, *Rev. Sci. Instrum.* **35**, 11 (1964).
- [115] S. A. Kolesnikov, A. A. Golubev, V. S. Demidov, S. V. Dudin, A. V. Kantsyrev, V. B. Mintsev, G. N. Smirnov, V. I. Turtikov, A. V. Utkin, B. Y. Sharkov, and V. E. Fortov, *High Press. Res.* **30**, 83 (2010).
- [116] U. Zastra, P. Sperling, C. Fortmann-Grote, A. Becker, T. Bornath, R. Bredow, T. Döppner, T. Fennel, L. B. Fletcher, E. Förster, S. Göde, G. Gregori, M. Harmand, V. Hilbert, T. Laarmann, H. J. Lee, T. Ma, K. H. Meiwes-Broer, J. P. Mithen, C. D. Murphy, M. Nakatsutsumi, P. Neumayer, A. Przystawik, S. Skruszewicz, J. Tiggesbäumker, S. Toleikis, T. G. White, S. H. Glenzer, R. Redmer, and T. Tschentscher, *J. Phys. B: At., Mol. Opt. Phys.* **48**, 224004 (2015).
- [117] T. Döppner, C. Fortmann, P. F. Davis, A. L. Kritcher, O. L. Landen, H. J. Lee, R. Redmer, S. P. Regan, and S. H. Glenzer, *J. Phys. Conf. Ser.* **244**, 032044 (2010).
- [118] M. G. Haines, P. D. LePell, C. A. Coverdale, B. Jones, C. Deeney, and J. P. Apruzese, *Phys. Rev. Lett.* **96**, 075003 (2006).

- [119] J. S. Dugdale and D. K. C. MacDonald, *Phys. Rev.* **89**, 832 (1953).
- [120] A. L. Kritcher, D. C. Swift, T. Döppner, B. Bachmann, L. X. Benedict, G. W. Collins, J. L. DuBois, F. Elsner, G. Fontaine, J. A. Gaffney, S. Hamel, A. Lazicki, W. R. Johnson, N. Kostinski, D. Kraus, M. J. MacDonald, B. Maddox, M. E. Martin, P. Neumayer, A. Nikroo, J. Nilsen, B. A. Remington, D. Saumon, P. A. Sterne, W. Sweet, A. A. Correa, H. D. Whitley, R. W. Falcone, and S. H. Glenzer, *Nature* **584**, 51 (2020).
- [121] J. Eggert, S. Brygoo, P. Loubeyre, R. S. McWilliams, P. M. Celliers, D. G. Hicks, T. R. Boehly, R. Jeanloz, and G. W. Collins, *Phys. Rev. Lett.* **100**, 124503 (2008).
- [122] W. J. Nellis, N. C. Holmes, A. C. Mitchell, R. J. Trainor, G. K. Governo, M. Ross, and D. A. Young, *Phys. Rev. Lett.* **53**, 1248 (1984).
- [123] W. J. Nellis, *Rep. Prog. Phys.* **69**, 1479 (2006).
- [124] L. M. Barker and R. E. Hollenbach, *J. Appl. Phys.* **43**, 4669 (1972).
- [125] P. M. Celliers, D. K. Bradley, G. W. Collins, D. G. Hicks, T. R. Boehly, and W. J. Armstrong, *Rev. Sci. Instrum.* **75**, 4916 (2004).
- [126] J. E. Miller, T. R. Boehly, A. Melchior, D. D. Meyerhofer, P. M. Celliers, J. H. Eggert, D. G. Hicks, C. M. Sorce, J. A. Oertel, and P. M. Emmel, *Rev. Sci. Instrum.* **78**, 034903 (2007).
- [127] S. T. Weir, A. C. Mitchell, and W. J. Nellis, *Phys. Rev. Lett.* **76**, 1860 (1996).
- [128] V. Ternovoi, S. Kvitov, A. Pyalling, A. Filimonov, and V. Fortov, *JETP Lett.* **79**, 6 (2004).
- [129] F. Soubiran, S. Mazevet, C. Winisdoerffer, and G. Chabrier, *Phys. Rev. B* **86**, 115102 (2012).
- [130] B. B. L. Witte, L. B. Fletcher, E. Galtier, E. Gamboa, H. J. Lee, U. Zastra, R. Redmer, S. H. Glenzer, and P. Sperling, *Phys. Rev. Lett.* **118**, 225001 (2017).
- [131] F. J. Rogers, F. J. Swenson, and C. A. Iglesias, *Astrophys. J.* **456**, 902 (1996).
- [132] P. Hakel, M. Sherrill, S. Mazevet, J. Abdallah, J. Colgan, D. Kilcrease, N. Magee, C. Fontes, and H. Zhang, *J. Quant. Spectrosc. Radiat. Transfer* **99**, 265 (2006).
- [133] P. Sterne, S. Hansen, B. Wilson, and W. Isaacs, *High Energ. Dens. Phys.* **3**, 278 (2007).
- [134] A. Förster, T. Kahlbaum, and W. Ebeling, *Laser Part. Beams* **10**, 253 (1992).

- [135] D. Saumon, G. Chabrier, and H. M. van Horn, *Astrophys. J. Suppl. Ser.* **99**, 713 (1995).
- [136] S. A. Khairallah and B. Militzer, *Phys. Rev. Lett.* **101**, 106407 (2008).
- [137] P. M. Kowalski, S. Mazevet, D. Saumon, and M. Challacombe, *Phys. Rev. B* **76**, 075112 (2007).
- [138] L. Stixrude and R. Jeanloz, *Proc. Natl. Acad. Sci. USA* **32**, 11071 (2008).
- [139] W. Zhang, Z. Li, Z. Fu, J. Dai, Q. Chen, and L. Cai, *Sci. Rep.* **7**, 41885 (2017).
- [140] B. Militzer and D. M. Ceperley, *Phys. Rev. Lett.* **85**, 1890 (2000).
- [141] M. A. Morales, C. Pierleoni, and D. M. Ceperley, *Phys. Rev. E* **81**, 021202 (2010).
- [142] N. D. Mermin, *Phys. Rev.* **137**, A1441 (1965).
- [143] E. Schrödinger, *Phys. Rev.* **28**, 1049 (1926).
- [144] W. Kohn, *Rev. Mod. Phys.* **71**, 1253 (1999).
- [145] M. Born and R. Oppenheimer, *Ann. Phys.* **389**, 457 (1927).
- [146] P. Hohenberg and W. Kohn, *Phys. Rev.* **136**, B864 (1964).
- [147] W. Kohn and L. J. Sham, *Phys. Rev.* **140**, A1133 (1965).
- [148] E. Fermi, *Z. Phys.* **36**, 902 (1926).
- [149] J. P. Perdew, A. Ruzsinszky, J. Tao, V. N. Staroverov, G. E. Scuseria, and G. I. Csonka, *J. Chem. Phys.* **123**, 062201 (2005).
- [150] W. Lorenzen, *Phase Transitions in Hydrogen-Helium Mixtures*, Ph.D. thesis, University of Rostock (2012).
- [151] J. P. Perdew and A. Zunger, *Phys. Rev. B* **23**, 5048 (1981).
- [152] J. P. Perdew and Y. Wang, *Phys. Rev. B* **45**, 13244 (1992).
- [153] J. Tao, J. P. Perdew, V. N. Staroverov, and G. E. Scuseria, *Phys. Rev. Lett.* **91**, 146401 (2003).
- [154] J. Sun, A. Ruzsinszky, and J. P. Perdew, *Phys. Rev. Lett.* **115**, 036402 (2015).
- [155] A. D. Becke, *J. Chem. Phys.* **98**, 5648 (1993).
- [156] J. Heyd, G. E. Scuseria, and M. Ernzerhof, *J. Chem. Phys.* **124**, 219906 (2006).

- [157] M. Dion, H. Rydberg, E. Schröder, D. C. Langreth, and B. I. Lundqvist, *Phys. Rev. Lett.* **92**, 246401 (2004).
- [158] J. P. Perdew, K. Burke, and M. Ernzerhof, *Phys. Rev. Lett.* **77**, 3865 (1996).
- [159] D. Rapaport, *The Art of Molecular Dynamics Simulation* (Cambridge Univ. Press, 2004).
- [160] W. Koch and M. C. Holthausen, “Front matter and index,” in *A Chemist’s Guide to Density Functional Theory* (John Wiley & Sons, Ltd, 2001).
- [161] D. Frenkel and B. Smit, in *Understanding Molecular Simulation (Second Edition)* (Academic Press, 2002).
- [162] R. M. Martin, *Electronic structure: basic theory and practical methods* (Cambridge Univ. Press, 2004).
- [163] J. Kohanoff, *Electronic structure calculations for solids and molecules: theory and computational methods* (Cambridge Univ. Press, 2006).
- [164] E. Engel and R. M. Dreizler, *Density Functional Theory: An Advanced Course* (Springer, 2011).
- [165] R. O. Jones and O. Gunnarsson, *Rev. Mod. Phys.* **61**, 689 (1989).
- [166] B. Holst, M. French, and R. Redmer, *Phys. Rev. B* **83**, 235120 (2011).
- [167] S. Nosé, *J. Chem. Phys.* **81**, 511 (1984).
- [168] W. G. Hoover, *Phys. Rev. A* **31**, 1695 (1985).
- [169] C. Niethammer, S. Becker, M. Bernreuther, M. Buchholz, W. Eckhardt, A. Heinecke, S. Werth, H.-J. Bungartz, C. W. Glass, H. Hasse, J. Vrabc, and M. Horsch, *J. Chem. Theory Comput.* **10**, 4455 (2014).
- [170] G. Kresse and J. Hafner, *Phys. Rev. B* **49**, 14251 (1994).
- [171] G. Kresse and J. Hafner, *Phys. Rev. B* **47**, 558 (1993).
- [172] G. Kresse and J. Furthmüller, *Phys. Rev. B* **54**, 11169 (1996).
- [173] G. Kresse and D. Joubert, *Phys. Rev. B* **59**, 1758 (1999).
- [174] J. Hafner, *J. Comput. Chem.* **29**, 2044 (2008).
- [175] P. E. Blöchl, *Phys. Rev. B* **50**, 17953 (1994).
- [176] A. Baldereschi, *Phys. Rev. B* **7**, 5212 (1973).
- [177] H. J. Monkhorst and J. D. Pack, *Phys. Rev. B* **13**, 5188 (1976).

- [178] R. A. Evarestov and V. P. Smirnov, *Phys. Status Solidi B* **119**, 9 (1983).
- [179] W. Lorenzen, *Wasserstoff-Helium-Mischungen unter hohem Druck: Zustandsgleichung und Mischungslücke*, Diplomarbeit, University of Rostock (2008).
- [180] W. Lorenzen, B. Holst, and R. Redmer, *Phys. Rev. Lett.* **102**, 115701 (2009).
- [181] X. Gonze, J.-M. Beuken, R. Caracas, F. Detraux, M. Fuchs, G.-M. Rignanese, L. Sindic, M. Verstraete, G. Zerah, F. Jollet, M. Torrent, A. Roy, M. Mikami, P. Ghosez, J.-Y. Raty, and D. Allan, *Comput. Mater. Sci.* **25**, 478 (2002).
- [182] X. Gonze, *Z. Kristallogr.* **220**, 558 (2005).
- [183] X. Gonze, B. Amadon, P.-M. Anglade, J.-M. Beuken, F. Bottin, P. Boulanger, F. Bruneval, D. Caliste, R. Caracas, M. Côté, T. Deutsch, L. Genovese, P. Ghosez, M. Giantomassi, S. Goedecker, D. Hamann, P. Hermet, F. Jollet, G. Jomard, S. Leroux, M. Mancini, S. Mazevet, M. Oliveira, G. Onida, Y. Pouillon, T. Rangel, G.-M. Rignanese, D. Sangalli, R. Shaltaf, M. Torrent, M. Verstraete, G. Zerah, and J. Zwanziger, *Comput. Phys. Commun.* **180**, 2582 (2009).
- [184] S. J. Clark, M. D. Segall, C. J. Pickard, P. J. Hasnip, M. I. J. Probert, K. Refson, and M. C. Payne, *Z. Kristallogr.* **220**, 567 (2005).
- [185] V. Blum, R. Gehrke, F. Hanke, P. Havu, V. Havu, X. Ren, K. Reuter, and M. Scheffler, *Comput. Phys. Commun.* **180**, 2175 (2009).
- [186] X. Ren, P. Rinke, V. Blum, J. Wieferink, A. Tkatchenko, A. Sanfilippo, K. Reuter, and M. Scheffler, *New J. Phys.* **14**, 053020 (2012).
- [187] S. V. Levchenko, X. Ren, J. Wieferink, R. Johanni, P. Rinke, V. Blum, and M. Scheffler, *Comput. Phys. Commun.* **192**, 60 (2015).
- [188] W. J. Hehre, W. A. Lathan, R. Ditchfield, M. D. Newton, and J. A. Pople, *Quantum Chemistry Program Exchange* **237** (1970).
- [189] J. M. Soler, E. Artacho, J. D. Gale, A. García, J. Junquera, P. Ordejón, and D. Sánchez-Portal, *J. Phys.: Condens. Matter* **14**, 2745 (2002).
- [190] R. Ahlrichs, M. Bär, M. Häser, H. Horn, and C. Kölmel, *Chem. Phys. Lett.* **162**, 165 (1989).
- [191] P. Giannozzi, S. Baroni, N. Bonini, M. Calandra, R. Car, C. Cavazzoni, D. Ceresoli, G. L. Chiarotti, M. Cococcioni, I. Dabo, A. Dal Corso, S. de Gironcoli, S. Fabris, G. Fratesi, R. Gebauer, U. Gerstmann, C. Gougoussis, A. Kokalj, M. Lazzeri, L. Martin-Samos, N. Marzari, F. Mauri, R. Mazzarello, S. Paolini, A. Pasquarello, L. Paulatto, C. Sbraccia, S. Scandolo, G. Sclauzero, A. P. Seitsonen, A. Smogunov, P. Umari, and R. M. Wentzcovitch, *J. Phys. Cond. Mat.* **21**, 395502 (2009).

- [192] P. Blaha, K. Schwarz, P. Sorantin, and S. Trickey, *Comput. Phys. Commun.* **59**, 399 (1990).
- [193] R. Kubo, *J. Phys. Soc. Jap.* **12**, 570 (1957).
- [194] D. A. Greenwood, *Proc. Phys. Soc.* **71**, 585 (1958).
- [195] M. Gajdoš, K. Hummer, G. Kresse, J. Furthmüller, and F. Bechstedt, *Phys. Rev. B* **73**, 045112 (2006).
- [196] M. French and R. Redmer, *Phys. Plasmas* **24**, 092306 (2017).
- [197] M. Born, E. Wolf, A. B. Bhatia, P. C. Clemmow, D. Gabor, A. R. Stokes, A. M. Taylor, P. A. Wayman, and W. L. Wilcock, *Principles of Optics: Electromagnetic Theory of Propagation, Interference and Diffraction of Light*, 7th ed. (Cambridge Univ. Press, 1999).
- [198] G. Röpke, C.-V. Meister, K. Kollmorgen, and W.-D. Kraeft, *Ann. Phys.* **491**, 377 (1979).
- [199] W.-D. Kraeft, D. Kremp, W. Ebeling, and G. Röpke, *Quantum Statistics of Charged Particle Systems* (Akademie-Verlag Berlin, 1986).
- [200] D. B. Melrose and R. C. McPhedran, *Electromagnetic Processes in Dispersive Media* (Cambridge Univ. Press, 1991).
- [201] S. Mazevet, J. D. Kress, L. A. Collins, and P. Blottiau, *Phys. Rev. B* **67**, 054201 (2003).
- [202] S. Mazevet, M. P. Desjarlais, L. A. Collins, J. D. Kress, and N. H. Magee, *Phys. Rev. E* **71**, 016409 (2005).
- [203] J. Eggert., *Phys. Z.* **20**, 570 (1919).
- [204] M. N. Saha, *Philos. Mag.* **40**, 472 (1920).
- [205] S. M. Vinko, O. Ciricosta, and J. S. Wark, *Nat. Commun.* **5**, 3533 (2014).
- [206] S. X. Hu, *Phys. Rev. Lett.* **119**, 065001 (2017).
- [207] K. P. Driver, F. Soubiran, and B. Militzer, *Phys. Rev. E* **97**, 063207 (2018).
- [208] M. Bethkenhagen, B. B. L. Witte, M. Schörner, G. Röpke, T. Döppner, D. Kraus, S. H. Glenzer, P. A. Sterne, and R. Redmer, *Phys. Rev. Research* **2**, 023260 (2020).
- [209] W. Thomas, *Naturwissenschaften* **13**, 627 (1925).
- [210] F. Reiche and W. Thomas, *Z. Phys.* **34**, 510 (1925).

- [211] W. Kuhn, *Z. Phys.* **33**, 408 (1925).
- [212] M. P. Desjarlais, J. D. Kress, and L. A. Collins, *Phys. Rev. E* **66**, 025401 (2002).
- [213] M. Preising and R. Redmer, *Phys. Rev. B* **100**, 184107 (2019).
- [214] B. Monserrat, N. D. Drummond, C. J. Pickard, and R. J. Needs, *Phys. Rev. Lett.* **112**, 055504 (2014).
- [215] A. B. Belonoshko, *Geochim. Cosmochim. Acta* **58**, 4039 (1994).
- [216] J. R. Morris, C. Z. Wang, K. M. Ho, and C. T. Chan, *Phys. Rev. B* **49**, 3109 (1994).
- [217] R. Ahuja, A. B. Belonoshko, and B. Johansson, *Phys. Rev. E* **57**, 1673 (1998).
- [218] A. B. Belonoshko, R. Ahuja, O. Eriksson, and B. Johansson, *Phys. Rev. B* **61**, 3838 (2000).
- [219] Y. Usui and T. Tsuchiya, *J. Earth Sci.* **21**, 801 (2010).
- [220] S. Root, L. Shulenburger, R. W. Lemke, D. H. Dolan, T. R. Mattsson, and M. P. Desjarlais, *Phys. Rev. Lett.* **115**, 198501 (2015).
- [221] A. B. Belonoshko and L. S. Dubrovinsky, *Am. Mineral.* **81**, 303 (1996).
- [222] H. L. Tepper and W. J. Briels, *J. Chem. Phys.* **115**, 9434 (2001).
- [223] W. Humphrey, A. Dalke, and K. Schulten, *J. Mol. Graph.* **14**, 33 (1996).
- [224] J. P. Perdew and M. Levy, *Phys. Rev. Lett.* **51**, 1884 (1983).
- [225] L. J. Sham and M. Schlüter, *Phys. Rev. Lett.* **51**, 1888 (1983).
- [226] V. Vlček, R. Baer, E. Rabani, and D. Neuhauser, (2017), arXiv:1701.02023 .
- [227] M. D. Knudson, M. P. Desjarlais, M. Preising, and R. Redmer, *Phys. Rev. B* **98**, 174110 (2018).
- [228] M. Preising and R. Redmer, *Phys. Rev. B* **102**, 224107 (2020).
- [229] P. Loubeyre, R. Le Toullec, and J. P. Pinceaux, *Phys. Rev. B* **36**, 3723 (1987).
- [230] W. J. Nellis, S. T. Weir, and A. C. Mitchell, *Phys. Rev. B* **59**, 3434 (1999).
- [231] F. Datchi, P. Loubeyre, and R. Le Toullec, *Phys. Rev. B* **61**, 6535 (2000).
- [232] V. Y. Ternovoi, A. S. Filimonov, A. A. Pyalling, V. B. Mintsev, and V. E. Fortov, *AIP Conf. Proc.* **620**, 107 (2002).

- [233] A. Dewaele, J. H. Eggert, P. Loubeyre, and R. Le Toullec, *Phys. Rev. B* **67**, 094112 (2003).
- [234] M. A. Mochalov, R. I. Il'kaev, V. E. Fortov, A. L. Mikhailov, Y. M. Makarov, V. A. Arinin, A. O. Blikov, A. Y. Baurin, V. A. Komrakov, V. A. Ogorodnikov, A. V. Ryzhkov, E. A. Pronin, and A. A. Yukhimchuk, *J. Exp. Theor. Phys.* **115**, 614 (2012).
- [235] M. A. Mochalov, R. I. Il'kaev, V. E. Fortov, A. L. Mikhailov, V. A. Arinin, A. O. Blikov, A. Y. Baurin, V. A. Komrakov, V. A. Ogorodnikov, A. V. Ryzhkov, and A. A. Yukhimchuk, *JETP Lett.* **96**, 158 (2012).
- [236] M. Zhernokletov, V. Arinin, V. Buzin, Y. Grigorieva, N. Davydov, and V. Khrustalev, *AIP Conf. Proc.* **1426**, 1411 (2012).
- [237] M. A. Mochalov, R. I. Il'kaev, V. E. Fortov, A. L. Mikhailov, V. A. Arinin, A. O. Blikov, V. A. Komrakov, A. V. Ryzhkov, V. A. Ogorodnikov, and A. A. Yukhimchuk, *JETP Lett.* **101**, 519 (2015).
- [238] R. S. McWilliams, D. A. Dalton, Z. Konôpková, M. F. Mahmood, and A. F. Goncharov, *Proc. Natl. Acad. Sci. USA* **112**, 7925 (2015).
- [239] J. Zheng, Q. F. Chen, Y. J. Gu, J. T. Li, Z. G. Li, C. J. Li, and Z. Y. Chen, *Phys. Rev. B* **95**, 224104 (2017).
- [240] R. Jeanloz, P. M. Celliers, G. W. Collins, J. H. Eggert, K. K. M. Lee, R. S. McWilliams, S. Brygoo, and P. Loubeyre, *Proc. Nat. Acad. Sci.* **104**, 9172 (2007).
- [241] J. Klimeš, D. R. Bowler, and A. Michaelides, *J. Phys.: Condens. Matter* **22**, 022201 (2010).
- [242] K. Lee, E. D. Murray, L. Kong, B. I. Lundqvist, and D. C. Langreth, *Phys. Rev. B* **82**, 081101 (2010).
- [243] J. Heyd, G. E. Scuseria, and M. Ernzerhof, *J. Chem. Phys.* **118**, 8207 (2003).
- [244] J. C. Smith, F. Sagredo, and K. Burke, "Warming up density functional theory," in *Frontiers of Quantum Chemistry* (Springer Singapore, 2018).
- [245] S. Brygoo, M. Millot, P. Loubeyre, A. E. Lazicki, S. Hamel, T. Qi, P. M. Celliers, F. Coppari, J. H. Eggert, D. E. Fratanduono, D. G. Hicks, J. R. Rygg, R. F. Smith, D. C. Swift, G. W. Collins, and R. Jeanloz, *J. Appl. Phys.* **118**, 195901 (2015).
- [246] D. Alfè, L. Vočadlo, G. Price, and M. Gillan, *J. Phys.: Condens. Matter* **16**, S973 (2004).

- [247] G. Robert, P. Legrand, P. Arnault, N. Desbiens, and J. Cl  rouin, *Phys. Rev. E* **91**, 033310 (2015).
- [248] A. B. Belonoshko and L. S. Dubrovinsky, *Geochim. Cosmochim. Acta* **59**, 1883 (1995).
- [249] A. Belonoshko and R. Ahuja, *Phys. Earth Planet. Inter.* **102**, 171 (1997).
- [250] D. Alf  , M. J. Gillan, and G. D. Price, *J. Chem. Phys.* **116**, 6170 (2002).
- [251] L. Ko  i, R. Ahuja, A. B. Belonoshko, and B. Johansson, *J. Phys.: Condens. Matter* **19**, 016206 (2007).
- [252] A. B. Belonoshko, L. Ko  i, and A. Rosengren, *Phys. Rev. B* **85**, 012503 (2012).
- [253] L. Ko  i, R. Ahuja, and A. B. Belonoshko, *Phys. Rev. B* **75**, 214108 (2007).
- [254] J. Bouchet, F. Bottin, G. Jomard, and G. Z  erah, *Phys. Rev. B* **80**, 094102 (2009).
- [255] J. R. Morris and X. Song, *J. Chem. Phys.* **116**, 9352 (2002).
- [256] D. Alf  , *Phys. Rev. B* **68**, 064423 (2003).
- [257] Q.-J. Hong and A. van de Walle, *J. Chem. Phys.* **139**, 094114 (2013).
- [258] M. Preising, W. Lorenzen, A. Becker, R. Redmer, M. D. Knudson, and M. P. Desjarlais, *Phys. Plasmas* **25**, 012706 (2018).
- [259] R. K. Crawford and W. B. Daniels, *J. Chem. Phys.* **55**, 5651 (1971).
- [260] R. L. Mills, D. H. Liebenberg, and J. C. Bronson, *Phys. Rev. B* **21**, 5137 (1980).
- [261] W. L. Vos, M. G. E. van Hinsberg, and J. A. Schouten, *Phys. Rev. B* **42**, 6106 (1990).
- [262] P. Bergeron, D. Saumon, and F. Wesemael, *Astrophys. J.* **443**, 764 (1995).
- [263] The Supplemental Material at <http://link.aps.org/supplemental/10.1103/PhysRevB.102.224107> contains an in-depth discussion of the calculation of the ionization degree, the band gap approaches and their convergence, as well as the convergence of the EOS, the DC conductivity, the reflectivity, and the ionization degree.
- [264] K. F. Herzfeld, *Phys. Rev.* **29**, 701 (1927).
- [265] N. F. Mott, *Proc. Phys. Soc. A* **62**, 416 (1949).

- [266] J. M. McMahon, M. A. Morales, C. Pierleoni, and D. M. Ceperley, *Rev. Mod. Phys.* **84**, 1607 (2012).
- [267] R. Smoluchowski, *Nature* **215**, 691 (1967).
- [268] E. E. Salpeter, *Astrophys. J.* **181**, L83 (1973).
- [269] V. Dzyabura, M. Zaghoo, and I. F. Silvera, *Proc. Natl. Acad. Sci. USA* **110**, 8040 (2013).
- [270] K. Ohta, K. Ichimaru, M. Einaga, S. Kawaguchi, K. Shimizu, T. Matsuoka, N. Hirao, and Y. Ohishi, *Sci. Rep.* **5**, 1 (2015).
- [271] M. Zaghoo, A. Salamat, and I. F. Silvera, *Phys. Rev. B* **93**, 155128 (2016).
- [272] M. A. Morales, C. Pierleoni, E. Schwegler, and D. M. Ceperley, *Proc. Natl. Acad. Sci. USA* **107**, 12799 (2010).
- [273] M. A. Morales, J. M. McMahon, C. Pierleoni, and D. M. Ceperley, *Phys. Rev. Lett.* **110**, 065702 (2013).
- [274] G. I. Kerley, “Molecular-based study of fluids,” (American Chemical Society, Washington, 1983) p. 107.
- [275] N. C. Holmes, M. Ross, and W. J. Nellis, *Phys. Rev. B* **52**, 15835 (1995).
- [276] M. Ross, *Phys. Rev. B* **54**, R9589 (1996).
- [277] M. Ross, *Phys. Rev. B* **58**, 669 (1998).
- [278] G. I. Kerley, Sandia National Laboratories **SAND2003-3613** (2003).
- [279] R. C. Clay, J. Mcminis, J. M. McMahon, C. Pierleoni, D. M. Ceperley, and M. A. Morales, *Phys. Rev. B* **89**, 184106 (2014).
- [280] M. D. Knudson and M. P. Desjarlais, *Phys. Rev. Lett.* **118**, 035501 (2017).
- [281] M. Zaghoo and I. F. Silvera, *Proc. Natl. Acad. Sci. USA* **114**, 11873 (2017).
- [282] I. Tamblyn and S. A. Bonev, *Phys. Rev. Lett.* **104**, 065702 (2010).
- [283] R. S. McWilliams, D. A. Dalton, M. F. Mahmood, and A. F. Goncharov, *Phys. Rev. Lett.* **116**, 255501 (2016).
- [284] E. Y. Chen and B. M. S. Hansen, *Mon. Not. R. Astron. Soc.* **413**, 2827 (2011).
- [285] L. Hedin, *Phys. Rev.* **139**, A796 (1965).
- [286] W. G. Aulbur, M. Städele, and A. Görling, *Phys. Rev. B* **62**, 7121 (2000).
- [287] F. Aryasetiawan and O. Gunnarsson, *Rep. Prog. Phys.* **61**, 237 (1998).

C. Curriculum vitae

Geboren am 12.08.1990 in Günzburg

Studium/Forschung

- seit 03/2016 Promotionsstudium an der Universität Rostock
- 08/2016 Teilnahme am Workshop
Putting the Theory Back in Density Functional Theory
in Los Angeles (USA)
- 11/2015 - 02/2016 Kurzzeitstipendium im Rahmen des Graduiertenkollegs
Wechselwirkung komplexer Systeme mit elektromagnetischer Strahlung
des SFB 652
- 09/2015 Master of Science in Physik
Masterarbeit:
Dispersionskräfte in der Dichtefunktionaltheorie mit Anwendung auf Helium
in der Gruppe von Prof. Dr. Ronald Redmer
- 12/2013 - 08/2014 Arbeit als wissenschaftliche Hilfskraft in der Gruppe von Prof. Dr. Ronald Redmer
- 2013 - 2015 Studium im Studiengang Physik (Master) an der Universität Rostock
- 09/2013 Bachelor of Science in Physik
Bachelorarbeit:
Das Phasendiagramm von festem Helium bei hohen Drücken
in der Gruppe von Prof. Dr. Ronald Redmer
- 2010 - 2013 Studium im Studiengang Physik (Bachelor) an der Universität Rostock

Schulbildung

- 07/2010 Abitur
2001 - 2010 Besuch des "Dossenberger-Gymnasiums", Günzburg
1997 - 2001 Besuch der "Montessori-Schule", Günzburg

Lehre an der Universität Rostock

- SS 2021 Betreuung des Seminars im Rahmen der Vorlesung
Plasma- und Astrophysik
- SS 2019, WS 2020/21 - SS 2021 Zweitbetreuung bei der Anfertigung von Bachelorar-
beiten
- WS 2019/20, WS 2020/21 Betreuung des Seminars im Rahmen der Vorlesung
Thermodynamik
- SS 2019 - 2021 Betreuung des Versuchs *Density Functional Theory
Molecular Dynamics Simulations for Carbon* im Rah-
men des physikalischen Forschungspraktikums
- WS 2017/18 - SS 2019 Betreuung von Versuchen im Rahmen des physikalischen
Praktikums

Liste der Veröffentlichungen

- M. Preising, W. Lorenzen, A. Becker, R. Redmer, M. D. Knudson und M. P. Desjarlais
Equation of state and optical properties of warm dense helium
Physics of Plasmas **25**, 012706 (2018)
8 Seiten
- M. D. Knudson, M. P. Desjarlais, M. Preising und R. Redmer
Evaluation of exchange-correlation functionals with multiple-shock conductivity measurements in hydrogen and deuterium at the molecular-to-atomic transition
Physical Review B **98**, 174110 (2018)
10 Seiten
- M. Preising und R. Redmer
High-pressure melting line of helium from ab initio calculations
Physical Review B **100**, 184107 (2019)
6 Seiten
- Y. Cytter, E. Rabani, D. Neuhauser, M. Preising, R. Redmer und R. Baer,
Transition to metallization in warm dense helium-hydrogen mixtures using stochastic density functional theory within the Kubo-Greenwood formalism
Physical Review B **100**, 195101 (2019)
8 Seiten
- M. Preising und R. Redmer
Metallization of dense fluid helium from ab initio simulations
Physical Review B **102**, 224107 (2020)
7 Seiten

Liste der Fachvorträge

- M. Preising und R. Redmer
The Metallization of Helium at High Densities from ab initio Simulations
11th Fundamental Science with Pulsed Power: Research Opportunities and User Meeting,
Online-Konferenz (2020)
- M. Preising und R. Redmer
The High-Pressure Melting Line and Band-Gap Closure of Helium 10th International Workshop on Warm-Dense-Matter 2019,
Travemünde, Deutschland (2019)
- M. Preising und R. Redmer
The High-Pressure Melting Line of Helium
6. Treffen des Graduiertennetzwerkes Life, Light and Matter 2019,
Rostock, Deutschland (2019)
- M. Preising und R. Redmer
The Melting Line and the Band Gap of Helium
9th Fundamental Science with Pulsed Power: Research Opportunities and User Meeting,
Albuquerque, USA (2018)
- M. Preising und R. Redmer
Thermal and Optical Properties of Dense Helium
6th Joint Workshop on High Pressure, Planetary and Plasma Physics,
Göttingen, Deutschland (2017)
- M. Preising und R. Redmer
Thermal and Optical Properties of Dense Helium
AMCP-Seminar (Atome, Moleküle, Cluster und Plasmen),
Rostock, Deutschland (2017)
- M. Preising, W. Lorenzen, A. Becker, R. Redmer, M. D. Knudson und M. P. Desjarlais
Metallization and Melting Line of Dense Helium
Graduiertenkolleg des Physikalischen Instituts,
Rostock, Deutschland (2016)

Liste der Posterpräsentationen

- APS March Meeting 2021,
Online-Konferenz (2021)
- 41st International Workshop on High Energy Density Physics with Intense Ion
and Laser Beams,
Online-Konferenz (2021)
- WE-Heraeus Seminar on Matter under Extreme Conditions,
Online-Konferenz (2020)
- 8th Joint Workshop on High Pressure, Planetary and Plasma Physics,
Dresden, Deutschland (2019)
- Workshop on High-Energy-Density Physics,
Rostock, Deutschland (2019)
- 10th International Workshop on Warm-Dense-Matter 2019,
Travemünde, Deutschland (2019)
- Matter in Extreme Conditions: from MATerial science to Plasmas for Labo-
ratory Astrophysics,
Montgenevre, Frankreich (2019)
- 7th Joint Workshop on High Pressure, Planetary and Plasma Physics,
Berlin, Deutschland (2018)
- 9th Fundamental Science with Pulsed Power: Research Opportunities and
User Meeting,
Albuquerque, USA (2018)
- 6th Joint Workshop on High Pressure, Planetary and Plasma Physics,
Göttingen, Deutschland (2017)
- Strongly Coupled Coulomb Systems,
Kiel, Deutschland (2017)
- 8th Fundamental Science with Pulsed Power: Research Opportunities and
User Meeting,
Albuquerque, USA (2017)
- Putting the Theory Back in Density Functional Theory,
Los Angeles, USA (2016)

Danksagung

Zuerst möchte ich mich bei meinem Betreuer Prof. Dr. Ronald Redmer bedanken. Dabei danke ich neben der sehr guten Betreuung aller meiner Arbeiten auch für das Vertrauen im Bezug auf die Administration der Rechentechnik unserer Arbeitsgruppe sowie für die Möglichkeit, meine Arbeit auf verschiedensten Konferenzen zu präsentieren. Allen meinen Kollegen danke ich für viele anregende, hilfreiche und interessante Gespräche sowie die fantastische Arbeitsatmosphäre. Außerdem möchte ich allen bisherigen Administratoren der Arbeitsgruppe für den Aufbau und die Instandhaltung eines exzellenten Computersystems danken, insbesondere Manuel Schöttler und Clemens Kellermann, die mir die Feinheiten unseres Systems beigebracht haben.

Die für diese Arbeit erforderliche Rechenleistung haben der HLRN-Verbund sowie die Cluster `venus` und `titan` am ITMZ bereitgestellt. Besonderer Dank geht hier an Daniel Cebulla und Martin French für die Bearbeitung der HLRN-Anträge sowie an Malte Willert für die Instandhaltung der Cluster am ITMZ.

Für die Stunden des Korrekturlesens und die vielen hilfreichen Kommentare danke ich Ronald Redmer, Fabian Krumm, Armin Bergermann, Julian Last sowie meinem Vater.

Im privaten Umfeld danke ich meiner Familie für die Unterstützung, vor allem meinen Eltern Cornelia und Burkhard und meinen Schwestern Sarah und Ann-Kristin. Außerdem danke ich allen meinen Freunden, insbesondere: Julian, Diemo und Roland für unsere Musik; meinen Studienkollegen für die gemeinsame Zeit; allen, mit denen ich je Musik gemacht habe; Daniel für die Wanderungen; Alex für die Handstände; Vincent, Diemo, Jochen und Jens für die Radtouren; Julian für das Tischtennispielen; Sven für die vollbrachten Wunder; Dr. Micheal Greger; allen Teilnehmern von Spieleabenden jeglicher Art. Außerdem danke ich dem 45 Grad Rostock und meinem treuen Fahrrad für die zahllosen Stunden Freude.

Erklärung

Ich versichere hiermit an Eides statt, dass ich die vorliegende Arbeit selbstständig angefertigt und ohne fremde Hilfe verfasst habe. Dazu habe ich keine außer den von mir angegebenen Hilfsmitteln und Quellen verwendet. Die den benutzten Werken inhaltlich und wörtlich entnommenen Stellen habe ich als solche kenntlich gemacht.

Rostock, den 30. April 2021

Martin Preising